Synthesis and Engineering of Metal-organic Frameworks for Liquid Phase Applications

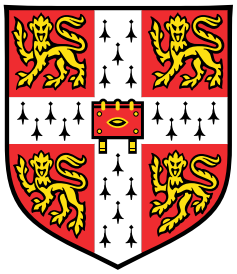

Diana Vulpe

Department of Chemical Engineering and Biotechnology

University of Cambridge

This dissertation is submitted for the degree of

Doctor of Philosophy

Magdalene College

February 2019

Declaration

I hereby declare that except where specific reference is made to the work of others, the contents of this dissertation are original and have not been submitted in whole or in part for consideration for any other degree or qualification in this, or any other university. This dissertation is my own work and contains nothing which is the outcome of work done in collaboration with others, except as specified in the text and Acknowledgements. This dissertation contains fewer than 65,000 words including appendices, bibliography, footnotes, tables and equations and has fewer than 150 figures.

Diana Vulpe

February 2019

Acknowledgements

First and foremost, I would like to express gratitude to my supervisor, David Fairen-Jimenez, for setting such a great example for all his students. For welcoming me in an open-minded and forward-looking research group. For offering us all the freedom in pursuing our own interests and scientific curiosity and challenge us to learn and become better researchers and better communicators. I could not have asked for a more supportive and understanding supervisor. Thank you.

To Dr. Peyman Z. Moghadam, for all the uplifting discussions and urging me to believe in my capabilities and in the strength of my work. To all my colleagues and friends, past and present, from Adsorption and Advanced Materials Laboratory, especially Sam Haddad, Tian Tian, Gonzalo Prados-Joya, Aurelia Li, Marta Aragones-Anglada for making this place feel like home as well as their encouragement, support and friendship both in and outside the office. To Drew Baker, for his friendship and constant support through the good times and the bad. To Jack Williams for frequently curing the blues with much needed doses of laughter!

Most importantly, to my family, especially my parents, for their unconditional love, for supporting my choices no matter what and offering me the opportunity to acquire the best education I could ever get. To my sister, my role-model, my anchor and the most self-less person I know. Thank you for always being there for me.

To all the running trails around Cambridge that I could escape to daily, may those vast open magnificent fields remain as I will always remember them. To nature.

The EPSRC is acknowledged for funding my research.

Abstract

Metal-organic frameworks (MOFs) are a class of highly versatile porous materials expressing previously unobserved high surface areas and tuneable both internal and external chemical environments. They are a product of a self-assembly process between metal ions and organic linker molecules which form infinite 3D nets with topologies specific to the coordination capabilities of the metals and available binding sites of the linkers. Thus due to the virtually infinite number of combinations possible, and hence, vast predictability of their fields of applications, MOFs have gained significant interest in the research community in the past two decades. MOFs are currently very well known for their gas capture, separation and storage capabilities, catalysis and drug delivery amongst many others, which entail exposure to liquid or humid media. However, the current shortfall of these structures is insufficient data on their chemical stability as well as the lack of a standardised stability testing approach across literature. The aims of the current dissertation are to: 1) address the gaps in the knowledge of water stability of MOFs by designing and applying an all-encompassing stability testing protocol as well as observing the key factors governing water stability of MOFs and 2) to test the performance of selected water resilient MOFs for micro-pollutant capture purposes and assess their suitability in such applications.

It was observed that whereas a high metal cluster connectivity is an important factor determining framework stability, such as that encountered in UiO-66, engineered missing linker crystal defects prove to be detrimental. On the other hand, the inclusion of functional groups on the linkers confer a metal cluster shielding effect and can thus effectively prevent the diffusion of attacking chemical species into the MOF structure, as observed in tagged UiO-66 structures such as UiO-66-NH_2 and UiO-66-NO_2. Furthermore, this work finds that, even in large pore size MOFs, the pore collapse inducing capillary effects taking place during direct activation from high surface tension solvents can be navigated by inclusion of

an increasing number of hydrophobic functionalities, with major differences being observed from the dimethyl PCN-56 to the tetramethyl PCN-57 structures.

The reason for the moderate stability of ZIF-8 is the high basicity and inherent hydrophobicity of the 2-methyl imidazole linker. Nevertheless, this work attests the very poor stability of ZIF-8 in acidic media, and moreover, a high degree of instability even under neutral conditions. More importantly, the kinetic stability of ZIF-8 is found to be dramatically improved by shaping. Indeed, when ZIF-8 is shaped into a high density pure phase monolith, the extent of linker release is reduced by 28% in neutral conditions followed by an impressive 76% reduction in acidic environment compared to the powdered form. Whereas the water stability of monolithic UiO-66 still needs to be improved, it was found that the large pore MOF-808 structure, whilst in monolithic configuration, is successfully activated from water after stability testing with almost complete retention of original porosity, whereas its powdered analogue suffered complete amorphisation under the same conditions.

The current dissertation also presents a highly reproducible in-situ growth and deposition procedure of ZIF-8 on highly mechanically stable open frontal area honeycomb like ceramic cordierite substrate. By tailoring the surface chemistry of the substrate, especially with ZnO, it was found that the growth of ZIF-8 was significantly enhanced, with consistent mass uptake to achieve a uniform and complete surface coverage. ZIF-8 particles appeared to stack on top of each other forming a thick outer layer comprising of highly crystalline ZIF-8. Moreover, good adherence of the film was attested during the ultrasonic cleaning procedures.

Finally, with knowledge of the water stability of the tested MOFs, ZIF-8 and UiO-66 were investigated for adsorption of endocrine disruptor micro-pollutant, bisphenol B (BPB). Whereas both MOFs promise very rapid uptake within less than 30 minutes of contact, their respective structural intricacies and stability limitations affect their removal capabilities. As such, powdered ZIF-8 demonstrates poor stability, especially in high concentrations of BPB, whereas the monolithic configuration yielded superior performance in both batch and flow mode conditions. Whereas UiO-66 presents larger pores and enhanced water phase stability in the powdered configuration, the adsorptive performance is hampered by presence of crystal defects which cause competitive adsorption with the surrounding water and thus returning a lower overall removal efficacy, compared to the hydrophobic ZIF-8.

In conclusion, this work presented a working framework for testing the water phase stability of MOFs, as well as applying this knowledge in order to effectively use said MOFs for liquid phase adsorption applications thus proving the promising potential of monolithic MOFs for water treatment and reuse applications.

Table of contents

List of figures

List of tables

Nomenclature

Q_e	Quantity adsorbed at equilibrium ($mg.g^{-1}$)
Q_{Ads}	Quantity adsorbed ($mg.g^{-1}$)
Q_t	Quantity adsorbed at time t ($mg.g^{-1}$)
Q_{max}	Maximum theoretical adsorption capacity ($mg.g^{-1}$)
K_L	Langmuir adsorption constant (-)
k_2	Pseudo second order kinetic rate constant ($mg.g^{-1}.min^{-1}$)
R^2	Dimensionless correlation coefficient
C	Dimensionless constant related to the enthalpy of adsorption
m	Mass (g or mg)
t	Time (min.)
V	Volume (L or mL)
C_0	Initial concentration (ppm)
C_e	Equilibrium concentration (ppm)
C_t	Concentration at time=t (ppm)
S_{BET}	Specific surface area (m^2/g)
A_m	Average area occupied by a molecule of adsorbate in the completed monolayer (Å)

N_A Avogadro constant (mol^{-1})

RMM_{ads} Relative molecular mass of the adsorbate gas (g/kmol)

P Partial vapour pressure of adsorbate gas in equilibrium with the surface at 77.4 K (Pa)

P_0 Saturated pressure of adsorbate gas (Pa)

V_a Volume of gas adsorbed at STP (mL)

V_m Volume of gas adsorbed at STP to produce one monolayer on the sample surface (mL)

θ Angle between incident light and lattice planes (°)

d Lattice spacing (nm)

λ Wavelength of incident light (nm^{-1})

m Integer related to order of the lattice

XRD X-ray Diffraction

pXRD Powder X-ray diffraction

SEM Scanning Electron Microscopy

TGA Thermo-gravimetric analysis

HPLC High pressure/performance liquid chromatography

$_{powd}$ZIF-8 Powdered ZIF-8

$_{mono}$ZIF-8(FP) Fully porous monolithic ZIF-8

$_{mono}$ZIF-8(SP) Semi-porous monolithic ZIF-8

$_{powd}$UiO-66 Powdered UiO-66

$_{mono}$UiO-66(DMF) DMF washed monolithic UiO-66

$_{mono}$UiO-66(EtOH) EtOH washed monolithic UiO-66

$_{powd}$MOF-808 Powdered MOF-808

$_{mono}$MOF-808(DMF) DMF washed monolithic MOF-808

$_{mono}$MOF-808(EtOH) EtOH washed monolithic MOF-808

ZAD Zinc acetate dihydrate

IPTES 3-(2-imidazolin-1-yl)propyltriethoxysilane

MEA Monoethanolamine

EtOH Ethanol

IPA Isopropanol

MeOH Methanol

DMF N,N-dimethylformamide

BDC Benzene-1,4-dicarboxylic acid

BTC Benzene-1,3,5-tricarboxylic acid

2-mIm 2-methyl imidazole

IPTES 3-(2-imidazolin-1-yl)propyltriethoxysilane

ZAD Zinc acetate dihydrate

BPB Bisphenol B

Chapter 1

Introduction

1.1 Motivation and Challenges

As global human population increases [1] we are in dire need of boosting sustainability and self-sufficiency. This comes at a time when we are ever more conscious of the efforts we need to address in order to mitigate the catastrophic effects of climate change as well as the rapid depletion of fresh drinking water resources. Even if the global forces have commited to act on the rapidly changing fate of our environment and livelihoods through policy implementations and international treaties [2], the vacillating and, somewhat, volatile nature of global politics today precludes these aims from being imminently met.

Efforts thus need to be geared towards implementing innovative downstream science that could bring sustainability closer to industrial reality than ever before. Key to this is the design, synthesis, and ultimately large-scale roll-out of novel chemical structures that would enable selective and efficient separation of chemical species detrimental to living beings.

Metal-organic frameworks (MOFs) have been an emerging disruptive force in porous materials research for the last 20 years. Indeed, their potential has been speculated in vast fields of scientific investigation and their applicability demonstrated through countless proof-of-concept studies. Moreover, few have been successful at bringing this technology to industrial attention and deployment as the knowledge on the subject-matter advances. Nevertheless, MOFs are currently far from industrial applicability firstly and foremostly due

to: a) the shape-induced disadvantage of MOFs being obtained as powdered materials, and, b) insufficient knowledge on their true physico-chemical stability.

The aim of the current work is to investigate and understand the role of MOF shaping into monolithic structures towards their applicability in liquid phase media. Furthermore it aims to understand the role of network composition as well as its macrostructure towards its overall stability in the liquid environment.

1.2 Literature Review

Metal-organic frameworks (MOFs), or porous coordination polymers (PCPs), are a class of highly versatile and minutely tunable materials expressing previously unobserved high surface areas, of up to 10 000 m^2/g [3]. They primarily consist of interconnected metal ion nodes or clusters coordinated to organic linker molecules in various combinations. Changing either one of the two counterparts indeed affects the physico-chemical characteristics, the pore sizes being easily adjusted by selecting linkers of different length [3]. This allows for finely tuned selective design in order to create MOFs of highly specified functionalities for different target applications. The applicability of MOFs is currently being investigated in a wide array of fields spanning from microelectromechanical sensor devices [4] to catalysis [5, 6], drug delivery [7, 8] and gas storage and separation [9–11], amongst many others [12].

These highly porous structures are synthesised via a self-assembly co-polymerisation process, numerous synthetic protocols existing for any one type of MOF, ranging from solvent-free sono and mechano-chemical to solvothermal procedures [13–15]. A schematic illustration of the assembling steps of metal nodes and organic linkers to form a 3D MOF is shown in Figure 1.1. The two components (metal and linker) are firstly mixed together,

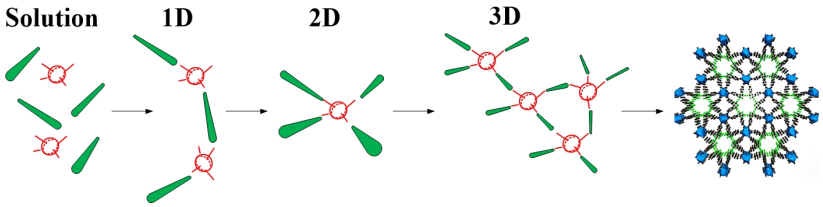

Fig. 1.1 Self-assembly process of metal ions and organic linkers to form 3D porous coordination polymers

instantaneously the organic linkers start forming a 1D coordination polymer with the metal cluster. As the reaction proceeds, a 3D MOF starts taking shape, its final morphology being largely dictated by reaction time, reactant concentration, solvent, temperature, pH, or any combination of these factors [15, 16].

1.2.1 Metal-organic Frameworks as Novel Liquid Phase Adsorbents

Due to their very high surface areas, MOFs have been receiving considerable attention in the scope of liquid phase adsorption applications, such as water treatment. Adsorptive capture and removal of toxic compounds is, perhaps, the most safe, side-product-free option, when considering techniques such as photocatalytic degradation, which inevitably introduce additional oxidative species [17–23]. Nevertheless, adsorptive water treatment technologies suffer from recyclability issues which impose a waste management concern [22].

Notwithstanding their limited water stability, discussed in the section to follow, MOFs have shown to outperform traditional liquid phase adsorbents such as activated carbons and zeolites in terms of adsorption capacity, and moreover, selectivity[24]. Whereas most MOFs can be freely used in their unfunctionalised form, showing excellent performance, their easy tunability means that MOFs can also be altered to offer an enhanced selectivity for different target chemistries. To date, numerous studies have shown the tremendous potential of MOFs for water treatment and reuse applications [22, 25, 26]. Indeed, MOFs have come at the fore-front of adsorptive removal research due to their diverse interaction mechanisms, which can include either or both, and are not limited to, chemical, such as coordination and acid-base interactions, as well as physical interaction mechanisms, such as electrostatic and van der Waals forces [18, 22].

Perhaps the most commonly researched applications in water treatment is targeted towards removal of ubiquitous pollutants from the textile industry such as dyes. Luo et al. [27] investigated the removal of methylene blue and malachite green using MIL-101 MOF with grafted sulfonic acid surface functionalities. This study found that the uptake capacity of this structure was highly pH dependent, reporting increasing uptake with increasing pH; however, the interaction mechanisms shifted - at low pH the π-π interactions dominated, whereas at high pH, electrostatic. In another report, Haque et al. [28] studied the adsorption of methyl orange dye using MIL-101 and MIL-53 using original and grafted versions of the frameworks.

This study proved the importance of pore size upon adsorption capacity, and moreover, of surface modification. With surface modified MOFs showing an enhanced rate of uptake and high equilibrium adsorption, even at the cost of pore size reduction with incorporation of bulky functional groups. All MOFs, functionalised and not, showed enhanced removal efficiency in contrast to activated carbon [27, 28].

Another particularly dominant problem is capture of heavy metal ions from water. Notably, traditional adsorbents have very weak binding capacity towards metal ions as well as very low specificity. Peng et al. [29] successfully created a broad spectrum heavy metal ion trap by creating high density available binding site structure through grafting EDTA on the large pore Zr-based MOF-808 [29]. The resultant functionalised MOF yielded excellent results in both batch and, more importantly, breakthrough studies with excellent reusability. Framework MOF-808 also proved successful in adsorption of inorganic selenium in a study conducted by Drout et al. [30], yielding very high gravimetric and volumetric adsorption capacity. Moreover, due to the large pore width exhibited by MOF-808, diffusion of selenium was facilitated to conclude equilibrium within less than 5 minutes of contact.

Major pollutants also emerge from agricultural waste, such as pesticides and herbicides, Seo et al. [31] investigated removal of methyl propionic acid with UiO-66 and found that the adsorption capacity exceeded that of activated carbon, especially at very low concentrations. Furthermore, the rate of uptake was found to be over 7 times higher than activated carbon [31]. At the same time, structures MIL-101 and MIL-53 were reported to have negligible uptake for the same target molecule. However, for UiO-66, the adsorption capacity held a strong pH dependence, with higher uptake in acidic conditions - however, the stability was not discussed. Other sources of water pollution arrive from cooling fluids and other anti-freezing products. Jiang et al. [32] studied the feasibility of using ZIF-8 as an adsorbent for benzotriazoles and found remarkably high adsorption capacities and favourable kinetics even in very high concentrations. Household wastes also commonly contain pollutants from pharmaceuticals and their metabolites, as well as other personal care products. Hasan et al. [24] have successfully proved the use of Cr and Fe based MIL-101 framework for removal of anti-inflammatory drug naproxen as well as bioactive metabolite clorfibric acid. The MOF expressed enhanced uptake relative to activated carbon due to strong electrostatic interactions, as well as large pore size.

However, the problem with most adsorption studies utilising various MOFs, but also other adsorbents, is that, as Dias et al. [22] pointed out, a direct comparison between the different MOFs as well as other adsorbents is frequently challenging. This is due to that the fact that various pollutant concentrations are used as well as differing adsorbent loadings. Moreover, adsorption is also studied at fixed pH, and, for the purpose of studying the adsorption mechanism, many studies report adsorption capacity as a function of pH, failing to discuss the pH stability implications of MOFs.

1.2.2 Stability of MOFs in the Liquid Phase

As pointed out above, when considering the use of MOFs for liquid phase applications, in aqueous systems especially, their stability must not be overlooked. Water stability, however, is not only important for liquid phase adsorption applications, such as water treatment; but in the gaseous phase as well. For those instances where MOFs are researched for CO_2 capture and storage potential, MOFs would also come in contact with moisture from flue gas, or even from the environment if they are exposed to the atmosphere [33–38]. Unfortunately, the vast majority of MOFs suffer from both moisture sensitivity and poor hydrothermal stability which sets back their industrial deployment [37–39].

Historically, the stability of MOFs has been assessed by exposing MOFs to certain test conditions, followed by material recovery and reactivation, ultimately, the crystallinity of the test material would be analysed. The problem with this, however, is that often if only a fraction of the test material is degraded, the remaining crystalline fraction is the one detected in routine X-ray diffraction scans [39–41], hence the vast majority of stability assessments are of a qualitative nature. Consequently, the majority of recovered MOFs are claimed to be stable, with unchanged crystallinity, and to date, there is no MOF stability assessment standard agreed upon across the research field [39, 42]. To counteract this, when assessing the stability of a MOF, the results must be accompanied by additional data, such as quantifying the adsorption capacity of the recovered material as well as the extent of dissolution [39]. Another problem is that many studies embark on application testing of MOFs reporting excellent results but failing to discuss the stability of their tested structures. For example, whilst some studies claim that ZIF-8 yields good adsorption capacity under highly acidic

conditions [43]; another report would state that the same MOF degrades even in neutral conditions at room temperature [44].

Water stability of MOFs is a complex phenomenon and is governed by an interplay of a number of factors. To start with, herein, stability is termed as the resistance to degradation under exposure to an aqueous environment. Furthermore, stability can be of thermodynamic or kinetic nature; the former entails long term resistance to degradation whereas the latter defines the stability of a framework under short exposure times [45].

Figure 1.2 illustrates the major factors governing stability of MOFs as well as known ways of improving their water stability. The choice of combination of metals and linkers defines the overall thermodynamic and architectural stability and is thus very important in the strategic design of water stable MOFs. First of all, the strength of the metal-linker bond must be higher than that of metal and water in order for a MOF to be water stable [37]. The metal must possess a high oxidation state, which will, in turn, tend to form stronger bonds with ligands; as the metals are Lewis acids, these have an inherent feature of forming stronger bonds with highly basic ligands, expressing high pK_a values [42, 45–47]. An increased charge of the metal centre will contribute to decreased lability by conferring an increased electrostatic interaction between metals and ligands, hence metals with lower oxidation states, such as Zn^{2+}, will be able to form weaker frameworks with hard bases.

Charge density also plays an important role, hard metal ions, such as Zr^{4+} or Cr^{3+} , can form stronger bonds with oxygen donor ligands. This is a feature elegantly showcased in the development of water stable MOFs such as the Zr-based UiO-66 and Cr-based MIL-101 [48]. Additionally, the metal must also possess a high valence as this will dictate the connectivity of the framework, and thus the number of ligands surrounding each metal or metal cluster [46]. This means that the framework will be able to withstand its architectural integrity even in the event of a certain degree of disconnection as a result of ligand substitution during hydrolysis [48]. Ligand length and hydrophobicity also play a major role [33]; typically, large linkers are used as a way of tuning the pore size of MOFs in order to create large pores, as required in drug loading applications for example [49]. However, this facilitates transport of attacking species within the MOF pore enabling easy access to the metal centre. This also poses a problem during activation of a framework, wherein as the solvent evacuates the internal pores it brings about capillary forces which contribute to framework collapse [39].

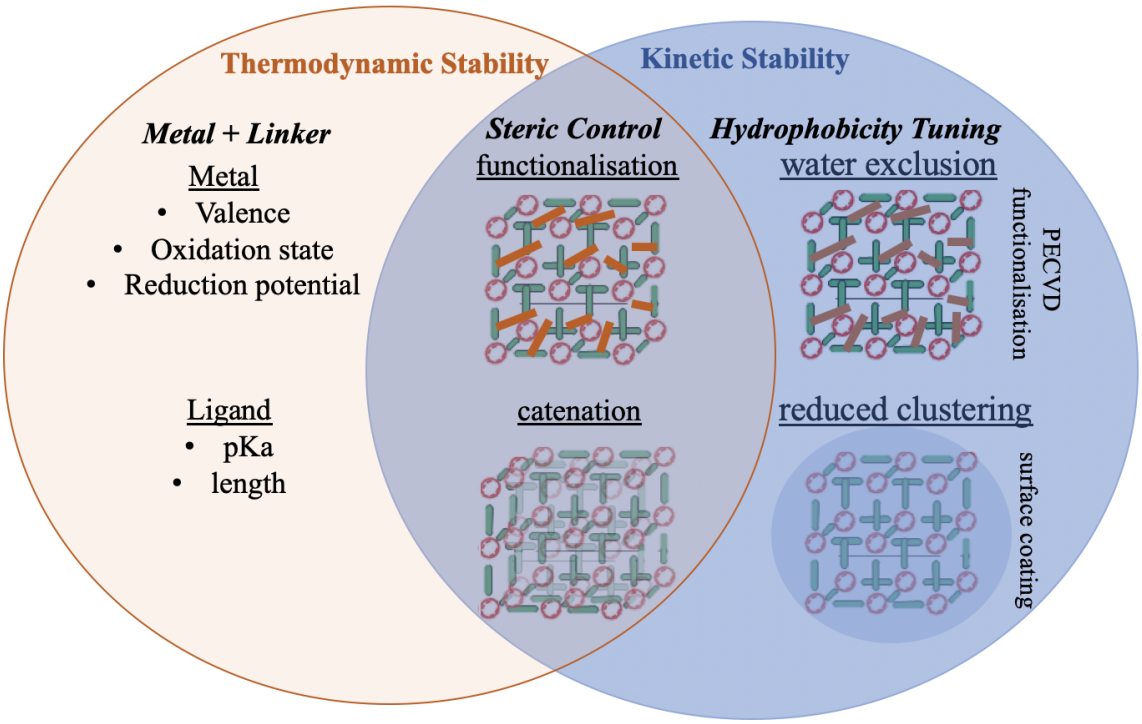

Fig. 1.2 Conceptual diagram illustrating factors affecting MOF thermodynamic and kinetic stability as well as ways of improving water stability. PECVD stands for plasma enhanced chemical vapour deposition.

The presence of functional groups on ligands, especially if they are short, can in principle, shield the metal centre from any attacking species, and, if they are hydrophobic, can prevent the diffusion of water into the pores [33, 50].

Nevertheless, for those instances where MOFs are required to withstand short-term exposure to moisture, several approaches can be used to improve their short term kinetic stability. These include incorporation of functional groups; either using functionalised linkers during the synthesis stage or post-synthetic modification. Inclusion of functional groups bring in two advantages: 1) they can be hydrophobic and 2) these create a steric hindrance effect conferring limited access to the metal centre, thus water cannot easily penetrate the pore and attack the metal cluster. Jasuja et al. [42] demonstrated that the incorporation of an increasing number of methyl groups along a dicarboxylic acid ligated Zn MOF improves its kinetic stability but at the same time, the exact positioning of the functionalities also played a major role. Hydrophobic moieties such as methyl and fluorinated groups have consistently

shown to improve kinetic stability of certain MOFs in a number of studies [36, 37, 40, 51, 52], but so far, the data reported was qualitative, providing routine X-ray diffraction patterns.

Another popular way of anchoring hydrophobic functionalities on MOFs is through plasma enhanced chemical vapour deposition. DeCoste et al. have previously attempted to incorporate fluoro functional groups on the highly water labile Cu paddlewheel framework, HKUST-1, the treated samples showed improved short term water stability [41]. However, this approach also caused significant volumetric capacity reduction, of around 25%, due to incorporation of the bulky functional groups. Another claim is that longer exposure to oxygen plasma slows down water uptake by pores of HKUST-1, also oxygen plasma can reactivate the pores following exposure to moisture [53]. At the same time plasma treatment can reduce crystallinity of a MOF due to chemical bond breaking; in fact, plasma treatment can be used to create post-synthetic hierarchical mesopores within a MOF, as was proved with UiO-66 (improving its hydrophobicity at the same time) [54].

Jasuja et al., in a separate study, have shown that the water stability of certain low oxidation state Zn MOFs can be improved through catenation, even with ligands expressing low pK_a values [55]. Catenation is a procedure wherein two frameworks are interpenetrated, conceptually illustrated in Figure 1.2. Another approach for protecting the MOF from attacking water species with a promising hydrophobic effect is carbon coating; however, this would have a significant effect on the result surface area of the material, and moreover, might prevent the desired species from entering the available pores [56].

1.2.3 Synthesis and Shaping of MOFs

Working towards expanding the library of MOF structures comes to no avail when considering the limited applicability of MOFs alone. Another factor dictating the applicability of MOFs is their morphology. MOFs are vastly obtained as fine powders which cannot be used directly in industrial settings. Typically, powders have to be compacted or pelletised in order to be packed into columns, powders also create very high pressure drops which requires more operational maintenance. Unfortunately, compaction and pelletisation are both processes detrimental to MOFs.

Nonethess, compaction under high pressure has been the most traditional MOF shaping method. As such, compacted materials express a higher density than powders, however, the

high pressures applied during the compaction process cause significant amorphisation of the MOF structure [57, 58]. For example, structures such as UiO-66 and ZIF-8 (discussed in the sections to follow) can only withstand pressures up to 200 MPa before experiencing amorphisation [58, 59]. Whereas the Cu-Cu paddlewheel structure, HKUST-1, demonstrates reduced performance at ∼70 MPa [60].

Attention of the research community is shifting towards the integration of the properties of these nano-scale structures into MOF-based composite materials. So far, significant proof-of-concept studies have laid the grounds to what is now a rapidly growing field of MOF research. Indeed, since the conception of MOF composites, the window of applicability of such materials has considerably broadened [15, 61–63]. Especially, with the current advancements in materials science, it is now not only possible to fabricate minute high aspect ratio structures, but to finely control and tune the film morphology, thickness, crystallographic orientation and surface functionalities [62]. This wealth of knowledge can thus be transferred and applied to the development of a diverse range of MOF composite materials with enhanced properties. Figure 1.3 illustrates some of the MOF-based composites obtained, including MOF nanowires and nanotubes, sponges and membranes. Some eloquent examples of such structures would

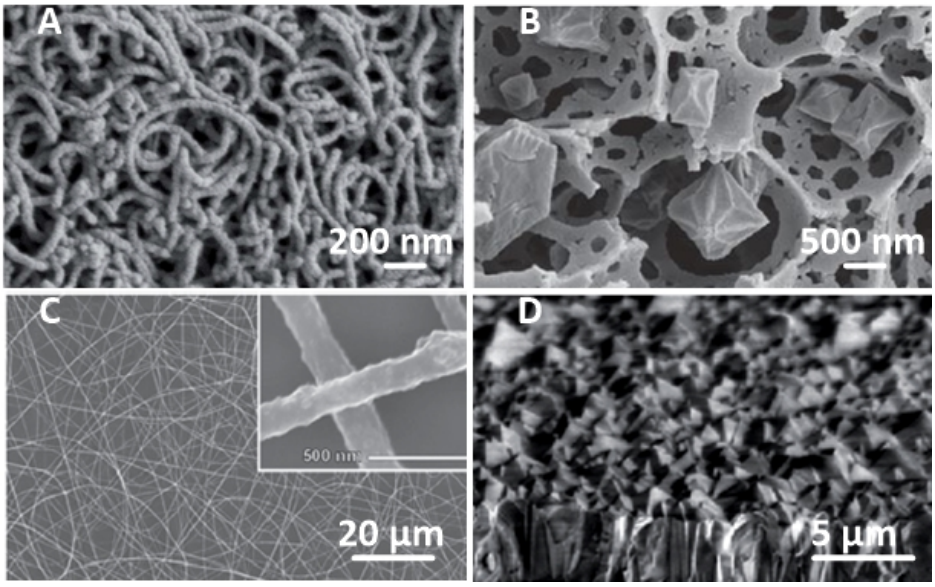

Fig. 1.3 Examples of MOF composites. **A)** ZIF-8 grown on carbon nanotubes reported by Yoo et al. [74] **B)** MOF-sponge composites obtained by Calvez et al. [72] **C)** ZIF-8 grown on ZnO nanorods developed by Hanan et al. [75] **D)** ZIF-8 membrane obtained by Bux et al. [76]

be MOFs studied for drug delivery applications where it is found that their biocompatibillity is significantly enhanced through encapsulation of the drug-loaded crystalline MOF into biopolymers [61]. Additionally, the integration of MOFs as chromatography stationary phases, in both liquid and gaseous media, is heavily contemplated in separation science [64–67]. Other more extensively explored composites entail MOF membranes, which act as sieving enhancers [68–70], MOF sponges and foams [71, 72]. Whereas most of MOF composite research has been angled towards the study of the properties and growth mechanism of MOF thin-films, a few have been employed into bench-scale applications such as catalysis and chemical separations [66, 73].

Recent advancements in MOF epitaxial patterning via dry etching techniques see the deployment of MOFs within microelectromechanical systems (MEMS) technology for sensing applications [77]. Several other approaches entail post-synthetic treatment and shaping, a typical example being that of immobilising MOFs onto ceramic beads or encapsulating into core-shell structures such as colloidosomes or nanotubes [74, 78–80]. Nonetheless, such structures require very tedious and long synthesis processes, frequently yielding issues in terms of reproducibility [61].

In light of the drawbacks of designing and synthesising MOF-based composites, especially for those applications which require pure MOF-phase materials in order to achieve a high performance, in recent years, we have developed a new sol-gel synthetic procedure for the synthesis of monolithic MOFs. The sol-gel procedure avoids the use of binders or high pressures [9, 81] in order to obtain pure monolithic MOFs expressing elevated mechanical resilience. Tian et al. first reported a mechanically superior monolithic ZIF-8 [81] in 2015, the room-temperature synthetic procedure was then extended to develop monolithic Cu-based HKUST-1 [9]. This procedure was later modified by Connolly et al. [82] to develop monolithic MOFs requiring high temperature synthetic protocols, such as the ubiquitous Zr-based MOFs UiO-66 and MOF-808.

This synthetic methodology, represented in Figure 1.4, primarily entails the use of a solvent with a low surface tension, followed by vigorous washing and careful drying of the product. These parameters are especially crucial towards the formation of a monolith because, as the solvent is removed from the wet gel during the drying phase, the stresses brought about by solvent evaporation influence the intergrowth of the primary particles. In the case

of powder synthesis, where the solvent is typically water and drying temperature is around 80-100°C, the fast removal of solvent from the interstices leaves discrete agglomerated particles. On the other hand, if a solvent with a low surface tension is used, such as a low molecular weight alcohol (e.g. ethanol), in conjunction with drying at room temperature and ambient pressure, the wet gel structure is maintained by means of the primary particles acting as binders within the evolving structure. The result is a densified, crystalline solid MOF with a glassy-like complexion and exhibiting elevated mechanical resilience [9].

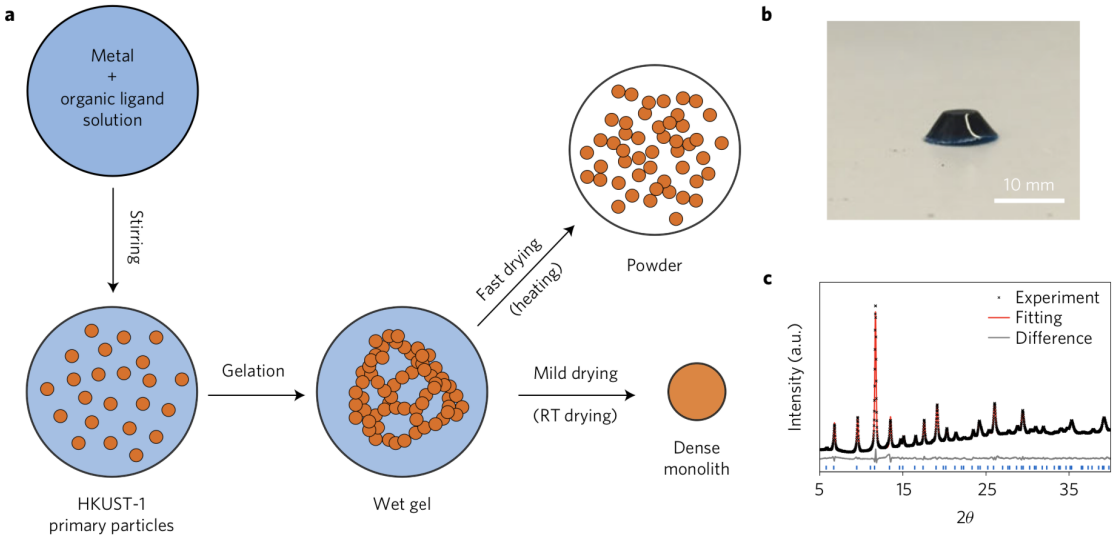

Fig. 1.4 Schematic representation of formation of monolithic and powdered MOFs. **a** the synthetic procedure follows a sol-gel formation protocol wherein a dense phase monolith is obtained by employing mild drying conditions on the wet gel whereas a powder is formed by using high temperatures; **b** an optical micrograph of HKUST-1 monolith and **c** comparison of XRD patterns of the formed monolithic HKUST-1 material (black symbols) the simulated Pawley fitting (red line) and the difference between the two (grey line) confirming the successful formation of HKUST-1. Adapted from Tian et al. [9]

1.2.4 Types of MOFs in this Work

This section will discuss the most important MOFs employed in this work, such as UiO-66, MOF-808 and ZIF-8. Special attention is drawn to these structures because we have been able to synthesise them in both powdered and monolithic configurations.

1.2.4.1 UiO-66

UiO-66 is a Zr(IV) based MOF first reported by Cavka et al. [83]. In search for structures with improved stability, Cavka et al. turned to group IV elements which have a strong interaction with oxygen and can thus form stable inorganic building bricks when in combination with oxygen containing linkers [83]. The secondary building unit (SBU) in UiO-66 consists of $[Zr_6O_4(OH_4)]^{+12}$ octahedrons and expresses the highest coordination number reported for a MOF to date [52, 83, 84]. A representation of UiO-66 framework is illustrated in Figure 1.5. Each Zr SBU in UiO-66 completes a unit cell with 12 deprotonated terephthalate (BDC) linkers via strong Zn-O bonds to form a cubic close-packed structure with net formula $Zr_6O_4(OH)_4(BDC)_6$. A carboxylate linker is favoured due to easy instantaneous deprotonation which is required for metal cluster bonding as well as their commercial ubiquity [85]. Defect-free UiO-66 yields a theoretical BET area (S_{BET}) of $\sim$ 1400 $m^2.g^{-1}$ and a pore volume (V_p) of $\sim$0.44 $cm^3.g^{-1}$ with a pore limiting diameter and large cavity diameters of 3.8 and 8.7 and 11 Å, respectively [83, 8, 86].

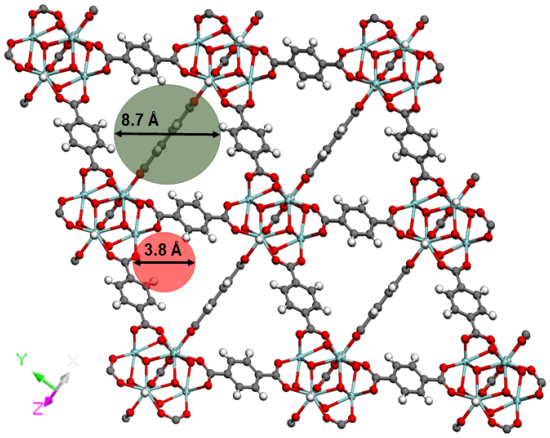

Fig. 1.5 Representation of UiO-66 MOF framework with primary pores (green) and secondary pores (orange). Zr, C, O and H atoms are represented by cyan, grey, red and white, respectively.

UiO-66 is considered to have unparalleled thermo-chemical and mechanical stability: it is known to withstand temperatures up to 500 °C [87] and high mechanical stress [83, 88] as well as exposure to both highly acidic and mildly alkaline conditions [87, 83, 84, 89]. This resilience has been attributed to the strong nature of the Zr-O bond as well as the unique ability of reversible rearrangement of the inorganic cluster, upon both dehydroxylation and

rehydration, without affecting the connecting terephthalate bridges [90, 83, 91]. Furthermore, the high coordination of the Zr-O bond as well as the metal cluster coordination, both contribute to restriction of coordination bond angles - these increase the overall mechanical resilience of the UiO-66 framework, but at the same time decrease it's flexibility [88].

To date, UiO-66 has been gaining major ground in catalysis [89, 92–96], drug delivery [7, 8, 97–99], sensors [100–104], energy storage [91, 105, 106], water adsorption [107–109] and water treatment [110–113] amongst numerous others. Figure 1.6 illustrates the number of papers published on UiO-66, each year, from 2009 up to 2018, 2008 being the year it was first reported by Cavka et al. [83]. Up to date, there are around 1200 accounts of UiO-66 related publications and, as observed in Figure 1.6, the number has been increasing steadily, with just over 350 publications appearing in 2018 alone. This is correlated with increasing number of research areas of UiO-66 applicability.

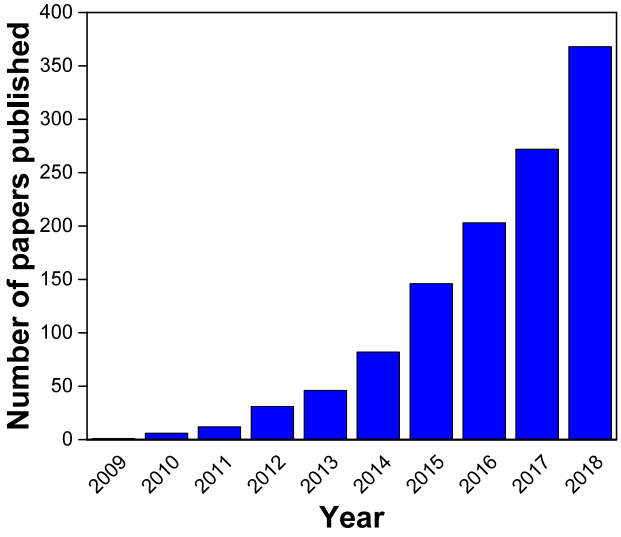

Fig. 1.6 Number of papers published featuring UiO-66 each year since 2009 up to 2018. Data source: *Web of Knowledge*. Search keywords: *UiO-66*

A number of different synthetic procedures are in place for UiO-66; the vast majority, however, are solvothermal batch methods involving the use of toxic DMF solvent and high temperatures, both during synthesis and activation [83]. More recently, UiO-66 has been successfully synthesised using electrochemical [103], atomic layer [100] and chemical vapour deposition techniques [102]. Others also reported faster microwave assisted procedures [112] and even continuous micro-reactor flow synthesis techniques offering very precise nanoparticle size control [99].

A theoretically perfect 12-coordinated UiO-66 structure is rarely attainable, Schaate et al. [114] concluded that most often a synthesis mixture consisting of metal and linker sources only leads to rapid precipitation of microsized aggregates with a high level of structural disorder and low specific surface areas. Therefore, as a way of slowing down the nucleation rate and obtaining some level of size and morphology control of the resulting MOF crystals [114–116], modulated synthesis was introduced. Modulation consists of addition of an acidic species with one coordination site which can compete with the linkers for metal cluster vacancy during a synthesis proceess. This can thus lead to the formation of defects consisting in either missing linkers or even missing metal clusters, depending on the type and ratio of modulator used [117, 118].

In particular, in UiO-66, missing linker or cluster defects are particularly easy to obtain and study, due to the high coordination and hence stability of the framework. Defect engineering has thus rapidly become a research interest within the MOF community. For example, Hui et al. [86] have shown that it can often improve the pore volume and surface area by as much as 150% and 60% respectively as well as improving the gas adsorption behaviour [86, 119]. Additionally, post-synthetic removal of modulators has proved to increase accessibility to the unsaturated metal sites and hence lead to enhanced activity in catalytic applications [93, 95, 96, 119].

1.2.4.2 MOF-808

MOF-808 is a Zr(IV) structure firstly reported by Furukawa et al. [120] in search for materials with a high water adsorption capacity and good aqueous phase stability. MOF-808 consists of $Zr_6O_4(OH)_4(\text{-}CO_2)_6$ SBUs which can connect with a maximum of 6 1,3,5-benzenetricarboxylic acid linkers (BTC) as well as 6 formate linkers for charge balancing purposes [120]. This yields a structure in the **spn** topology with net formula $Zr_6O_4(OH)_4(BTC)_2(HCOO)_6$ with a theoretical S_{BET} of 2060 $m^2.g^{-1}$ and a micropore volume of 0.84 $cm^3.g^{-1}$ [120]. In MOF-808, each linker is connected to 3 SBUs to form tetrahedral cages with an internal pore diameter of 4.8 Å. In turn, the tetrahedral cages share vertices so as to form larger adamantane cages with an internal pore diameter of 18.5 Å [120] as well as a pore limiting diameter of 12.4 Å, these are illustrated in Figure 1.7.

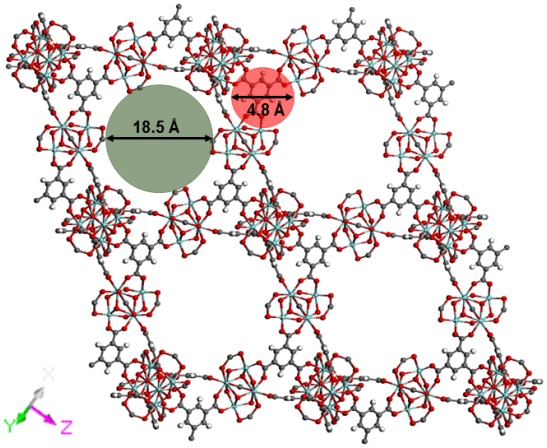

Fig. 1.7 Representation of MOF-808 structure with primary pores (green) and secondary pores (orange). Zr, C, O and H atoms are represented by cyan, grey, red and white, respectively.

The first reported solvothermal synthesis methology of MOF-808 by Furukawa et al. [120] involved the use of high temperatures and long reaction times requiring up to 7 days, involving multiple tedious solvent exchange steps so as to ensure careful solvent evacuation procedures without collapsing the large pores. However, various groups have attempted to shorten the reaction time since; for example, Li et al. [121] have reported a facile synthesis methodology using microwave irradiation for as little as 5 minutes followed by a simple wash in DMF, leading to improved yield. Reinsch et al. [122] have managed to successfully develop an environmentally-friendly synthesis route for MOF-808 in water, without requiring toxic DMF solvent, or sources of metal posing explosive risk in scale-up scenarios, such as those comprising of nitrates or chlorides, without compromising reaction yield and crystal quality [122].

Figure 1.8 illustrates the number of papers published on MOF-808 since it was first reported in 2014 up to 2018; in 2018 alone just over 20 papers appeared suggesting a rapidly exanding research potential. MOF-808 proves attractive for a number of different applications firstly due to the perceived stability of Zr-based cluster, but also due to the large pore size, which can incorporate large guest molecules and also facilitate mass transport across the structure. The use of MOF-808 has indeed been reported by various groups for catalytic applications [123–126], sensing [127], water harvesting and dehumidifying [120] and, more specifically, water treatment for removal of arsenic [121] and heavy metal ion

capture [29] leading to excellent results. Similarly to UiO-66, defect engineering in MOF-808 is also proving to be a route for chemical feature tunning, for example, various groups have successfully managed to induce catalytically and gas sorption active missing linker defects in MOF-808 [128–130]. However, very little is known about the actual stability of MOF-808 and indeed, to date, comprehensive and quantitative stability data on MOF-808 is inexistent.

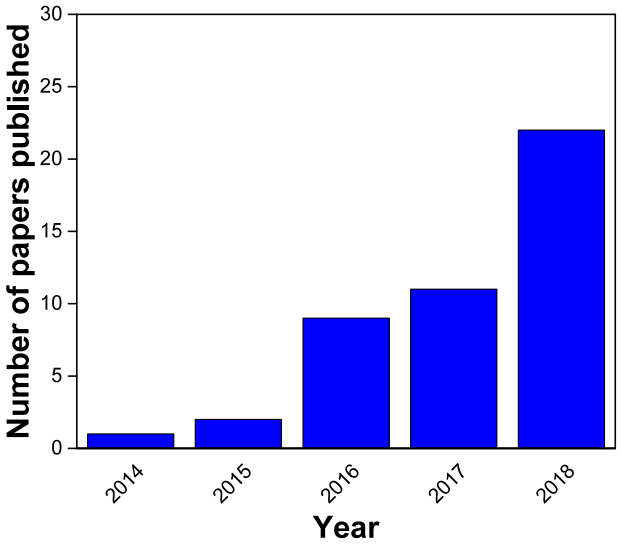

Fig. 1.8 Number of papers published featuring MOF-808 year on year since 2014 up to 2018. Data source: *Web of Knowledge*. Search keywords: *MOF-808*

1.2.4.3 ZIF-8

ZIF-8 was first reported by Park et al. in 2006 [131] in a publication detailing a new subclass of MOF structures - zeolitic imidazolate frameworks (ZIFs), which were synthesised in an attempt to mimic the thermo-mechanical resilience of zeolites. Prior to this, few papers reported the formation of Fe [132], Co [133] and Zn [134] imidazole frameworks, however, they exhibited a high degree of structural disorder as well as low porosity. ZIFs borrow the four-fold coordination chemistry, with the 145 ° bond angle and hence topologies similar to those encountered in aluminosilicate zeolites [68, 135]. ZIFs are also known to possess exceptional hydrophilic/hydrophobic tunability [131, 136, 137]. This is owed, in part, to the shielding of the Zn-N bonds by the imidazole ligands, as well as the potential of adding functional groups on the imidazole llinker, such as methyl. This property being especially sought for exploitation in industrial media, where, for example, the presence of polar water

molecules can trigger competitive adsorption and may thus hinder the capture of desired chemical species [136].

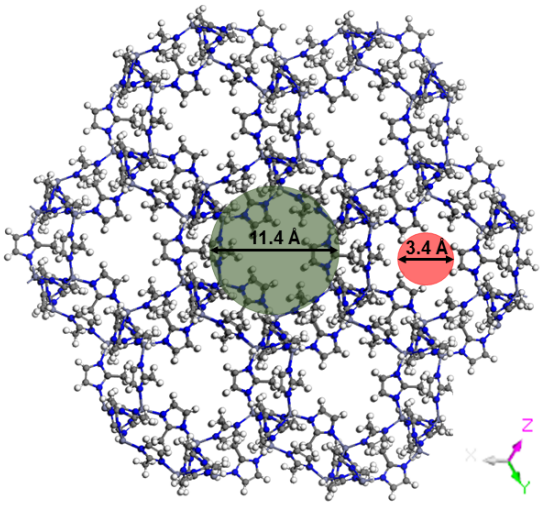

Fig. 1.9 Representation of ZIF-8 MOF with primary pores (green) and pore window (orange).

Whereas many still debate whether such geometrical arrangement would offer the prospect of conferring the resilience of zeolites to ZIFs, it has been proved that, in fact, only a few of the ZIFs known to have been synthesised fit this assumption [135, 138], amongst them is ZIF-8. An illustration of ZIF-8 is represented by Figure 1.9. ZIF-8 consists of Zn atoms coordinated by 4 2-methyl imidazole linkers to form a net with sodalite topology (**sod**) with a theoretical S_{BET} of 1700 $m^2.g^{-1}$ and a micropore volume of $\sim$0.5 $cm^3.g^{-1}$ [139]. It consists of larger 6 membered cavities of 11.4 Å pore diameter and smaller 4-ring windows with 3.4 Å openings [139–142].

Like all MOFs, a number of different synthesis techniques are in place for ZIF-8 and they span from solvothermal methods using DMF or low molecular weight alcohols [143, 144] to sonochemical [144], mechanochemical [145], steam assisted conversion [146] and chemical vapour deposition [147] processes amongst many others [143]. Although, compared to most MOFs, ZIF-8 can be obtained in room temperature conditions, in water, using very short reaction times down to 10 minutes [81, 148–150]. Figure 1.10 illustrates the number of research papers appearing year on year, since ZIF-8 was first reported in 2006; as observed, the number of publications only keeps increasing with over 600 publications appearing in 2018 alone. This is attributed to the vast areas of applicability of ZIF-8. Up to date, the

suitability of ZIF-8 has been demonstrated in catalysis [144, 151, 152], water treatment [43, 153, 150] and desalination [154], gas separation [155–157] and sensing [158] amongst many others.

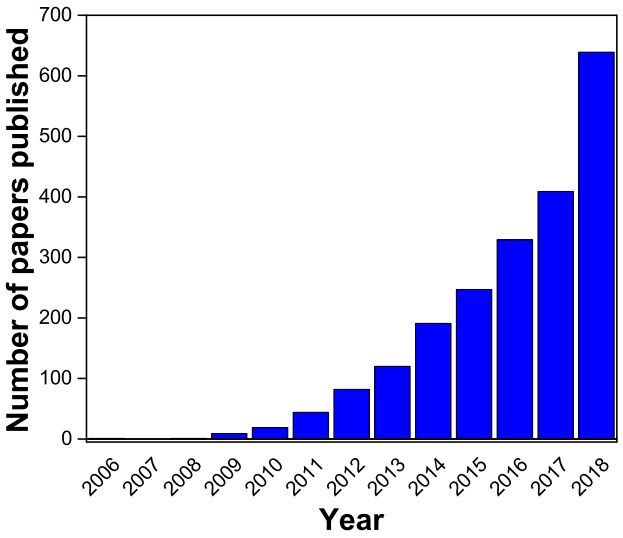

Fig. 1.10 Number of papers published featuring ZIF-8 year on year since 2006 up to 2018. Data source: *Web of Knowledge*

In addition to the high level of hydrophobicity displayed, another interesting feature is attributed to ZIF-8. While researching molecular sieving on ZIF-8, Fairen-Jimenez et al. showed that ZIF-8 presents structural flexibility during adsorption of guest molecules due to the rotation of imidazolate linkers in a phenomenon called "swing effect" [140]. The change in orientation of the linkers makes the 6-membered windows much wider, allowing for access to guest molecules larger than the original ring aperture size, similar, to ring opening experienced by ZIF-8 with increasing pressure which was earlier reported by Moggach et al. [159]. It was later proved that, in fact, several MOFs can be either rigid or flexible, the flexibility being triggered by changes in both temperature and/or pressure to adsorb molecules larger than their initial pore sizes [140, 160–162].

At the same time, conflicting reports on the stability of ZIF-8 are published, whilst some claim ZIF-8 to yield good adsorption capacity under highly acidic environments [43], others have claimed ZIF-8 to be unstable even under neutral conditions at room temperature [44].

1.3 Aims and Objectives of this Dissertation

The current dissertation has two aims:

1. To prove the potential of MOFs as liquid phase adsorbents
2. To investigate the applicability and importance of MOF shaping for liquid phase applications

In order the achieve this, the volume of work is divided into the following objectives:

- To synthesise both powdered and monolithic configurations of narrow and wide-pore MOFs: ZIF-8, UiO-66, MOF-808 and to perform full material characterisation in order to confirm the phase and porosity.
- To develop a fully standardised stability assessment protocol and apply it to study the liquid phase stability of the chosen MOFs
- To study the feasibility of synthesised MOFs in batch mode liquid phase adsorption applications using a model adsorbate and to compare the performance of powdered and monolithic configurations
- To investigate the flow-mode adsorption capability of pure-phase monolithic MOFs
- To synthesise an ZIF-8 MOF composite and perform full material characterisation and to contrast the flow-mode adsorption capability with pure-phase monolithic MOF

1.4 Supervision, Collaborations and Organisational Details

The work presented in this dissertation was performed as a project within the Adsorption and Advanced Materials Laboratory (AAML) research group at the Department of Chemical Engineering & Biotechnology, University of Cambridge, under the supervision of Dr. David Fairen-Jimenez.

1.4.1 Publications Relevant to this Work

1. **D. Vulpe**, J.P. Mehta, T. Tian, A.E.H. Wheatley, D. Fairen-Jimenez. *Sol-gel monolithic ZIF-8 for water purification*. **Under review**.

2. **D. Vulpe**, S. Buchele, S. Griffin, B. Connolly, D. Xie, R. Forgan, P.Z. Moghaddam, D. Fairen-Jimenez. *Towards a Standardised Approach for Aqueous Stability Screening of MOFs*. **In preparation**.

3. T. Tian, Z. Zeng, **D. Vulpe**, M. E. Casco, G. Divitini, P. A. Midgley, J. Silvestre-Albero, J.C. Tan, P.Z. Moghadam, D. Fairen-Jimenez. *A sol-gel monolithic metal-organic framework with enhanced methane uptake*. **Nature Materials**, 17:174-179, 2018.

4. B. M. Connolly, M. Aragones-Anglada, J. Gandara-Loe, N. A. Danad, D. C. Lamb, J. P. Mehta, **D. Vulpe**, S. Wuttke, J. Silvestre-Albero, P. Z. Moghadam, A. E. H. Wheatley and D. Fairen-Jimenez. *Tuning porosity in macroscopic monolithic metal-organic frameworks for exceptional natural gas storage*. **Nature Communications**, 20:2345, 2019

1.4.1.1 Other contributions

1. W.Zhang, J. Maul, **D. Vulpe**, P. Z. Moghadam, D. Fairen-Jimenez, D. M. Mittleman, J. A. Zeitler, A. Erba and M. T. Ruggiero. *Probing the Mechanochemistry of Metal–Organic Frameworks with Low-Frequency Vibrational Spectroscopy*. **J. Phys. Chem. C**, 122(48):27442-27450, 2018.

2. F.C.N. Firth, M.J. Cliffe, **D. Vulpe**, M. Aragones-Anglada, P.Z. Moghadam, D. Fairen-Jimenez, B. Slater, C.P. Grey. *Engineering New Defective Phases of UiO type Metal-organic Frameworks with water*. **J. Mater. Chem. A**, 7:7459-7469, 2019.

3. J.W.M. Osterrieth, D. Wright, H. Noh, C.-W. Kung, **D. Vulpe**, A. Li, J.E. Park, R. van Duyne, P.Z. Moghadam, J.J. Baumberg, O.K. Farha and D. Fairen-Jimenez. *CoreShell Gold Nanorod@Zirconium-Based MetalOrganic Framework Composites as in Situ Size-Selective Raman Probes*. **J. Am. Chem. Soc.** 141:9:3893-3900, 2019

1.4.2 Collaborations and Institutions

The vast majority of the work presented in this work has been carried out at the Department of Chemical Engineering & Biotechnology, University of Cambridge. Characterisation and other analyses were conducted in the following institutions:

- *MOF synthesis, stability testing and liquid phase adsorption*. Conducted by myself at Department of Chemical Engineering & Biotechnology, University of Cambridge
- *UiO-66 and MOF-808 monolith synthesis*. Conducted by myself, Bethany Connoly and Daijun Xie at Department of Chemical Engineering & Biotechnology and Department of Chemistry, University of Cambridge
- *XRD, SEM, FT-IR, TGA*. Conducted by myself at both Department of Metallurgy and Materials Science and Department of Pathology, University of Cambridge
- *HPLC analysis, UV spectrophotometry*. Conducted by myself at Department of Chemical Engineering & Biotechnology, University of Cambridge with Dr. Ljiljana Fruk's permission
- *Flow-mode adsorption*. Conducted by myself at Department of Chemical Engineering & Biotechnology, University of Cambridge with Dr. Ljiljana Fruk's permission, training provided by Dr. Arthur Kouyoumdjian and Dr. Antonina Kerbs
- *Nitrogen adsorption*. Conducted by myself at both Department of Chemical Engineering & Biotechnology and Institute for Manufacturing (IfM), University of Cambridge
- *Synthesis of Zr-based MOFs L1-L8*. Conducted by Sarah Griffin at Department of Chemistry, University of Glasgow

1.4.3 Organisation of the Thesis

The current work is divided into the following Chapters and Appendices:

- *Chapter 1*: outlines a general introduction of the scope of the current work and provides literarary background content to the task at hand as well as general administrational and supervisory detail

- *Chapter 2*: provides a full description of the experimental techniques employed with specific detail to the current work
- *Chapters 3, 4 and 5*: the central discussion chapters outlining experimental findings and discussion
  - *Chapter 3*: *Stability Assessment of MOFs in the Liquid Phase*, outlines and describes the aqueous stability testing procedures applied on powdered and monolithic MOFs employed in this work.
  - *Chapter 4*: *Development of High Surface Area Structures via Growth of ZIF-8 on Honeycomb Cordierite Substrate (ZIF-8@Cordierite)*, explores the viability of bottom-up layer-by-layer in-situ synthesis ZIF-8 growth and deposition procedure on functionalised and unfunctionalised substrate
  - *Chapter 5*: *Monolithic MOFs as Candidates for Adsorption of Bisphenol B Micropollutant*, describes the synthesis and characterisation of powdered and monolithic MOFs and their capability for batch and flow-mode adsorption of Bisphenol B (BPB). Additionally, the BPB adsorption capabilities of ZIF-8@Cordierite composites are tested.
- *Chapter 6*: *Final Conclusions and Future Work*, presents the final conslusions derived from the current dissertation as well as plans and suggestions for future work
- *Appendix A*: *Calculations and Fittings*, provides a detailed calculational procedure for evaluating surface areas using the Rouquerol Criteria as well as pseudo-second order kinetic rate model fittings for liquid phase adsorption
- *Appendix B*: *Additional Data*, provides additional data on stability of HKUST-1 as well as PCN materials, also provides additional BPB removal data with UiO-66 and ZIF-8.

Chapter 2

Characterisation Techniques and Methods

2.1 Gas Adsorption and Surface Area Estimation - Chapters 3, 4, 5

2.1.1 Principle and Instrumentation

Gas adsorption is a physical charaterisation technique used to quantify the surface area and pore volume of a given porous material. Nitrogen is most often used as the adsorbate due to its inertness, precluding chemical interactions with the test materials, low vapour pressure and low relative cost. Indeed, to this day, the nitrogen adsorption capacity and, hence, surface area, is the go-to benchmark serving as a quantifiable comparison between materials.

A typical measurement thus occurs under controlled conditions, in a closed space at a prescribed pressure. As illustrated in Figure 2.1, the activated sample is firstly brought to full vacuum and submerged in a constant temperature bath. For the purpose of most measurements, this would be the boiling temperature of the adsorbate gas, typically that of nitrogen (77.3 K). A known dose of adsorbate gas is then injected into the manifold and allowed to enter the sample chamber, at this point, some of the gas will have been taken up by the sample resulting in a decrease of pressure. The pressure reading is monitored and

allowed to stabilise so as to reach equilibrium. The same adsorbate dosing procedure is repeated in a step-wise fashion until saturation pressure is reached.

By measuring this decrease in pressure of the gas [163], or the increase in the weight of the sample, the amount of gas adsorbed by a material can be determined [164]. The quantity of adsorbed gas is dependent on the relative pressure of the adsorbate gas and is proportional to the total external and internal surface of the material under consideration; the relationship between the amount of gas adsorbed and relative pressure is known as the adsorption isotherm, the shape of which can reveal much about the structure of the material being studied [163, 165].

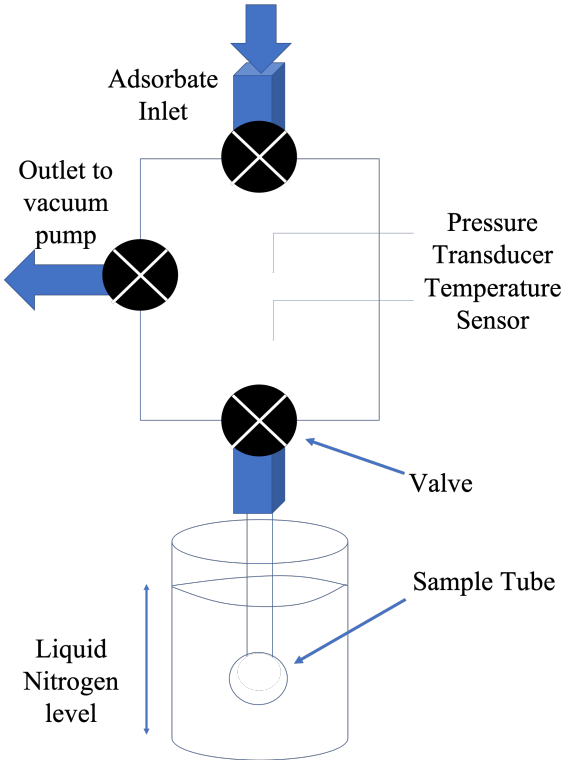

Fig. 2.1 Schematic representation of an adsorption apparatus set-up

2.1.2 Types of Adsorption Isotherms

The shape of an adsorption isothem serves as a basis for material classification, generally 6 different types of isotherm curves have been identified, these are illustrated in Figure 2.2 [163]. *Type I* isotherms are most commonly used to characterise microporous materials and are thus widely encountered in MOF research. These are described as reaching a plateau, or

isotherm shoulder, from low relative pressure up to saturation pressure at which point bulk condensation occurs. The plateau is a result of gradual micropore filing wherein progressively larger micropores fill, thus, the point at which the isotherm shoulder occurs can serve as a good indicator of pore size. Microporous materials are considered to be those possessing pore widths of less than 20 Å. *Types II* and *IV* are general descriptors of either non- or macro-porous materials exhibiting very steep tails near the saturation pressure, indicative of multi-layer adsorption. In these cases, the point between mono and multi-layer adsorption can be visually inferred from the isotherm itself and it most commonly occurs at the mid-range of an adsorption isotherm. Moreover, *Type IV* is also characterised by the presence of a hysteresis loop, which suggests capillary condensation most commonly encountered in mesoporous materials, with pore pore widths ranging from 20 Åto 500 Å. *Types III* and *V*

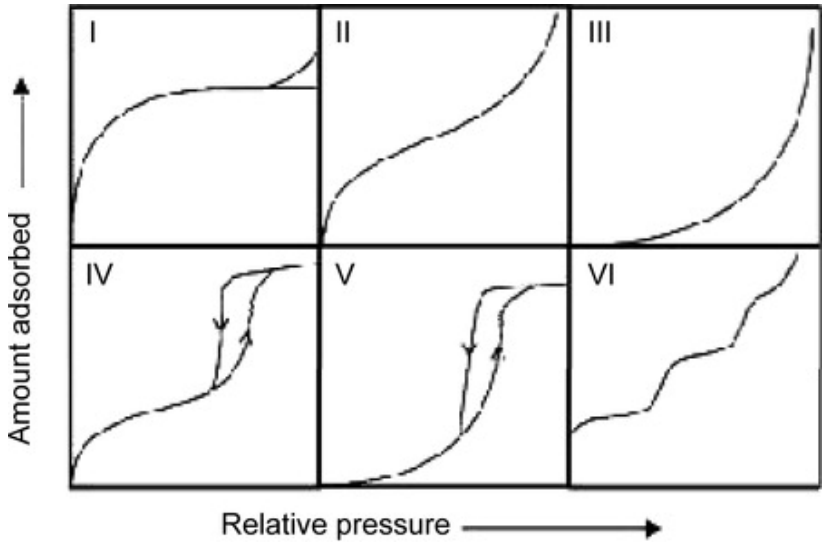

Fig. 2.2 The 6 IUPAC classifications of adsorption isotherms. Adapted from [163]

are characterised by negligible followed by very steep uptake in the low and high pressure regions, respectively. This behaviour is commonly observed in those cases where weak fluid-solid interactions are observed. Again, for those cases where the behaviour follows a *Type V* pattern, the hysteresis implies the presence of mesopores. Finally, the least encountered *Type VI* is indicative of a mostly non-porous solid with a uniform surface wherein each isotherm step represents the completion of monolayer adsorption.

In most cases, adsorption isotherms do not follow strictly one classification and can, in fact, be a mixture of 2 isotherms. In microporous materials research, Type I isotherms

are mostly encountered but the saturation pressure behaviour can vary depending on the type of formed material and especially, in those cases where, for example, hierarchical MOF structures are expected, a distribution of pore size can give rise to Type IV behaviour indicating hysteresis loops.

2.1.3 Rouquerol Consistency Criteria for BET Area Estimation for Microporous Materials

The surface area of materials is evaluated by using the Brunauer, Emmett and Teller (BET) model, based on multi-layer adsorption of gases on the external and internal surfaces [166, 164]. The BET model is an extension of the earlier proposed Langmuir theory, which only accounts for monolayer adsorption. The linear BET relationship is described by Equation 2.1 as follows:

$$\frac{P/P_0}{V\,(1-P/P_0)} = \frac{1}{V_m C} + \frac{C-1}{V_m C} \times \frac{P}{P_0} \tag{2.1}$$

where P is the partial vapour pressure of adsorbate gas in equilibrium with the surface at 77.3 K; P_0 is the saturated pressure of adsorbate gas; V is the volume of gas adsorbed; V_m is the volume of gas adsorbed, at standard temperature and pressure, to produce an apparent monolayer on the sample surface and C is a dimensionless constant related to the enthalpy of adsorption.

Traditionally only data in a certain linear P/P_0 range would be used for BET area evaluation, the general recommendations for microporous materials would range between 0.05 and 0.2 P/P_0, whereas for mesoporous materials, up to 0.3 P/P_0 [164]. However, this approach often results in over-estimation of the actual surface area of the material, especially in those cases where the materials concerned are microporous. Moreover, the linear range chosen following this route would involve significant human error and hence the resulting BET area values would differ drastically from study to study.

For microporous materials, the linear BET range is often difficult to locate, hence the Rouquerol criteria have been devised in order to overcome this difficulty and eliminate any subjectivity in the monolayer BET capacity, in order to locate the linear range the following guidelines would be followed [167–170]:

1. Only a range where $V(1 - P/P_0)$ continuously increases with P/P_0 should be selected

2. The resulting value of the C constant should always be positive as long as the correlation coefficient from the linear regression analysis is higher than 0.995

3. The monolayer loading, V_m, evaluated after steps 1) and 2) should correspond to a P/P_0 value within the selected linear region

4. The P/P_0 value corresponding to the V_m calculated from BET theory ($1/\sqrt{C}$ + 1) should be equal to the P/P_0 determined in step 3) within a tolerance of 20%

Once all criteria are satisfied and the linear regression is sucessful, the following equation is used to evaluate the BET area.

$$S_{BET} = \frac{V_m A_m N_A 10^{-20}}{RMM_{ads}}, \tag{2.2}$$

where S_{BET} is the BET area, A_m is the average area occupied by a molecule of adsorbate in the completed monolayer; N_A is the Avogadro constant and RMM_{ads} is the relative molecular mass of adsorbate gas.

In the current work, gas adsorption experiments were conducted in order to confirm the porosity of MOFs, to determine the maximum nitrogen uptake capacity and hence evaluate the BET area. Nitrogen adsorption was performed at 77 K with commercial equipment supplied by Micromeritics using either a TriStar II PLUS or 3Flex apparatus. The TriStar II equipment allowed for routine analysis of the adsorption capacity of a material whereas the 3Flex apparatus allowed for more in-depth understanding for the low pressure behaviour. Unless otherwise stated, all measured samples were degassed for a set period of time at a specified temperature prior to characterisation, the specific conditions are indicated in the relevant Result Chapters. Measurements were collected by employing high purity N_2 (99.998% purity, BOC UK). The saturation pressure of the gas was continuously measured throughout the analysis by means of a pressure transducer. Once the adsorption data acquisition was complete, warm and cold free space correction measurements were performed with high purity He gas (Grade A, 99.996% purity, BOC UK). The BET area of the samples was evaluated by applying the four criteria, a detailed example is provided in Appendix 1.

2.2 X-Ray Diffraction - Chapters 3, 4, 5

X-ray diffraction is a robust analytical tool used for crystal phase identification and unit cell evaluation of a particular test material [171]. The concept is illustrated in Figure 2.3. It operates on the principle that atoms within a crystal lattice form regularly shaped and spaced planes with a defined lattice distance, d, once a beam of known wavelength is directed at a given material the resulting diffraction pattern can be used to infer the nature of the atomic lattice. The diffraction pattern is a result of the constructive interference of reflected photons, which takes place on the premise that the path difference is an integer multiple of the wavelength of incident light [172]. This leads to the determination of the precise molecular structure of a substance. The d spacing, can be evaluated by use of Bragg's law (Equation 2.3).

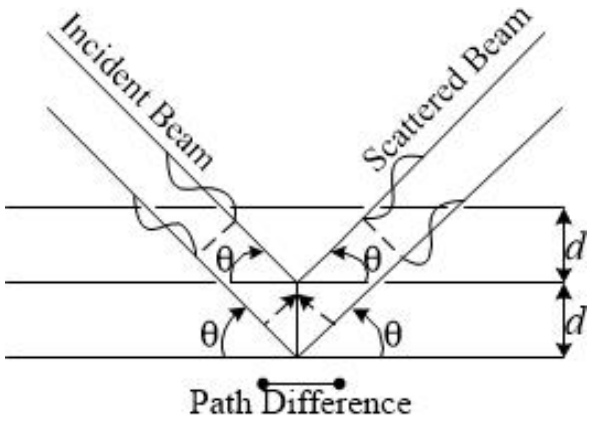

Fig. 2.3 Bragg's law of diffraction: a beam of X-rays of wavelength λ incident on a surface with regular arrays of reflecting planes at an angle θ is always reflected at the same angle, provided the path difference between adjacent planes is equal to some integer m allows constructive interference of scattered and incident X-rays [172].

Mathematically, Bragg's law takes the following form, with its components defined in Figure 2.3:

$$2d\sin\theta = m\lambda \tag{2.3}$$

The XRD set-up is illustrated in Figure 2.4. In a typical XRD set-up, a current is applied to a filament located inside a sealed tube under vacuum in order to generate X-rays, the higher the current, the greater the number of emitted electrons. The X-ray detector then

performs an angular movement around the sample to measure the intensity of light scattered away from the sample, enabling the computation of the peak intensity and position.

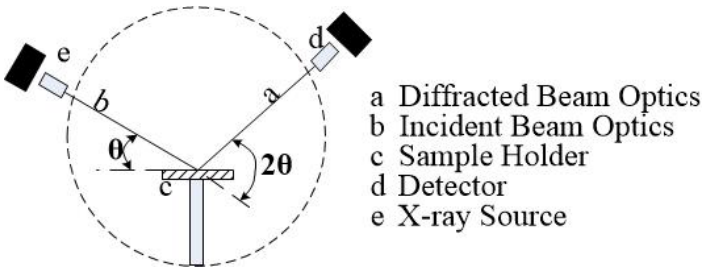

Fig. 2.4 An illustration of powder X-ray diffraction set-up

Thus, in this context, X-rays are used for their short wavelength, which matches the expected range of *d*-spacing. Phase identification can be performed by analysing both position and intensity of diffraction peaks, each of which is indicative of the presence of a known phase. The mathematical significance of diffraction peaks and unit cell parameters is described elsewhere [173].

In the current work, all samples were subject to activation under vacuum before characterisation. Measurements were performed using a Bruker D8 Advance diffractometer with monochromatic Cu Kα radiation (1.54 Å) at 40 kV and 40 mA, respectively. Diffraction patterns were recorded in steps of 0.01° at a scanning speed of 0.01 $^{\circ}s^{-1}$ from values of 2θ from 5 to 40°.

2.3 Scanning Electron Microscopy- Chapters 4 and 5

Scanning electron microscopy (SEM) is a versatile characterisation tool with high spatial resolution offering insights from the nano- to the microscale with both imaging and chemical charaterisation capabilities [174, 175]. The principle of operation is illustrated in Figure 2.5: a beam of electrons is accelerated through a voltage difference between a cathode and an anode which is then focused by one or two of the condensor lens. This is then picked up by scanning coils or deflector plates which deflects the beam into x and y axes so as to generate a 2D image. Imaging modes and other details are described elsewhere [176].

In this work, SEM was used to observe the resultant MOF and MOF film morphology and uniformity. Images were acquires with an FEI Nova NanoSEM FEG microscope in secondary

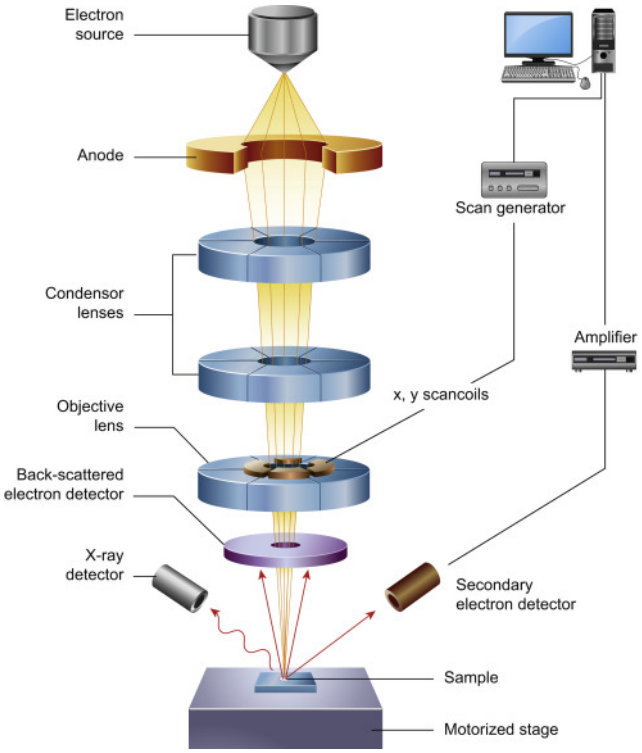

Fig. 2.5 An illustration of a SEM lens and sample set-up equipped with an EDX detector [175]

electron mode set a voltage of 5 kV. Sample preparation technique included affixation of samples on 1 cm diameter aluminium stub using double-sided carbon adhesive tape and coating with a fine layer of platinum.

2.4 Thermogravimetric Analysis - Chapter 4

Thermogravimetric analysis (TGA) is a destructive characterisation tool used describe the thermal degradation pathways and thermal stability of a known test material. In a typical measurement set-up, a known quantity of material is placed on a micro-scale enclosed in either an inert or reactive atmosphere, the temperature is then ramped up and the remaining weight of material is continuousy measured to yield a thermal degradation profile.

In this work TGA characterisation was carried out in a N_2 atmosphere with a TA Instruments Q500 analyser, set at a flowrate of 40 mL.min^{-1} and 60 mL.min^{-1} for the balance and the sample, respectively. The mass loss curve was registered from 30 to 800° C at a ramp rate of 10° C.min^{-1}. Resultant data is displayed without further refinement.

2.5 Batch Mode Adsorption- Chapter 5

The suitability for liquid phase adsorption of MOFs was tested by employing a model pollutant, Bisphenol B (BPB). A set of solutions of known concentrations of pollutant (in the ppm range) were prepared and a known dose of adsorbent was placed in the test solutions. At pre-determined time intervals, liquid samples were drawn from the solutions and the residual concentration of the pollutant was evaluated. Thus, adsorption of a compound onto a chemical adsorbent, in a batch mode set-up, was quantified using the following relationship:

$$Q_t = \frac{C_0 - C_t}{m} \times V \tag{2.4}$$

where Q_t represents the quantity of pollutant adsorbed at time t (mg.g^{-1}), C_0 and C_t represent the concentrations of pollutant in the supernatant at time $t = 0$ and $t = t$, respectively (mg.mL^{-1}). m represents the mass of adsorbent (g) and V is the solution volume (mL). This data enabled the collection of dynamic adsorption curves, expressed as a function of contact time and equilibrium adsorption isotherms, as a function of equilibrium concentration.

2.5.1 Pseudo-second order Rate Model

Following the dynamic adsorption profile of BPB on MOF adsorbents, the adsorption behaviour was identified as following the pseudo-second order kinetic behaviour. Therefore, the kinetics of adsorption in the current study was characterised using the linear form of pseudo-second order kinetic rate model, represented by the following equation:

$$\frac{t}{Q_t} = \frac{1}{k_2 \times Q_e^2} + \frac{t}{Q_e} \tag{2.5}$$

where Q_e is the equilibrated adsorption capacity (mg.g^{-1}) and k_2 is the pseudo-second order rate constant (g.mg^{-1}min^{-1}). A plot of t/Q_t against t is obtained and, after linear regression, k_2 and Q_e were evaluated from the slope and intercept of the line of best fit. After re-arrangement, the pseudo-second order kinetic curve was plotted on the Q_t vs t graph. This procedure was applied for both ZIF-8 and UiO-66 samples. The fitting parameters and plots are detailed in Appendix 1.

2.5.2 Langmuir Model Fitting

Similarly, the equilibrium adsorption isotherms of BPB on MOF adsorbents, namely UiO-66, was identified as following the Langmuir model. The equilibrium fittings were achieved by applying the Langmuir equation, shown below:

$$Q_e = \frac{Q_{max} K_L C_e}{1 + K_L C_e} \tag{2.6}$$

where Q_{max} is the maximum theoretical adsorption capacity (mg.g^{-1}), K_L is the Langmuir adsorption constant associated with binding energy and C_e is the concentration of BPB in the supernatant at equilibrium (mg.mL^{-1}).

Equation 2.6 was re-arranged in order to obtain a linear form and perform linear regression:

$$\frac{1}{Q_e} = \frac{1}{Q_{max} K_L C_e} + \frac{1}{Q_{max}} \tag{2.7}$$

The goodness of fit was judged by using the reduced chi-squared statistic (in-built Origin function). This fitting was only applied for the UiO-66 samples, which showed ideal adsorption behaviour. Langmuir fitting parameters can be found in Appendix 1.

2.5.3 Flow-mode Adsorption

Flow mode adsorption of BPB pollutant was attained by employing a Fast Protein Liquid Chromatography (FPLC) set-up, wherein the column consisted of either hand-packed ZIF-8 or UiO-66 monolithic adsorbent. Prior to injecting BPB solutions, with specified starting concentrations, the columns were equilibrated by pumping deionised water for 1 column volume.

The BPB binding capacity of the tested monolithic columns was evaluated by taking into account the adsorption capacity at 10% saturation as well as the column dead volume. An illustration of the evaluation methodology is shown in Figure 2.6, including the end point (shown as volume at which point absorbance is 10% of maximum absorption obtained at saturation) as well as the start point (defined from column dead volume). Thus, the 10% adsorption capacity of a column is obtained from the area of section **(1)** which is obtained

as the difference between the areas of sections **(3)** and **(2)**, section **(3)** being the rectangle represented by the dashed lines in Figure 2.6.

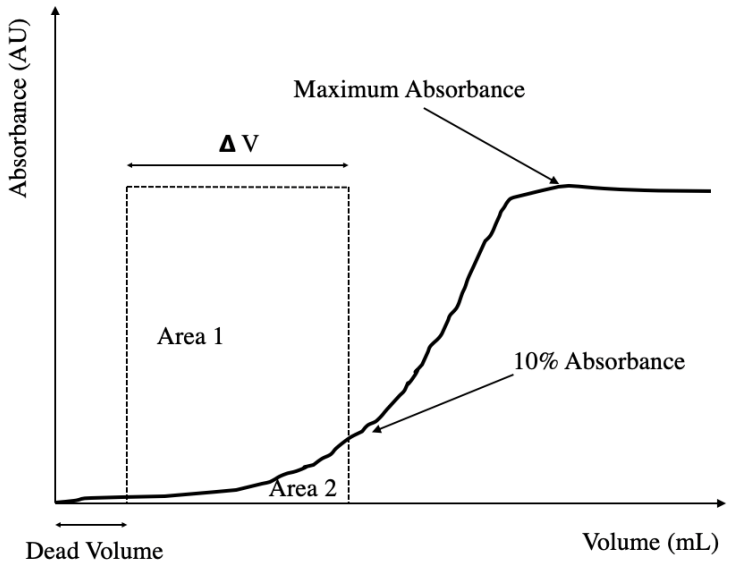

Fig. 2.6 A representation of the method used for evaluating the binding capacity in flow mode adsorption

Thus, firstly, the area of **(2)** was obtained by using the trapezoidal rule as shown:

$$\textbf{(2)} = \frac{1}{2}\sum_{i=1}^{n-1}(x_{i+1}-x_i)(f(x_{i+1})+f(x_i)) \tag{2.8}$$

where n represents the number of data points, i is the respective data point, x_i and $f(x_i)$ are the volume and absorbance at point i, respectively. Area of section **(3)** was evaluated as follows:

$$\textbf{(3)} = h_{Sat} \times \Delta V \tag{2.9}$$

where h_{Sat} represents the saturation height and V is the change in volume from the start to the end point. Once the area of **(1)** was obtained, the 10% adsorption capacity was evaluated using the following relationship:

$$10\%Q_{Ads} = \frac{(1)}{h_{Sat}} \times \frac{C_0}{m} \tag{2.10}$$

where C_0 is the starting concentration of the BPB solution injected and m is the mass of MOF adsorbent.

Chapter 3

Stability Assessment of MOFs in the Liquid Phase

3.1 Introduction

One restrictive aspect to applicability of MOFs is both troublesome chemical stability as well as limited knowledge of their true chemical integrity, most importantly, there is an imperative need to examine stability under humid or aqueous conditions. In recent years, a significant efforts towards the development of water stable MOFs have been reported [39]. To date, many structures have been claimed to be stable under various aqueous conditions and pH ranges [32, 90, 131, 177–185]. However, comparing stability between the various structures is somewhat problematic because different testing conditions are used and results are often presented mainly in a qualitative way [39].

Generally, the chemical stability of MOFs is mostly governed by the metal-linker bond, since this is the weakest chemical bond within these structures. Under aqueous conditions, MOFs can undergo hydrolysis reactions that result in the breakage of metal-linker bonds [39]. These can be accelerated in acidic conditions yielding protonated linkers or in basic conditions yielding hydroxide (or water) ligated metal nodes.

Burtch et al. [45] outline the following factors governing MOFs' stability. Firstly, thermodynamic stability is determined by the inertness of the metal cluster, which is influenced by factors such as pK_a value of the linker, oxidation state of the metal and ionic

radii. Secondly, the kinetic stability is determined by hydrophobicity as well as steric factors: if the structure is generally hydrophobic, water molecules are prevented from diffusing into the inner pores and therefore no degradation can take place [45]. Additionally, steric effects brought about by anchoring functional groups on linkers close to metal sites can make it harder for water to coordinate to metal nodes.

There are generally two ways in which a MOF can be degraded in aqueous conditions. On the one hand, material can be lost because of dissolution during the immersion of the MOF in solution, and on the other hand the internal structure of the material can become amorphous, thus without any substance being dissolved, this concept is illustrated in Figure 3.1. When choosing the analytical techniques to assess the stability of a MOF one should keep in mind these two pathways of degradation. Otherwise, if only the MOF is analysed after testing one could have a perfectly intact structure, but a substantial part of the substance could have been lost in the solution.

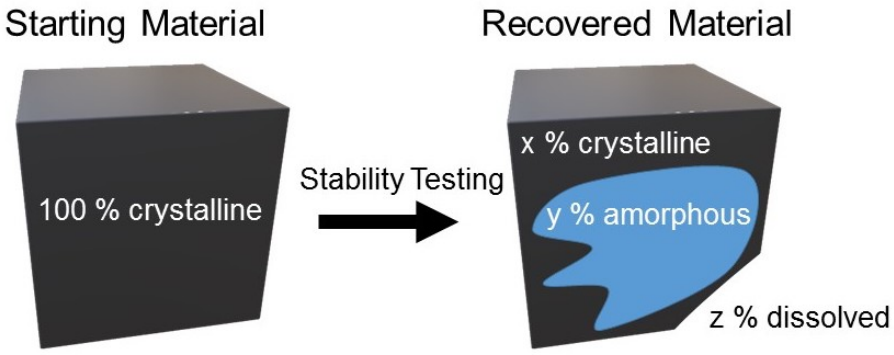

Fig. 3.1 Schematic showing different ways of how a MOF can be degraded during stability testing in aqueous solutions. If an initially perfect 100% crystalline material is assumed, there will be a proportion x of the material that is still in its original crystalline structure after testing (black). Another proportion y will still be solid but in a different state (blue; e.g. non-porous/ non-crystalline) and a third proportion z will be dissolved completely in the aqueous solution.

The primary aim of this investigation is to develop a testing procedure which enables the study of aqueous stability of MOFs in a more comprehensive and comparable way. In addition to studying variables such as MOF composition (metal, linker, connectivity), the influence of characterisation technique is discussed. pH evolution monitoring is provided when a MOF is submerged in solution in order to indicate chemical processes occurring

within the solution/framework. Furthermore, the recovered MOF solids are analysed with X-ray diffraction technique in order to study the crystallinity, and further, by nitrogen adsorption in order to confirm the extent of porosity remaining. The liquid solutions are also screened for the presence of dissolved linker. It is later concluded that indeed, the combination of porosity characterisation and dissolved linker quantification provides the ultimate stability diagnostic. Such a procedure is needed to provide more clarity in future work on MOF stability and could serve as a standard convention to enable quantitative comparisons.

3.1.1 MOFs Studied

This study focuses on a few very widely applied MOFs. Specific importance is placed on those MOFs which we have been able to obtain in monolithic form. In this context, monolithic MOFs refer to a new configuration, relative to that of typical powdered MOFs, and is described by the formation of glassy-like shiny macrostructures comprised of a pure phase MOF, expressing enhanced bulk density and volumetric surface area. For the purpose of the study in this chapter, the mechanism of monolith formation and physical properties are described in more detail in Chapter 5. To date, we have been able to synthesise monolith analogues of ZIF-8 [81], UiO-66, MOF-808 and HKUST-1 [9]. However, due to the very high susceptibility towards hydrolysis of the Cu-linker bond, the stability of HKUST-1 in water is still extremely poor, hence this MOF has been omitted from the current study. Stability data on HKUST-1 powder can be found in Appendix B. Furthermore, we have been able to attain our monolithic materials of varying degree of porosity and density; ZIF-8 monoliths are herein presented with fully and semi-exposed porosities whereas MOF-808 and UiO-66 structures have been obtained in both high and low density configurations.

This chapter also presents and discusses the water stability of a class of isoreticular MOFs, based on the UiO topology with functionalised and elongated linkers. Figure 3.2 illustrates the structure of the linkers used. Structure Zr-L1 is UiO-66, however, in this section - Zr-L1 is obtained using a different synthetic procedure, namely one without the use of modulators hence the effect on stability of the synthesis mechanism of UiO-66 is also briefly discussed. Structures L2 to L4 are isostructural to UiO-66 and are incorporated to study the effect of functional group inclusion on the overall thermodynamic stability of UiO-66. Structures L5 through to L8 are dicarboxylic acid elongated linkers and are employed to obtain larger

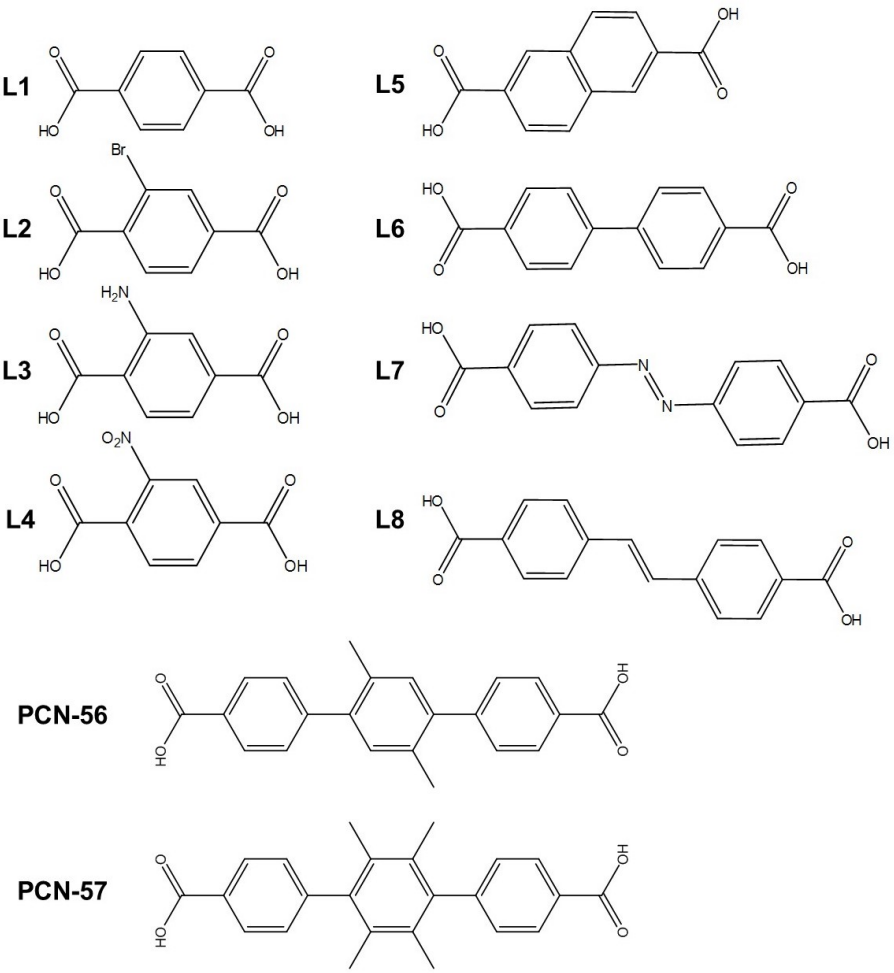

Fig. 3.2 Carboxylate linkers used in the synthesis of Zr-L1 through to -L8. Where **L1** - terephthalic acid (UiO-66), **L2**- 2-bromo-benzenedicarboxylic acid, **L3**- 2-nitro-terephthalic acid, **L4**- 2-amino-terephthalic acid, **L5**- 2,6-naphthalene-dicarboxylic acid, **L6**- 4,4'-diphenic acid (UiO-67), **L7**- azobenzene-4,4'-dicarboxylic acid, **L8**- stilbene-4,4'-dicarboxylic acid. Linkers used in structures PCN-56 and PCN-57, respectively

pores for various applications, however, little is known about their respective liquid phase stabilities. Structures PCN-56 and PCN-57 are studied in order to observe the effect of the number of methyl-groups placed on the linkers on the kinetic and thermodynamic stabilities of the respective frameworks.

3.1.2 Collaborative Work

Stability studies on powdered ZIF-8, HKUST-1 and UiO-66 were performed by Simon Buchele at Department of Chemical Engineering and Biotechnology, University of Cambridge during June-August 2017 and are outlined in MPhil thesis named "Evaluating Chemical Stability of Metal-organic Frameworks in Aqueous Solutions". Samples of $_{mono}$UiO-66 and $_{mono}$MOF-808 were provided by Bethany Connolly and Daijun Xie, respectively, from Department of Chemistry at University of Cambridge. Samples Zr-L1 to Zr-L8 as well as PCN-56 and PCN-57 were provided by Sarah Griffin from Department of Chemistry at Glasgow University.

Parts of the current chapter have contributed to the following publications:

D. Vulpe, S. Buchele, S. Griffin, B. Connolly, D. Xie, R. Forgan, P.Z. Moghaddam, D. Fairen-Jimenez. *Towards a Standardised Approach for Aqueous Stability Screening of MOFs*. **In writing**.

3.2 Materials and Methods

$Zn(O_2CCH_3)_2{\cdot}2H_2O$ (>98%), $Zn(NO_3)_2{\cdot}6H_2O$ (98%), 2-methyl imidazole (2-mIm) (97%), $ZrCl_4$ (>99.5%), $Cu(NO_3)_2{\cdot}3H_2O$ (>99%) and N,N-dimethylformamide (DMF) (99%) were purchased from Alfa Aesar. Benzene-1,3,5-tricarboxylic acid (BTC) (95%), Benzene-1,4-dicarboxylic acid (BDC) (98%), $ZrOCl_2{\cdot}8H_2O$ (99.5%), ethanol (EtOH) (> 99%) and isopropanol (IPA) (>99%) were purchased from Sigma Aldrich. HCl (37%), glacial acetic acid (99.7%) and formic acid (97%) were purchased from Alfa Aesar. All chemicals were used as received without further treatment.

3.2.1 MOF Synthesis

3.2.1.1 ZIF-8 Powder and Monolith

ZIF-8 synthesis was carried out using three different protocols in order to obtain ZIF-8 as a powder ($_{powd}$ZIF-8), fully and semi-porous monoliths ($_{mono}$ZIF-8(FP) and $_{mono}$ZIF-8(SP), respectively). $_{powd}$ZIF-8 was synthesised based on a method reported by Tanaka et al. [186]. 12.3 g of 2-mIm were dissolved in 90 mL distilled water and 0.549 g $Zn(O_2CCH_3)_2{\cdot}2H_2O$

in 10 mL distilled water; the latter solution was poured into the former and allowed to stir at room temperature for 30 minutes. $_{mono}$ZIF-8(FP) was obtained according to the method developed by Tian et al. [81]; 0.81 g of 2-mIm and 0.29 g of $Zn(NO_3)_2 \cdot 6H_2O$ were dissolved in separate 20 mL EtOH; the two solutions were then mixed together and stirred for 10 minutes. Similarly, $_{mono}$ZIF-8(SP) was obtained using the same Tian et al. procedure, but using IPA solvent instead of EtOH.

All MOFs were recovered by centrifugation at 5000 g for 10 min and washed in 10 mL pure EtOH twice and further centrifuged at 5000 g for 10 min after each washing step. $_{powd}$ZIF-8 was allowed to dry overnight in an oven set at 80° C, whereas the monoliths were dried at room temperature in a fume-cupboard. Prior to use and characterisation, all MOFs were activated in a vacuum oven at 120° C overnight.

3.2.1.2 UiO-66 Powder and Monolith

Powdered UiO-66 ($_{powd}$UiO-66) was obtained by dissolving 2.5 g $ZrCl_4$ in 100 mL N,N-dimethylformamide (DMF) as well as 20 mL hydrochloric acid (HCl) (37%). 2.46 g 1,4-benzenedicarboxylic acid (BDC) is dissolved in 200 mL DMF and added to the previous solution. The mixture was poured in a Schott bottle and placed in a reaction oven set at 80° C overnight. The final product was poured in centrifuge tubes, spun for 10 min. at 5500 g and the mother liquor decanted. The white solid was further washed with 15 mL DMF (x2), 15 mL virgin EtOH (x2) and centrifuged for the same amount at time and at the same speed in between every washing step.

Monolithic UiO-66 samples were synthesised using a sol-gel synthetic method. Firstly, the UiO-66 gel was obtained in one-pot synthesis via dissolving 1.2 g BDC and 1.61 g $ZrOCl_2 \cdot 8H_2O$ in 30 mL DMF solvent. This was followed by addition of 1.5 mL 37% HCl and 2.0 mL glacial acetic acid under vigurous stirring. The resulting solution was placed in a tightly sealed Schott bottle and heated to 100° C for 2 hours. The resulting thick white gel was then removed from the oven and diluted with 50 mL DMF under vigurous stirring to create a dilute suspension, which was then poured into centrifuge tubes, spun for 3 min. at 5500 g and decanted.

The respective UiO-66 monoliths were then produced by following different washing procedures. For $_{mono}$UiO-66(EtOH), the decanted gel was washed with 30 mL virgin EtOH

and sonicated until a fully homogenised mixture was achieved. This was then centrigufed for 10 min. at 5500 g. The washing step in EtOH was repeated 3 times and finally, the gel was allowed to dry for 5 days in an incubator set at 30° C.

For $_{mono}$UiO-66(DMF), the decanted gel was washed with 30 mL DMF and sonicated until fully homogenised, this was then centrifuged for 10 min at 5500 g. The resulting densified gel was allowed to dry at 30° C for 5 days. The obtained monolith was soaked in acetone (3 x 5 mL, 24 hours) and methanol (3 x 5 mL, 24 hours) followed by drying at room temperature overnight. Prior to use and characterisation, all MOFs were activated in a vacuum oven at 120° C overnight.

3.2.1.3 MOF-808 Powder and Monolith

Powdered MOF-808 was synthesised following a technique adapted from Furukawa et al. [120]. 0.33 g benzene-1,3,5-tricarboxylic acid (BTC) and 0.48 g $ZrOCl_2 \cdot 8H_2O$ were dissolved in 60 mL DMF, this was followed by addition of 60 mL formic acid. The mixture was placed in a Shott bottle and heated at 100° C for 7 days. The samples were washed in DMF (30 mL x 2) and EtOH (30 mL x 2) and centrifuged in between every washing step for 10 min at 5000 g. Finally, the white residue was dried at 80° C overnight.

Monolithic MOF-808 samples were synthesised using sol-gel procedures, as per UiO-66. Firstly, the MOF-808 gel was obtained via separately dissolving 1.1 g BTC in 10 mL DMF and 4.8 g $ZrOCl_2 \cdot 8H_2O$ in 10 mL DMF solvent. The solutions were then mixed together and 20 mL formic acid was added. The resulting solution was placed in a tightly sealed Schott bottle and heated to 150° C for 2 hours. The resulting thick white gel was then removed from the oven and diluted with 40 mL DMF under vigurous stirring to create a dilute suspension, which was then poured into centrifuge tubes, spun for 3 min. at 5500 g and decanted.

The respective MOF-808 monoliths are then produced by following different washing procedures. For $_{mono}$MOF-808(EtOH), the decanted gel was washed with 30 mL virgin EtOH and sonicated until a fully homogenised mixture was achieved. This was then centrifuged for 10 min. at 5500 g. The washing step in EtOH was repeated 3 times and, finally, the gel was allowed to dry for 5 days in an incubator set at 30° C. For $_{mono}$MOF-808(DMF), the decanted gel was washed with 30 mL DMF and sonicated until fully homogenised, this was then centrifuged for 10 min. at 5500 g. The resulting densified gel was allowed to dry at 30°

C for 5 days. The obtained monolith was soaked in methanol overnight (3 x 5 ml) followed by drying at room temperature overnight. Prior to use and characterisation, all MOFs were activated in a vacuum oven at 120° C overnight.

3.2.1.4 Zr-based MOFs with tagged and elongated linkers

Zr-L1 (UiO-66), Zr-L2 and Zr-L3 were synthesised by mixing 0.9 mmol of the respective linker with 0.9 mmol of $ZrCl_4$ in 20 mL DMF. Zr-L5, Zr-L6 (UiO-67), Zr-L7, Zr-L8, PCN-56 and PCN-57 were obtained by mixing 0.9 mmol of the respective linker with 0.9 mmol of $ZrCl_4$ and 2.5 mmol of l-proline in 20 mL DMF. In all cases, the contents were gently sonicated followed by addition of 80 µl HCl before being placed in an oven for 24 hours at 120° C followed by centrifugation and washing in DMF (15 mL x 2) and acetone (15 mL x 2).

PCN-56 and PCN-57 materials were synthesised by mixing 0.225 mmol of the respective ligand with 0.225 mmol of $ZrCl_4$ and 1.125 mmol of L-proline modulator; these were added to a 50 mL screw-top jar and dissolved in 10 mL DMF followed by the addition of 0.04 mL 37% HCl. The mixtures were placed in a reaction oven set at 120° C for 36 hours. The products were washed in DMF (1 x 15 mL) and acetone (15 mL x 2) before being dryed in the dessicator. These materials were then stored in chloroform for 3 consecutive days, exchanging with fresh solvent each day before being dried in vacuum. Finally, all materials were activated at 100° C under vacuum overnight before use.

3.2.2 Stability Testing

The pH profiles (short-term pH evolution tests) were measured by submerging 50 mg of MOF material in 30 mL aqueous solution. According to the desired starting pH, 0.001 M solutions of either HCl or NaOH were used for adjustment. A pH probe was kept submerged in the test solution whilst it was being continuously stirred.

The overnight stability tests were performed by submerging 50 mg of the respective MOF material in 3 mL of aqueous solution at set pH. The materials were placed on a roller mixer overnight. The final pH of the solutions was measured and a liquid sample was taken for

quantification, the materials were collected by centrifugation, washed and dried at 100° C. Prior to characterisation, all materials were activated in a vacuum oven at 100° C.

3.2.3 Characterisation

Powder X-ray Diffraction patterns were measured using with a Bruker D8 Advance diffractometer with monochromatic Cu Kα radiation (1.54 Å) at 40 kV and 40 mA. Patterns were recorded in steps of 0.01° at a scanning speed of 0.01°s^{-1} from values of 2θ = 5° to 40°. Nitrogen isotherms were measured at 77 K using a Micromeritics TriStar II PLUS. Data was collected from relative pressure P/P_0 0.001 to 0.995. All samples were degassed for at least 7 hours at 120 °C under vacuum prior to characterisation.

Amount of linkers found in the aqueous solutions were quantified by use of an HPLC system equipped with a UV detector (Agilent Technologies 1260 Infinity II) and a EC-C18 column (pore size: 2:7 µm). The UV absorbance was set at 285, 205 and 213 nm for BDC, 2-MIM and BTC, respectively. For detection of BDC and BTC: mobile phase A (0.1% vol. trifluoroacetic acid in deionised water) and mobile phase B (methanol, MeOH) were used with a flow rate of 1 mL.min^{-1} in gradient mode. For 2-mIm: mobile phase A (0.005 M NH_4HCO_3 in deionised water) and mobile phase B (0.005 M NH_4HCO_3 in MeOH) were used with a flow rate of 0.8 mL.min^{-1} and a ratio of 70% A.

3.3 Results and Discussion

3.3.1 Short-term pH Evolution

The rationale of using pH monitoring as means of testing the chemical stability in a given medium stems from the very nature of MOFs, which consist of organic linker molecules coordinating to metal centres. Any of these components can have either basic or acidic properties, which can, in turn, generate a chemical response consisting in a change of pH.

Most MOFs in this study are built from carboxylate (UiO-66, Zr L2-L8, MOF-808) linkers which are the conjugated bases of organic acids. These linkers are incorporated into the MOF in their deprotonated from, which makes them weak bases when they are released. In turn, ZIF-8 is built with 2-mIm linkers which is a weak base incorporated into the MOF in a deprotonated form, this makes it an even stronger base upon release. Furthermore, when a bond between a metal and linker is disconnected, the metal node possesses one free coordination site which increases its Lewis acidity. Consequently, in an aqueous medium, these Lewis acids can capture OH^- moieties thus altering the pH value.

Considering these facts alone, the nature of the pH change cannot be easily predicted if a MOF is fully degraded. However, if the pH reading does change, this could be indicative of MOF reactivity with the testing environment. Alternatively, if the pH reading stays constant, this could also indicate that there is no degradation taking place.

3.3.1.1 ZIF-8

In all cases, measurements were taken as soon as the solid MOF materials came in contact with the respective solutions. When an equilibrium pH value was reached, denoted by a plateau, the pH was readjusted, this being indicated by a sharp increase or decrease to initial pH value. This was repeated until there was no observable change with subsequent readjustments.

Figure 3.3 shows the pH evolution of $_{powd}$ZIF-8, $_{mono}$ZIF-8(FP) and $_{mono}$ZIF-8(SP). In the case of $_{powd}$ZIF-8 (Figure 3.3 **a**), in basic conditions there is no observable change even after 40 minutes of contact, when the same material is submerged in water set at an initial pH value of 7, the pH drastically increases to reach equilibrium at pH $\sim$8. This equilibrium value decreases to pH $\sim$7.5 with subsequent pH readjustments after 10, 20 and 30 minutes.

Finally, when the same material is submerged in water set at an initial pH 3, the pH drastically increases to an equilibrium value of ∼8, this value decreases to pH ∼7, ∼6.2 and 3 after 3 subsequent readjustments. The lack of pH response after readjusting is likely to be due to complete MOF degradation.

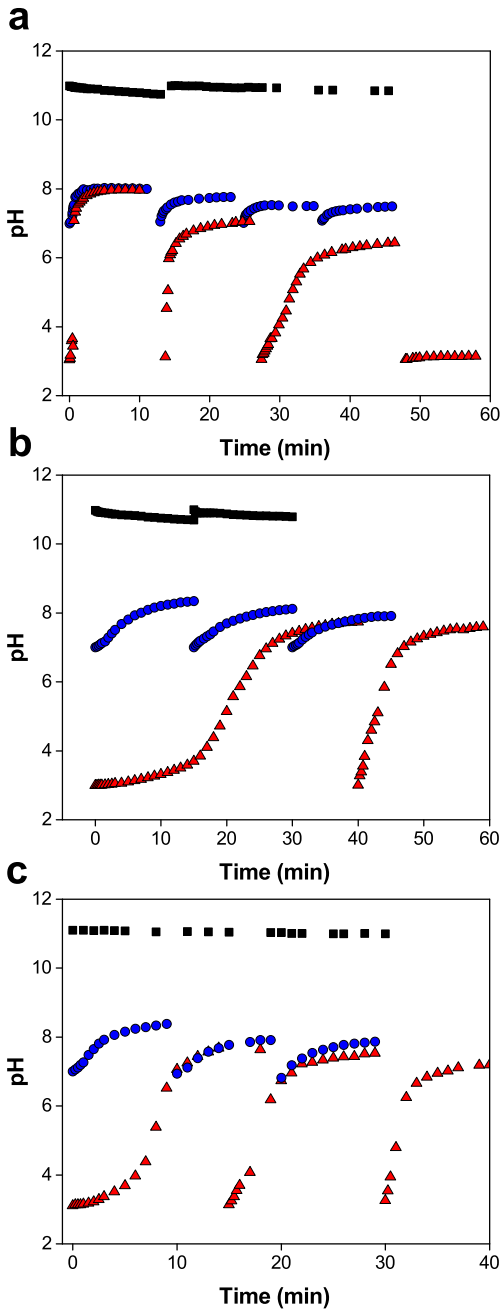

Fig. 3.3 pH evolution curves of **a** *powd*ZIF-8, **b** *mono*ZIF-8(FP) and **c** *mono*ZIF-8(SP). **Black squares**, **blue circles** and **red triangles** indicate basic, neutral and acidic conditions, respectively.

Similarly, for both $_{mono}$ZIF-8(FP) and $_{mono}$ZIF-8(SP) (Figure 3.3 **b** and **c**) the same pH response is observed, wherein the same equilibrium pH values are reached for the same starting conditions. Interestingly, the initial rate of change of pH is much slower than seen in the powdered configuration. For $_{mono}$ZIF-8(FP) in initially acidic conditions, the equilibrium pH value is reached only after 30 minutes of contact whereas for $_{mono}$ZIF-8(SP) equilibration is achieved after $\sim$14 min, this is in contrast with $_{powd}$ZIF-8, which equilibrates within less than 5 minutes. This is thought to be due to the higher density of the formed monolithic configurations which bring about diffusion limitations and hence a slowed down rate of pH response.

From this information alone it is understood that, irrespective of the configuration used, ZIF-8 is highly unstable in acidic conditions and less so under neutral pH. On the other hand, ZIF-8 is thought to be highly stable in alkaline conditions. However, the rate of MOF degradation is observed to slow down drastically from the powdered to the monolithic configurations. This is especially the case in acidic conditions, where ZIF-8 is thought to be highly unstable in powdered form and is thought to be primarily due to diffusive limitations through the formed monolithic material at this point.

3.3.1.2 UiO-66

UiO-66 MOF, composed of Zr_6 SBUs and terephthalic acid (BDC) linkers, was also subject to the same testing conditions. Two different monolithic configurations were also investigated, in addidion to the standard powdered UiO-66. In this case, the monolithic configurations were either prepared in EtOH or DMF as washing solvents. The choice of washing solvent is known to yield monoliths with different densities. Mercury porosimetry has revealed apparent densities of 0.961 and 0.467 g.cm^{-3} for $_{mono}$UiO-66(DMF) and $_{mono}$UiO-66(EtOH), respectively. The mechanism of monolith network formation is described in Chapter 5.

Figure 3.4 illustrates the pH evolution curves of $_{powd}$UiO-66, $_{mono}$UiO-66(EtOH) and $_{mono}$UiO-66(DMF). In this case, due to the nature of the linker in UiO-66, which is a conjugated base of an acid, the pH response tends to equilibrate in the acidic region. Sample $_{powd}$UiO-66 (Figure 3.4 **a**) shows no response in the acidic region, at a starting pH of 3. On the other hand, very sharp pH decrease is registered in neutral starting conditions, where the equilibrium pH value increases from $\sim$3.8 to $\sim$6.5 after 3 pH readjustments and 60 minutes

of contact. The same behaviour is observed at a starting pH of 11, wherein the pH drastically

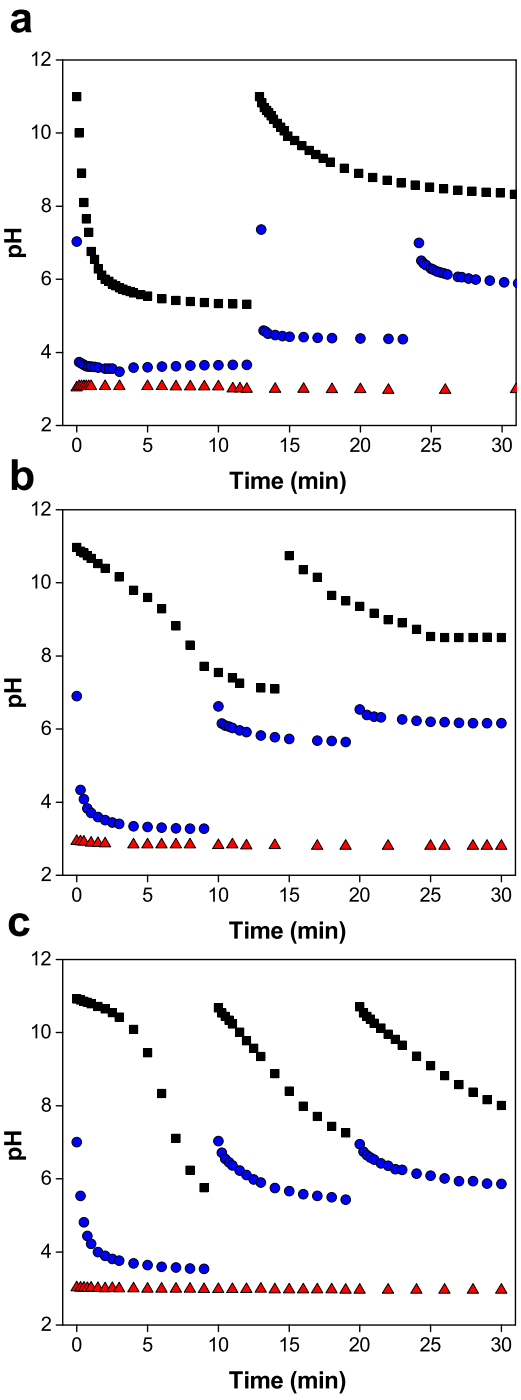

Fig. 3.4 pH evolution curves of **a** $_{powd}$UiO-66, **b** $_{mono}$UiO-66(EtOH) and **c** $_{mono}$UiO-66(DMF). **Black squares**, **blue circles** and **red triangles** indicate basic, neutral and acidic conditions, respectively.

decreases to reach an equilibrium of ∼5.5 within 5 minutes of contact, after 2 readjustments and 60 minutes of contact there was no more observable change.

For $_{mono}$UiO-66(EtOH) (Figure 3.4 **b**) the same behaviour is shown for acidic and neutral conditions, however the rate of pH change at basic conditions is drastically slowed down. In this instance, equilibrium occurs at a pH of ∼7 within 10 minutes. On the other hand, $_{mono}$UiO-66(DMF) (Figure 3.4 **c**) shows a different behaviour in basic conditions, where, at first, only minute pH change is observed until after ∼4 minutes of contact. The pH then drastically decreases for a further 6 minutes. However, after readjustment, equilibrium is not observed, which could indicate degradation. This might mean that, in spite of expecting slower mass transfer through the material due to the increased density of $_{mono}$UiO-66(DMF), the monolith appears to be unstable in the aqueous medium.

At this stage, it is inferred that UiO-66 is stable in acidic conditions, highly unstable in basic and moderately unstable in neutral pH.

3.3.1.3 MOF-808

MOF-808 consists of 6-connected Zr_6 clusters to acidic linkers, in this case the linker being a tricarboxylic acid. Therefore, the pH response is expected to be similar to that of UiO-66 in that it would tend to stabilise in acidic regions. Figure 3.5 illustrates the pH curves for MOF-808, monolithic MOF-808 samples were obtained in a similar way to those of UiO-66, wherein a higher density monolith was achieved via using DMF as the washing solvent.

For $_{powd}$MOF-808 (Figure 3.5 **a**) at initially acidic conditions (pH 3), the pH reading remains unchanged for the entire duration of the test. Under neutral conditions (starting pH of 7), the pH drastically drops within 1 minute of contact to an equilibrium value of 4, which increases with subsequent readjustments to a pH of 4.8 and 6 after 10 and 20 minutes of contact, respectively. At a starting pH of 11, the pH decreases more gradually to attain an equilibrium value of 7 after 10 minutes, the equilibrium value then attains pH of 10 and 10.5 after further readjustments.

Similarly, as previously shown for $_{mono}$UiO-66, the pH response for monolithic MOF-808 samples (Figure 3.5 **b,c**) is considerably slowed down, especially in basic conditions. As seen for the powder, the $_{mono}$MOF-808(EtOH) sample registers no pH change at initially acidic conditions, however, at starting neutral conditions, the pH drops to 3.5 within 10 minutes,

a lower equilibrium value than the powder. After subsequent readjustments, the rate of pH

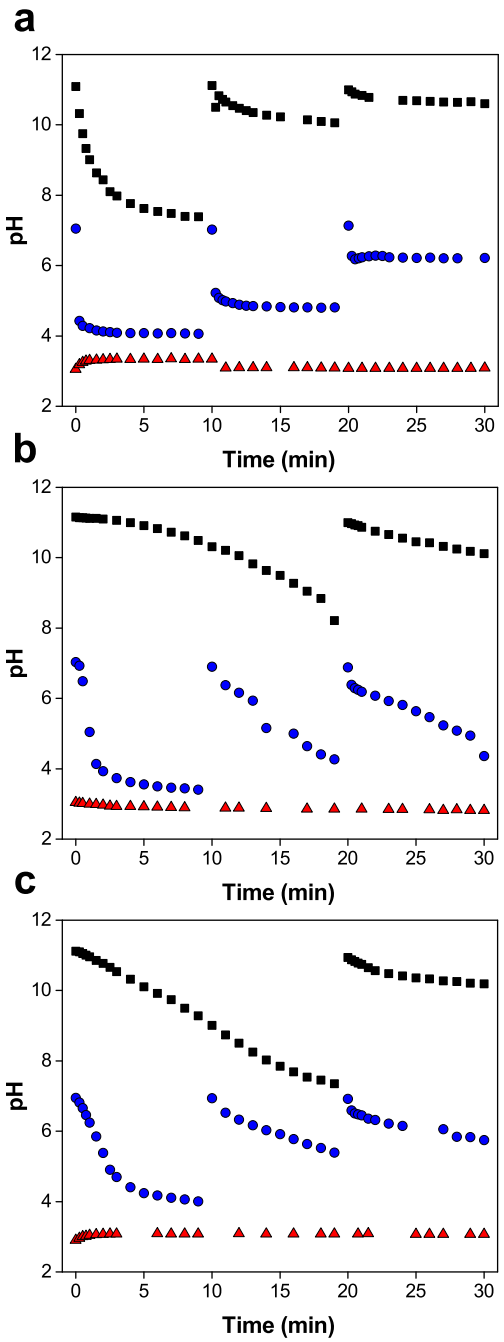

Fig. 3.5 pH evolution curves of **a** $_{powd}$MOF-808, **b** $_{mono}$MOF-808(EtOH) and **c** $_{mono}$MOF-808(DMF). **Black squares**, **blue circles** and **red triangles** indicate basic, neutral and acidic conditions, respectively.

decrease starts to slow down but equilibrium is not attained. This is more so under basic starting conditions, where equilibrium is not observed until at readjustment after 20 minutes

of contact. The same behaviour is observed in acidic conditions for $_{mono}$UiO-66(DMF), however, under neutral starting conditions the initial equilibrium value is higher (pH 4) than that of $_{mono}$UiO-66(EtOH), similarly though, with further pH readjustments, pH equilibrium is not observed. At a starting pH of 11, the pH decrease is very slow and gradual, reaching a pH of 7.5 within 20 minutes, after readjustment, the equilibrium value resembles that of $_{mono}$UiO-66(EtOH) (pH 10).

The slow pH response is, again, correlated with the increased density of the monolithic phase in comparison to the standard powder. However, as seen for $_{mono}$UiO-66(DMF), sample $_{mono}$MOF-808(DMF) shows a more steady and accelerated pH drop than $_{mono}$MOF-808(EtOH), which might suggest that the monolithic network, formed as a result of DMF, expresses lower water stability than its' EtOH analogue. Again, at this stage, MOF-808, irrespective of configuration, is expected to be stable in acidic conditions and less so in neutral and basic conditions.

3.3.1.4 Zr-based MOFs with tagged and elongated linkers

Following the above examples, the same testing procedure was applied in order to probe the aqueous stability of 7 isoreticular UiO-type MOFs. Figure 3.6 illustrates the pH evolution of Zr-L1 to -L8 MOFs for the same starting pH values. It must be noted that Zr-L1 is UiO-66 synthesised following a different method, in which the use of modulators has been omitted, this means that this UiO-66 structure contained less defects than the previously discussed $_{powd}$UiO-66 sample. Due to the acidic nature of all carboxylate linkers (Figure 3.2), it is observed that when all MOFs are exposed to a starting pH of 3, no change in the pH value is observed throughout the length of pH monitoring. On the other side, a decrease in pH value is seen in basic conditions starting at pH 11.

This behaviour becomes less and less pronounced from BDC (L1, UiO-66) to 2-Br-BDC (L2), 2-NO_2-BDC (L3) and 2-NH_2-BDC (L4) and reaches an equilibrium value of around pH 4.5 for BDC (L1) and pH 5 for the latter 3 structures. For the same 4 structures (L1-L4), as the pH is readjusted to pH 11, no further charge in seen for L1-L3, however, the pH keeps dropping to reach an equilibrium value of 9 for the aminated linker (L4). Similarly, for structures L5-L8, the same final equilibrium pH value of $\sim$8 is reached upon contact with an initial pH of 11, however, following pH readjustment, a further decrease in pH value is

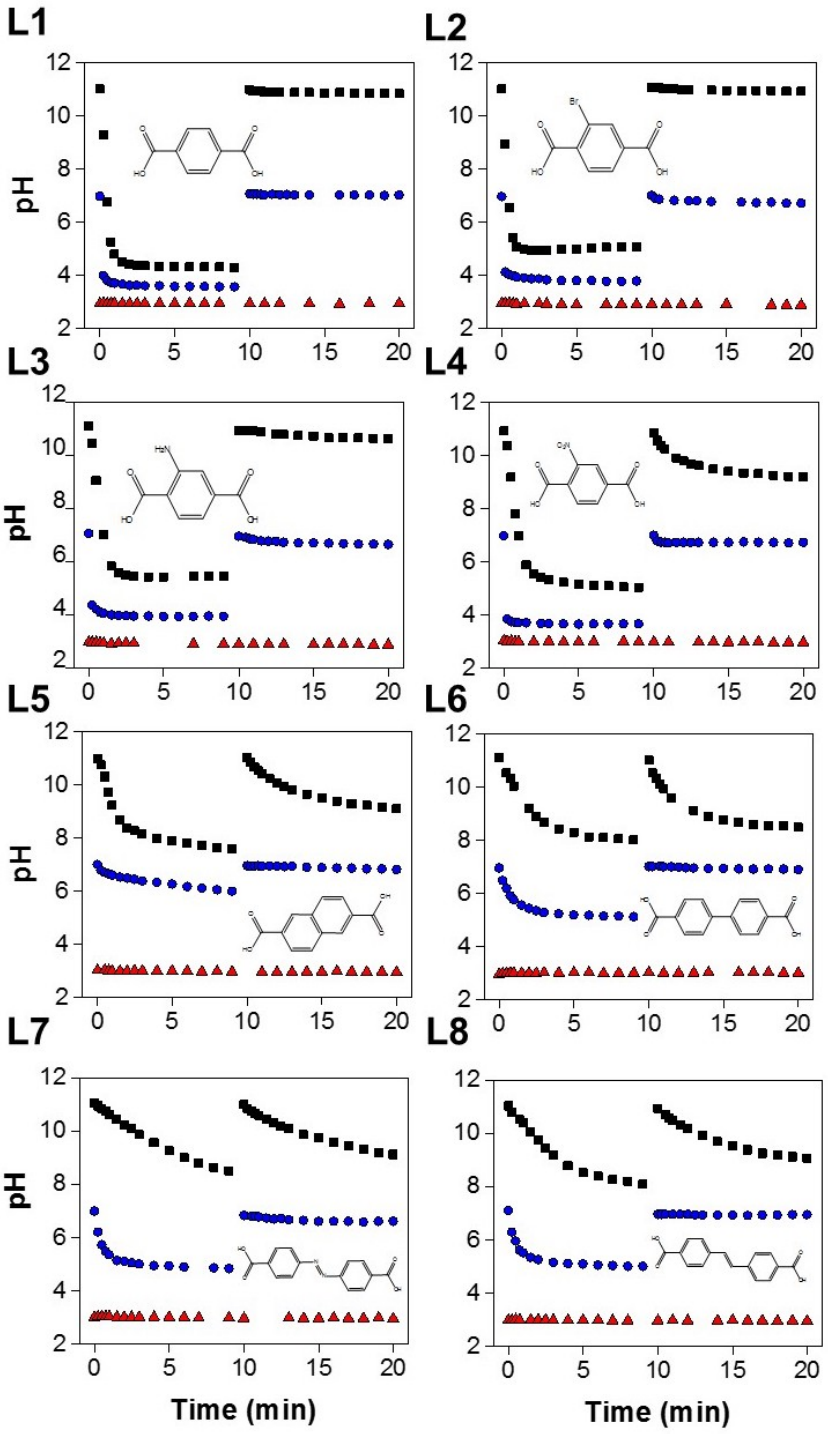

Fig. 3.6 pH evolution curves of Zr-L1 to Zr-L8 samples. **Black squares**, **blue circles** and **red triangles** indicate basic, neutral and acidic conditions, respectively.

seen, this could potentially suggest that the structure is still degrading as more protons are released.

When contacted with water in neutral pH, single benzene-ring structures L1-L4 express the same initial rate of pH decrease to reach an equilibrium value of pH $\sim$ 3.8, however, upon readjustment, no further change is observed. On the other hand, when subjected to the same initial pH value, the only fused benzene ring structure (L5) expresses a higher equilibrium pH value of around pH 6, noting an overall change of 1 pH unit, with no further change upon readjustment. This differs from the same pH starting value for the double benzene ring structures L6-L8, which show an accelerated rate of pH decrease to reach an equilibrium value of pH $\sim$5, as seen in all other cases, these structures show no observable change in pH upon readjustment to pH 7. As previously observed for the pH monitoring of UiO-66 alone, all these Zr-based UiO-type structures are, at this stage, assumed to be stable in acidic conditions and unstable in neutral and basic environments.

Similarly, Figure 3.7 illustrates the pH evolution curves of PCN-56 and PCN-57 materials. It is observed that with increasing number of methyl groups from 2 in PCN-56 and to 4 in PCN-57, the rate of pH response is drastically slowed down, especially under neutral conditions where little variation in pH is observed for the tetramethyl structure.

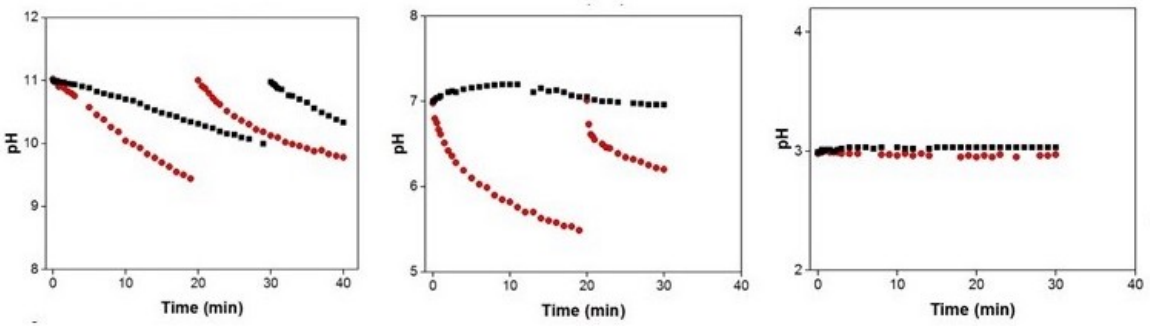

Fig. 3.7 pH evolution curves of PCN materials with di- and tetramethyl functional groups represented by **red circles** and **black squares**, respectively. In basic (left), neutral (centre) and acidic (right) conditions, respectively.

Under basic conditions, again, PCN-57 sees a slow pH response, with as little change as 1 pH unit within 30 minutes of contact; on the other hand, PCN-56 registers a change of $\sim$1.5 pH units within an initial of 20 minutes of contact. Under acidic conditions, both materials show no change in pH for the entire duration of contact. Thus, the drastic difference between these two materials relies on the higher degree of hydrophobicity attain by anchoring 2 extra

methyl groups on PCN-57, expecting a higher degree of both kinetic and thermodynamic stability of the framework.

3.3.2 Overnight Stability Assessment

3.3.2.1 ZIF-8

Following exposure of the MOF samples to the same starting conditions overnight, the samples were recovered, washed and dried. Powder X-ray diffraction characterisation was performed in order to ascertain the crystallinity of the recovered samples, whereas nitrogen adsorption isotherms at 77 K were measured in order to confirm the extent ot porosity remaining in the solid MOF phase.

Figure 3.8 illustrates the XRD patterns of recovered ZIF-8 samples. In the case of $_{powd}$ZIF-8 (Figure 3.8 **a**), none of the sample could be recovered following exposure in acidic conditions due to complete dissolution. However, after exposure to water in neutral and basic conditions, the same Bragg peaks are observed as for the untreated and simulated material. Namely, a 100% intensity peak at $\sim$ 7.5° 2θ followed by 10.5, 15 and 18° 2θ. This indicates crystallinity being recovered in the respective conditions. Monolithic samples $_{mono}$ZIF-8(FP) and $_{mono}$ZIF-8(SP) (Figure 3.8 **b, c**) show slightly altered XRD patterns of untreated MOF, with a noticeably increased intensity of the 10.5 and 13° 2θ peaks relative to the 100% 7.5° 2θ peak. This difference is more pronounced in the IPA synthesised $_{mono}$ZIF-8(SP) sample and may indicate crystalline defects, such as missing metal nodes, in addition to solvent blocking the porosity. Nonetheless, both monolithic samples retain crystallinity in all conditions, this is in contrast to the respective pH evolution curves which showed a similar response to the powdered sample, especially for those samples subjected to acidic treatment.

Figure 3.9 illustrates the adsorption isotherms of recovered ZIF-8 samples. As shown, $_{powd}$ZIF-8 appears more stable in basic conditions, where the adsorption capacity is reduced from $\sim$410 to $\sim$380 $cm^3.g^{-1}$ and less so in pH 7, after which it is reduced to $\sim$300 $cm^3.g^{-1}$. This marked decrease in adsorption capacity was not attested by X-ray diffraction, which only confirmed the presence of a highly crystalline phase.

Monolithic sample $_{mono}$ZIF-8(FP) (Figure 3.9 **b**) shows a decreased adsorption capacity in comparison to the powder in the untreated sample, this might be due to using a different

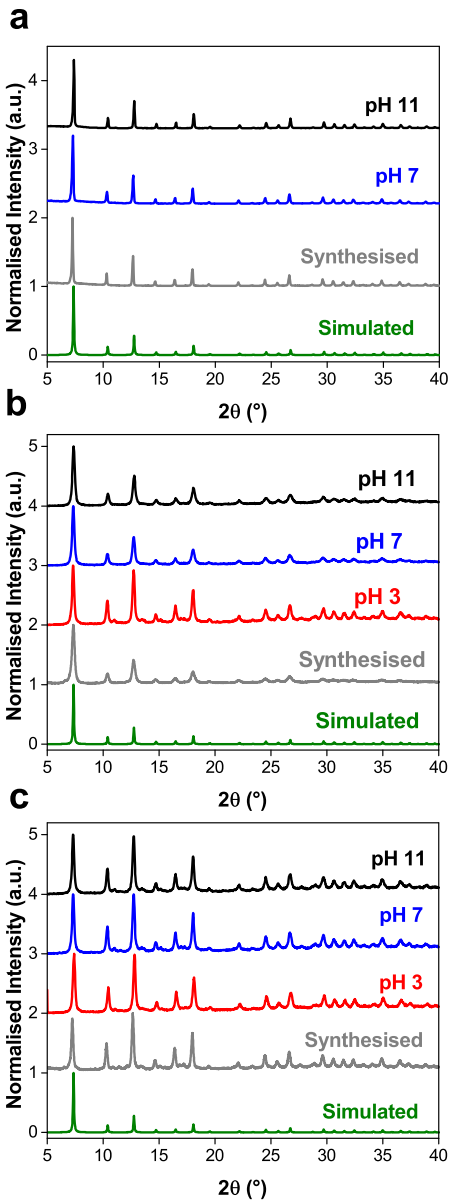

Fig. 3.8 Powder X-ray diffraction patterns from 5 to 40° 2θ of **a** $_{powd}$ZIF-8, **b** $_{mono}$ZIF-8(FP) and **c** $_{mono}$ZIF-8(SP). With samples recovered from exposure to basic (**black line**), neutral (**blue line**) and acidic (**red line**) conditions, respectively. Whereas **gray** and **green** lines indicate untreated and simulated material, respectively.

synthesis technique. On the other hand, recovered $_{mono}$ZIF-8(FP) samples exposed to pH 7 and 11 show an adsorption capacity of ∼100 $cm^3.g^{-1}$, with virtually no difference between the two. Unexpectedly, the sample treated in pH 3 observes an altered isotherm shape, denoted by a sharp increase to ∼200 $cm^3.g^{-1}$ up to 0.1 P/P_0, followed by a further increase up to ∼300 $cm^3.g^{-1}$ until saturation pressure (1.0 P/P_0). This signifies the formation of

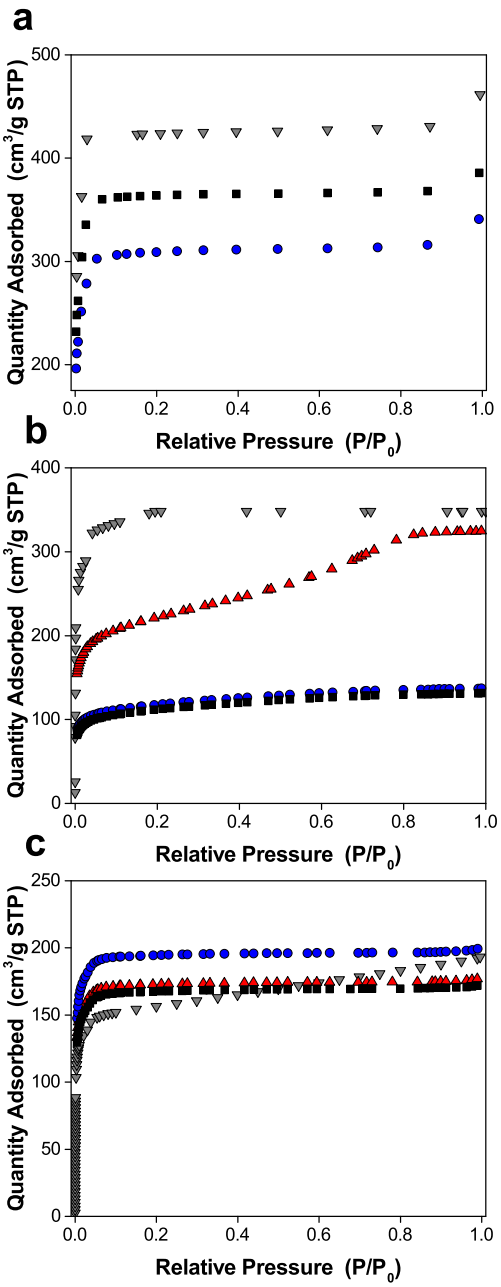

Fig. 3.9 Nitrogen adsorption isotherms at 77K of **a** *powd*ZIF-8, **b** *mono*ZIF-8(FP) and **c** *mono*ZIF-8(SP). With samples recovered from exposure to basic (**black squares**), neutral (**blue circles**) and acidic (**red triangles**) conditions, respectively. Whereas inverted **gray** triangles indicate untreated material.

a mesoporous phase, in addition to the remaining microporous MOF and it might mean extensive structural change.

The semi-porous monolithic sample $_{mono}$ZIF-8(SP) (Figure 3.9 **c**), shows a significantly improved adsorption capacity, especially in acidic conditions. At pH 7, however, the same sample reached $\sim$190 $cm^3.g^{-1}$, relative to $\sim$150 $cm^3.g^{-1}$ of the untreated sample. This could potentially indicate a structural defect, wherein the pore volume is increased through a missing linker defect. In order to ascertain whether the reduced adsorption capacity of the recovered materials is accompannied by framework disintegration, the liquid aliquots collected prior to solid recovery were analysed for presence of dissolved linker.

Figure 3.10 illustrates the amount of linker found in the liquid solutions. As expected from XRD and nitrogen adsorption, the amount of linker found in solution decreases drastically from the powdered to the monolithic samples. At pH 3 $_{powd}$ZIF-8 could not be recovered, in this case, the amount of linker dissolved was $\sim$78% of the total expected. Under neutral conditions, the same sample experiences a linker loss of $\sim$25%, which is comparable to the $\sim$25% reduction in adsorption capacity shown in Figure 3.9 **a**. Similarly, under basic conditions, only $\sim$3% of linker is dissolved - this is less than expected following nitrogen adsorption characterisation - and it might be due to the recovered solid MOF returning a partially amorphous phase. Between the two monolithic samples, more linker is observed in solution under acidic conditions in sample $_{mono}$ZIF-8(FP) ($\sim$2.5%) in comparison to the semi-porous monolith $_{mono}$ZIF-8(SP) ($\sim$1.8%). Under neutral conditions, the amount of linker observed for both samples is about the same, whereas in basic conditions, the $_{mono}$ZIF-8(SP) sample expresses a difference of 0.2 % lower relative to $_{mono}$ZIF-8(FP) .

So far, pH measurement has proved to be more indicative of chemical processes occuring when ZIF-8 contacts water even more so than X-ray characterisation. For example, in the case of $_{powd}$ZIF-8, the largest pH change was observed under acidic conditions - at this pH none of the material could be recovered due to complete dissolution. Another big change was observed in the pH profile of this material under neutral conditions, however, X-ray characterisation revealed an intact crystal structure; at the same time, porosity characterisation has revealed a significant reduction in adsorption capacity. The same phenomenon is observed for testing at basic conditions. Therefore, it is concluded that porosity characterisation paired with linker dissolution monitoring gives the best insight into the water stability of a MOF; pH monitoring however, only qualitatively indicating some degree of reactivity with the environment and therefore can provide an insight into the kinetic stability of a material.

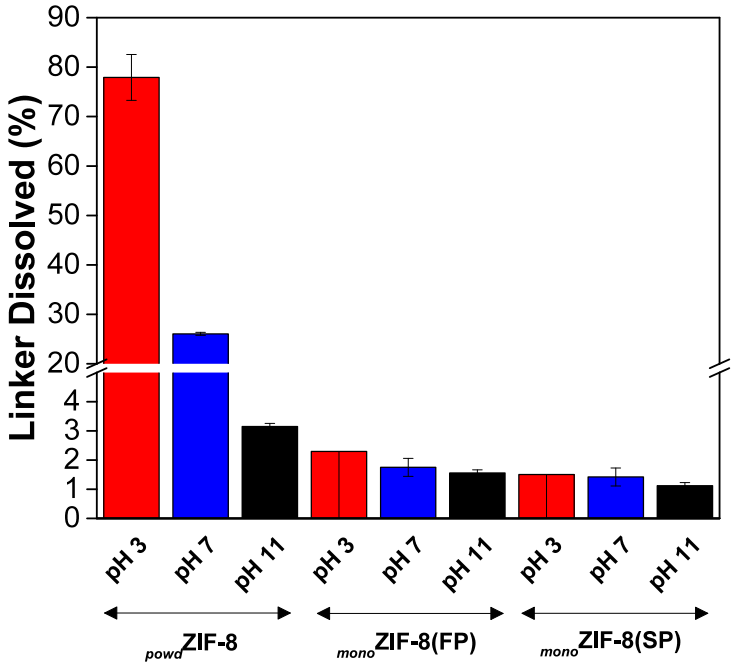

Fig. 3.10 Extent of linker dissolution of ZIF-8 samples

Overall, this data elucidated that shaping ZIF-8 into a monolithic configuration drastically improved the overall framework stability. As inferred from nitrogen adsorption characterisation, the semi-porous $_{mono}$ZIF-8(SP) sample appears to be more stable than the fully porous monolithic one $_{mono}$ZIF-8(FP). This can be due to the IPA solvent blocking the internal pores and conferring the medal nodes with a shielding effect therefore impeding hydrolysis of the metal-linker bond.

Nonetheless, even if the fully porous monolithic material expresses significant pore collapse after reactivation - the amount of linker released to the liquid environment is minute in comparison to the powdered MOF this being a major improvement over the powder configuration. In conclusion, shaping ZIF-8 into a densified monolithic structure proves to drastically improve the stability in aqueous medium, especially under acidic conditions where the standard powdered configuration dissolves in solution.

3.3.2.2 UiO-66

Similarly, UiO-66 samples were subject to the same testing conditions. Figure 3.11 illustrates the powder X-ray diffraction patterns of recovered UiO-66 samples. Pristine powdered

UiO-66 yields three main narrow Bragg peaks at 7.4 and 8.6 and 25.5° 2θ. In comparison, the two untreated monolithic UiO-66 samples (Figure 3.11 **b, c**) indicate significant peak broadening. The peak broadening, or Scherrer broadening, is correlated to a decreased primary particle size in closely packed monolithic UiO-66.

For $_{powd}$UiO-66 (Figure 3.11 **a**), all recovered samples show excellent crystallinity. On the other hand, recovered $_{mono}$UiO-66(EtOH) and $_{mono}$UiO-66(DMF) samples show broadened 100% intensity peaks. Moreover, for both monoliths the resolution of the diffractograms decreases with increasing pH, this is possibly due to decreased crystallinity and an increase in the proportion of the amorphous phase. The diffractograms of the recovered UiO-66 samples are in line with the respective pH evolution curves, which showed increased chemical response with increasing pH (Figure 3.4).

Nitrogen adsorption (Figure 3.12) reveals that, indeed, the adsorption capacity of UiO-66 decreases with increasing pH, registering a 47% reduction at a starting pH of 11. Porosity also appears to reduce under neutral conditions, registering an adsorption capacity of ∼300 $cm^3.g^{-1}$, a reduction of ∼26% from untreated UiO-66. Consequently, at a starting pH of 3, the registered reduction in adsorption capacity is less than 2%. These drastic changes were not observable in the respective X-ray diffractograms.

For $_{mono}$UiO-66(EtOH), the untreated sample expresses a fair amount of mesoporosity, characterised by a slope in the adsorption isotherm towards saturation pressure, and also by the hysteretic behaviour. However, as samples are recovered from exposure to water at differing starting pH, the isotherms approach Type I behaviour, as expected for standard microporous UiO-66 powder. Indeed, as the solid UiO-66 MOF is recovered, the monolithic UiO-66 network appears to disintegrate and return a powder. This effect is observed for both types of monoliths. When exposed to initial pH of 7 and 11, both monoliths return an adsorption capacity of $\sim$ 100 $cm^3.g^{-1}$ with a Type I behaviour. Sample $_{mono}$UiO-66(EtOH) yields a higher adsorption capacity than $_{mono}$UiO-66(DMF) in acidic conditions, suggesting improved stability over the higher density sample.

Figure 3.13 shows the amount of BDC linker found in liquid solutions. As expected for the $_{powd}$UiO-66 sample, the highest amount of dissolution occurs at pH 11 (∼45%) followed by pH 7 (∼4%). At pH 3 a dissolution of less than 0.5% is observed, this was attested by a minutely decreased adsorption capacity. For samples $_{mono}$UiO-66(EtOH) and

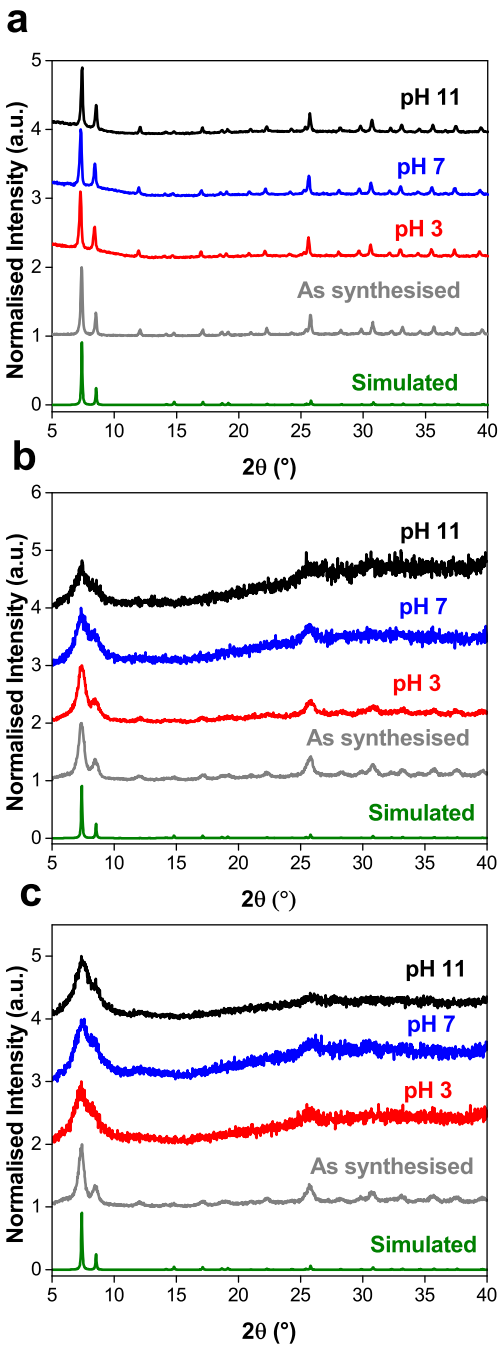

Fig. 3.11 Powder X-ray diffraction patterns from 5 to 40° 2θ of **a** $_{powd}$UiO-66, **b** $_{mono}$UiO-66(EtOH) and **c** $_{mono}$UiO-66(DMF). With samples recovered from exposure to basic (**black line**), neutral (**blue line**) and acidic (**red line**) conditions, respectively. Whereas **gray** and **green** lines indicate untreated and simulated material, respectively.

$_{mono}$UiO-66(DMF) virtually the same quantity of linker is observed in the liquid aliquots for pH 3 and 7 of less than 0.5%, at pH 11, however, for $_{mono}$UiO-66(DMF) this value reaches

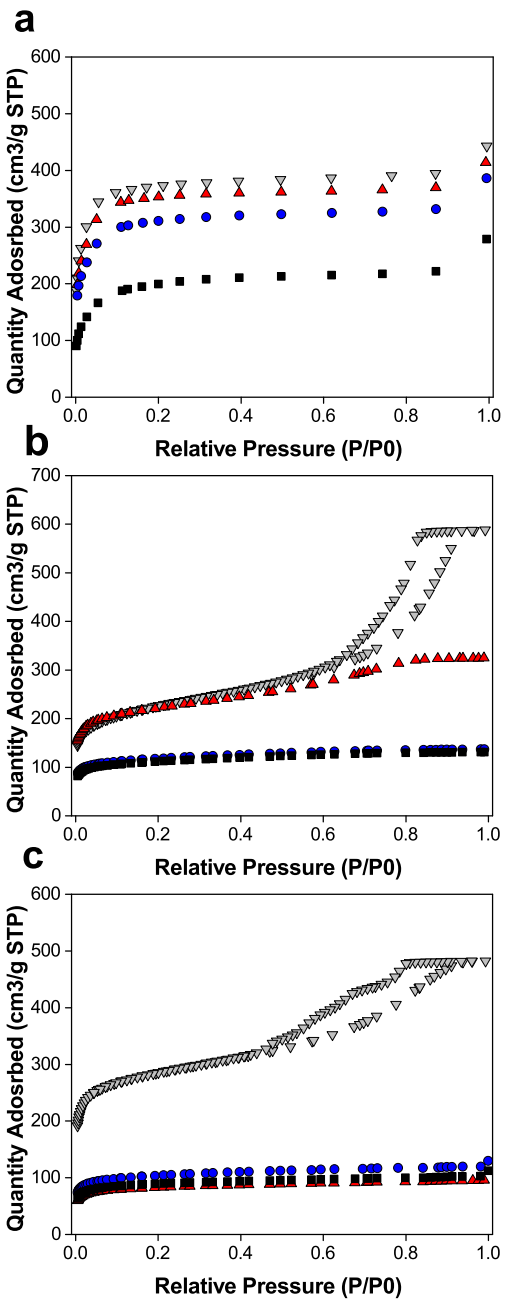

Fig. 3.12 Nitrogen adsorption isotherms at 77K of **a** $_{powd}$UiO-66, **b** $_{mono}$UiO-66(EtOH) and **c** $_{mono}$UiO-66(DMF). With samples recovered from exposure to basic (**black squares**), neutral (**blue circles**) and acidic (**red triangles**) conditions, respectively. Whereas inverted **gray** triangles indicate untreated material.

$\sim$2%. Whilst such low quantities of dissolution can't be correlated with the drastically decreased adsorption capacities observed for both monolithic samples, another contributing

factor might be the decreased solubility of BDC in water as well as the formation of amorphous UiO-66.

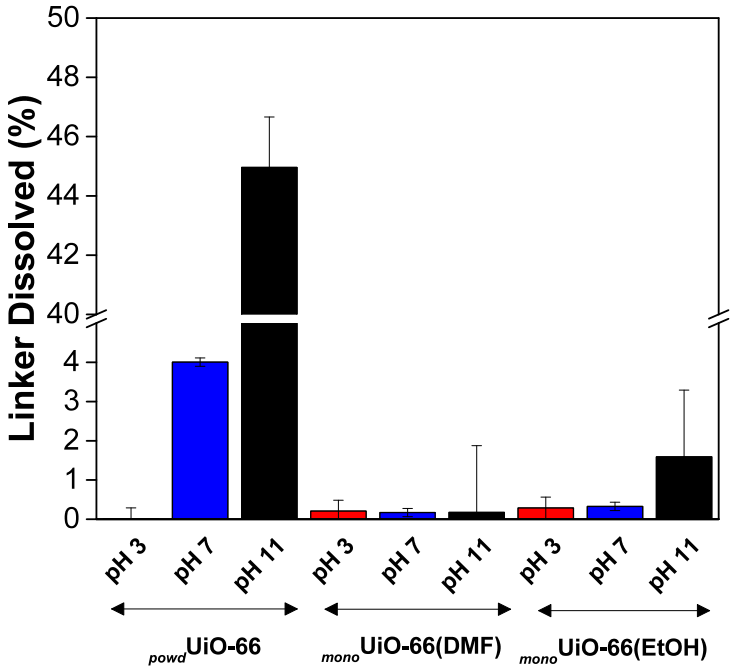

Fig. 3.13 Extent of linker dissolution of UiO-66 samples

In conclusion, whilst enhanced liquid phase stability was observed for the densified monolithic ZIF-8 samples, the same was not attested for the UiO-66 monoliths. After treatment in acidic, neutral and basic media, powdered UiO-66 still returns a highly crystalline phase with an adsorption capacity reduced by a maximum of 47%. Monolithic UiO-66 obtained in ethanol subject to the same treatment returns what is mostly a powdered configuration of UiO-66 expressing more pore collapse than the initially obtained UiO-66 powder at pH 7 and 11. In pH 3, the same sample only shows a reduction in mesoporosity. The slightly higher density monolithic sample, obtained using DMF solvent, returns a mostly powdered sample with significant pore collapse even after acidic treatment. Therefore, in terms of overall stability $_{powd}$UiO-66 is still the most resilient, followed by $_{mono}$UiO-66(EtOH) and finally, $_{mono}$UiO-66(DMF) being the least stable under all testing conditions.

3.3.2.3 MOF-808

Similarly, MOF-808 samples were subject to the same treatment after characterisation. Figure 3.14 shows the X-ray diffraction patterns of recovered MOF-808 samples. The

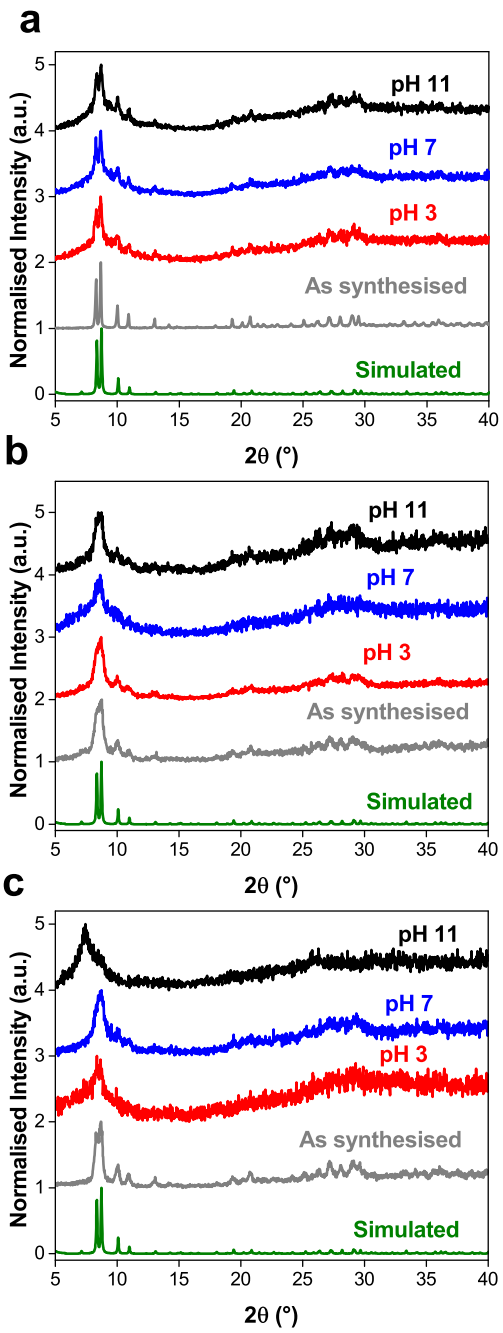

Fig. 3.14 Powder X-ray diffraction patterns from 5 to 40° 2θ of **a** $_{powd}$MOF-808, **b** $_{mono}$MOF-808(EtOH) and **c** $_{mono}$MOF-808(DMF). With samples recovered from exposure to basic (**black line**), neutral (**blue line**) and acidic (**red line**) conditions, respectively. Whereas **gray** and **green** lines indicate untreated and simulated material, respectively.

untreated powder shows sharp high intensity peaks at ∼8, 10 and 10.9° 2θ, however, the recovered $_{powd}$MOF-808 samples return noisier diffraction patterns with broader and more

convoluted peaks in the same region. As previously mentioned, this could signify extensive amorphisation.

As per monolithic UiO-66, untreated $_{mono}$MOF-808(EtOH) and $_{mono}$MOF-808(DMF) show significant peak broadening. The XRD patterns of recovered $_{mono}$MOF-808(EtOH) show a better retention of crystallinity than $_{mono}$MOF-808(DMF), especially at pH 3.

Nitrogen adsorption isotherms, in Figure 3.15, reveal complete pore collapse for $_{powd}$MOF-808 under all conditions, which registers an initial adsorption capacity of $\sim$410 $cm^3.g^{-1}$ and a S_{BET} of 1170 $m^2.g^{-1}$. On the other hand, tremendously improved stability is seen for $_{mono}$MOF-808(EtOH) which is seen to retain most of its adsorption capacity in the microporous range (up to 0.1 P/P_0), with significant loss of mesoporosity, characterised by both absence of hysteresis and sharp decrease in adsorption capacity at saturation pressure relative to the untreated sample. In this case, at pH 3, $_{mono}$MOF-808(EtOH) is seen to achieve a minutely higher adsorption capacity than at pH 7 and 11. On the other hand, the higher density $_{mono}$MOF-808(DMF) returns a non-porous phases at pH 7 and 11, at pH 3, the adsorption capacity is reduced drastically to $\sim$100 $cm^3.g^{-1}$, from $\sim$300 $cm^3.g^{-1}$ at 0.1 P/P_0. This is in line with the higher density monolith of UiO-66, which also registered more pronounced pore collapse in comparison to the lower density analogue.

Upon linker quantification (Figure 3.16), it observed that, for $_{powd}$MOF-808 only around 1.2% of total linker is found in solution at all pH conditions. This might suggest that the loss of porosity and crystallinity corresponds to the formation of an amorphous phase, in which the metal-linker connectivity is still in place but the long-range periodic lattice order is lost [187] - this corresponds to diffuse XRD patterns and, moreover, yields the non-porous materials revealed under nitrogen adsorption characterisation (Figure 3.15).

Similarly, $_{mono}$MOF-808(DMF) shows 1.6% dissolution for all 3 different initial pH conditions whereas for $_{mono}$UiO-66(EtOH) only around 1% of linker is seen in solution at pH 7 and 11 and less than 1% in pH 3. As powdered MOF-808 returned a non-porous phase which is largely non-crystalline, and moreover, shows the same amount of linker dissolution, it is concluded that this sample formed an amorphous phase. The same holds for $_{mono}$UiO-66(DMF). In contrast, $_{mono}$MOF-808(EtOH) shows a significant improvement over water stability of the MOF-808 framework, demonstrating good pore retention under all pH conditions. However, as observed for UiO-66 monoliths, the monolithic macrostructure

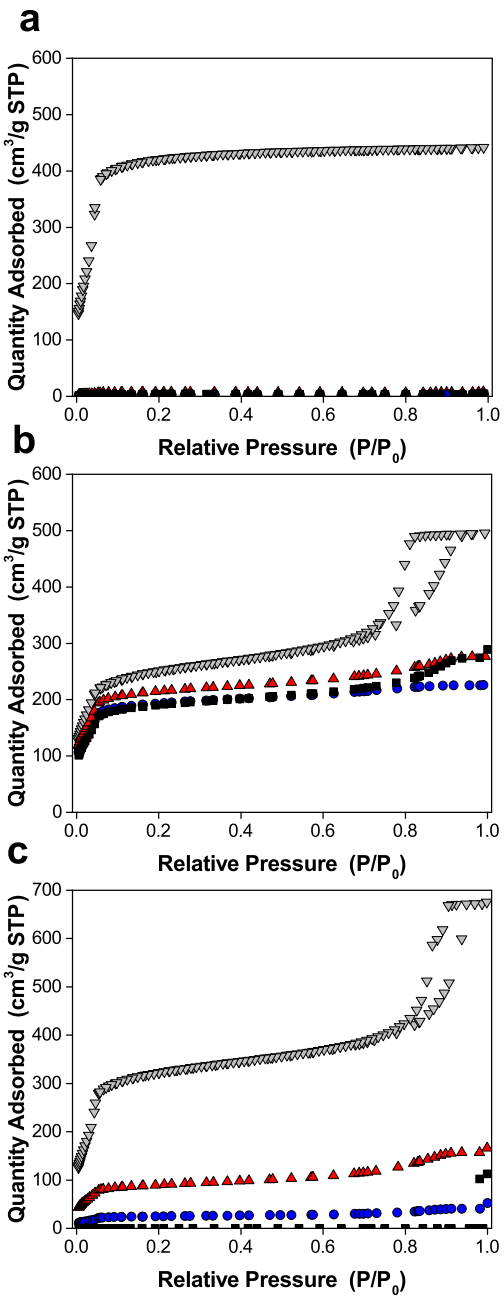

Fig. 3.15 Nitrogen adsorption isotherms at 77K of **a** $_{powd}$MOF-808, **b** $_{mono}$UiO-66(EtOH) and **c** $_{mono}$MOF-808(DMF). With samples recovered from exposure to basic (**black squares**), neutral (**blue circles**) and acidic (**red triangles**) conditions, respectively. Whereas inverted **gray** triangles indicate untreated material.

is lost for monolithic MOF-808 returning mostly powdered phases after being recovered from the testing conditions.

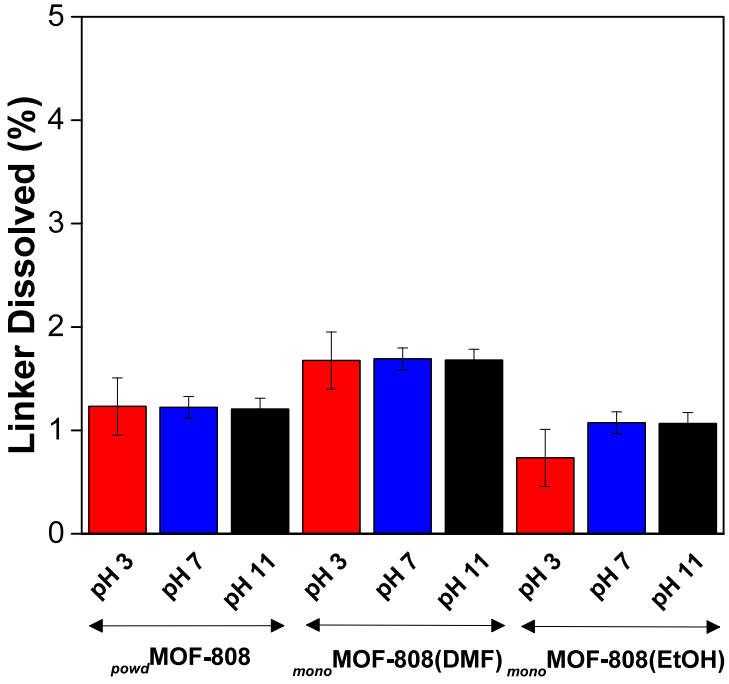

Fig. 3.16 Extent of linker dissolution of MOF-808 samples

One more factor to account for in the judgement of water stability of MOF-808 in this stability study is the capillary effect. As MOF-808 was recovered following exposure to water, and moreover, re-activated under vacuum, the solvent removal at high rate under a high temperature might have brought about structural stresses that contributed towards pore collapse. This is an especially delicate problem with high pore width MOFs and will be explored in more detail in the following subsection. Moreover, being a Zr-based MOF as UiO-66, the poorer stability of MOF-808 might be due to the fact that it holds a lower connectivity; 6 linkers per node, in contrast to the standard 12 in defect-free UiO-66, leaving a more exposed metal centre more prone to hydrolysis.

3.3.2.4 Zr-based MOFs with tagged and elongated linkers

Zirconium-based samples with elongated and functionalised dicarboxylate linkers, Zr-L1 to -L8, were also subject to the same testing conditions overnight. Figure 3.17 represents the X-ray diffraction patterns of untreated and recovered samples. As structures Zr-L1, -L2, -L3 and -L4 consist of BDC, BDC-Br, BDC-NH_2 and BDC-NO_2 linkers, respectively, the

structures are expected to be iso-structural, this is confirmed by their respective diffraction patterns which reflect Bragg peaks at ∼7.3 and 8.4° 2θ.

On the other hand, samples Zr-L5 to -L8 are formed with elongated dicarboxylate linkers, this, in turn, creates larger pore sizes and thus larger unit cells. The increase in unit cell length is thus successfuly attested by the decrease in the diffraction angle, as long as comparing structures have the same topology. A good indicator for this is the 100% peak for Zr-L5 to -L8 samples; the 100% peak in each sample is observed at 6.4, 5.7, 5.2, and 5.1° 2θ, respectively. Very good crystallinity is observed when samples Zr-L1, -L2, -L3 and -L4 are subject to acidic, neutral and basic treatment. Conversely, large cavity size samples Zr-L5, -L6, -L7 and -L8 return amorphous structures with very broad and diffuse peaks in the same region as their respective 100% peaks.

The findings for materials Zr-L1, Zr-L2 and Zr-L4 in line with Kandiah et el. [90], who synthesised and tested their water stability, however, they only provided pXRD patterns of the recovered materials. Interestingly, their study indicates that Zr-L3 expresses very poor stability under basic environment (pH 14) even during 2 hours of contact. On the other hand, our Zr-L3 MOF shows good crystallinity at pH 11 even for 24 hours of exposure. The reason for this discrepancy might be down to differences in synthetic protocols.

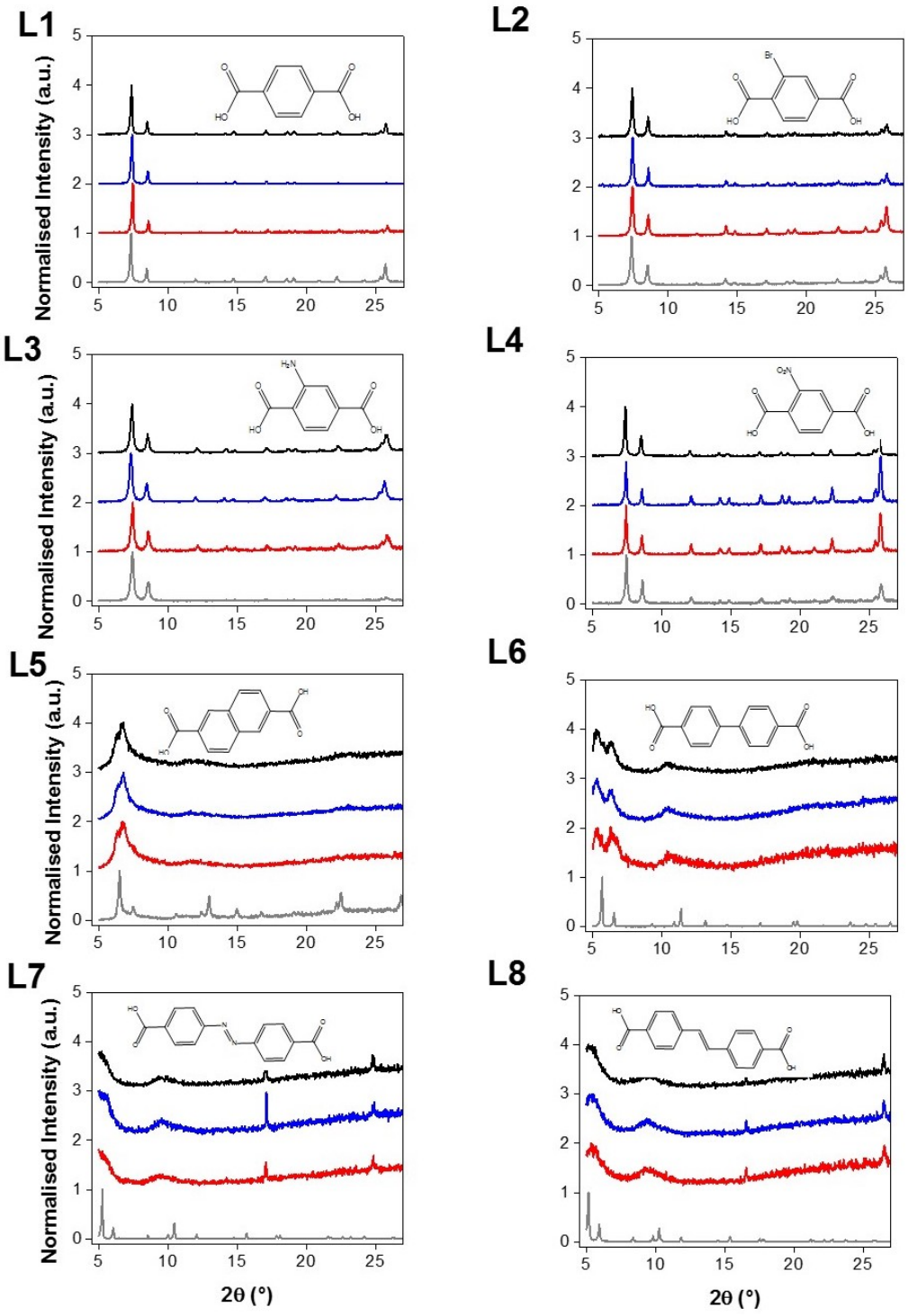

Fig. 3.17 Normalised powder X-ray diffraction patterns from 5 to 27° 2θ of Zr-L1 through to -L8. With samples recovered from exposure to basic (**black line**), neutral (**blue line**) and acidic (**red line**) conditions, respectively. Whereas **gray** lines indicate untreated material.

The nitrogen adsorption isotherms of the same samples are shown in Figure 3.18. The adsorption capacity for Zr-L1 attains ∼300 $cm^3.g^{-1}$, accompannied by a S_{BET} of 1208 $m^2.g^{-1}$, which is ∼21% lower than the previously discussed $_{powd}$UiO-66 sample (365 $cm^3.g^{-1}$ and 1446 $m^2.g^{-1}$, respectively). In this case, UiO-66 was produced following a different technique which did not make use of HCl modulator. The absence of modulators in the reaction mixture means less competition for the metal cluster binding site, hence all available binding sites will have been occupied by linkers, as expected in a defect-free, theoretically perfect structure. This would therefore decrease the pore volume and hence adsoption capacity; these effects of modulation have been previously reported in literature by numerous groups [188–191].

The addition of functional groups on the BDC linkers increases the framework mass and diminishes the pore size. This, in turn, contributes to a lower gravimetric adsorption capacity. Therefore, the functionalised UiO-66 structure with the heaviest functional group, UiO-66-Br (Zr-L2), reaches an adsorption capacity of ∼177 $cm^3.g^{-1}$, followed by UiO-66-NO_2 (Zr-L4) with 235 $cm^3.g^{-1}$ and finally, the lightest, UiO-66-NH_2 (Zr-L3) with 176 $cm^3.g^{-1}$. Whilst the abrupt increase in nitrogen uptake of UiO-66-NO_2 cannot be correlated with the increased linker mass, there is a possibility that this framework contains defects.

Consequently, an increase in linker length is correlated with larger pore volume and hence increased adsorption capacity. Structure Zr-L5, containing two fused benzene rings, experiences an increase in adsorption capacity to ∼300 $cm^3.g^{-1}$. Likewise, structure Zr-L6 shows an increased uptake up to ∼620 $cm^3.g^{-1}$. Zr-L7 and Zr-L8 differ in the inclusion of N=N and C=C bonds between the two benzene rings. The length of a N=N bond is 1.25 Å, shorter than the 1.35 Ålong C=C bond, therefore the pore volume of Zr-L7 structure is expected to be smaller. Indeed, this MOF registers a nitrogen uptake of ∼680 $cm^3.g^{-1}$, compared to 720 $cm^3.g^{-1}$ for Zr-L8 at 0.1 P/P_0.

As previously suggested by the X-ray diffraction patterns, Zr-L1 through to -L4 samples show to maintain porosity after exposure to aqueous media in pH 3, 7 and 11. In this case, Zr-L1 marginally loses adsorption capacity after exposure in pH 3, it being reduced by 13%, from ∼300 $cm^3.g^{-1}$ to 260 $cm^3.g^{-1}$. On the other hand, after exposure to pH 7 and 11, the same sample expresses a residually increased uptake (6 %) of ∼320 $cm^3.g^{-1}$, this can be explained by minor loss of linker in the aqueous environment which resulted in a minutely

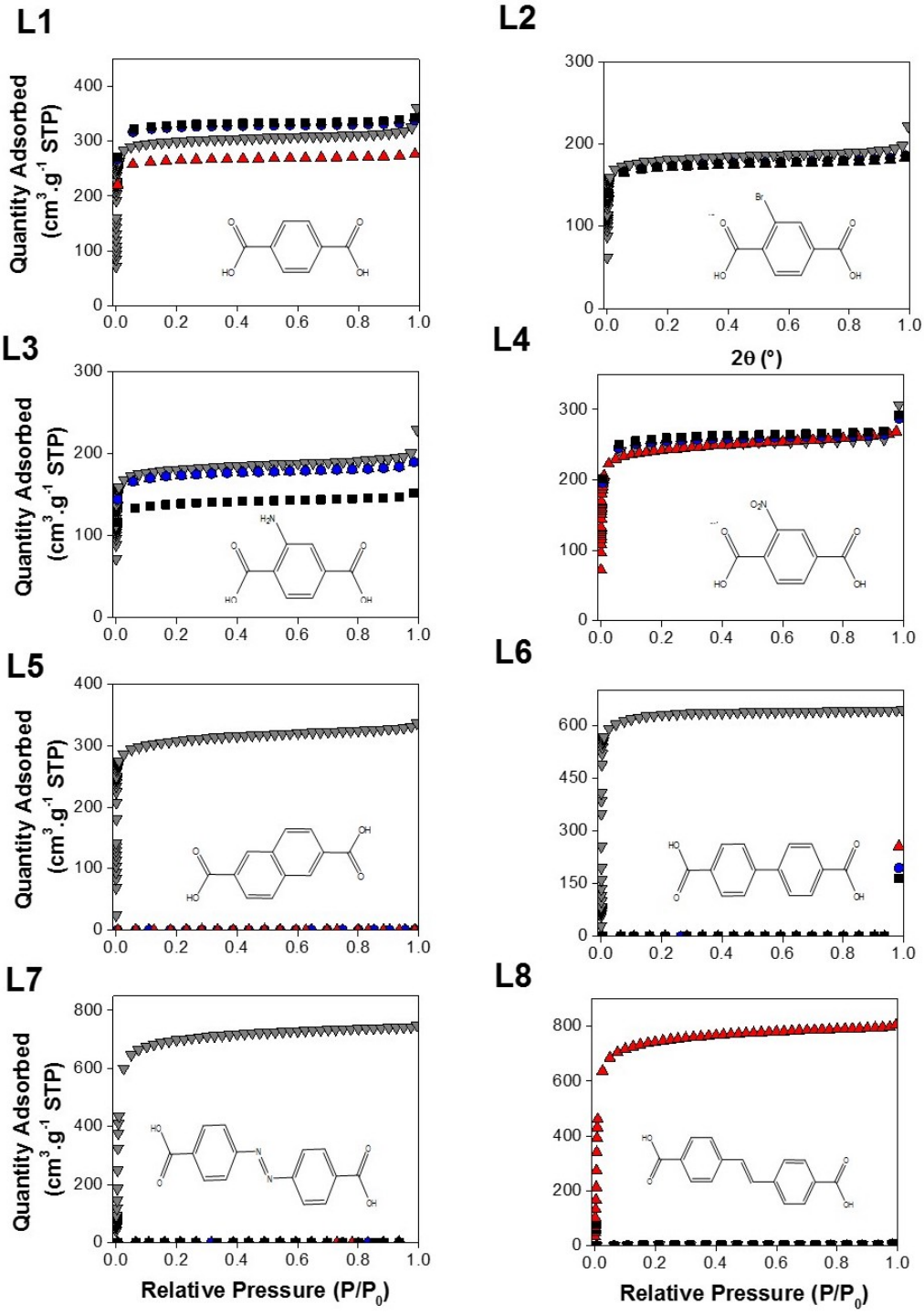

Fig. 3.18 Nitrogen adsorption isotherms at 77 K of samples Zr-L1 through to -L8 after being recovered from the respective test solutions set at initial pH of 3 (**red triangles**), 7 (**blue circles**) and 11 (**black squares**), altogether with the respective patterns of untreated samples (**gray squares**).

increased pore volume relative to the untreated sample. Samples Zr-L2 and Zr-L4 express the same adsorption capacity after being recovered form the testing environment, offering improved aqueous stability even over the unfunctionalised Zr-L1 sample. This might be due to the bulkier functional groups shielding the metal cluster and thus protecting the Zn-O bonds from attacking species but also due to altered electronic effects around the benzene ring. Sample Zr-L4 contains the -NO_2 electron withdrawing group whereas Zr-L2 contains the inductively electron withdrawing -Br substituent, both contributing to a decreased electron density around the benzene ring and thus a lower reactivity. Sample Zr-L3 shows the same nitrogen adsorption capacity in acidic and neutral media, however, under basic conditions, it elucidates a reduction of $\sim 24\%$. The same effect is observed for sample Zr-L4, wherein the adsorption capacity only minutely increases after exposure to all pH conditions. Zr-L3 loses adsorption capacity by 20%, from 175 $cm^3.g^{-1}$ to 140 $cm^3.g^{-1}$ after being exposed to pH 7, and finally, Zr-L2 shows only a very minute decrease in uptake.

On the other hand, large cavity size MOFs, Zr-L5, -L6, -L7 and -L8 confirm complete loss of porosity, as attested by their respective diffraction patterns in Figure 3.17. All elongated linker structures return non-porous frameworks under all conditions upon direct activation from water. The open geometry of the larger cavity size MOFs would be expected to offer increasingly exposed metal centres, moreover, it would facilitate easy diffusion of attacking species which could cause rupture of the metal-linker connection. Upon closer inspection of the UV spectrum of liquid samples, no linkers were detected; this means that the lack of stability of elongated linker samples is driven by the capillary effect rather than linker hydrolysis. This attests the findings on UiO-67 (Zr-L6) reported by Mondloch et al. [192], which have shown that channel collapse is indeed, driven by capillary force when the sample is activated directly from water under neutral conditions but not when the same sample is subject to solvent exchange with acetone.

Similarly, Figure 3.19 illustrates the X-ray diffractograms of recovered and untreated PCN materials. It is observed that, for PCN-56, all treated samples return amorphous materials irrespective of pH condition; characterised by very diffuse broad peaks in lieu of a well defined 100% intensity peak at 9.8° 2θ. Interestingly, in the tetramethyl material PCN-57, good crystallinity is observed for the samples recovered from neutral and acidic conditions.

The sample samples being recovered from exposure to pH 11 returns an amorphous material.

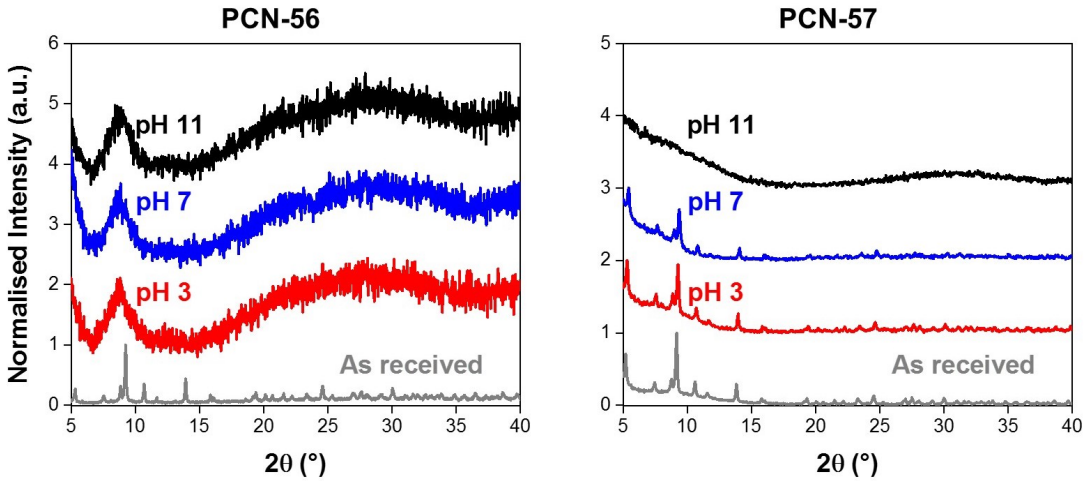

Fig. 3.19 X-ray diffraction patterns of recovered PCN materials. With samples recovered from exposure to basic (**black line**), neutral (**blue line**) and acidic (**red line**) conditions, respectively. Whereas **gray** lines indicate untreated material.

Figure 3.20 shows the nitrogen adsorption isotherms of the same PCN samples. As suggested from the respective X-ray diffractograms, recovered PCN-56 materials are accompanied by complete loss of porosity, from the original adsorption capacity of ~420 $cm^3.g^{-1}$ seen in the as synthesised material. A dramatic improvement is seen in the tetramethyl PCN-57 material, which registers an original adsorption capacity of ~580 $cm^3.g^{-1}$ followed by good retention of porosity in pH 3 with only a 14% reduction in adsorption capacity. After being recovered from exposure to pH 7, the same material registers a further reduction of 31% and finally, followed by 87% in pH 11. Therefore, stability of this Zr-cluster material, is as expected, highly dependent on pH as previously observed for UiO-66. However, linkers could not be detected in the liquid samples due to their very poor solubility in water.

The dramatic difference in stability between these materials is attributed to be solely due to incorporation of hydrophobic functional groups. Thus proving both short-term kinetic and longer-term thermodynamic stability of a large pore MOF can be improved by incorporation of hydrophobic functionalities. Furthermore, in the PCN-57 material, the capillary effects are also reduced, leaving a porous structure after being directly activated from water, especially after being treated in low pH.

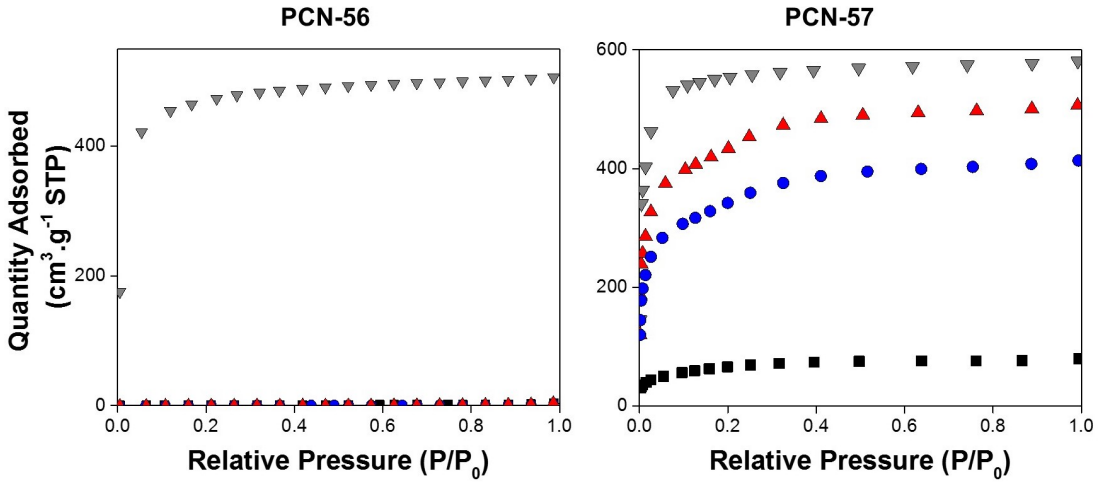

Fig. 3.20 Nitrogen adsorption isotherms at 77 K of untreated and recovered PCN materials. With samples recovered from exposure to basic (**black squares**), neutral (**blue circles**) and acidic (**red triangles**) conditions, respectively. Whereas inverted **gray** triangles indicate untreated material.

3.4 Conclusions

This chapter explored the water stability of ZIF-8, UiO-66, MOF-808 as well as 7 MOFs in the UiO-66 topology with functionalised and elongated linkers under acidic, neutral and basic conditions; the stability of given MOFs was explored in terms of their respective short-term pH response as well as their overnight stability using techniques such as linker quantification, X-ray diffraction and nitrogen adsorption. Additionally, for those MOFs for which monolithic configurations were obtained such as ZIF-8, UiO-66 and MOF-808; the role of macroscopic morphology was observed upon water stability. This chapter also briefly investigated the water stability of a series of MOFs synthesised in the UiO-66 topology with functionalised and elongated dicarboxylate linkers.

When observing the pH response of ZIF-8, comprised of the basic 2-methyl imidazole linker, it tends to equilibrate in the basic region when immersed in starting acidic and neutral conditions. For powdered ZIF-8, the rate of pH change tended to be more accelerated in comparison to both monolithic configurations. The starting pH conditions, 3 and 7, for which the largest pH change was observed also tended to elucidate structural changes, pronounced by a decrease in adsorption capacity when the same structures were recovered from the testing environment. This was especially relevant for powdered ZIF-8, which disintegrated entirely under acidic conditions and showed a 7% decrease in adsorption capacity even under

basic environment. Shaping ZIF-8 into a monolith drastically improves the water stability, especially in acidic conditions. Whereas the fully porous monolithic ZIF-8 structure yielded reduced adsorption capacity under neutral and basic conditions, the monolithic network seems to reform into a slight meso-porous structure, aided by a 4% linker dissolution. Conversely, the semi-porous monolithic ZIF-8 shows very good stability under all conditions, and this is thought to be due to a considerable shielding effect on the metal centre by the unevacuated solvent, this being attested by less than 2% linker dissolution even with a increased adsorption capacity, of maximum 33%, thought to be due to evacuation of trapped IPA solvent during contact with water.

This study reported that water stability of UiO-66 holds a strong correlation with both pH and synthetic procedure. Indeed, at the highest starting pH condition, powdered UiO-66 registered a 47% reduction in adsorption capacity and 45% linker dissolution thus concluding bad stability at this condition. Whereas shaping UiO-66 into monoliths precludes the release of linker into the testing environment, the monolithic samples registered the highest overall reduction in adsorption capacity. The UiO-66 monolithic network also disintegrated in the process to yield powdered materials upon reactivation, which means that the monolithic form of UiO-66 is unstable.

The powdered form of the larger pore Zr MOF, MOF-808, proved unstable under all pH conditions when directly activated from water; however, very minute extent of linker dissolution is observed ($\sim$1.2 %) before reactivation which means that the poor stability of this structure is not due to hydrolysis but to capillary force effects upon activation and also aided by the presence of missing linker defects as a result of the synthetic procedure. In comparison to UiO-66, which is 12-connected with largest cavity diameter of 8.7 Å, MOF-808 is 6-connected and contains pores as wide as 18.5 Å. Both the large pore size and the low degree of connectivity are big contributing factors to the framework stability. Shaping MOF-808 into monolithic macrostructures, however, has a positive effect on not only the kinetic stability, especially upon direct reactivation from water, and if the monolith is prepared using EtOH solvent.

In comparison to UiO-66, synthesised with the addition of modulators in the reaction mixture, tagged UiO-66 frameworks, especially if functionalised with bromo and nitro groups, present enhanced water stability under all testing conditions - retaining all adsorption

capacity and without loss of linkers. UiO-66-NH_2, on the other hand, still demonstrated excellent water stability under acidic and neutral conditions, with 20% loss of porosity in a high pH. UiO-type frameworks with elongated linkers showed total loss of porosity and crystallinity upon direct reactivation from water and whereas this is thought to be partly due to capillary effects upon solvent evacuation, this is also believed to be caused by very exposed metal centres. Furthermore, the addition of hydrophobic functional groups, even in large pore MOFs, can improve their thermodynamic stability.

Chapter 4

Direct Growth of ZIF-8 on Cordierite Substrate

4.1 Introduction

MOFs are vastly obtained as fine powdered materials; this is especially problematic for those synthetic methods which occur at high temperatures in high surface tension solvents. The rapid evaporation of solvents from MOF films or gels induces significant intra-particle stresses and ultimately yield discrete particles to form powders [81, 9]. Powders have to be shaped in such a way so as to be used in industrial settings, in order to avoid clogging, high pressure drops and/or other operational complications. Typical procedures involve pelletisation, using binders or compaction, involving high pressures. This is especially detrimental to MOFs since the former can block the porosity, whereas the latter can cause complete or partial pore collapse and amorphisation [81].

One way of circumventing this issue is to grow and deposit MOFs onto high aspect ratio substrates in a way which favours easy operation and scalability. For example, in liquid phase applications such as water treatment, it is both important that the contact area with the active phase is maximised however, this has to be optimally designed so as to obtain a low flow resistance and thus prevent high pressure drops [193, 194].

A widely employed substrate is the cordierite monolith, which presents an attractive geometrical configuration with a large open frontal area, viable for both gas and liquid phase

applications. Cordierite itself is a highly mechanically stable ceramic material, composed of various ratios of magnesium, aluminium and silicon oxides, enabling this material to withstand both high temperature and pressure [195, 193]. Cordierite itself is a macroporous material with very low BET surface area, however, its honeycomb-like configuration and surface properties offer the advantage of coating various materials for a wide array of uses; such as catalyst supports for heterogeneous catalysis and adsorption applications [196–198]. To date, few groups have reported deposition of MOFs on monolithic cordierite substrates, these included direct extrusion of HKUST-1 with cordierite [194] and a combination of layer-by-layer with in-situ crystallisation and seeding techniques of MOF-74(Ni), UTSA-16 (Co) and MIL-101(Cr) [199, 200] .

This chapter explores the room temperature ZIF-8 deposition on cordierite monoliths, using a bottom-up in-situ crystallisation & layer-by-layer growth technique. The experimental methodology is summarised in Figure 4.1; the aim is to study the deposition efficacy using both chemically modified and unmodified substrate, be it an initial chemical modification with the MOF metal (oxide of Zn) or linker (imidazolic silane compound). Additionally, the quality of ZIF-8 substrate is investigated using two different synthesis techniques employing either water or ethanol solvents.

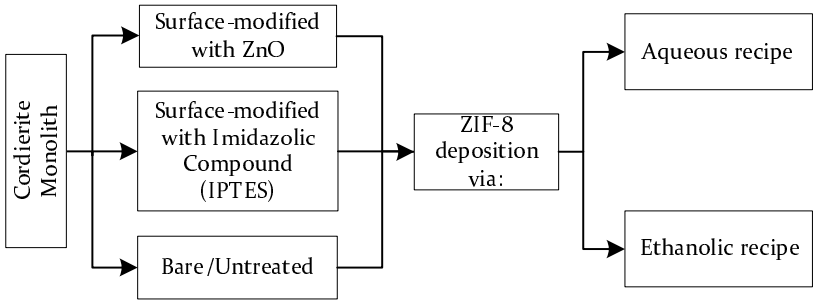

Fig. 4.1 Experimental methodology of cordierite monolith coating with ZIF-8

Table 4.1 below, illustrates the physico-chemical properties of the cordierite monolith chosen for this study.

Table 4.1 Physico-chemical properties of selected cordierite monolith substrate

Composition	MgO: SiO_2: Al_2O_3
Molar Ratio of Respective Oxides	2:5:2
Channels per square inch (cpsi)	400
Channel geometry	square
Wall thickness (μm)	178
Geometrical area ($m^2.m^{-3}$)	2710
Void fraction	0.74
S_{BET} ($m^2.g^{-1}$)	$\leq$4

4.2 Materials and Methods

4.2.1 Cordierite Functionalisation

In order to compare the deposition efficacy of ZIF-8, the cordierite substrate is subjected to ZIF-8 growth in three different configurations. In the first instance, the cordierite monolith is used as received; secondly, the substrate is modified with the oxide of the metal specific to ZIF-8 and, lastly, the surface chemistry of cordierite is modified via anchoring of an imidazolic compound - again, consistent with the organic linker specific to ZIF-8.

4.2.1.1 ZnO Growth

Zinc oxide thin films were grown homogeneously on the surface of cordierite monoliths via a sol-gel synthesis route by a dip coating technique, adapted from Ghodsi et al. [201]. For the preparation of the Zn precursor gel, 3.3 g of zinc acetate dihydrate (ZAD) (Alfa Aesar, >98%) was dissolved in 70 mL isopropyl alcohol (IPA), the mixture was stirred at room temperature at 400 rpm for 30 minutes until a white solution was obtained. This was followed by the addition of 4 mL of stabilizer monoethanolamine (MEA) (Alfa Aesar, >99 %) under constant stirring at 60 °C for 2 hours, yielding a transparent solution. Finally, the product was aged for 24 hours at room temperature. The coating technique consisted of dipping the cordierite substrate into the stirred solution for 15 minutes. Once removed, the coated structures were dried in air at 100 °C for 30 minutes. This process was repeated 10 times for each substrate and was followed by calcination in air for 24 hours at 300 °C. The

complexion of the cordierite monoliths thus changed from pale yellow to dark brown after calcination. The presence of ZnO was attested by X-ray diffraction technique.

4.2.1.2 IPTES Functionalisation

The reactivity of the cordierite surface was also modified by incorporation of an imidazolic silane compound, 3-(2-imidazolin-1-yl)propyltriethoxysilane (IPTES). This was easily enabled due to the relatively high molar ratio of exposed SiO_2 on the cordierite substrate, thus eliminating the need for prior acidic treatment. Thus an imiadazolic silane based compound was selected in order to attain a relatively simplistic method of surface modification. The method described below is a modified protocol as per Kida et al. [149]. Figure 4.2 illustrates a diagram of the set-up employed. A section of clean powder-free cordierite block was inserted into a 100 mL round-bottomed flask prior to it being connected to a reflux condensor. The flask was submerged into a stirred silicone oil (Alfa Aesar) bath, constantly kept at 80° C via a programmed temperature controller connected to the heater/stirrer. A syringe attached to a vacuum hose was then inserted into one of the ports in order to evacuate the set-up in order to ensure the atmosphere is free of moisture. The cooling fluid recirculator (ethylene glycol) was then switched on and its inlet temperature set at -5° C. Once the required temperature was achieved, the vacuum pump was switched off and 20 mL toluene (Sigma Aldrich, >99.9%) was injected, followed by 1 mL IPTES (Sigma Aldrich, >97.0 %). The set-up was allowed to operate for 24 hours. The cordierite block was then removed and washed in acetone (Alfa Aesar, >99.0%) twice and allowed to dry at 60° C for 12 hours. The presence of imidazole surface groups on cordierite was attested via FT-IR spectroscopy.

4.2.2 ZIF-8 Growth and Synthesis

ZIF-8 was grown using two different synthetic procedures. The methods applied herein were selected due to the quality of ZIF-8 crystals obtained at room temperature using two different solvents, namely, water and ethanol. For the proof-of-concept studies, cordierite samples weighing around 1 g were selected for ZIF-8 deposition.

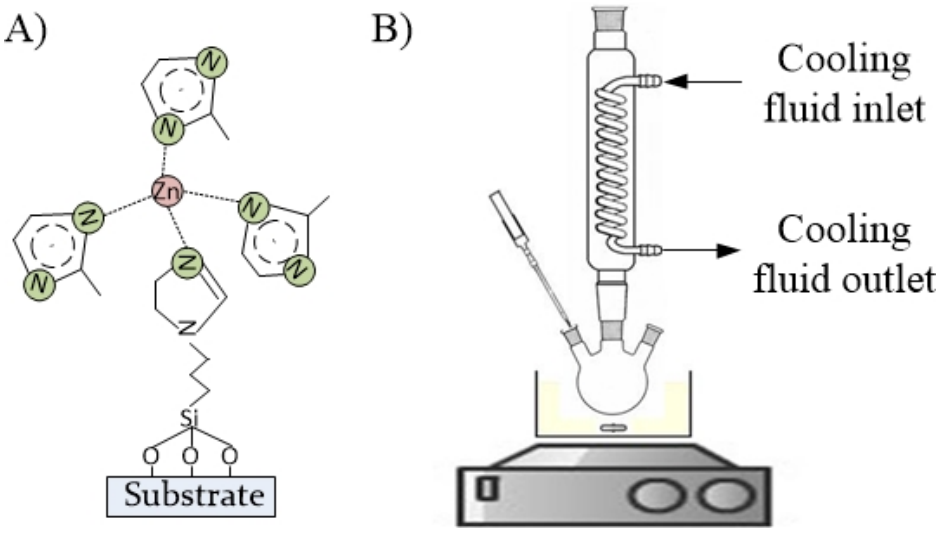

Fig. 4.2 IPTES modification of cordierite. A) Strategy for surface functionalisation of cordierite (modified from Kida et al. [149]) showing an imidazolic group bound to the substrate and connected to a Zn atom via coordination bonds, and 3 deprotonated 2-methyl imidazole linkers. B) IPTES modification set-up. The syringe has been used to evacuate the system and to insert toluene solvent and IPTES.

4.2.2.1 Synthesis in Ethanol

This synthetic protocol of ZIF-8 was considered due to it being able to yield highly mechanically and thermally stable transparent ZIF-8 'aggregates'; this methodology was developed by Tian et al. [81]. In any one batch synthesis, 0.805 g of 2-methyl imidazole (2-mIm) (Alfa Aesar, >97%) was dissolved in 20 mL ethanol (Sigma Aldrich, absolute, >99.8%). In a separate 20 mL ethanol, 0.292 g of $Zn(NO_3)_2 \cdot 6H_2O$ was dissolved. The cordierite monolith block was submerged in the 2-mIm solution, after which the Zn solution was poured. The mixture was stirred at 400 rpm, room temperature, for 10 minutes. The substrate was then removed from the mixture and dried at 100° C for 15 minutes, followed by washing under ultrasonication for 2 minutes in 20 mL fresh EtOH and drying at the same conditions.

4.2.2.2 Synthesis in Water

The second synthetic protocol employed in this work is known to yield discrete and fairly monodisperse ZIF-8 particles in an aqueous medium with a relatively high yield (90% based on the zinc source); this method was adapted from Kida et al. [149]. 12.3 g of 2-methyl imidazole was dissolved in 90 mL distilled water and, separately, 0.549 g of ZAD (Alfa

Aesar, >98.0%) was dissolved in 10 mL distilled water. The cordierite substrate is submerged in the 2-mIm solution, followed by pouring the Zn solution. The mixture was stirred at 400 rpm, room temperature, for 30 minutes, noticing the formation of a milky white solution. The substrate was then removed from the mixture and dried at 100° C for 30 minutes, followed by washing under ultrasonication for 2 minutes in 20 mL fresh EtOH and drying at the same temperature for 15 minutes.

4.2.3 Scaled-up 10 cm Cordierite Composites

The same surface modification and ZIF-8 deposition protocols were followed on a series of long cordierite monolith blocks; all reaction volumes were scaled up proportionally with the mass of cordierite. Firstly, ZIF-8 was grown in-situe on a 5 cm long cordierite block, sections of this block were then analysed for uniformity of deposition. Ultimately, the scale-up procedure was repeated for 10 cm long cordierite monoliths. The application of these samples will be later encountered in Chapter 5.

4.2.4 Characterisation

Materials were characterised for porosity, crystallinity and thermal stability using techniques previously described. Sample preparation techniques and measurement parameters are detailed in Chapter 2. Additionally, FT-IR spectroscopy was performed using a Bruker Tensor 27 FTIR instrument within the range of 500 to 4000 cm^{-1}. The resultant data was displayed as obtained.

4.3 Results and Discussion

4.3.1 Substrate Functionalisation

4.3.1.1 ZnO Growth

Figure 4.3 shows the XRD patterns of unmodified and ZnO modified cordierite monoliths, the mass gain of the treated sample illustrated below registered 4%. As illustrated by the symbols above the respective Bragg peaks, distinctive lower intensity peaks are observed in ZnO modified cordierite at around 32°, 36.5° and 36.9° 2θ, pertaining to the ZnO phase. The similarity of the newly appeared peaks was compared against existing literature data [202, 203] thus confirming successful deposition of ZnO.

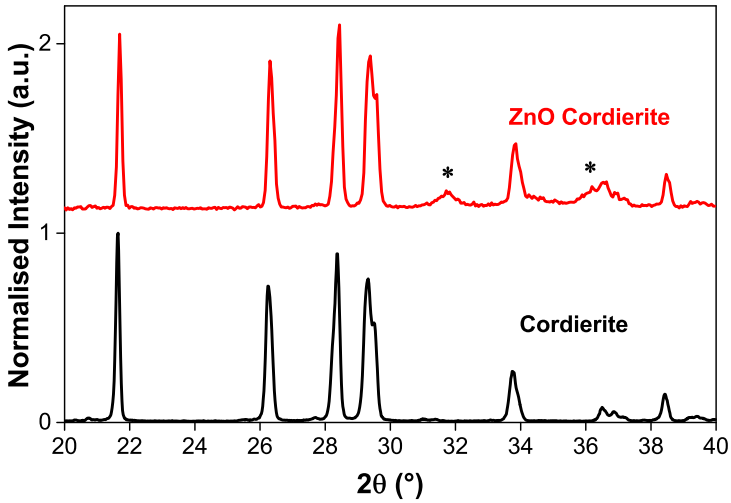

Fig. 4.3 Powder XRD patterns of cordierite (black line) and ZnO@Cordierite (red line). Asterisk symbols define ZnO specific peaks.

4.3.1.2 IPTES Modification

The presence of imidazole surface groups on cordierite monoliths was attested prior to ZIF-8 growth. Figure 4.4 illustrates the FT-IR spectra of unmodified and IPTES modified cordierite, the spectra of ZIF-8 and 2-methyl-imidazole being included for comparison purposes. As observed, cordierite gives rise to absorption bands only within the region 1250 to 500 cm^{-1}. This can be attributed to Si-O bond vibration and stretching. The band appearing at 1843 cm^{-1} for 2-methyl-imidazole only is attributed to N-H stretching, this is not observed for

ZIF-8 since 2-methyl-imidazole deprotonates in order to form a coordination bond with the metal, this confirms the findings of Tran et al. [204]. Furthermore, the deprotonation of the imidazole ring can also be observed from the clear wide peak of 2-methyl imidazole from ∼2200 to 3200 cm^{-1}, representing N-H – N hydrogen bonds [204, 205], this is not located for ZIF-8. On the other hand, ZIF-8 expresses a low intensity peak at ∼3000 cm^{-1} which can characterise N – Zn hydrogen bonds. IPTES-modified cordierite, on the other hand, registers a distinct band at 2357 cm^{-1} and lower intensity bands at 1578 and 1431 cm^{-1}, the latter two being observed also in 2-methyl-imidazole and ZIF-8, which suggest C-H stretching vibrations of the imidazole ring and thus successful anchoring of the IPTES molecule on cordierite substrate.

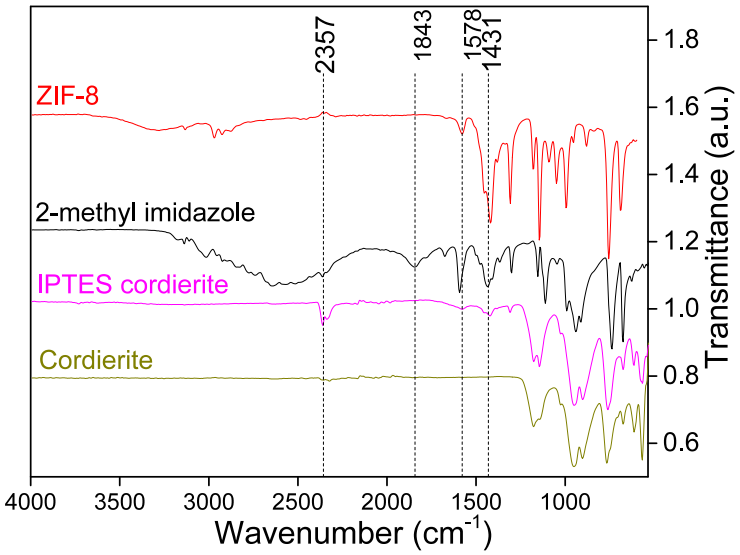

Fig. 4.4 FT-IR spectra of unmodified and IPTES modified cordierite, in addition to those of 2 methyl imidazole and ZIF-8, the dashed lines illustrating fingerprint regions

4.3.2 ZIF-8 Growth

4.3.2.1 Influence of Substrate Modification and Synthetic Technique

In-situ ZIF-8 synthesis and deposition was performed on ZnO and IPTES functionalised cordierite, as well as unmodified cordierite, over 30 growth cycles using both an aqueous and an ethanolic synthetic procedure. The accumulated data, obtained by measuring the mass of recovered samples with an analytical balance, allows to assess wether the deposition

efficacy is aided by modification of the substrate, and furthermore, any influence on ZIF-8 film quality. The synthetic procedures applied in this study were selected due to the ease of obtaining ZIF-8 at room temperature. Furthermore, the aqueous recipe is known to express a higher yield of reaction (nearing 90%) [149], whereas that in ethanol is significantly lower (around 40%) [81]. At the same time, the former produces both a large quantity of MOF with a larger particle size than the latter.

Figure 4.5 illustrates the mass growth profiles of ZIF-8 on cordierite substrate. The results are represented as a function of the number of growth cycles applied. From hereon, the IPTES and ZnO functionalised and unfunctionalised samples will be referred to as $_{IPTES}$ZIF-8@Cordierite, $_{ZnO}$ZIF-8@Cordierite and $_{U}$ZIF-8@Cordierite, respectively, samples synthesised in water and ethanol will be referred to as ZIF-8@Cordierite(Aq) and ZIF-8@Cordierite(EtOH), respectively.

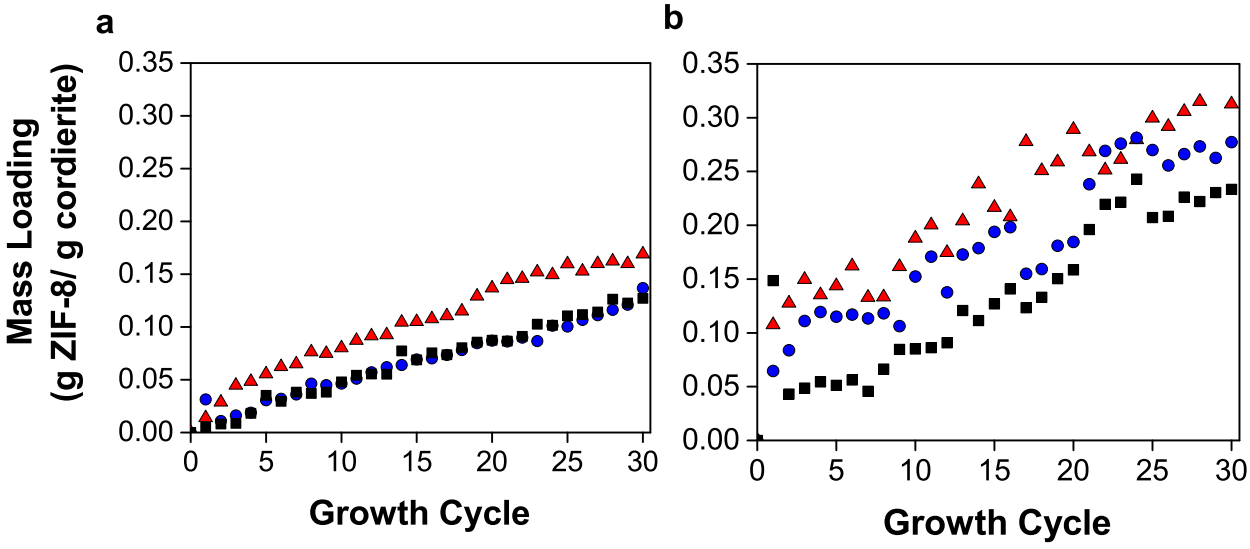

Fig. 4.5 Mass gained across 30 growth cycles following synthesis in **a** Ethanol and **b** Water on ZnO modified cordierite (red triangles), IPTES functionalised cordierite (blue circles) and unmodified cordierite (black circles)

$_{ZnO}$ZIF-8@Cordierite(Aq), $_{IPTES}$ZIF-8@Cordierite(Aq) and $_{U}$ZIF-8@Cordierite(Aq) show the most enhanced mass gain overall (Figure 4.5 **b**), most importantly, during the 1^{st} growth cycle, which shows a mass loading between 0.05 and 0.15 g ZIF-8/g cordierite, and conclude to a final mass gain ranging from ∼0.22 to ∼0.31 g ZIF-8/g cordierite after 30

growth cycles; marking significant mass gain-loss fluctuations in between 1 and 30 growth cycles.

Whilst samples $_{IPTES}$ZIF-8@Cordierite(Aq) and $_{U}$ZIF-8@Cordierite(Aq) express the highest fluctuations, a clearer trend is seen to develop from the 24^{th} growth cycle, which leads to conclude that, indeed, the overall mass gain ranges, in decreasing order, from ZnO modified to IPTES functionalised substrate and, finally unmodified cordierite.

In comparison, sample with ZIF-8 synthesised in ethanol ($_{ZnO}$ZIF-8@Cordierite(EtOH), $_{IPTES}$ZIF-8@Cordierite(EtOH) and $_{U}$ZIF-8@Cordierite(EtOH)) in Figure 4.5 **a** illustrate more uniform mass growth profiles over the same number of growth cycles. In this case, a distinguishable difference between the mass gain of sample $_{ZnO}$ZIF-8@Cordierite(EtOH) and those of $_{IPTES}$ZIF-8@Cordierite(EtOH) and $_{U}$ZIF-8@Cordierite(EtOH) is seen - the profiles of the latter two being virtually similar, reaching a final mass gain of $\sim$0.13 g ZIF-8/g cordierite, whereas that of $_{ZnO}$ZIF-8@Cordierite(EtOH) concludes to a mass gain of $\sim$0.17 g ZIF-8/g cordierite. In both synthetic techniques, ZnO substrate modification appears to play an important factor in directing ZIF-8 growth and deposition on cordierite substrate.

The mass fluctuations of the samples subjected to ZIF-8 synthesis and deposition in water are presumed to be due to the fact that ZIF-8 grown on top of the initially deposited ZIF-8 monolayer (especially on $_{ZnO}$ZIF-8@Cordierite(Aq) and $_{IPTES}$ZIF-8@Cordierite(Aq)) are discrete particles that do not adhere well to the underlying layers, especially during the washing step under ultrasonication. On the other hand, samples subjected to ZIF-8 growth in ethanol are more resilient to ultrasonic treatment, this being attested by the uniformity of the respective mass growth profiles (Figure 4.5 **a**). This suggests that ZIF-8 acts as a monomer polymerising to form a continuous film, rather than distinct particles, this aided by the ethanol solvent. Nonetheless, all samples which have been initially functionalised prior to ZIF-8 growth, irrespective of the synthetic technique applied, express elevated mass uptake. This is especially well denoted in the trend during the first 3 growth cycles, which might suggest the point at which complete surface ZIF-8 monolayer coverage occurs, from there onwards, significant mass fluctuations can be explained by additional ZIF-8 particle stacking on top of the initial monolayer.

In order to confirm whether the mass gain of the samples corresponds to presence of ZIF-8, the crystallinity of the samples was confirmed via pXRD. Figure 4.6 illustrates the XRD

patterns of ZIF-8@Cordierite(EtOH) (**a**) and ZIF-8@Cordierite(Aq) (**b**) including those of pristine cordierite and ZIF-8. All samples subjected to ZIF-8 deposition in water (Figure 4.6 **b**) express high intensity Bragg peaks specific to ZIF-8, especially at ∼7° and ∼12° 2θ. On the other hand, samples with ZIF-8 synthesised in ethanol (Figure 4.6 **a**) give rise to lower intensity ZIF-8 peaks, located at the same 2θ positions. The lower intensity of the ZIF-8 specific peaks relative to those of cordierite in ethanol synthesised samples is attributed to the lower overall mass gain, especially in samples $_{IPTES}$ZIF-8@Cordierite(EtOH) and $_{U}$ZIF-8@Cordierite(EtOH).

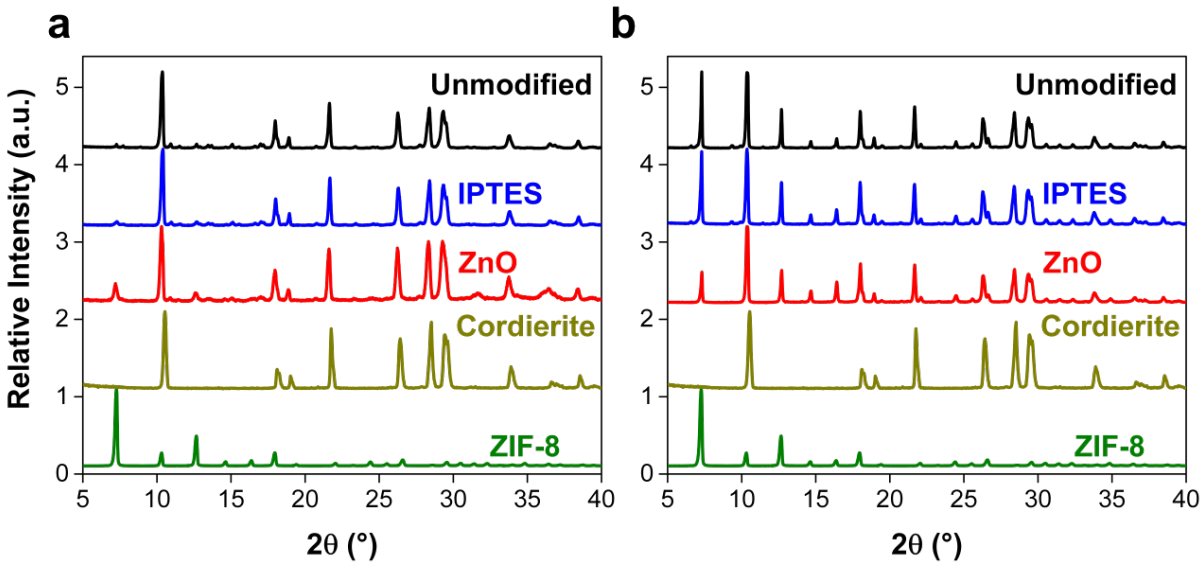

pt
Fig. 4.6 Powder X-ray Diffraction patterns from 5 to 40° 2θ of **a** ZIF-8@Cordierite(EtOH) and **b** ZIF-8@Cordierite(Aq) samples as well as pristine cordierite and ZIF-8 powders

Nitrogen adsorption measurements were performed in order to determine the porosity of deposited ZIF-8 phase on cordierite substrate. Figure 4.7 shows the N_2 adsorption isotherms of all investigated samples. The adsorption isotherm of pristine cordierite shows virtually no adsorption, suggesting the absence of microporosity, thus any increase in adsorption capacity, relative to pristine cordierite, corresponds to the presence of the microporous ZIF-8 phase.

The shape of the adsorption isotherms in all other cases is of Type I behaviour, typical of microporous phases, wherein the adsorption capacity increases sharply up to 0.1 P/P_0 and forming a plateau up to saturation pressure. As inferred from the X-ray diffraction patterns of samples synthesised in ethanol (Figure 4.6 **a**), the adsorption capacity is not significantly

increased relative to that of pristine cordierite. In this case, $_{ZnO}$ZIF-8@Cordierite(EtOH) shows the highest adsorption capacity of ∼13 $cm^3.g^{-1}$, followed by $_{IPTES}$ZIF-8@Cordierite(EtOH) and $_{U}$ZIF-8@Cordierite(EtOH) with 1.3 and 0.5 $cm^3.g^{-1}$, respectively, with negligible S_{BET} values. The mass gain registered by these samples thus, corresponds to the presence of a largely amorphous phase, previously suggested by very low intensity Bragg peaks for the ZIF-8 phase. On the other hand, samples synthesised in water (Figure 4.6 **b**) demonstrate excellent adsorption capacity relative to pristine cordierite, and, again registering a well-defined trend between functionalised samples. As expected, the adsorption capacity decreases in order of ZnO, IPTES and unmodified cordierite substrate with ∼90, ∼83 and ∼78 $cm^3.g^{-1}$, respectively. This confirms that, overall, functionalising the cordierite substrate with ZnO proves to be the most efficacious way of depositing ZIF-8 MOF on cordierite. Likewise, depositing and synthesising ZIF-8 via the aqueous synthetic recipe yields highly crystalline and porous films with good substrate adhesion.

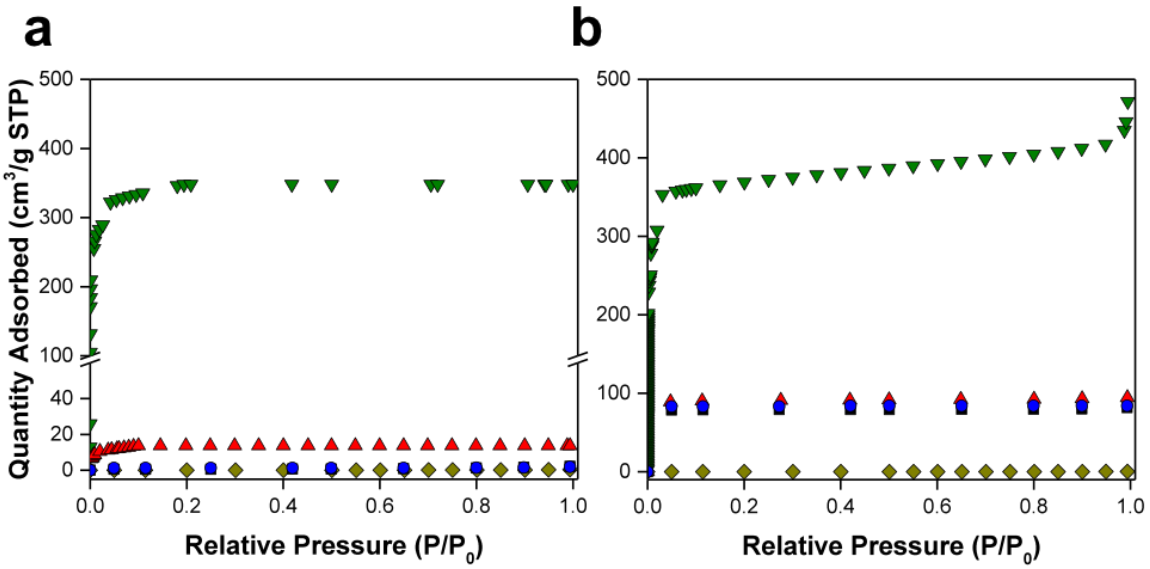

Fig. 4.7 Nitrogen adsorption isotherms at 77 K of **a** ZIF-8@Cordierite(EtOH) and **b** ZIF-8@Cordierite(Aq) samples as well as pristine cordierite and ZIF-8 powder. Grey triangles and olive rectangles represent ZIF-8 powder and pristine cordierite, respectively. Red triangles, blue and black rectangles represent ZnO, IPTES and unmodified cordierite substrate, respectively

4.3.2.2 Influence of Number of Growth Cycles

The influence of the number of growth cycles applied was also briefly studied, for this purpose a ZnO functionalised sample was used, the same layer-by-layer & in-situ crystallisation growth technique was used, employing ZIF-8 synthesis in water. Figure 4.8 shows the evolution of the adsorption capacity of sample $_{ZnO}$ZIF-8@Cordierite(Aq) after 5, 30 and 47 growth cycles, respectively. As observed in the graph on the left, the amount of gas adsorbed increases with the number of growth cycles applied, registering ∼55 and ∼130 $cm^3.g^{-1}$ after 5 and 47 growth cycles, respectively. The data for the same sample after 47 growth cycles, indicates a linear growth from 0.1 to 1 P/P_0. This is due to an instrumental calibration error during free volume correction, however, the plateau is observed to occur at ∼ 0.13 P/P_0. The semi-logarithmic plot in Figure 4.8, right, focuses on the isotherm behaviour at very low relative pressure. After 5 and 47 growth cycles a steep rise in quantity adsorbed is seen to take place at around $1e^{-4}$, followed by a bump between 0.01 and 0.1 P/P_0, the latter being observed in all three cases, consistent with the pore filling behaviour observed in ZIF-8 microporous phase, as reported in literature [81].

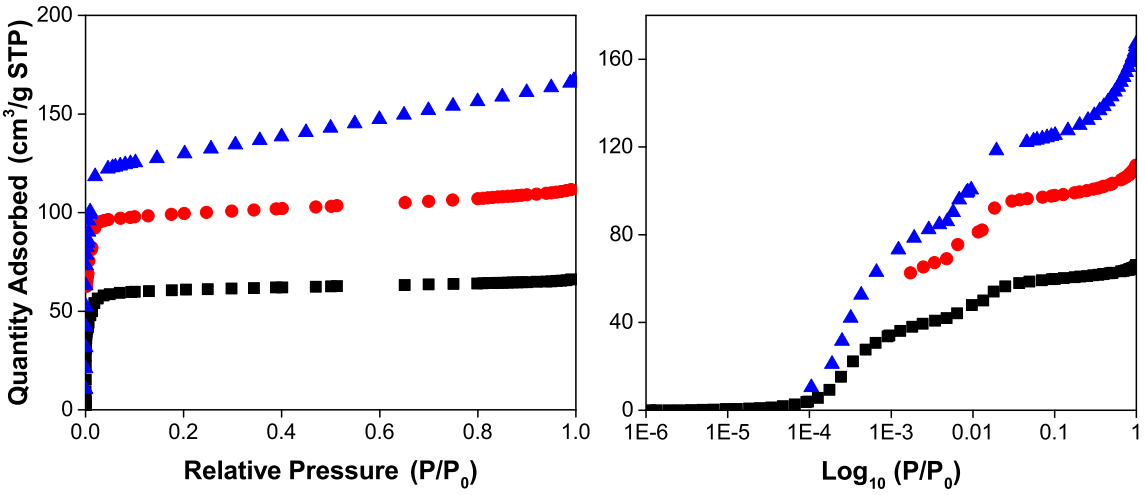

Fig. 4.8 Nitrogen adsorption isotherms at 77 K of $_{ZnO}$ZIF-8@Cordierite(Aq) after 5, 30 and 47 growth cycles represented by black squares, red circles and blue triangles, respectively.The graph on the right is a semi-log representation of the same data.

Table 4.2 shows the calculated and theoretical S_{BET} of $_{ZnO}$ZIF-8@Cordierite(Aq) after 5, 30 and 47 cycles, altogether with those of pure cordierite and ZIF-8. As inferred from the adsorption capacities of the respective samples, the BET area tends to increase with an

increasing number of growth cycles. The most drastic increase is registered with as little as 5 growth cycles, from 0.17 to 250 $m^2.g^{-1}$, at which point the ZIF-8 deposit measures ∼0.15 g ZIF-8/g cordierite. Moreover, the value of the theoretical BET area, which is obtained

Table 4.2 Calculated and theoretical S_{BET} of selected samples

Sample	Calculated S_{BET} ($m^2.g^{-1}$)	Theoretical S_{BET} ($m^2.g^{-1}$)	Mass Loading (%)
Cordierite	0.17	-	-
ZIF-8	1249	-	-
5 cycles	250	222	17.8
30 cycles	450	390	31.2
47 cycles	552	543	43.5

assuming that 100% of the mass gained by cordierite is pristine ZIF-8, is in good agreement to the calculated S_{BET}, with errors of less than 16 %. In all cases, the S_{BET} values are indeed slightly over-estimated, this can be due to minute defects in the deposited ZIF-8 structure such as missing linkers, which in turn cause an elevated pore volume and thus adsorption capacity.

Figure 4.9 represents the trend in S_{BET} area as a function of mass loading obtained from applying a differing number of growth cycles, described by Table 4.2. The S_{BET} area appears to follow a linear trend with proportional increase from 250 to 543 $m^2.g^{-1}$ at 17.8 and 43.5 % mass loading, respectively. This attests that the surface area of the composite holds a strong

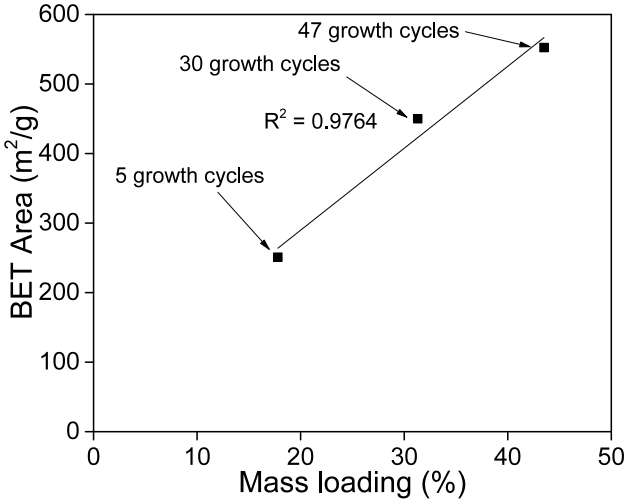

Fig. 4.9 S_{BET} of sample $_{ZnO}$ZIF-8@Cordierite(Aq) after 5, 30 and 47 growth cycles as a function of ZIF-8 mass loading after the respective number of growth cycles

correlation with the amount of MOF phase growth cycles applied.

4.3.2.3 Thermal Stability

Thermogravimetric analysis (TGA) was performed in order to determine the thermal stability of all samples, as well as to be able to match the degradation profile of deposited samples relative to that of pristine ZIF-8. Figure 4.10 **a** shows the TGA of ZIF-8@Cordierite(EtOH) samples whereas **b** shows ZIF-8@Cordierite(Aq) samples. Cordierite monolith is omitted as it does not degrade below at least 1200 °C, hence the mass losses can be solely attributed to deposited matter.

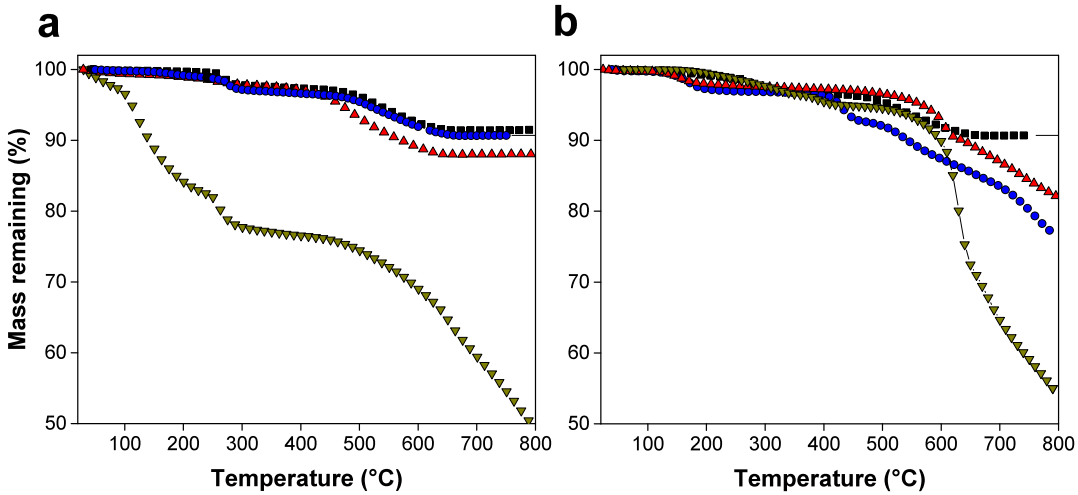

Fig. 4.10 TGA profiles from 50 to 800° C for **a** ZIF-8@Cordierite(EtOH) samples and **b** ZIF-8@Cordierite(Aq) with ZnO modified cordierite (**red triangles**), IPTES functionalised cordierite (**blue circles**), unmodified cordierite (**black squares**), pristine ZIF-8 (**olive triangles**)

Pristine ZIF-8 synthesised in ethanol (Figure 4.10 **a**) expresses accelerated mass loss between 100 and 220 °C of around 18 %, this is attributed to the evaporation of interstitial ethanol and has been previously encountered with monolithic ZIF-8 by Tian et al. [81]. The bump in the mass loss curve located at ∼250 °C is recognised as the first ZIF-8 degradation step, followed by a plateau up to ∼450 °C and, finally continuous mass loss up to 800 °C. On the other hand, pristine ZIF-8 synthesised in water (Figure 4.10 **b**) expresses very small mass loss up to ∼250 °C of less than 1 % followed by gradual decomposition up to around ∼500 °C. Similar mass loss profiles for ZIF-8 have been reported in the literature [206, 81, 131].

ZIF-8@Cordierite(EtOH) samples express similar mass loss profiles to ZIF-8 synthesised in water; this is due to the layer-by-layer growth process, which entailed washing and drying between ever growth step. This, in turn, helped to evacuate more solvent trapped within the pores and interstices of deposited ZIF-8. All ZIF-8@Cordierite(EtOH) sample profiles illustrate a shoulder at ∼250 °C, a plateau up to ∼500 °C followed by more degradation up to ∼600 °C. Sample $_{ZnO}$ZIF-8@Cordierite(EtOH) expresses the highest losses, of around 12 % - consistent with the 16 % mass gain following deposition; samples $_{IPTES}$ZIF-8@Cordierite(EtOH) and $_{U}$ZIF-8@Cordierite(EtOH) show mass losses of ∼9 %, both attaining the same mass gain during the ZIF-8 growth and deposition stage.

ZIF-8@Cordierite(Aq) samples express minor losses up to ∼200 °C followed by the ZIF-8 specific step at ∼250 °C and, finally continuous mass loss from ∼450 °C; the former is attributed to evaporation of interstitial water whereas the latter two to decomposition of ZIF-8. Sample ZIF-8@Cordierite(Aq) forms a plateau after registering mass losses of ∼ 9%; this plateau is not observed for samples $_{ZnO}$ZIF-8@Cordierite(Aq) and $_{IPTES}$ZIF-8@Cordierite(Aq) as degradation is still taking place due to their higher mass gain.

4.3.2.4 Film Morphology

The deposited ZIF-8 film morphology and thickness was observed under scanning electron microscopy (SEM). Figure 4.11 illustrates ZIF-8 crystals synthesised via the two procedures, on the left (**A**) being ZIF-8 obtained in ethanol whereas the micrograph on the right (**B**) illustrates ZIF-8 synthesised in water. ZIF-8 obtained in ethanol yields small nanometre-size ZIF-8 primary particles with sizes up to 70 nm [81]. On the other hand, ZIF-8 obtained in water yields discrete and monodisperse ZIF-8 particles of larger diameter ($\leq$1 μm) with distinctive 4 and 6 membered facets typical of the sodalite topology of ZIF-8.

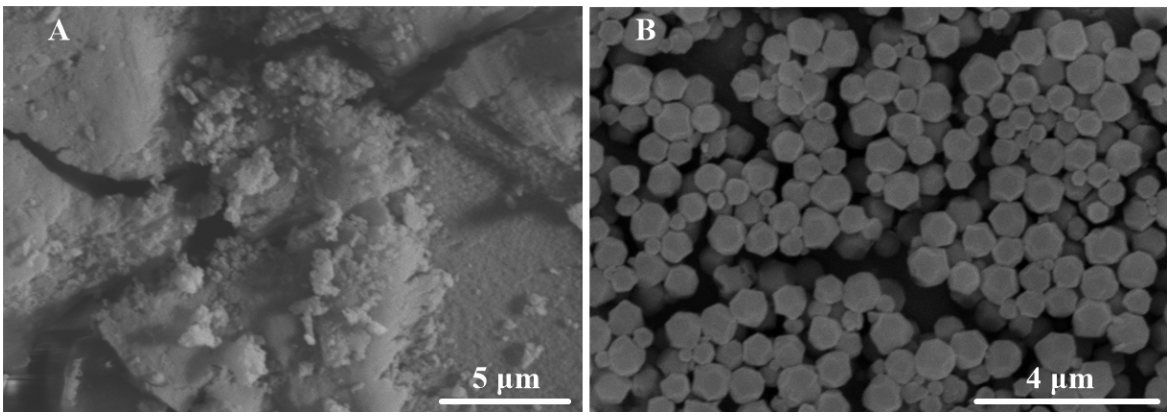

Fig. 4.11 SEM micrographs of ZIF-8 powders synthesised in **A** ethanol and **B** water

Figure 4.12 illustrates cross-sectional and lateral close-ups of the clear cordierite substrate. The substrate itself contains surface imperfections expressed by large 'sponge-like' macroporous cavities, and a morphology drastically different from that of ZIF-8, enabling an easier visual differentiation between the film and the substrate.

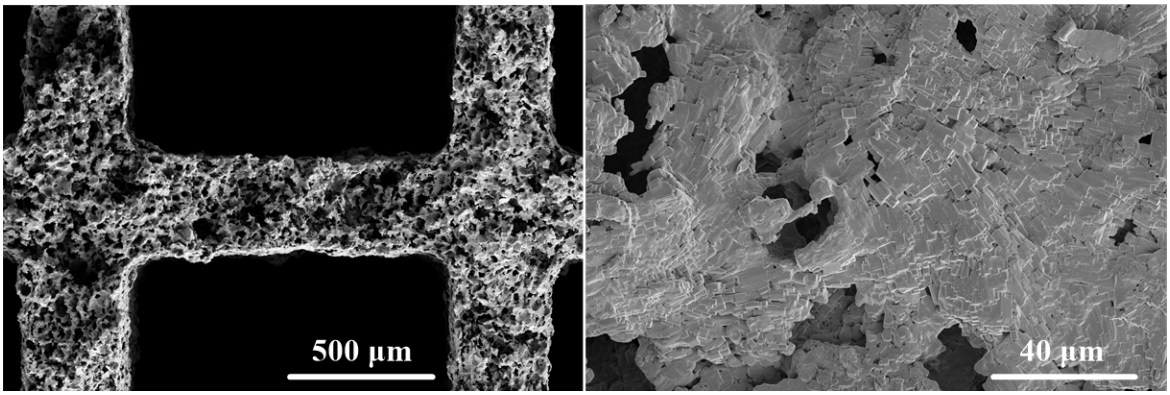

Fig. 4.12 SEM micrographs of cordierite with cross-sectional and lateral view close-up

Figure 4.13 shows the SEM close-ups of $_{ZnO}$ZIF-8@Cordierite(Aq) after 30 growth cycles. As observed, a thick and closely packed film is observed to have formed on the cordierite substrate, the morphology of this deposit is visually distinctive from that of pure cordierite. Additionally, discrete ZIF-8 particles seem to be deposited within the cavities of the substrate.

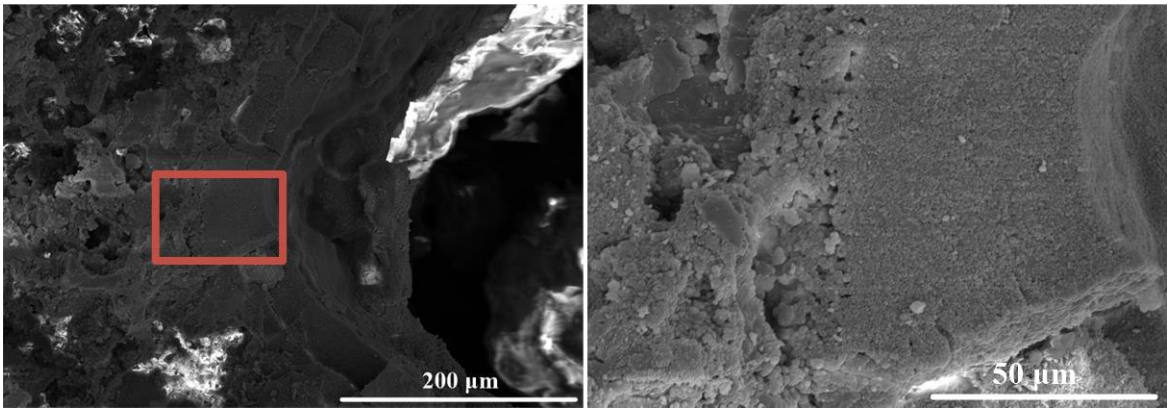

Fig. 4.13 Cross-sectional SEM micrographs of sample $_{ZnO}$ZIF-8@Cordierite(Aq) after 30 growth cycles; the red square on the left selects the zoomed-in region on the right

Figure 4.14 illustrates cross-sectional micrographs of sample $_{ZnO}$ZIF-8@Cordierite(EtOH) after 30 growth cycles. As suggested by the considerably lower mass gain of this sample in comparison to $_{ZnO}$ZIF-8@Cordierite(Aq), the deposited film is thinner and visually harder to distinguish.

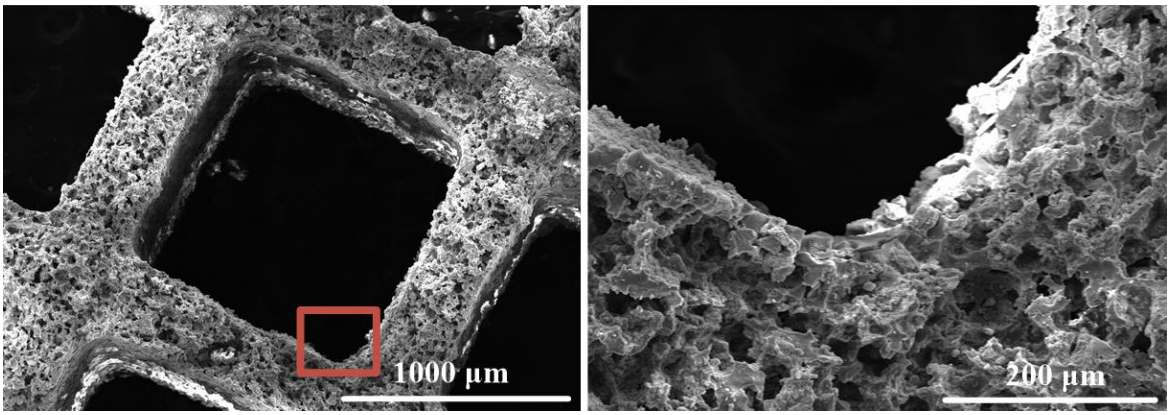

Fig. 4.14 Cross-sectional SEM micrographs of sample $_{ZnO}$ZIF-8@Cordierite(EtOH) after 30 growth cycles; the red square on the left selects the zoomed-in region on the right

Figure 4.15 shows SEM-EDX analysis of a zoomed in region on a section of a film from $_{ZnO}$ZIF-8@Cordierite(EtOH); the yellow rectangles represent scanned regions. The purpose of this is to show that the surface film is indeed comprised of Zn metal from ZIF-8 MOF.

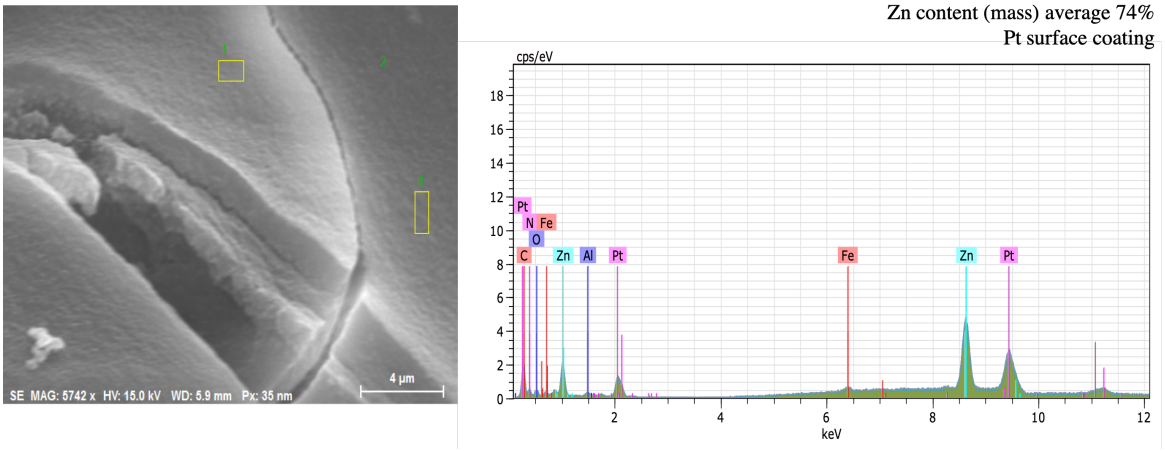

Fig. 4.15 SEM-EDX for a selected region of $_{ZnO}$ZIF-8@Cordierite(EtOH) film

Figure 4.16 illustrates selected zoomed in regions of films synthesised in ethanol and water. Figure 4.16 **A** concentrates on a film crack region that illustrates very closely packed particles of small diameter. On the other hand, Figure 4.16 **B** shows a film section consisting of closely packed, larger ZIF-8 particles, with 6 and 4 membered facets, as expected from this respective synthesis procedure.

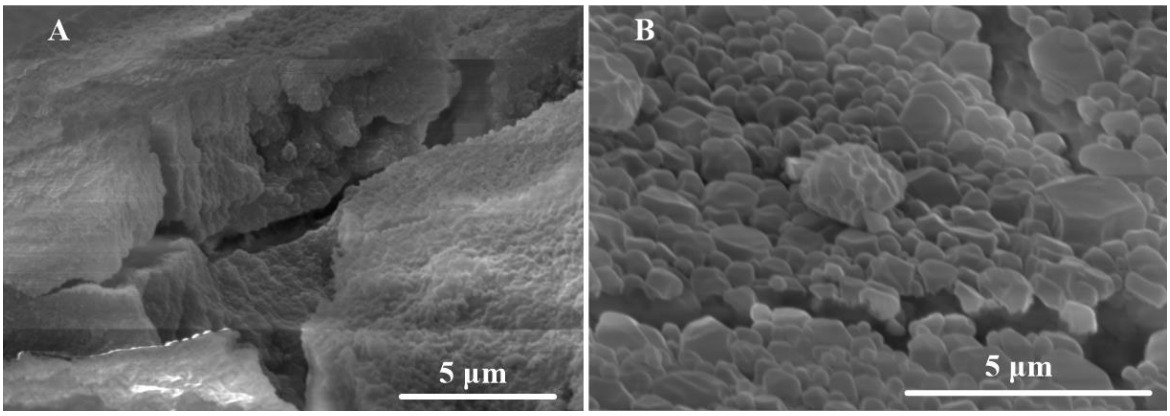

Fig. 4.16 Lateral SEM micrographs of ZIF-8 films **A** ZIF-8@Cordierite(EtOH) and **B** ZIF-8@Cordierite(Aq)

4.3.3 Scaled-up 10 cm Cordierite Composites

The same synthetic procedure was applied to larger cordierite samples of 1 cm in diameter and 10 cm in length with a total mass of $\sim$ 6.5 grams. The reaction volumes were proportionally scaled-up. Figure 4.17 illustrates the mass growth profiles of scaled-up samples across 50 deposition cycles. For those samples with synthesis and deposition in EtOH, the mass of samples uniformly increases with each deposition cycle. As expected, sample $_{ZnO}$ZIF-8@Cordierite(EtOH) consistenly registers the highest ZIF-8 deposition, attaining $\sim$0.128 g ZIF-8 per g of cordierite after 50 growth cycles. In comparison to the bench scale sample which registered 0.17 g of ZIF-8 per g cordierite after 30 deposition steps, this scaled-up attempt registers 0.08 g ZIF-8 per g of cordierite after the same number of growth cycles. Additionally, samples $_{IPTES}$ZIF-8@Cordierite(EtOH) and $_{U}$ZIF-8@Cordierite(EtOH) show similar mass growth profiles, as seen for the previous bench-scale samples. After 50 growth cycles, these both attain 0.095 g.g^{-1}, minutely lower than the previously discussed smaller mass cordierite samples ($\sim$0.12 g.g^{-1}).

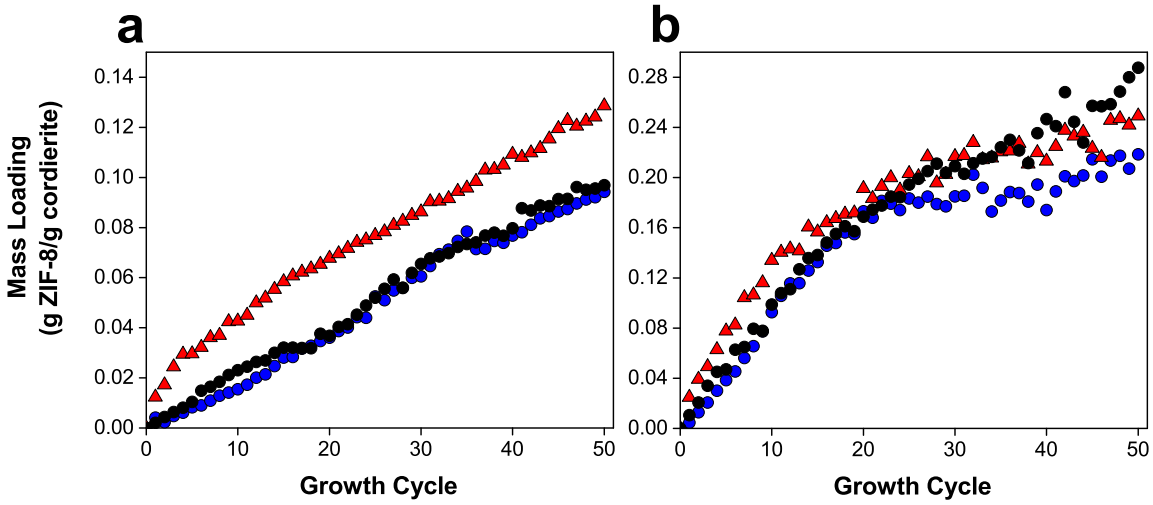

Fig. 4.17 Mass gained across 50 growth cycles for scaled-up cordierite monoliths following synthesis in **a** Ethanol and **b** Water on ZnO modified cordierite (red triangles), IPTES functionalised cordierite (blue circles) and unmodified cordierite (black circles)

For samples which followed growth and deposition of ZIF-8 in water, a distinctive pattern is seen to emerge: for all samples the mass grows steadily and consistently for up to 20 consecutive growth cycles after which it starts to level off and register only minute changes for a further 30 growth cycles. In this case, the unmodified substrate attains the

highest mass growth after 50 cycles, with 0.28 g.g^{-1}, followed by $_{ZnO}$ZIF-8@Cordierite(Aq) with 0.25 g.g^{-1} and, finally, $_{IPTES}$ZIF-8@Cordierite(Aq) with 0.22 g.g^{-1}. In this synthetic procedure, the total mass loading achieved is comparable to the previously discussed bench-scale samples. After 30 deposition cycles, the scale-up samples $_{ZnO}$ZIF-8@Cordierite(Aq), $_{IPTES}$ZIF-8@Cordierite(Aq) and $_{U}$ZIF-8@Cordierite(Aq) register 0.22, 0.18 and 0.21 g.g^{-1} , respectively, this differs from the previously discussed bench-scale samples, which register 0.31, 0.26 and 0.24 g.g^{-1}, respectively.

The smaller amount of mass deposited on scale-up cordierite samples might be due to decreasing yield of synthesis as a result of larger reaction volumes. Whereas the exact uniformity of deposition in these samples is not studied; since it would be a destructive technique; a separate, 5 cm long, smaller sample is studied in the following sections.

4.3.3.1 Uniformity of Deposition

A separate 5 cm long ZnO modified cordierite sample was subject to ZIF-8 growth and deposition using the aqueous synthesis technique. The aim of this was to study the uniformity of axial ZIF-8 growth and deposition along the thin cordierite channels upon scale up. The sample was synthesised and activated under vacuum in order to remove solvent and cut in 1 cm long sections; these sections were investigated for presence of ZIF-8. Figure 4.18 illustrates the FT-IR spectra of each 1 cm section of sample, along with those of pristine cordierite and ZIF-8. Pristine cordierite registers distinctive peaks in the region between 1200 and 500 cm^{-1}, this is attributed to the Si-O-Si bond stretching and vibrations. On the other hand, pristine ZIF-8 shows distinct peaks at $\sim$1400-1300 cm^{-1}, also observable in all sections of the sample.

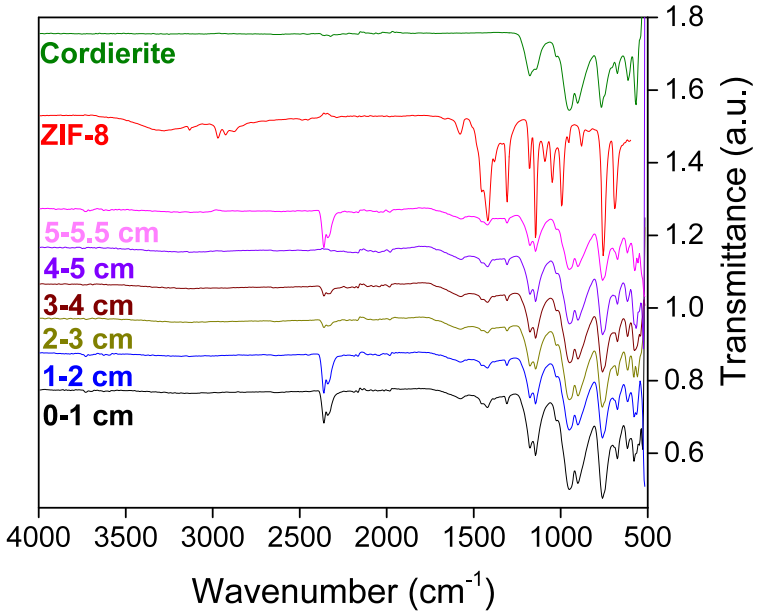

Fig. 4.18 FT-IR spectra of sections of the scaled-up 5 cm long ZIF-8@Cordierite Composite

Figure 4.19 illustrates the powder X-ray diffraction patterns of the same sample sections. As suggested by the ZIF-8 specific diffraction peaks, all sections reflect the same Bragg peaks, especially at ∼7 and 12.5 2θ, confirming the presence of the crystalline ZIF-8 phase.

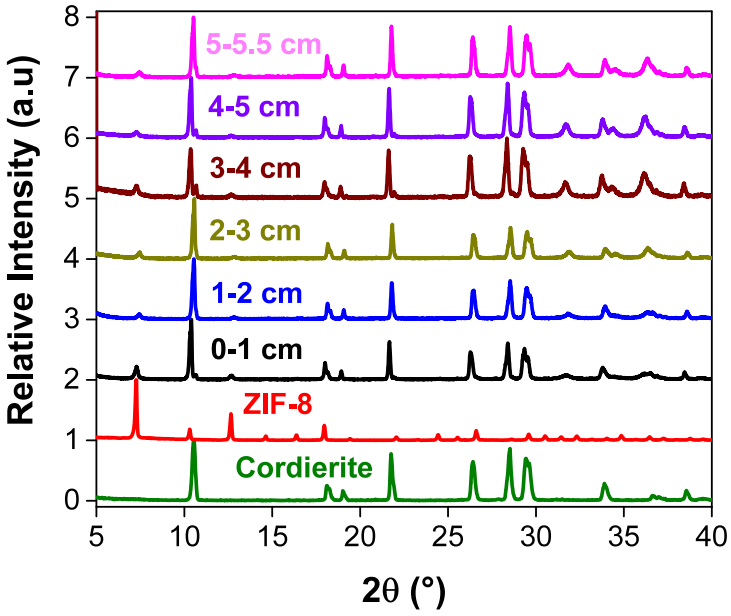

Fig. 4.19 Powder X-ray Diffraction patterns of sections of the scaled-up 5 cm long ZIF-8@Cordierite Composite

Figure 4.20 illustrates the TGA curves of the same sections, the aim of TGA here is to confirm uniform mass loss characteristics from section to section, as well as to ensure uniform total mass loss as a way of assessing uniformity of ZIF-8 deposition. As observed,

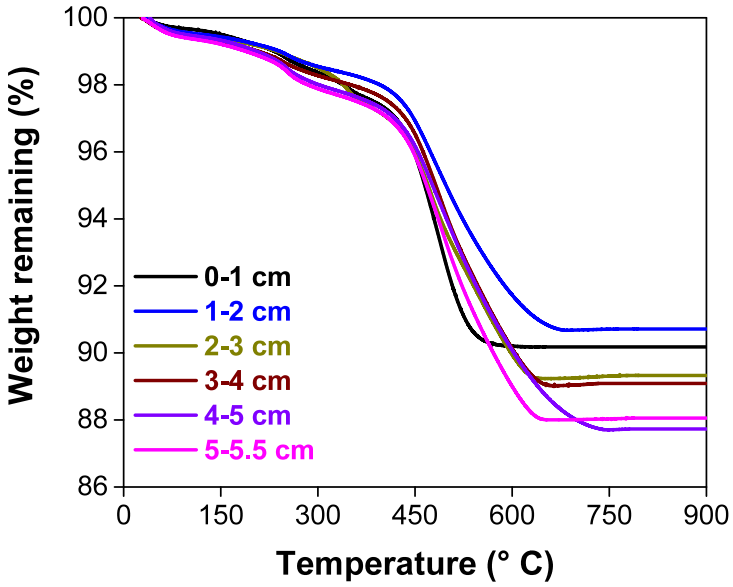

Fig. 4.20 TGA curves in Ar of sections of the scaled-up ZIF-8@Cordierite composite

all TGA curves illustrate similar behaviour to the previously discussed ZIF-8@ Cordierite films with minute loss of mass up to 450 °C, ultimately, all sample sections plateau with mass losses ranging from 9 to 13 % between one end to another end of the sample (1-2 and 4-5 cm, respectively), indicating a good degree of uniformity.

4.4 Conclusions

This chapter presents a ZIF-8 deposition technique on a high geometrical area cordierite substrate. The effect of substrate surface chemistry modification was investigated in the context of ZIF-8 deposition efficiency and film quality. The effect of incorporation of ZnO and imidazole, similar to the type of metal node and linker molecule, respectively, specific to the desired MOF was investigated in order to direct a uniform and multi-directional growth of films with good adherence to the substrate. The obtained structures were characterised with a variety of techniques tailored to attest the presence of crystalline microporous ZIF-8.

It was successfully shown that the growth of ZIF-8 film is promoted on the chemically modified substrate, specifically, the ZnO modified surface has overall yielded the most rapid mass growth and the highest adsorption capacity. The difference between imidazole-modified and unmodified substrate was virtually naught with no difference between the overall deposition eficiency, this might have been due to insufficient surface modification due to the limited number of exposed SiO_2 sites available for anchoring the silane imidazole functionality.

ZIF-8 loading limits were reached in order to ascertain the stability of the composite structure, with values of circa 45 and 22 % for ZnO modified cordierite with ZIF-8 synthesised in water and ethanol, respectively, in the initial bench-scale samples. The mass growth profiles of the ethanol synthesised samples expressed good film adherence in between each growth step when they were subject to ultrasonic treatment, however, the resultant films showed very poor crystallinity and porosity due to the remarkably low quantity deposited. These same samples, showed the presence of a very thick and closely packed film deposited and concentrated on the outer cordierite channels. This was opposed to ZIF-8 synthesised and deposited in water, in which case, the discrete large ZIF-8 particles firstly fill the void spaces of the substrate prior to forming a thick outer layer. On the other hand, ZIF-8 deposited via synthesis in water proves an efficacious coating route, not as much for conferring a higher mass gain but for successfully proving that ZIF-8 can form highly packed films with good adherence to the substrate and good stability.

Nonetheless, the surface areas of the composite structures is, as expected, highly correlated with the number of growth cycles applied, this is especially the case for those samples expressing good crystallinity, with ZIF-8 synthesised in water. For the highest number of cycles applied, the maximum S_{BET} reached $\sim$550 $m^2.g^{-1}$ with excellent thermal stability up to to $\sim$450 °C.

When separately studying a 5 cm long ZnO modified composite sample, good overall uniformity of deposition was observed. Therefore, the same ZIF-8 growth rationale was scaled-up in order to obtain large 10 cm long monoliths, in these samples, the point of complete surface coverage is better observed, characterised by a linear growth region followed by a high extent of scatter indicated poor film adherence at a high number of growth cycles.

Chapter 5

Monolithic MOFs as Candidates for Adsorption of Bisphenol B Micropollutant

5.1 Introduction and Motivation

Water pollution is a crucial issue facing modern society. A rapidly increasing population in need of a plethora of economic goods comes hand in hand with intensive water use in both industrial and public sectors [207]. Among the different chemicals that may enter into water courses, endocrine-disruptor chemicals (EDCs) are an emerging class of pollutants that are increasingly being detected in fresh drinking water sources [208]. EDCs are thought to affect living organisms through hormone-mimicking pathways and, therefore, to interfere with homeostatic, reproductive and other developmental processes in the body [208]. Some of the most worrying EDCs are bisphenol-type compounds, such as highly toxic Bisphenol A (BPA). BPA has been extensively used as a starting material for obtaining various plastics and is thus presently subject to major social attention due to its ubiquity in water supplies, personal care products, food and water storage containers as well as in vast arrays of products that even entail medical usage [17, 209, 210]. Recent efforts to curtail the use of BPA resulted in the development and industrial deployment of new BPA analogues [209], amongst which

is Bisphenol B (BPB), though this is now known to exhibit similar metabolic activities to BPA in living organisms [209].

The water treatment and purification research community has directed considerable efforts to tackling the emerging concern over the presence of EDCs in potable water supplies. So far, extensive literature reports the successful removal of BPA from water via photocatalysis, filtration [211], ozonation [212] and adsorption [213–215]. However, limited research has been addressed towards the removal of BPB and other BPA substitutes. Whilst the vast majority of water treatment research targeting pollutants, such as catalytic degradation, proves to be effective, it can also create side products that are still toxic [17]. In contrast, adsorption on a solid can offer a safe, side-product-free alternative for removing chemical species with undesirable physico-chemical properties [17–23], on the other hand, one notable issues with adsorptive water treatment is the waste generated when considering limited material recyclability. Metal-organic frameworks (MOFs) have the potential for water treatment through the adsorption and removal of pollutants [17, 18].

MOFs are gaining substantial popularity in a number of research fields, and only recently their prospects as candidates in liquid phase applications have been realised [19, 20]. Currently, MOF adsorbents are thought to perform better than zeolites, activated carbons and other traditional liquid phase adsorbents. Successful tests have already proved the efficacy of MOFs as adsorbents for the liquid phase removal of industrial dyes [28] and pharmaceuticals [20], amongst many other chemicals [32, 210, 216, 217].

Although MOFs can show outstanding applied benefits, most of their syntheses are based on the production of powders. This poses an impediment towards their industrial applicability through powder compaction and clogging, leading to higher operating and maintenance costs. On the other hand, shaping techniques such as pelletisation, compaction or the use of binders prove detrimental to MOFs, causing complete or partial structural collapse and/or amorphisation [81, 218].

In recent years, we have developed a new sol-gel synthetic procedure for the synthesis of monolithic MOFs that avoids using binders or high pressures [9, 81]. This synthetic methodology primarily entails the use of a solvent with a low surface tension, followed by vigorous washing and careful drying of the product. These parameters are especially crucial towards the formation of a monolith because, as the solvent is removed from the wet gel

during the drying phase, the stresses brought about by solvent evaporation influence the intergrowth of the primary particles. In the case of powder synthesis, where the solvent is typically water and drying temperature is around 80-100°C, the fast removal of solvent from the interstices leaves discrete agglomerated particles. On the other hand, if a solvent with a low surface tension is used, such as a low molecular weight alcohol (e.g. ethanol), in conjunction with drying at room temperature and ambient pressure, the wet gel structure is maintained by means of the primary particles acting as binders within the evolving structure (Figure 5.1). The result is a densified, crystalline solid MOF with a glassy-like complexion and exhibiting elevated mechanical resilience [9].

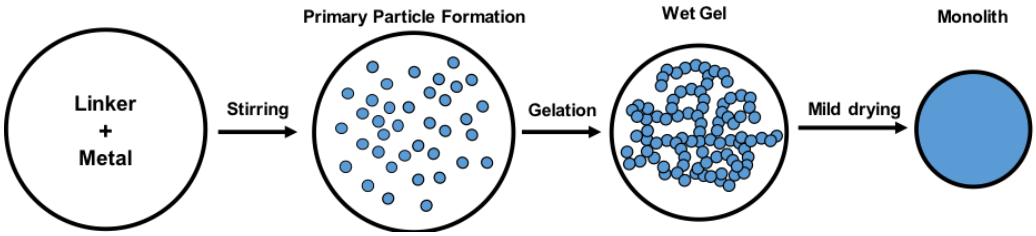

Fig. 5.1 Schematic representation of the synthesis process for a high density MOF monolith, describing the generation of the primary particles in the solution that will create a gel

This study focuses on the application of monolithic ZIF-8 and UiO-66 for the adsorption and capture of BPB from water. Special attention is given to the role of MOF morphology upon liquid phase adsorption and, in particular, the stability of the MOF during prolonged exposure to both the pollutant and the aqueous environment. The influence of the degree of inner porosity is briefly explored via the introduction of both fully and semi-activated ZIF-8 monoliths. In a separate sub-study, the influence of monolith density towards capture and adsorption of BPB is studied by introducing low and high density UiO-66 monoliths. Additionally, monolithic ZIF-8 adsorbent is compared with its powdered analogue in batch adsorption experiments and, ultimately, its performance is analysed in more realistic – from the application point of view – flow-mode adsorption.

5.1.1 Collaborative Work

Synthesis and characterisation of adsorbents, design of experiments and adsorption experiments were performed by myself. Development of $_{mono}$UiO-66 as well as ICP analysis were done by Bethany Connoly. Parts of the current chapter have contributed to the following publications:

D. Vulpe, J.P. Mehta, T. Tian, A.E.H. Wheatley, D. Fairen-Jimenez. *Sol-gel monolithic ZIF-8 for water purification*. **Under review**.

B. M. Connolly, M. Aragones-Anglada, J. Gandara-Loe, N. A. Danad, D. C. Lamb, J. P. Mehta, **D. Vulpe**, S. Wuttke, J. Silvestre-Albero, P. Z. Moghadam, A. E. H. Wheatley and D. Fairen-Jimenez. *Tuning porosity in macroscopic monolithic metal-organic frameworks for exceptional natural gas storage*. **Under review**.

5.2 Materials and Methods

Bisphenol B (analytical grade) was purchased from TCI chemicals. Water (HPLC grade) and acetonitrile (far UV/ gradient grade, >99.9%) were purchased from Alfa Aesar and used without further teatment. Structure of BPB is shown in Figure 5.2.

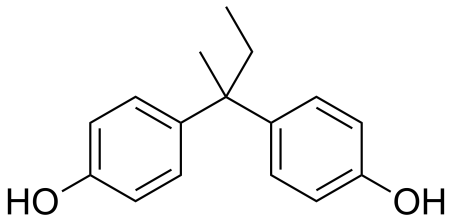

Fig. 5.2 Structure of Bisphenol B

5.2.1 MOF Synthesis

ZIF-8 and UiO-66 powders and monoliths were synthesised according to the methods described in Chapter 3. Prior to use and characterisation, all MOFs were activated in a vacuum oven at 120° C for 24 hours.

5.2.2 Batch Mode Adsorption

Bisphenol B was firstly dissolved in acetonitrile to make up a 1000 ppm solution. This was further diluted in distilled water in order to prepare required concentrations. For the prolonged equilibrium adsorption experiments the following methodology was followed: a given mass of adsorbent was placed into a falcon tube followed by a stated volume of BPB solution for every single starting concentration tested (50-500 ppm). The tubes were

placed on a roller-mixer and liquid samples were collected every 24 hours up to 144 hours of contact time. For the short kinetic adsorption experiments, a precise mass of adsorbent was placed into a falcon tube followed by a given volume of BPB solution of 200 ppm starting concentration. The tubes were placed on a roller mixer and liquid samples were collected every 3 minutes up to 10 minutes, every 10 minutes up to 1 hour and every hour up to a total of 3 hours of contact time. All adsorption experiments were triplicated. In all cases, the amount of BPB in the liquid aliquots was quantified with an Agilent Infinity 1260 II HPLC coupled with a diode-array UV detector set at 280 nm and an Agilent EC-C18 column (2.7 μm pore size, 4.6 x 100 mm). The analytical method was run in isocratic mode wherein the mobile phase, acetonitrile/water (4:1, v/v), was flowing at 1.0 mL.min^{-1}, samples were injected in volumes of 20 μl.

5.2.3 Flow Mode Adsorption

Flow mode adsorption was conducted with the use of Akta Explorer FPLC coupled with a UV detector set at 280 nm. Before use, the MOF sample was dispersed in 5 mL deionised water in order to create a slurry, which was then ultra-sonicated to remove air-bubbles. This was then hand-packed in an empty glass column (5 x 1 cm), making sure that no air bubbles are trapped in the column. The column was coupled to the system and deionized water was flown at a rate of 1 mL.min^{-1} for a total of 5 column volumes for equilibration. The BPB solution was then introduced in the system via a pump set at 0.25 mL.min^{-1} which was allowed to flow until saturation of noticed (C/C_0 =1). The amount of BPB adsorbed onto the column was then evaluated by measuring the difference between the area of the MOF column breakthrough curve and that of an empty column run at the same conditions.

5.2.4 Characterisation

Nitrogen adsorption isotherms (N_2 >99.999% purity, BOC) were collected at 77 K with a Micromeritics 3Flex equipment. Furthermore, the samples were degassed in-situ at 120°C for 10 hours. Void space correction was applied via free volume measurements with He (>99.999% purity, BOC) gas. BET area was evaluated using the Rouquerol criteria [219]. Powder X-ray diffraction patterns were collected with a Bruker D8 Advance diffractometer

with monochromatic Cu Kα radiation (1.54 A) at 40 kV and 40 mA, patterns were recorded in steps of 0.01° at a scanning speed of 0.1°s^{-1}, simulated X-ray diffraction patterns were obtained using Mercury 3.9 software.

5.3 Results and Discussion

5.3.1 Material Characterisation

5.3.1.1 ZIF-8

Powdered ZIF-8 ($_{powd}$ZIF-8) was first produced via an aqueous synthesis procedure, followed by drying overnight at 80°C. Using recent advances in the sol-gel synthesis, two monolithic ZIF-8 MOFs were produced using isopropanol and ethanol solvents, respectively. The sol-gel process follows the same principles described for the synthesis of organic/inorganic aerogels, where nano-sized primary particles are first created, following which agglomeration and gelation process the gel is dried to conform the monolith [9]. The use of ethanol solvent allows for complete activation of the monolith under vacuum leaving a fully porous ZIF-8 structure; herein this fully porous monolithic material is referred to as $_{mono}$ZIF-8(FP). Additionally, and as described below, it was found that when substituting ethanol solvent with isopropanol, the same monolithic configuration is retained. However, the porosity of the final product is significantly reduced, leaving a partially porous MOF, this samples will be reffered to as $_{mono}$ZIF-8(SP). This is attributed to incomplete activation of the MOF due to insufficient removal of isopropanol from the porosity, which is thought to be due to the larger kinetic diameter of 4.7 Å of isopropanol [220].

Before use, the crystalline structure of all samples was firstly confirmed via powder X-ray diffraction. Figure 5.3 shows the diffraction patterns of the ZIF-8 samples prepared, compared with the predicted pattern. All samples retain the crystalline structure specific of ZIF-8, although the pattern for $_{mono}$ZIF-8(SP) appears noisier, probably due to the presence of isopropanol in the porosity.

Figure 5.4 shows the N_2 adsorption isotherms obtained at 77 K. While $_{powd}$ZIF-8 and $_{mono}$ZIF-8(FP) show comparable porosity (S_{BET} = 1551 and 1243 $m^2.g^{-1}$ and V_p = 0.598 and 0.538 $cm^3.g^{-1}$, respectively), the adsorption capacity of $_{mono}$ZIF-8(SP) is 43 % lower (S_{BET} = 713 $m^2.g^{-1}$, V_p = 0.256 $cm^3.g^{-1}$) than that of $_{mono}$ZIF-8(FP). This therefore confirms only partially successful activation of the porosity when using isopropanol as the solvent.

Figure 5.5, right, shows the SEM images of the three adsorbents; the surface of both $_{mono}$ZIF-8(FP) and $_{mono}$ZIF-8(SP) is flat and glassy-like as expected for monolithic structures

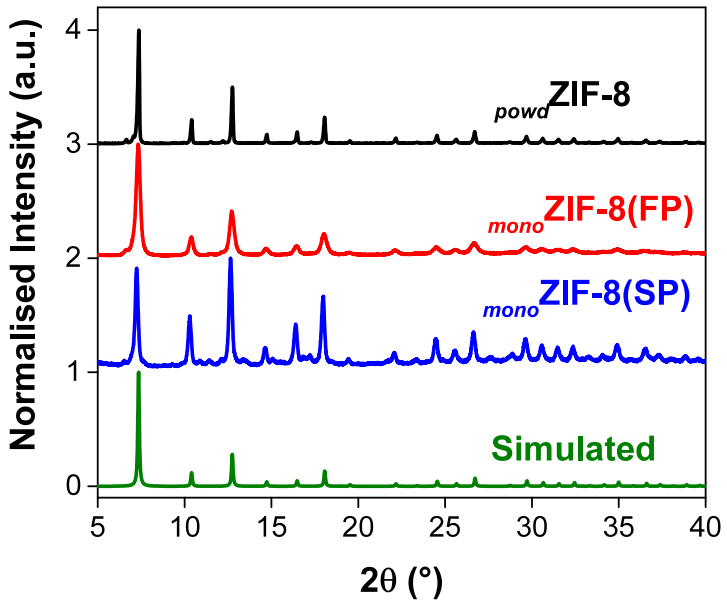

Fig. 5.3 X-ray diffraction patterns from 5 to 40° 2θ of $_{powd}$ZIF-8, black line, $_{mono}$ZIF-8(FP), red line, and $_{mono}$ZIF-8(SP), blue line, as well as the simulated pattern of ZIF-8, green line

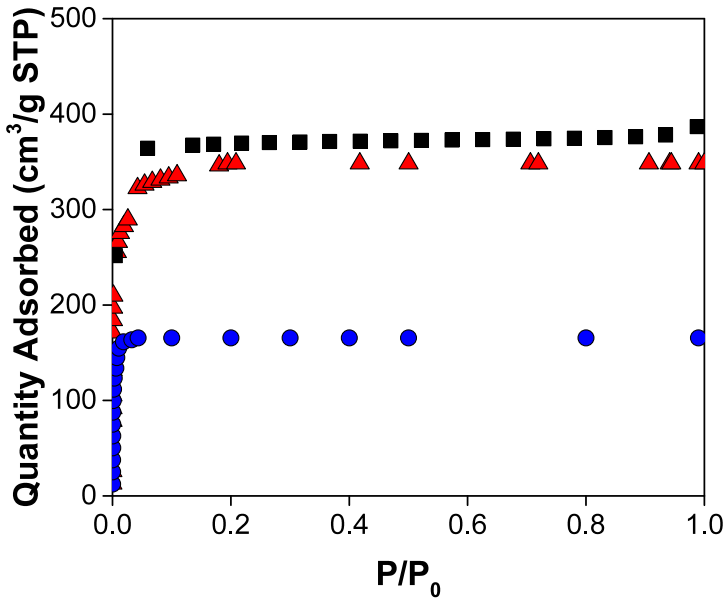

Fig. 5.4 Nitrogen adsorption isotherms at 77 K of $_{powd}$ZIF-8, black squares, $_{mono}$ZIF-8(FP), red triangles, and $_{mono}$ZIF-8(SP), blue circles

[217]. $_{mono}$ZIF-8(FP) appears translucent whereas $_{mono}$ZIF-8(SP) is mostly opaque and, finally, $_{powd}$ZIF-8 consists of approximately 360 nm (± 70 nm) particles. In a study focusing on development of HKUST-1 monoliths, Tian et al. [9] reported that particle size also plays a

major influence, along with drying temperature and choice of solvent, in the formation of the monolithic materials. Hence, ZIF-8 monoliths are expected to attain primary particle sizes less than 70 nm [9], as demonstrated by Tian et al. in a separate report [81].

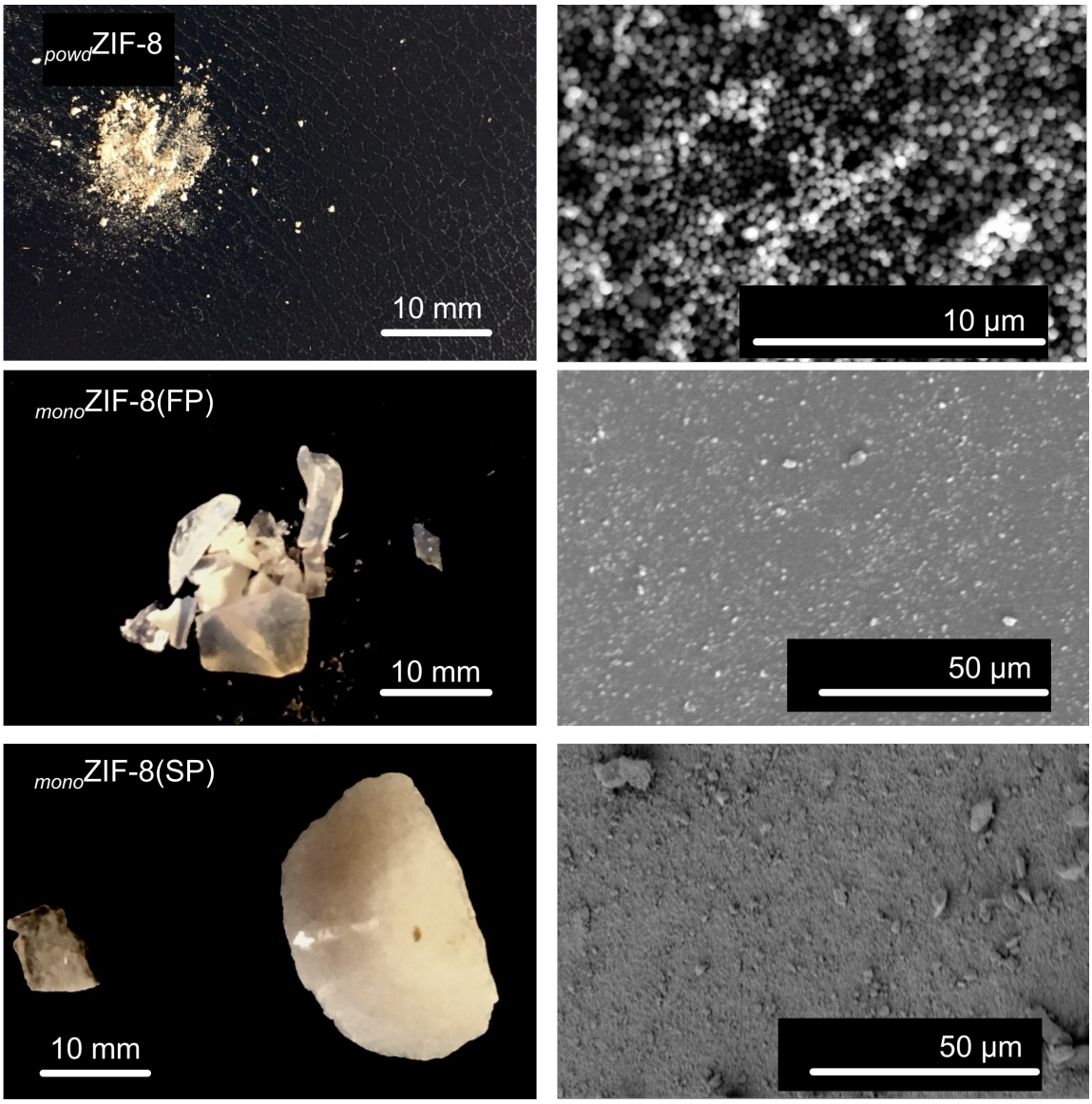

Fig. 5.5 Optical pictures (left) and SEM (right) micrographs of ZIF-8 samples

5.3.1.2 UiO-66

Similarly, the UiO-66 phase is first ascertained via X-ray diffraction, Figure 5.6 illustrates the powder X-ray diffraction patterns of all UiO-66 samples. In all cases, the UiO-66

specific peaks at 7.4, 8.5° 2θ are present, however, significant peak broadening is observed for samples $_{mono}$UiO-66(EtOH) and $_{mono}$UiO-66(DMF). This is known as Scherrer line broadening and is inversely correlated to nano-crystallite size, which is reduced in monolithic samples.

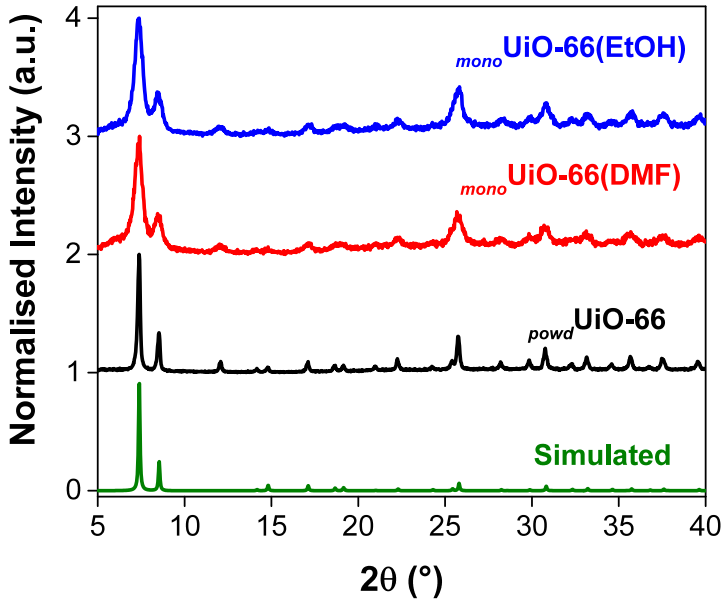

Fig. 5.6 X-ray diffraction patterns from 5 to 40° 2θ of $_{powd}$UiO-66, black line, $_{mono}$UiO-66(DMF), red line, and $_{mono}$UiO-66(EtOH), blue line, as well as the simulated pattern of UiO-66, green line

The porosity was, again, confirmed with nitrogen adsorption measurements at 77 K, Figure 5.7 illustrates the adsorption isotherms of all samples. $_{powd}$UiO-66 expresses an isotherm of Type I, as expected for a microporous phase, with a plateau forming from 0.1 P/P_0 reaching an adsorption capacity of $\sim$ 280 $cm^3.g^{-1}$ (S_{BET} = 1136 $m^2.g^{-1}$ and V_p = 0.461 $cm^3.g^{-1}$). On the other hand, both monolithic samples express Type IV behaviour with presence of microporosity, demonstrated by a steep uptake up to 0.05 P/P_0, as well as meso-porosity, denoted by increasing multi-layer uptake as well as a hysteresis loop between 0.45 and 0.9 P/P_0. No inherent difference is observed between the adsorption isotherms of $_{mono}$UiO-66(EtOH) (S_{BET} = 904 $m^2.g^{-1}$ and V_p = 0.939 $cm^3.g^{-1}$) and $_{mono}$UiO-66(DMF) (S_{BET} = 903 $m^2.g^{-1}$ and V_p = 0.939 $cm^3.g^{-1}$), both reaching an adsorption capacity of $\sim$200 $cm^3.g^{-1}$ at low pressure, and up to $\sim$610 $cm^3.g^{-1}$ at saturation pressure.

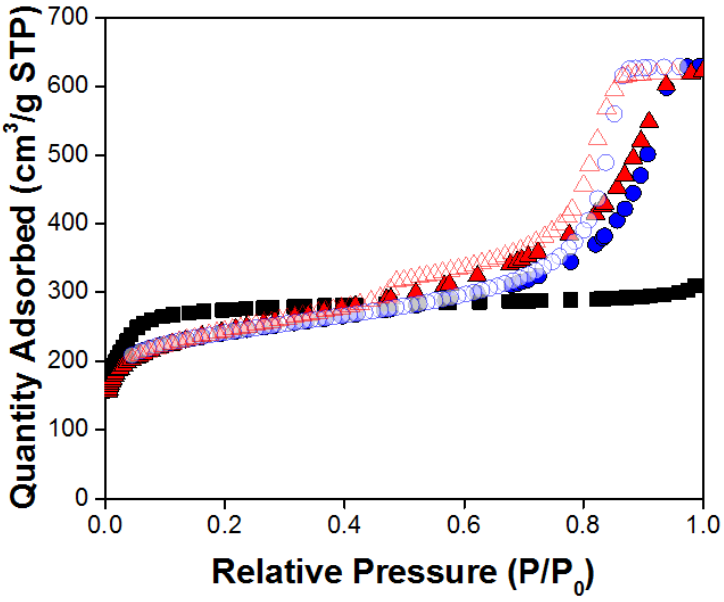

Fig. 5.7 Nitrogen adsorption isotherms at 77 K of $_{powd}$UiO-66, black squares, $_{mono}$UiO-66(DMF), red triangles, and $_{mono}$UiO-66(EtOH), blue circles. Open symbols illustrate desorption steps

Figure 5.8 illustrates close-ups of all UiO-66 samples. Sample $_{powd}$UiO-66 shows discrete particles with a good degree of monodispersity and samples $_{mono}$UiO-66(DMF) and $_{mono}$UiO-66(EtOH) show the flat surfaces trypical of monolithic structures, as previously discussed for monolithic ZIF-8. In this case however, no distinction is made between the external appearance of $_{mono}$UiO-66(EtOH) and $_{mono}$UiO-66(DMF), both expressing a glassy-like feel and an opaque white colour. However, upon closing up, the $_{mono}$UiO-66(DMF) sample shows an increased surface roughness, observed by the presence of conglomerated particles. This was possibly caused during evaporation of DMF solvent which possesses an increased surface tension (37.1 mN.m^{-1} in comparison to ethanol, 22.1 mN.m^{-1} at 20° C), wherein the increased stresses brought by solvent evaporation disrupt the delicate MOF "polymer" film to leave structural dents, accompannied by powder-like bits of material.

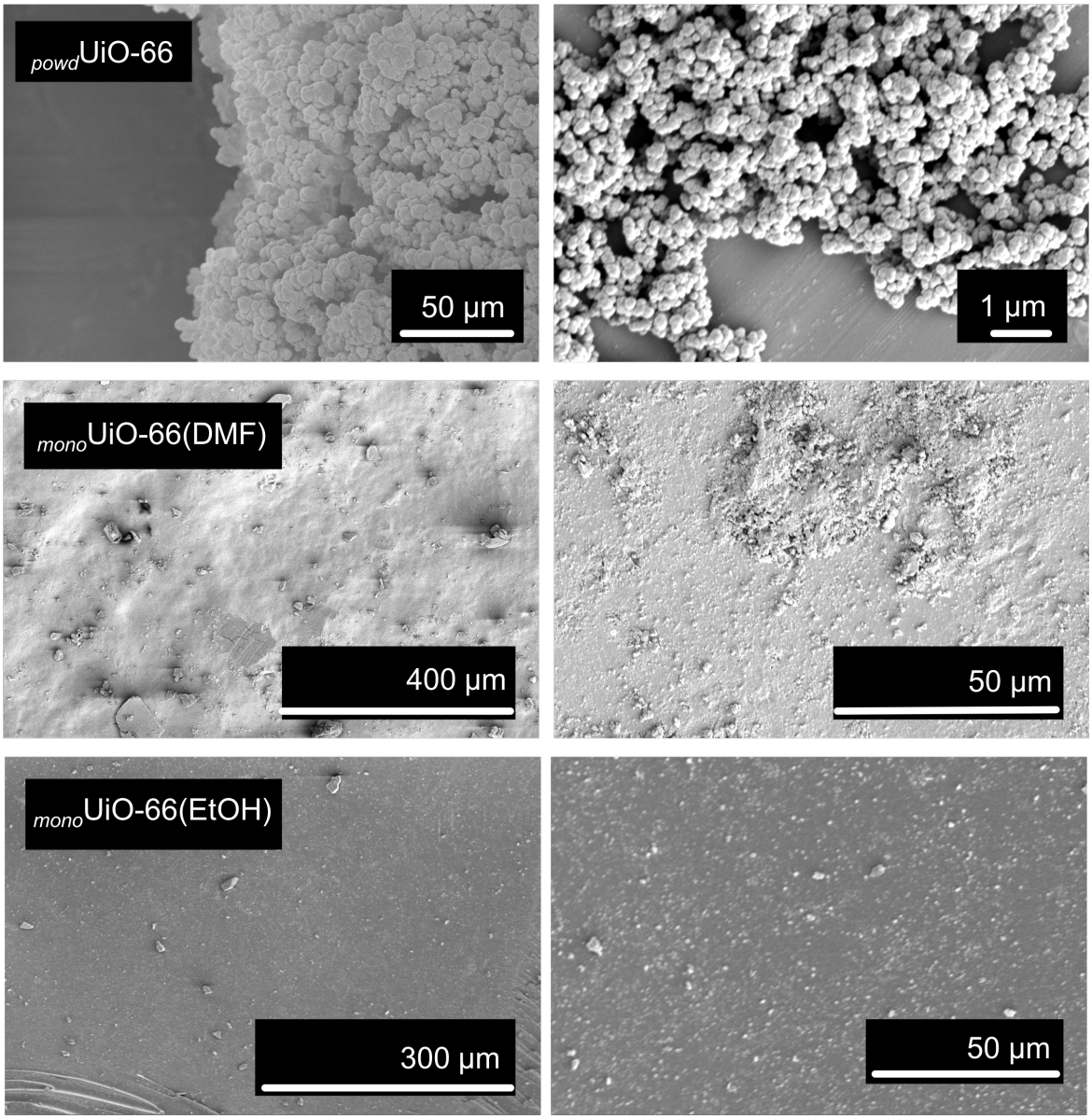

Fig. 5.8 SEM micrographs of UiO-66 samples

5.3.2 Bisphenol B Adsorption Performance

5.3.2.1 ZIF-8

The adsorption efficacy of the ZIF-8 samples was tested for BPB in concentrations ranging from 50 to 500 ppm at room temperature. Figure 5.9 shows the adsorption isotherms of BPB (left) and greater resolution in the low concentration range (right) illustrated as a function of initial concentration. In all cases, the adsorption equilibrium is reached within the first 24

hours, with maximum adsorption capacities of 10.4, 12.7 and 11.9 mg.g^{-1} for $_{powd}$ZIF-8, $_{mono}$ZIF-8(SP) and $_{mono}$ZIF-8(FP), respectively. When studying the amount adsorbed as a function of the initial concentration, the shape of the curves follows an unexpected trend. First of all, the three samples register a linear increase in the amount of BPB adsorbed when increasing the concentration of pollutant up to 250 ppm, recognised as Stage I. This is then followed by a decrease in the amount adsorbed for concentrations between 300 and 500 ppm (Stage II). At these concentrations, $_{mono}$ZIF-8 shows virtually no adsorption, whereas $_{mono}$ZIF-8(SP) and $_{mono}$ZIF-8(FP) adsorption is slightly reduced, to approximately 10 mg.g^{-1}.

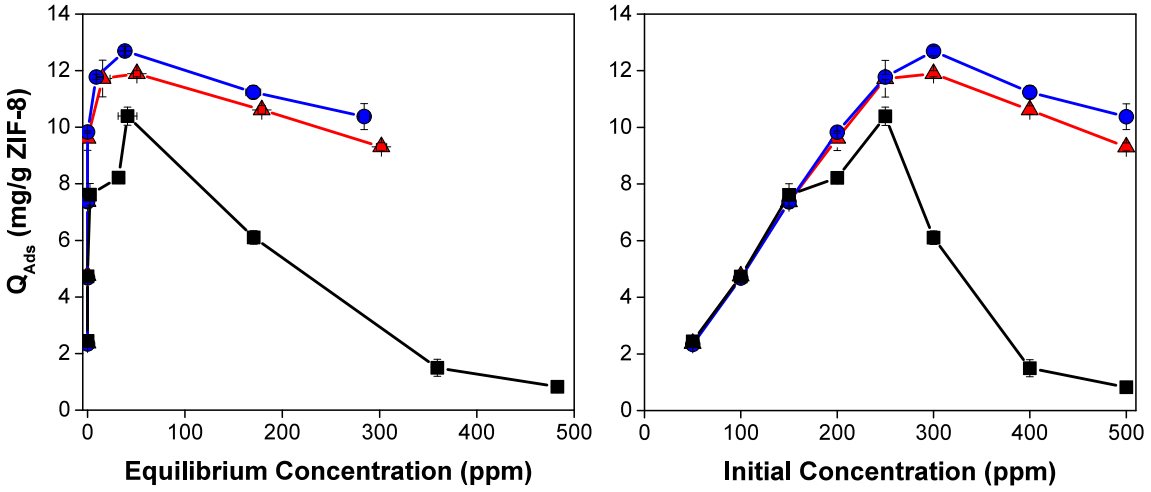

Fig. 5.9 Adsorption isotherms (left) and amount adsorbed, Q_{Ads}, as a function of the initial concentration (right) of BPB with m = 100 mg, V = 5 mL on $_{powd}$ZIF-8, black squares; $_{mono}$ZIF-8(SP), blue circles; $_{mono}$ZIF-8(FP), red triangles.

As the concentration of BPB increases, the pH decreases to render the solution slightly more acidic, registering a pH of 6.44 at 300 ppm. Previously published literature indicates high chemical stability of ZIF-8 only in neutral and basic conditions [28]. In line with this, it is observed that the slightly acidic environment created at high BPB concentrations proves detrimental to ZIF-8 adsorption performance, also discussed earlier in Chapter 3. The lack of stability can be observed from the shape of the BPB adsorption isotherms, especially in the case of $_{powd}$ZIF-8, which, instead of yielding a plateau at high equilibrium concentrations, results in significantly reduced uptake (Figure 5.9 left). On the other hand, samples $_{mono}$ZIF-

8(SP) and $_{mono}$ZIF-8(FP) retain a better performance at higher BPB concentrations due to the significantly higher inherent density of their monolithic structures.

Figure 5.10 illustrates the evaluated S_{BET} of the adsorbents in contrast to the maximal BPB uptake obtained. It is seen that even though $_{powd}$ZIF-8 attains the highest surface area, it renders the lowest uptake, whereas the uptake of $_{mono}$ZIF-8(FP) is marginally decreased relative to that of $_{mono}$ZIF-8(SP), even though the surface area of the former is almost twice as high. This is explained by the fact that, due to the large kinetic diameter of BPB (6.3 Å), adsorption occurs only on the available external surface sites of ZIF-8. Hence, in spite of the ZIF-8 swing-effect [139, 140], which opens the hexagonal windows towards larger adsorbates, the inner porosity of the monoliths does not play a significant role in the overall removal efficacy of BPB. Taken together, these data leads to conclude that it is the poor stability of $_{powd}$ZIF-8 that is the limiting factor in its overall removal performance of BPB, and that the behaviour of the monoliths is only explicable by their higher inherent densities conferring improved stability, highlighting the importance and the benefits of shaping the ZIF-8 material.

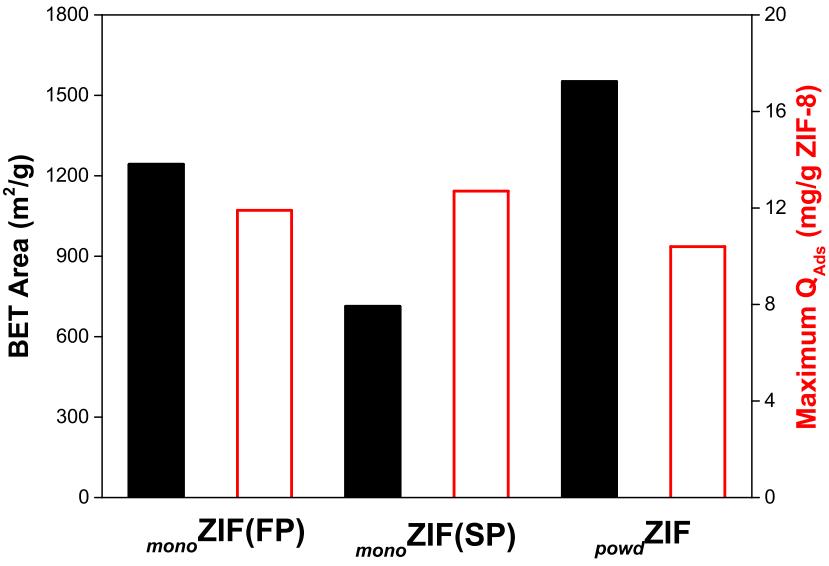

Fig. 5.10 Comparison of BET area versus maximum BPB adsorption capacity (from Figure 5.9) on ZIF-8 samples.

Although the equilibrium isotherms described above provide crucial information about the adsorption process, in applications regarding the removal of pollutants from water, a

24 hour exposure time or longer is not practical. To get more insights about the dynamics of adsorption, the adsorption kinetics behaviour was closely tracked for 3 hours of contact. In contrast with the equilibrium experiments described above, BPB solution volume was doubled to 10 mL whilst the initial BPB concentration was kept at 300 ppm (C_0). Using a relatively low concentration allowed to operate under the assumption that degradation of ZIF-8 samples was not taking place, while using larger volumes for the solutions increased, in principle, the amount of BPB that could be removed using the same adsorbent dosage.

Figure 5.11 shows the evolution of uptake of BPB over time for the three adsorbents, fitted with a pseudo-second-order kinetic rate model; Table 5.1 shows the pseudo-second order kinetic rate parameters. For all three samples, extremely fast uptake is observed,

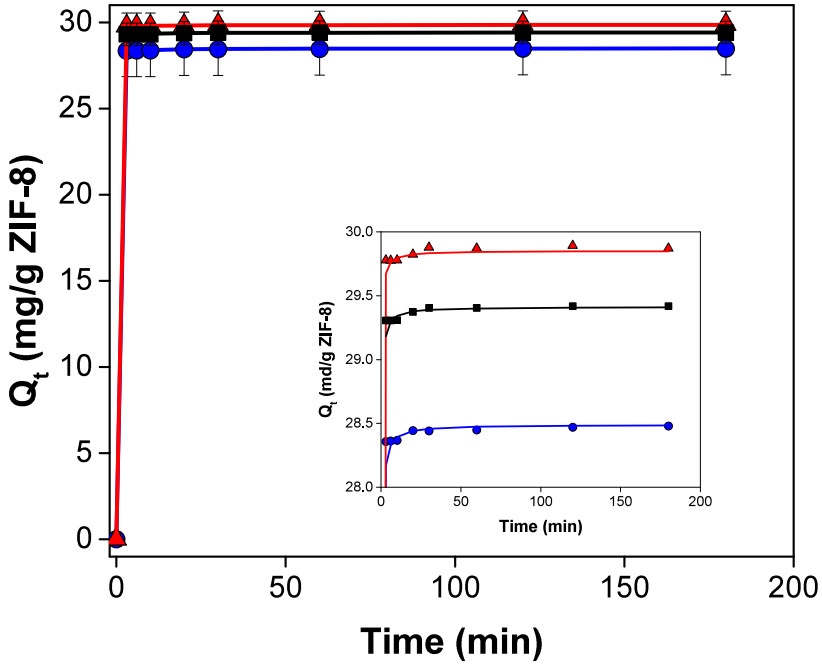

Fig. 5.11 Dynamic adsorption of BPB on ZIF-8 adsorbent in 10 mL solutions and fitted pseudo-second-order rate curves with C_0 = 300 ppm where $_{powd}$ZIF-8, black line and black squares; $_{mono}$ZIF-8(SP), blue line and blue circles; $_{mono}$ZIF-8(FP), red line and red triangles. Error bars represent the standard deviation of each data point.

reaching equilibrium within less than 30 minutes of contact, each sample achieving similar maximum uptakes. Overall, during these experiments $_{mono}$ZIF-8(FP) adsorbed the highest quantity of BPB, reaching 29.9 mg.g^{-1}, followed by $_{powd}$ZIF-8 and $_{mono}$ZIF-8(SP) with 29.4 and 28.5 mg.g^{-1}, respectively. These amounts are, as expected, higher than the equilibrium

ones observed in Figure 5.9, due to the larger adsorbent dosage (100 mg in 10 mL volumes). On the one hand, $_{mono}$ZIF-8(FP) attains a comparable adsorption uptake to that of $_{powd}$ZIF-8, with similar calculated (Table 5.1) and experimental Q_e. However, the respective k_2 values differ, the powdered sample yielding a lower k_2; this indicates that, overall, the adsorption kinetics is faster on the fully porous monolithic sample than on the powder and, in turn, slower on the semi-porous monolith than on the powder. Again, confirming that the available internal surface area does not play a role neither on the equilibrium nor on the kinetics of adsorption.

Table 5.1 Pseudo-second order kinetic constant, k_2, and capacity, Q_e, derived from the kinetic adsorption experiments conducted with 10 mL of 300 ppm BPB and 0.1 gram of adsorbent.

Sample	k_2 x 10^3 (g.mg^{-1}.min^{-1})	Q_e (mg.g^{-1})	R^2
$_{mono}$ZIF-8(FP)	187.0	29.9	1
$_{mono}$ZIF-8(SP)	102.7	28.5	1
$_{powd}$ZIF-8	128.4	29.4	1

Whereas research literature does not contain any data on removal of BPB, this performance can be contrasted with adsorption of Bisphenol A, which is structurally similar but lacks one methyl group. Both monolithic adsorbents are found to outperform traditional adsorbents such as modified and unmodified activated carbons and zeolites, in terms of adsorption capacity, but in a lower batch volume of 10 mL [221, 222]. Furthermore, in comparison to a recent study presented by Onundi et al. [223], monolithic ZIF-8 promises 100% removal of BPB even in very high concentrations, up to 200 ppm, within less than 30 minutes of contact, without introducing additional oxidative species.

However, in addition to fast kinetics, it is also important for the adsorbents to be able to maintain the same level of performance over prolongued and repetitive usage. Figure 5.12 illustrates the equilibrium adsorption of the ZIF-8 samples over an exposure time of 6 days with intervals of 24 hours with solutions of starting concentrations ranging from 50 to 500 ppm. As expected from the previously discussed adsorption isotherms, sample $_{mono}$ZIF-8(SP) is able to attain the highest adsorption capacity at an initial concentration of 300 ppm, the adsorption capacity is maintained very well for up to 144 hours with very little variation. When the same sample is exposed to initial concentrations of 400 and 500 ppm, the

adsorption capacity starts to drop after 48 hours of contact, to ∼10 and 6 mg.g^{-1}, respectively, after 144 hours. In all other cases, the adsorption capacity is perfectly maintained for the entire duration of exposure with concentrations up to 300 ppm.

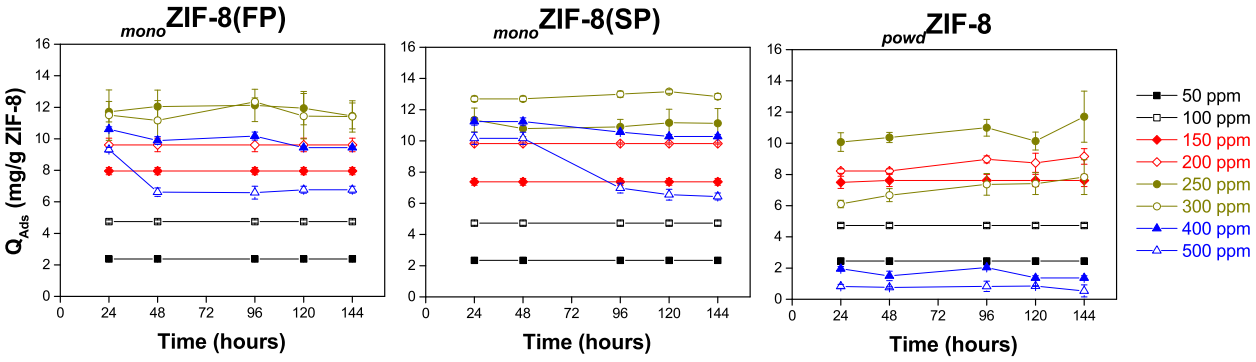

Fig. 5.12 Stability of ZIF-8 over 6 days of exposure in BPB solutions

For sample $_{mono}$ZIF-8(FP) the adsorption capacity is nearly the same at initial concentrations 250 and 300 ppm, suggesting that this sample begins to lose performance at around 250 ppm. In all other cases, the adsorption capacity is very well maintained for the entire duration of exposure. Once in contact with starting concentrations of 400 and 500 ppm, the adsorption capacity is seen to decrease from ∼10 and 11 mg.g^{-1} to 10 and 6.5 mg.g^{-1}, respectively. In comparison to sample $_{mono}$ZIF-8(SP), the adsorption capacity of sample $_{mono}$ZIF-8(FP) sharply decreases after 24 hours of contact, thus confirming a lower overall stability. Finally, powdered sample $_{powd}$ZIF-8 confirms lower stability in the BPB solutions; the highest adsorption capacity is observed at a starting concentration of 250 ppm, registering marked variations every 24 hours. Once starting concentration is increased to 300 ppm, the adsorption capacity decreased remarkably.

In addition to good stability and adsorption capacity, it is also important to be able to regenerate and reuse the adsorbents. Figure 5.13 shows the performance during a second adsorption cycle, in terms of removal, of reused adsorbents after being washed in ethanol and water; during this measurement, the samples were contacted with an initial concentration of 300 ppm BPB. In all cases, when sorbents were washed with ethanol and reused, the removal registers a slight increase, most notably for the monolithic samples, which both show a removal of over 80 % during a second adsorption cycle. At the same time, when the

same samples are washed in water, the removal decreases to ∼40, 70 and 33 % in $_{mono}$ZIF-8(FP), $_{mono}$ZIF-8(SP) and $_{powd}$ZIF-8, respectively. The reason for a better performance after regeneration is due to the stronger surface and pore interaction of ethanol with the hydrophobic ZIF-8, which lead to loss of the surface adsorbed BPB. Additionally, the crystallinity of the material is very well maintained after regeneration and no linker is observed in the supernatant following HPLC quantification, suggesting very good stability of the monolithic materials; this was previously discussed in Chapter 3 and is supported by additional X-ray diffraction patterns of recovered samples in Appendix B (Figure B.3).

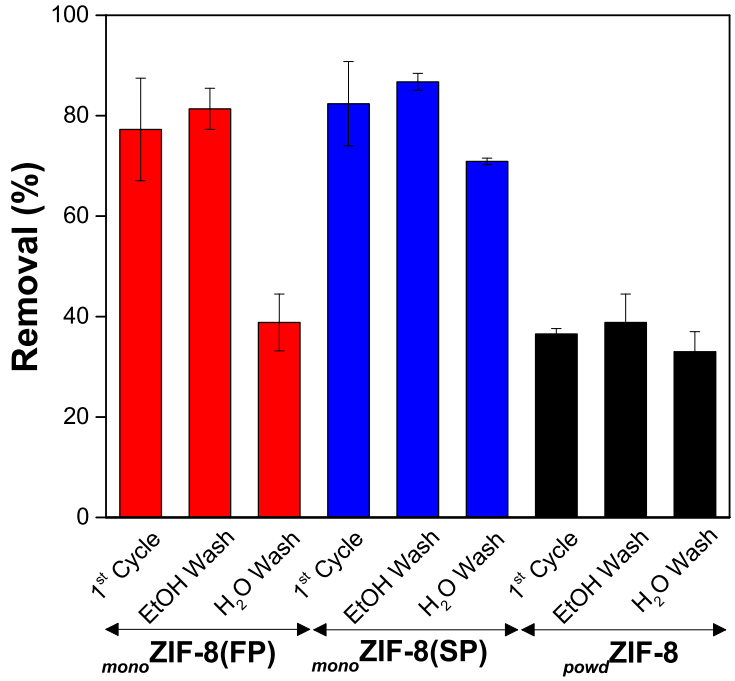

Fig. 5.13 Removal of BPB with reused samples after of EtOH and water wash. Experiments were conducted with m = 100 mg, V = 5 mL and C_0 = 300 ppm

Judging from the nature of ZIF-8 as well as the structure of the BPB molecule, the suggested mechanism of adsorption relies heavily on the hydrophobic characteristic of ZIF-8, which precludes competition with water, as well as π-π stacking between the benzene rings in BPB and C=C of the imidazole linker. Unfortunately, the amount of BPB adsorbed on the unwashed adsorbent is too small in order to be clearly observed using FT-IR and spectra obtained fail to show the presence of -OH bonds at high wavenumbers (Figure B.4 in Appendix B). Another common form of studying interactions in adsorption studies is to

subject the tests to measurements at differing pH values. As previously shown in Chapter 3, this is a major problem when studying adsorption on MOFs as their stability is, indeed, pH dependent; this is especially the case for ZIF-8, which is extremely unstable at low pH and also presents some level of degradation in neutral conditions whilst being highly stable in high pH. At the same time, speciation is also extremely important; BPB, is expected to be negatively charged at pH values higher than 10 [224], which will favour electrostatic repulsion between adsorbates and thus lead to a lower adsorption capacity. However, in this study, the test solutions were prepared in water at pH 7, at which point BPB is found in its neutral form.

For the purpose of industrial applicability, however, batch mode operations are often time and energy demanding. It is, therefore, crucial to develop processes to deal with large volumes of water on a continuous basis. In this context, the efficacy of a chosen monolithic adsorbent, $_{mono}$ZIF-8(FP), was tested, in a proof-of-concept flow-mode adsorption study entailing fast protein liquid chromatography (FPLC) equipment, which enabled the fast collection of BPB breakthrough curves. In this scenario, the use of monolithic ZIF-8 is especially favourable since ZIF-8 in its original, powdered configuration would need to be compacted, pelletized or immobilized on beaded supports in order to yield low-pressure drops and maintain a constant bed volume. Indeed, preliminary experiments using solely powdered ZIF-8 failed to maintain the stability of the adsorbent bed, causing significant bed expansion even at very small flow rates. For experiments with $_{mono}$ZIF-8(FP), the cartridge was hand-packed by firstly dispersing 2 g of the monolithic material in deionised water, before transferral to the column. This quantity of $_{mono}$ZIF-8(FP) yielded a 5 cm tall column of 1 cm diameter, exhibiting very low backpressure at a range of flow-rates up to 1 ml.min^{-1}. Figure 5.14 illustrates the BPB breakthrough curve of a $_{mono}$ZIF-8(FP) cartridge in comparison to a control experiment with no adsorbent.

As the BPB solution flows through the packed bed, no BPB is seen to leave until after being exposed to circa 56 minutes of contact time, equivalent to 14 mL of 50 ppm BPB solution. The exit concentration of BPB then starts to increase rapidly and ultimately plateaus after contact with a further 13 mL of BPB solution, i.e. circa 110 minutes of exposure and 27 mL in total. From the same figure, it is observed that when the same solution flows through a control bed (red circles), no BPB is detected during the initial 12 minutes, i.e. 3 mL of BPB

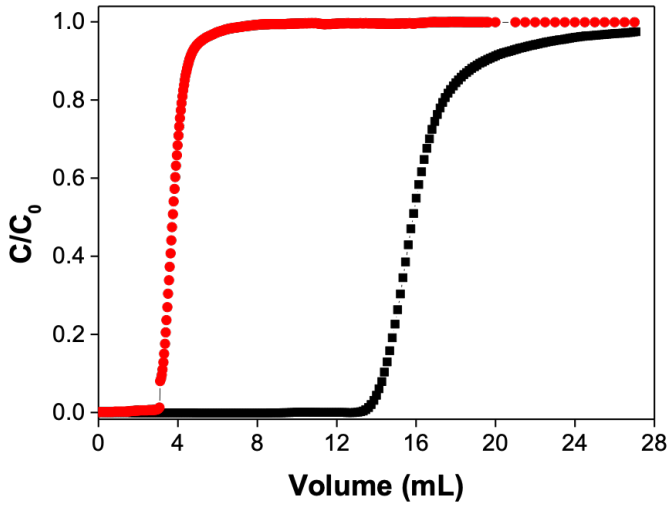

Fig. 5.14 Breakthrough curve for 50 ppm BPB solution flowing at 0.25 mL.min^{-1} over a 5 x 1 cm cartridge composed of 2 g of $_{mono}$ZIF-8(FP), black squares, and over a blank experiment, red circles. C stands for concentration at time t and C_0 is the initial concentration

solution, this is accounted as dead column volume. The difference between the areas under the curves thus translates to the total amount of BPB bound to the adsorbent until saturation is reached; in this case, the adsorption capacity reaches 0.573 mg.g^{-1} of ZIF-8. Whilst this is significantly lower than batch adsorption studies at the same BPB concentration, which has yielded a maximum adsorption capacity of 2.4 mg.g^{-1} for the same adsorbent (Figure 5.9), flow mode configurations are more industrially attractive since batch operations are too costly and time-consuming. Overall, for practical applications, where bisphenols are typically encountered in ppb concentrations, a $_{mono}$ZIF-8(FP) cartridge offers an attractive solution due to not only its high adsorption capacity and ease of manufacture, but for the very fast and efficacious removal of BPB in both batch and flow mode operations.

5.3.2.2 UiO-66

Adsorbents from the MOF UiO-66 series, previously introduced in Chapter 3, were also subject to the same liquid phase adsorption testing with model pollutant BPB. In this case, however, the role of mesoporosity of the monolithic UiO-66 samples towards adsorption of BPB is observed.

Similarly, the adsorption capacities of the UiO-66 samples were determined by conducting equilibrium studies at room temperature with BPB solutions ranging from 50 to 800 ppm, the

results are shown in Figure 5.15, these tests were carried out with an adsorbent loading of 6.67 $g.L^{-1}$. In comparison to the ZIF-8 samples, which demonstrated lower adsorption capacities at high BPB concentrations due to framework degradation, the UiO-66 samples show good stability. This is illustrated by the fitted Langmuir isotherms. For $_{powd}$UiO-66, the adsorption capacity increased drastically up to $\sim$ 47.3 $mg.g^{-1}$ at an equilibrium concentration (C_e) of 85 ppm, at which point the initial concentration (C_0) is 300 ppm, the adsorption capacity then reaches a plateau with a maximum Q_{Ads} of 67.6 $mg.g^{-1}$ with C_e = 350 ppm. For $_{mono}$UiO-66(EtOH) the adsorption capacity increases more drastically than for $_{powd}$UiO-66, with a plateau forming at $\sim$ 42 $mg.g^{-1}$ and $\sim$ C_e = 20 ppm, the data point at C_e = 580 ppm is considered an anomaly and was thus not included in the Langmuir fitting. Similarly, the isotherm of sample $_{mono}$UiO-66(DMF) closely follows that of $_{powd}$UiO-66 at low equilibrium concentrations, up to 40 ppm, after which a plateau forms at $\sim$ 43 $mg.g^{-1}$ at $\sim$ C_e = 112 ppm with a maximum Q_{Ads} of 53.6 $mg.g^{-1}$ with C_e = 443 ppm. Whereas the adsorbent loading used for UiO-66 is smaller than for that of ZIF-8, hence the larger adsorption values, the removal efficacy between the two adsorbents differ. It is noted that, regardless of UiO-66 adsorbent loading, the largest removal efficacy of BPB achieved does not exceed 90% (Figure B.7, whereas ZIF-8 is able to achieve 100% whilst in the monolithic configuration (Figure B.5).

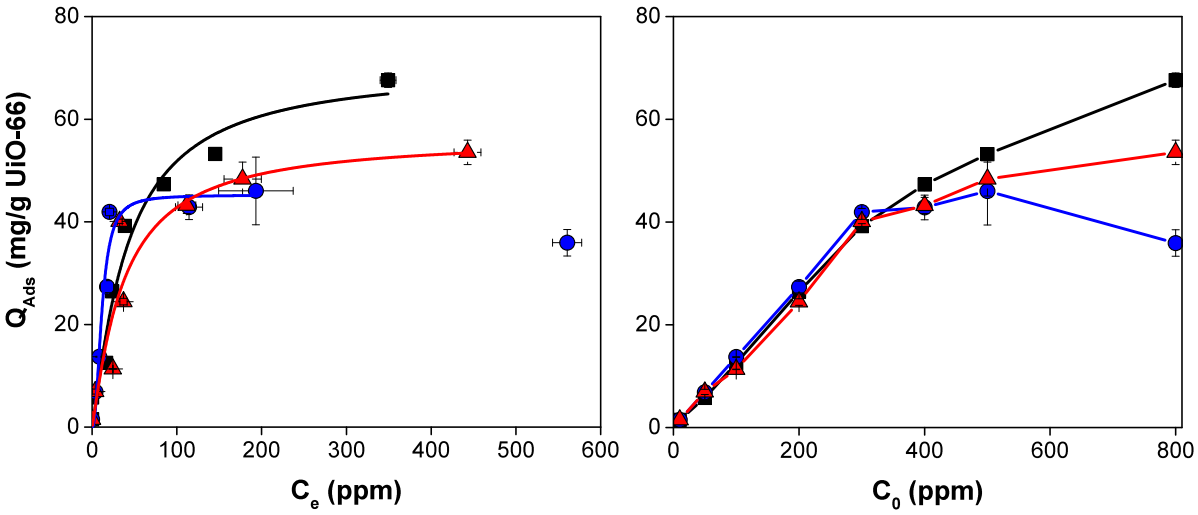

Fig. 5.15 Adsorption isotherms (left) and amount adsorbed, Q_{ads}, as a function of the initial concentration (right) of BPB with m = 100 mg, V = 15 mL on $_{powd}$UiO-66, black squares; $_{mono}$UiO-66(EtOH), blue circles; $_{mono}$UiO-66(DMF), red triangles.

The reason for which the $_{powd}$UiO-66 sample attains a higher overall adsorption capacity is only attributed to the higher S_{BET} in comparison to the monolithic materials as well as the dispersity of the powdered material in the batch conditions, which overall, contributes to an improved mass transfer and hence uptake of BPB. The difference in the density of the monolithic samples, however, is illustrated in their respective adsorption isotherms; for the lower density $_{mono}$UiO-66(EtOH) material, the shoulder of the isotherms forms at a much lower equilibrium concentration, ~40 ppm, whereas for $_{mono}$UiO-66(DMF), this occurs at ~100 ppm. This is also reflected in higher adsorption capacity of the $_{mono}$UiO-66(DMF) sample. As observed from Figure 5.15 (right), the adsorption capacity increases linearly up to an initial concentration of BPB of 300 ppm, with all three adsorbents showing similar behaviour. Increasing the concentration up to 800 ppm elucidates diverging uptake characteristics, namely with $_{powd}$UiO-66 performing the best out of all 3 configurations, followed by $_{mono}$UiO-66(DMF) and ultimately, $_{mono}$UiO-66(EtOH).

The kinetic adsorption capabilities of the different UiO-66 samples were compared, the results are illustrated in Figure 5.16. As expected, the $_{powd}$UiO-66 material attains the highest uptake, of ~39 mg.g^{-1} after 180 minutes of contact, with equilibrium being reached within 30 minutes.

Table 5.2 Pseudo-second order kinetic constant, k_2, and capacity, Q_e, derived from the kinetic adsorption experiments conducted with 15 mL of 300 ppm BPB and 0.1 gram of adsorbent.

Sample	k_2 x 10^3 (g.mg^{-1}.min^{-1})	Q_e (mg.g^{-1})	R^2
$_{mono}$UiO-66(DMF)	5.58	36.9	0.994
$_{mono}$UiO-66(EtOH)	14.3	35.0	0.998
$_{powd}$UiO-66	12.3	38.9	0.999

As observed from the equilibrium adsorption measurements, the monolithic samples attain a lower uptake, with sample $_{mono}$UiO-66(DMF) reaching ~37 mg.g^{-1}, followed by $_{mono}$UiO-66(EtOH), with ~35 mg.g^{-1}. Again, the main difference in the monolithic materials is suggested by the difference in equilibrium conditions of the respective materials. For the lower density $_{mono}$UiO-66(EtOH) monolith, the plateau forms at ~20 minutes whereas for $_{mono}$UiO-66(DMF) this occurs at ~30 minutes. This is also supported by the drastically

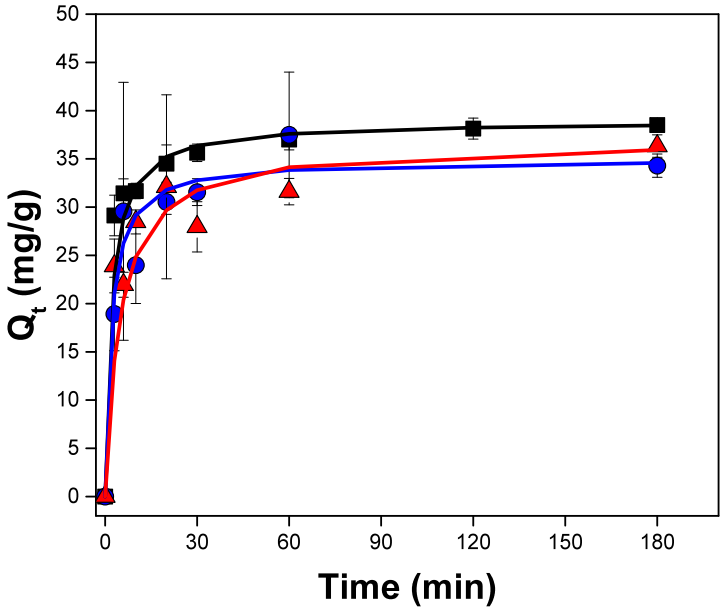

Fig. 5.16 Dynamic adsorption of BPB on UiO-66 adsorbent with V = 15 mL and m = 0.1 g and fitted pseudo-second-order rate curves with C_0 = 300 ppm where $_{powd}$UiO-66, black line and black squares; $_{mono}$UiO-66(EtOH), blue line and blue circles; $_{mono}$UiO-66(DMF), red line and red triangles. Error bars represent the standard deviation of each data point.

reduced pseudo-second order kinetic constant (Table 5.2), which is almost 2.5 times lower than that of $_{mono}$UiO-66(EtOH).

The activated $_{powd}$UiO-66 sample used for this study expresses an adsorption capacity of $\sim$280 $cm^3.g^{-1}$ with an equivalent S_{BET} of 1136 $m^2.g^{-1}$. This differs from the computationally derived adsorption capacity and S_{BET} for defect-free UiO-66, which is found to be $\sim$ 300 $cm^3.g^{-1}$ and $\sim$1400 $m^2.g^{-1}$ [225]; suggesting the presence of defects in the structure, such as missing linkers. Moreover, as shown in Figure B.7, the removal efficiency for this sample plateaus at an adsorbent dosage of 6.67 $g.L^{-1}$, at which point a maximal removal efficiency of 90% is achieved. It has been shown that the presence of defects in the UiO-66 structure, such as missing linkers, tremendously alters the hydrophobicity of the framework. In the case of UiO-66, Pritha et al. [108] showed that missing as little as 2 linkers from the 12-connected Zr node, enables water condensation in UiO-66 at as little as 30% relative humidity, from the expected 70% in an ideal framework [108]. Furthermore, Katz et al. [226] reported that using a ratio of HCl to DMF of 1:5 during the synthesis process of UiO-66, similar to this study, can yield defects consisting in as much as 8 linkers per metal node instead of

the defect-free 12. They also reported that this can result in a S_{BET} area of 1550 $m^2.g^{-1}$ corresponding to an increase in pore size from ∼8 to 11 Å [226]. This is expected to facilitate the adsorption of BPB in the internal UiO-66 pores and ensure a high uptake. Considering the applicability of MOFs for water treatment applications, it is therefore important that the chosen framework is as hydrophobic as possible so as to minimise the affinity for water. A hydrophilic framework would competitively adsorb water over the target molecule and therefore result in a reduced adsorption capacity [227, 228], suggesting that the maximum removal efficiency in UiO-66, which barely reached 90%, is due to residual water uptake. Nevertheless, at the dosage of UiO-66 studied in this work, the BPB adsorption capacity is remarkably high; again, yielding a better performance and faster uptake than many traditional adsorbents mentioned previously, such as activated carbons and zeolites.

On the other hand, monolithic UiO-66 samples, attain a lower adsorption capacity for BPB in contrast to the powdered configuration. Nevertheless, the structures of the monolithic UiO-66 samples are expected to be very close to the theoretically perfect UiO-66 structure (supported by ICP data in Appendix B Table B.1), which might mean that the monolithic UiO-66 samples express decreased hydrophilicity relative to $_{powd}$UiO-66; however, their performance is hampered by their decreased liquid phase stability, previously discussed din Chapter 3. Flow-mode adsorption has been attempted with $_{mono}$UiO-66(EtOH) and is illustrated in Figure 5.17. However, due to the low stability of this structure, the degradation of the adsorbent is observed instead and is defined by a monotonic increase in exit concentration from the point of BPB injection.

In contrast, ZIF-8 attains 100% removal at a dosage of 10 $g.L^{-1}$ (Figure B.5) at the same initial concentration of BPB used, suggesting better selectivity for BPB over water. However, the caveat with ZIF-8 is its poor stability with increasing concentration of BPB as well as lower overall framework stability in the aqueous medium, especially in the powdered configuration. It is suggested that BPB interacts with UiO-66 in a similar fashion to ZIF-8 wherein strong π-π surface interactions, between the BDC linkers and BPB, govern the adsorption mechanism.

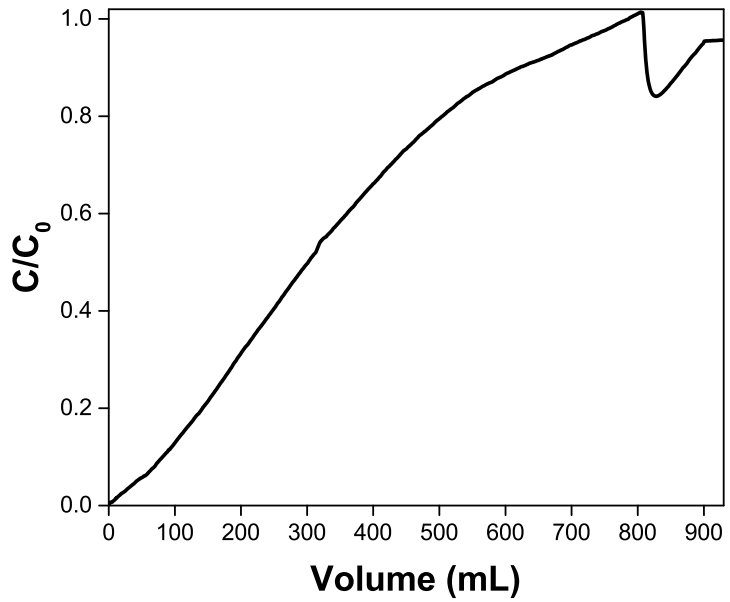

Fig. 5.17 Flow-mode adsorption of BPB on a 2 g monolithic column comprising of $_{mono}$UiO(EtOH) showing decreased stability of adsorbent, defined by monotonic increase in C/C_0 up to 800 mL, point at which injection was stopped, followed by release of adsorbed BPB during the washing step from 825 to 900 mL

5.3.2.3 Scaled-up ZIF-8@Cordierite Composites

The BPB adsorption performance of the scaled-up ZIF-8@Cordierite samples, previously described in Chapter 4, was also tested in flow mode capacity. In contrast to the monolithic ZIF-8 cartridge, the ZIF-8@Cordierite cartridges allowed for a safe and easy flow-mode operation even at high flowrates up to 10 mL.min^{-1} and higher without any bed expansion or pressure drop. Samples with ZIF-8 synthesised and deposited in both water and ethanol were observed with C_0 10 ppm BPB solutions. The resultant cartridges were approximately 10 cm in height and 1 cm in diameter weighing approximately 4 grams. Figure 5.18 illustrates the breakthrough curves for ZIF-8@Cordierite(EtOH) samples as well as pure cordierite as a control. Relative to the pure cordierite column, an improvement in breakthrough time is observed for samples containing ZIF-8, which achieve complete saturation after injecting 100 mL of 10 ppm BPB solution, for $_{ZnO}$ZIF-8@Cordierite(EtOH) and ZIF-8@Cordierite(EtOH), and 50 mL for $_{IPTES}$ZIF-8@Cordierite(EtOH), respectively. On the other hand, breakthrough is not observed for the control cordierite sample, as there is no surface interaction between BPB and cordierite. However, the performance of an adsorbent column is measured in

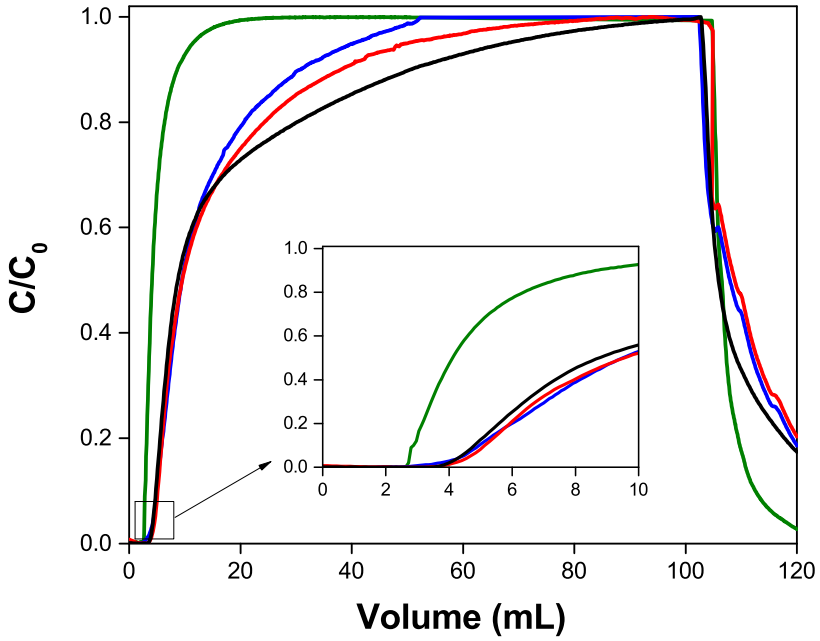

Fig. 5.18 BPB breakthrough for scaled-up ZIF-8@Cordierite(EtOH) with C_0 10 ppm flowing at 1 mL.min^{-1} with approximately 4 g of composite. Olive, red, blue and black curves represent control untreated cordierite, $_{ZnO}$ZIF-8@Cordierite(EtOH), $_{IPTES}$ZIF-8@Cordierite(EtOH) and $_{U}$ZIF-8@Cordierite(EtOH), respectively.

10% binding capacity, that is, the time/amount it takes for the adsorbent to reach 10% saturation. Almost no difference can be discerned between all samples at 0.1 C/C_0 hence, irrespective of the amount of ZIF-8 mass deposited, the 10% binding capacity reaches approximately 6.09 µg.g^{-1} (of composite structure) for all samples. In this case, it is concluded that the amount of ZIF-8 deposited on each sample does not influence the binding capacity. By contrast, Table 5.3 outlines the 10% binding capacities evaluated per gram of composite and per gram of deposit on the cordierite structures, assumed to be crystalline ZIF-8. Whereas the adsorption capacity per gram of composite stays in the same range, the same adsorption capacity expressed in terms of ZIF-8 deposited is, in fact, 47.6, 64.1 amd 64.2 for $_{ZnO}$ZIF-8@Cordierite(EtOH), $_{IPTES}$ZIF-8@Cordierite(EtOH) and $_{U}$ZIF-8@Cordierite(EtOH), respectively. This means that, in spite of the higher mass of gain of the ZnO-modified sample, the adsorption capacity per gram of deposit is, in fact, lower than expected. As aforementioned in Chapter 4, this could be due to crystalline defects brought

about during in-situ growth and synthesis which resulted in amorphous phases altogether with crystalline ZIF-8.

Table 5.3 10% Adsorption capacities in flow-mode configuration of ZIF-8@Cordierite(EtOH) samples per gram of composite structure and per gram of ZIF-8 deposited

Sample	Q_{Ads} $\mu g.g^{-1}$ (comp.)	Q_{Ads} $\mu g.g^{-1}$ (ZIF-8)	ZIF-8 (% wt.)
$_{ZnO}$ZIF-8@Cord.(EtOH)	6.09	47.6	12.8
$_{IPTES}$ZIF-8@Cord.(EtOH)	6.09	64.1	9.5
$_{U}$ZIF-8@Cord.(EtOH)	6.10	64.2	9.5

Figure 5.19 illustrates the breakthrough curves for BPB for all ZIF-8@Cordierite(Aq) composites. For these composite structures, the saturation capacity is reached fairly rapidly, after injecting ∼50 mL of BPB solution. All samples illustrated very good porosity, reaching a N_2 adsorption capacity of ∼100 $cm^3.g^{-1}$ and expressing good crystallinity. Relative to the ZIF-8@Cordierite(EtOH) samples, the 10% binding capacity is improved for $_{IPTES}$ZIF-8@Cordierite(Aq), reaching 10.3 $\mu g.g^{-1}$. On the other hand, $_{ZnO}$ZIF-8@Cordierite(Aq) and $_{U}$ZIF-8@Cordierite(Aq) both of attain 5.5 $\mu g.g^{-1}$. Whereas the adsorption, or binding, capacity of $_{IPTES}$ZIF-8@Cordierite(Aq) is higher than that of ZIF-8@Cordierite(EtOH) samples, due to the significantly higher mass of crystalline ZIF-8, the binding capacities of the latter two samples are significantly lower than expected. Similarly, Table 5.4 illustrates the 10% adsorption capacities per gram of both composite and per gram of ZIF-8 deposited altogether with the overall mass gain of the structures. The highest adsorption capacity per gram of ZIF-8 deposited is achieved by $_{IPTES}$ZIF-8@Cordierite(Aq) with 46.8 $\mu g.g^{-1}$, followed by $_{ZnO}$ZIF-8@Cordierite(Aq) and $_{U}$ZIF-8@Cordierite(Aq) with 22.0 and 19.6 $\mu g.g^{-1}$, respectively. As previously discussed in Chapter 3, both the crystallinity and BET areas of these samples indicate the good quality of ZIF-8, however, the performance in flow-mode configuration does not suggest much improvement over the ZIF-8@Cordierite(EtOH) samples, which contain a significantly lower quantity of MOF phase. This can only indicate that the experimental conditions and configuration of the set-up was possibly unfavourable for optimal BPB uptake with possibly insufficient contact between the stationary adsorbent and the mobile BPB solution.

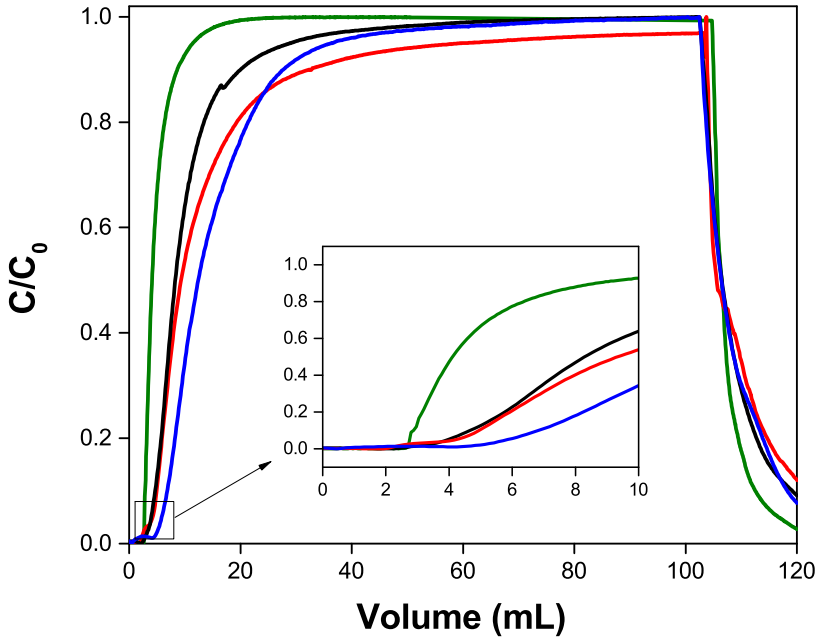

Fig. 5.19 BPB breakthrough for scaled-up ZIF-8@Cordierite(Aq) with C_0 10 ppm flowing at 1 mL.min^{-1} with approximately 4 g of composite. Olive, red, blue and black curves represent control untreated cordierite, $_{ZnO}$ZIF-8@Cordierite(Aq), $_{IPTES}$ZIF-8@Cordierite(Aq) and $_{U}$ZIF-8@Cordierite(Aq), respectively.

Table 5.4 10% Adsorption capacities in flow-mode configuration of ZIF-8@Cordierite(Aq) samples per gram of composite structure and per gram of ZIF-8 deposited

Sample	Q_{Ads} µg.g^{-1} (comp.)	Q_{Ads} µg.g^{-1} (ZIF-8)	ZIF-8 (% wt.)
$_{ZnO}$ZIF-8@Cord.(Aq)	5.5	22.0	25.0
$_{IPTES}$ZIF-8@Cord.(Aq)	10.3	46.8	22.0
$_{U}$ZIF-8@Cord.(Aq)	5.5	19.6	28.0

Additionally, ZIF-8@Cordierite structures did not attain the same flow mode performance as the pure monolithic ZIF-8 column due to the considerably lower ZIF-8 phase available in these composites, at the same time, due to the open channel configuration it might have been possible that insufficient residence time of the liquid could have caused a poorer performance. In the monolithic ZIF-8 cartridge, the tortuous nature of the flow-path of liquid allowed for an enhanced contact and improved retention of BPB analyte but at the downside of operating carefully at low flowrates.

5.4 Conclusions

The feasibility of using ZIF-8 and UiO-66 MOFs as adsorbents for BPB pollutant from liquid water was investigated. All adsorbents were presented in three configurations. For ZIF-8, the conventional powdered ZIF-8, the fully porous ethanol-synthesised ZIF-8 monolith and, finally, the semi-porous isopropanol-synthesised ZIF-8 monolith. The latter two have been specially designed so as to observe the role of full or incomplete activation of the material towards use in aqueous media, and therefore the role of external and internal porosity. For UiO-66, this consisted in conventional powdered UiO-66 as well as monolithic UiO-66 structures exhibiting both higher and lower density, obtained in DMF and EtOH solvents, respectively. It is concluded that adsorption of BPB occurs fast, ensuring complete removal within 30 minutes or less of contact time in batch mode, irrespective of the type of configuration or type of MOFs used.

For ZIF-8 it is observed that the monoliths perform better than the powder, allowing both a longer exposure time to the aqueous environment and a higher concentration of BPB to be used. Furthermore, it is found that whether the material is fully activated or not has little effect on the adsorption of BPB. This points to BPB being adsorbed on the external surface of ZIF-8 rather than in available internal pore sites. This model is especially relevant given the difference in the BET area of the monolithic structures, which showed to play no role in the overall BPB adsorption capacity. Furthermore, it is concluded that the reduced performance of $_{powd}$ZIF-8 might be due to a lower chemical stability, as previously discussed in Chapter 3. In addition to the batch adsorption experiments conducted, this work presents the first report of a pure, unsupported MOF having been successfully employed for a flow-mode, liquid phase adsorption application. In this configuration, monolithic ZIF-8 presented significant advantages over powdered ZIF-8, which would need to be immobilized on a support via costly and time-consuming in situ synthesis coating methods or via pelletisation and compaction – techniques which often result in detrimental performance.

Furthermore, the previously introduced MOF composites consisting of ZIF-8 grown on cordierite ceramic supports were investigated for flow-mode adsorption of BPB. Whereas the BPB binding capacity reached was considerably lower than for that of pure monolithic ZIF-8, the very open frontal area of these structures allowed for a safe, problem-free operation at higher flowrates without indicating any pressure drop, however, this was at the cost of

isufficient contact between the stationary adsorbent and the mobile pollutant-containing solution.

On the other hand, whereas UiO-66 promises an improved adsorption capacity over ZIF-8 due to the larger pore size and increased liquid phase stability in the powdered configuration, it was found that, in fact, the presence of defects is detrimental to BPB capture. This is due to the fact that the synthesis procedure employed HCl modulator, this has induced missing linker structural defects which, in turn, affected the hydrophilicity of the adsorbent. Thus, incomplete removal, even at very high adsorbent dosage, was attained due to competitive adsorption with water. Furthermore, the monolithic UiO-66 structures could not be used for flow-mode adsorption due to their poor water stability, leading to collapse of the monolithic macrostructure when in prolongued contact with water.

Overall, the adsorption mechanism is concluded to rely on π-π stacking interactions between the linkers and the BPB molecule and adsorbents can be subsequently recovered with a wash in EtOH. Whereas it is possible to exploit the large pore size of UiO-66 for BPB adsorption, when in powdered form for batch applications, the inherent hydrophobicity of ZIF-8 leads to a better overall removal efficiency for BPB both in batch and flow-mode conditions; however, in this case the monolithic ZIF-8 configuration is a safer alternative due to negligible linker release to the environment.

Chapter 6

Final Conclusions and Future Work

6.1 Conclusions

The current dissertation focused on evaluating the overall applicability of metal-organic frameworks (MOFs) in liquid phase adsorption applications. The major topics of concern in this work addressed the role of MOF configuration on both overall MOF stability in the aqueous environment as well as for adsorption of a model micro-pollutant, bisphenol B (BPB). Moreover, few of the most widely applicable MOFs were subject to full aqueous phase stability investigations under a range of different parameters. These included powdered and monolithic configurations of Zr based MOFs such as UiO-66 and MOF-808 as well as the Zn-based ZIF-8. Stability of powdered configurations of MOFs synthesised in the UiO topology with tagged and elongated linkers was also briefly investigated. Overall, the main objectives of this work were met and whilst there is still future work to be done in the research community in order to roll-out MOFs for pollutant capture purposes, their potential proves very promising, especially for monolithic MOFs.

In this work, monolithic MOFs refer to a pure phase MOF macrostructure, expressing a high bulk density as well as a volumetric surface area higher than the conventional MOF powders. Monolithic MOFs also possess a substantially higher rigidity and enhanced mechanical properties. The monolithic phase is allowed to form from dense MOF gels prepared in low surface tension solvents during slow drying process at ambient temperature. In this way, surface nucleation of the retained precursors directs an epitaxial growth process

between the existing nanosized primary particles, thus acting as a binder and resulting in a dense MOF phase. Monolithic MOFs offer a substantially improved way of applying MOFs in industrial settings, which otherwise would require compacted or pelletised phases; both methodologies known to be largely detrimental to MOFs.

Structures ZIF-8, UiO-66 and MOF-808 were investigated due to their, previously, well-known resilience in the aqueous environment. Moreover, these provided a working strategy for studying the role of pore size, metal cluster connectivity, linker basicity and metal oxidation state on the overall water stability. Furthermore, we have been able to obtain these same structures in various monolithic forms which offer a great alternative to development of MOF composites for flow-mode applications. Additional structures obtained in the UiO topology with functionalised and elongated linkers also offered a pathway to observe the importance of chemical functionality and metal cluster shielding or exposure towards water stability.

Firstly, for the correct application of MOFs, it is of paramount importance to be able to acknowledge and understand their stability in the intended medium of use. For an aqueous environment, it is concluded that the stability of MOFs is, indeed, highly pH dependent. Even those MOFs which have been long recognised as fully stable under a wide range of pH conditions, this work has proved that this is not the case. For example, this work found that water stability of UiO-66 holds a strong correlation with pH, wherein degradation of this MOF is accelerated with increasing pH. Moreover, at the highest starting pH condition, powdered UiO-66 synthesised using HCl modulator registered a 47% reduction in adsorption capacity and 45% linker dissolution whereas the sample obtained from a modulator-free synthesis registers an unchanged adsorption capacity after treatment. This proves that, as discussed in other important works in the research field, the introduction of modulators during the synthesis step, which is known to induce missing linker defects, not only affects the hydrophilicity of the framework but also leads to decreased stability due to a higher exposure of the metal node to foreign species.

Moreover, structures obtained in the UiO topology, with added functional groups such as amino, bromo or nitro functionalised UiO-66 improves the overall water stability, especially in high pH. This proves that addition of functional groups creates a shielding effect on the metal centre, precluding easy access of attacking species. On the other hand, large

pore structures within the same topology, express drastically reduced water stability with completely collapsed crystallinity and porosity after direct activation from water. Nevertheless, it was subsequently shown that, even if a MOF is constructed with a large linker, such as that encountered in UiO-68, the thermodynamic stability can be improved, with very good porosity retention even after direct activation from water, with the addition of hydrophobic functional groups and, indeed, the number and positioning of these groups play an important role. Such is the case with tetramethyl-UiO-68 (or, PCN-57).

Consequently, the larger pore sized Zr-based MOF studied, MOF-808, is found to be unstable under all pH conditions whilst in powdered form and whereas the actual extent of dissolution could not be quantified due to the very poor linker solubility in water, it is also taken into account that the reason for returning a low crystallinity and porosity after treatment might also be partly due to capillary force effects during direct activation from water. However, a lower stability is expected relative to UiO-66 due to the lower connectivity of the framework as well as a lower linker acid dissociation constant, which leaves the metal site more accessible to attacking species and the metal-linker bond more labile, respectively. On the other hand, shaping this MOF into a monolith dramatically improves its liquid phase stability. Most notably, the lower density monolithic configuration returned crystalline samples with good porosity. Nonetheless, the monolithic macrostructure is not very well maintained neither for MOF-808 nor for UiO-66, returning mostly powdered material accompanied by a noticeable decrease in mesoporosity. At the same time, shaping these structures in the monolithic configuration precludes linkers being released in the testing environment.

On the other hand, it was found out that the hydrophobic ZIF-8, whilst in powdered configuration is highly unstable in acidic conditions experiencing complete dissolution. Moreover, a fair amount of porosity collapse is also demonstrated in neutral conditions, followed by improved stability at high pH. In comparison to UiO-66 and MOF-808 monoliths, monolithic ZIF-8 presents a dramatically improved stability especially under acidic conditions with negligeable linker release and good porosity retention. Most notably, shielding the metal centre via incomplete activation of the structure indeed improves water stability of this framework under a wider range of pH conditions.

This work also explored the possibility of in-situ ZIF-8 synthesis and deposition on a chemically altered high geometrical area honeycomb cordierite substrate, the choice of substrate is influenced by the need to apply these materials in liquid phase applications, especially, where low pressure drops are required in order to ensure good operation. It was found that prior growth of an oxide of the MOF metal, ZnO, on the cordierite substrate, accelerates the formation of ZIF-8, yielding films with good porosity and good surface adhesion. At the same time, surface anchoring of linker-like functionalities results in as much ZIF-8 deposition as the chemically unaltered substrate. It was also observed that choice of synthetic methodology applied also influences the quality of the resultant films, for example, an aqueous synthesis procedure with a high yield is favoured and results in films with very high crystallinity and surface area, of up to 550 $m^2.g^{-1}$. Furthermore, this synthesis and deposition strategy proved highly reproducible upon scale-up.

Finally, the feasibility of using MOFs as adsorbents for BPB pollutant from liquid water was investigated. BPB is a substance of high concern, being a known endocrine disruptor chemical deployed as a substitute for bisphenol A. Endocrine disruptors affect living organisms through hormone-mimicking pathways and therefore are known to interfere with homeostatic, reproductive and other development processes in the body. In this context, ZIF-8 and UiO-66 were studied as well as their 3 different configurations. Both structures showed excellent BPB adsorption capabilities with excellent removal in both batch and flow conditions. Moreover, their performance was found to be comparable to traditional adsorbents and offering very fast uptake within less than 30 minutes of contact. For ZIF-8, even though the stability of the powdered configuration is overall poorer, it yielded complete removal in all batch tests, however, in ZIF-8 the adsorption of BPB is only mediated by the external surface due to very small pore openings which preclude uptake within the internal cavities. More importantly, the monolithic configuration proved to offer a remarkably improved performance over the traditional powder, reaching a higher adsorption capacity as well as improved stability in high analyte concentrations. On the other hand, the performance of UiO-66, being more thermodynamically stable and possessing larger pores, is hampered by the presence of structural defects which cause competitive adsorption with water in the powdered configuration. In comparison to monolithic ZIF-8, monolithic UiO-66 performed

poorer than its powdered counterpart, due to both its decreased stability in the aqueous environment and lower surface area.

Finally, a proof-of-concept monolithic ZIF-8 cartridge was constructed and tested. To the best of my knowledge, this was the first instance in which a pure, unsupported MOF phase was successfully employed for flow-mode liquid phase adsorption applications. The performance of the monolithic cartridge was benchmarked against the ZIF-8@Cordierite composite structure. Whereas the open frontal area cordierite composite offers no pressure drop at high flowrates, the binding capacity was remarkably lower than for the monolithic ZIF-8 cartridge which offers better contact with the liquid phase. Overall, the proposed adsorption mechanism of BPB on UiO-66 and ZIF-8 relies on π-π staking on the respective MOF linkers. Moreover, ZIF-8 also holds the advantage of hydrophobic interactions, which increase its overall removal efficiency.

6.2 Future Work

Whereas the main objectives of this work were met, substantially more effort is required by the research community in order to improve the applicability of MOFs for liquid phase adsorption applications. The following ideas and suggestions for future experiments are outlined in order to gain a better understanding of the water stability of MOFs as well as for their potential future use in water treatment.

6.2.1 Role of solvent exchange prior to activation

The water stability experiments described in Chapter 3 were designed to study the retention of porosity and crystallinity following direct activation from water. One problem with this technique is that, for those MOFs which posses large pores especially, rapid evaporation of water, which has a large surface tension, brings about capillary forces which cause pore collapse. As a result, the recovered structure is therefore non-crystalline and non-porous. Moreover, if the linker has a low solubility in water, it will not be detected during aliquot composition analysis, even in the event of in-situ framework dissociation. Therefore, solvent exchange for a low surface tension solvent, such as ethanol or even acetone, would offer a

way of recovering the tested materials whilst maintaining their porosity and dissolving the dissociated linker.

6.2.2 Crystal defects and their role on water stability

This dissertation presented powdered UiO-66 synthesised using two different techniques; with and without the use of modulators. Based on the nitrogen adsorption isotherms of the respective samples, it was inferred that the samples obtained via modulated synthesis expressed crystalline defects involving missing linkers. The same sample also expressed a lower water stability than the modulator-free framework. At the same time, powdered MOF-808 was obtained using only one synthesis technique involving the use of modulators, whereas its stability is correlated to the significantly lower framework connectivity, the potential presence of defects might have also hampered its stability. It is therefore proposed to conduct a full study on the influence of synthetic technique, and hence crystalline defects, upon the water stability of both UiO-66 and MOF-808.

6.2.3 Computational screening to pin-point water stable MOFs

With the parameters affecting water stability of MOFs in mind, a high throughput computational simulation would greatly speed-up the roll out of water stable MOFs. In addition to numerous literature studies and reviews existent in literature, this dissertation has pointed the following rules of thumb in order for any given MOF to be water stable:

- High metal oxidation state
- High linker pKa (i.e. increased basicity)
- High metal cluster connectivity
- Pore size (large or small)
- Functional groups & metal cluster shielding

With these variables in mind and the voluminous library of MOFs, it would be possible to identify those structures which fit all the parameters, their behaviour in water simulated and, ultimately, compared with experimental data.

6.2.4 Pollutant capture from water samples

An important aspect of water treatment studies is testing the materials with water samples beyond laboratory grade stock solutions. It would be thus beneficial to test the monolithic ZIF-8 adsorbent with samples of greywater or riverwater, which, in reality, contain a 'soup' of chemical micro-pollutants. The interaction and selectivity with other species is an important aspect to consider and study.

References

[1] Max Roser and Esteban Ortiz-Ospina. World population growth. *Our World in Data*, 2019. https://ourworldindata.org/world-population-growth.

[2] Multilateral environmental agreements. http://ec.europa.eu/environment/international_issues/agreements_en.htm. Accessed: 2019-04-09.

[3] H. Furukawa, K. E. Cordova, M. O'Keeffe, and O. M. Yaghi. The chemistry and applications of metal-organic frameworks. *Science*, 341(6149), 2013.

[4] X. Fang, B. Zong, and S. Mao. Metal–organic framework-based sensors for environmental contaminant sensing. *Nano-Micro Letters*, 10(4):64, Jul 2018.

[5] X. Yu, L. Wang, and S.M. Cohen. Photocatalytic metal–organic frameworks for organic transformations. *CrystEngComm*, 19:4126–4136, 2017.

[6] C. J. Doonan and C. J. Sumby. Metal–organic framework catalysis. *CrystEngComm*, 19:4044–4048, 2017.

[7] C. Orellana-Tavra, S. A. Mercado, and D. Fairen-Jimenez. Endocytosis mechanism of nano metal-organic frameworks for drug delivery. *Advanced Healthcare Materials*, 5(17):2261–2270, 2016.

[8] C. Orellana-Tavra, E. F. Baxter, T. Tian, T. D. Bennett, N. K. H. Slater, A. K. Cheetham, and D. Fairen-Jimenez. Amorphous metal–organic frameworks for drug delivery. *Chemical Communications*, 51:13878–13881, 2015.

[9] T. Tian, Z. Zeng, D. Vulpe, M. E. Casco, G. Divitini, P. A. Midgley, J. Silvestre-Albero, J.-C. Tan, P. Z. Moghadam, and D. Fairen-Jimenez. A sol–gel monolithic metal–organic framework with enhanced methane uptake. *Nature Materials*, 17:174–179, 2018.

[10] E. Barea, C. Montoro, and J. A. R. Navarro. Toxic gas removal - metal-organic frameworks for the capture and degradation of toxic gases and vapours. *Chemical Society Reviews*, 43:5419–5430, 2014.

[11] H. Li, K. Wang, Y. Sun, C.T. Lollar, J.L. Li, and H.C. Zhou. Recent advances in gas storage and separation using metal–organic frameworks. *Materials Today*, 21(2):108 – 121, 2018.

[12] P. Falcaro, R. Ricco, C. M. Doherty, and et al. Mof positioning technology and device fabrication. *Chemical Society Reviews*, 43:5513–5560, 2014.

[13] M. Klimakow, P. Klobes, A.F. Thunemann, K. Rademann, and F. Emmerling. Mechanochemical synthesis of metal-organic frameworks: A fast and facile approach toward quantitative yields and high specific surface areas. *Chemistry of Materials*, 22(18):5216–5221, 2010.

[14] K. Uzarevic, T. C. Wang, and S.-Y.and et al. Moon. Mechanochemical and solvent-free assembly of zirconium-based metal-organic frameworks. *Chemical Communications*, 52:2133–2136, 2016.

[15] N. Stock and S. Biswas. Synthesis of metal-organic frameworks (MOFs): Routes to various mof topologies, morphologies, and composites. *Chemical Reviews*, 112(2):933–969, 2012.

[16] Y.Sun and H.-C. Zhou. Recent progress in the synthesis of metal–organic frameworks. *Sci. Tech. Adv. Mat.*, 16(5):054202, 2015.

[17] A. Bhatnagar and I. Anastopoulos. Adsorptive removal of bisphenol a (bpa) from aqueous solution: A review. *Chemosphere*, 168:885 – 902, 2017.

[18] Z. Hasan and S. H. Jhung. Removal of hazardous organics from water using metal-organic frameworks (mofs): Plausible mechanisms for selective adsorptions. *Journal of Hazardous Materials*, 283:329 – 339, 2015.

[19] K. A. Cychosz, R. Ahmad, and A. J. Matzger. Liquid phase separations by crystalline microporous coordination polymers. *Chem. Sci.*, 1:293–302, 2010.

[20] K. A. Cychosz and A. J. Matzger. Water stability of microporous coordination polymers and the adsorption of pharmaceuticals from water. *Langmuir*, 26(22):17198–17202, 2010. PMID: 20923216.

[21] H. Jasuja, N. C. Burtch, Y. Huang, Y. Cai, and K. S. Walton. Kinetic water stability of an isostructural family of zinc-based pillared metal–organic frameworks. *Langmuir*, 29(2):633–642, 2013. PMID: 23214448.

[22] E. M. Dias and C. Petit. Towards the use of metal–organic frameworks for water reuse: a review of the recent advances in the field of organic pollutants removal and degradation and the next steps in the field. *Journal of Materials Chemistry A*, 3:22484–22506, 2015.

[23] M. N. Chong, B. Jin, C. W.K. Chow, and C. Saint. Recent developments in photocatalytic water treatment technology: A review. *Water Research*, 44(10):2997 – 3027, 2010.

[24] Z. Hasan, J. Jeon, and S.H. Jhung. Adsorptive removal of naproxen and clofibric acid from water using metal-organic frameworks. *Journal of Hazardous Materials*, 209-210:151 – 157, 2012.

[25] A. J. Howarth, Y. Liu, J. T. Hupp, and O. K. Farha. Metal–organic frameworks for applications in remediation of oxyanion/cation-contaminated water. *CrystEngComm*, 17:7245–7253, 2015.

[26] Y. Bian, N. Xiong, and G. Zhu. Technology for the remediation of water pollution: A review on the fabrication of metal organic frameworks. *Processes*, 6:122, 08 2018.

[27] X.P. Luo, S.Y. Fu, Y.M. Du, J.Z. Guo, and B. Li. Adsorption of methylene blue and malachite green from aqueous solution by sulfonic acid group modified MIL-101. *Microporous and Mesoporous Materials*, 237:268 – 274, 2017.

[28] E. Haque, J. E. Lee, I. T. Jang, Y. K. Hwang, J.-S. Chang, J. Jegal, and S. H. Jhung. Adsorptive removal of methyl orange from aqueous solution with metal-organic frameworks, porous chromium-benzenedicarboxylates. *Journal of Hazardous Materials*, 181(1):535 – 542, 2010.

[29] Y. Zhang C. Kang S. Chen L. Song D. Liu Y. Peng, H.Huang and C. Zhong. A versatile MOF-based trap for heavy metal ion capture and dispersion. *Nature Communications*, 9(187), 2018.

[30] R. J. Drout, A.J. Howarth, K. Otake, Ti. Islamoglu, and O.K. Farha. Efficient extraction of inorganic selenium from water by a Zr metal–organic framework: investigation of volumetric uptake capacity and binding motifs. *CrystEngComm*, 20:6140–6145, 2018.

[31] Y.S. Seo, N.A. Khan, and S.H. Jhung. Adsorptive removal of methylchlorophenoxypropionic acid from water with a metal-organic framework. *Chemical Engineering Journal*, 270:22 – 27, 2015.

[32] J.-Q. Jiang, C.-X. Yang, and X.-P. Yan. Zeolitic imidazolate framework-8 for fast adsorption and removal of benzotriazoles from aqueous solution. *ACS Applied Materials & Interfaces*, 5(19):9837–9842, 2013. PMID: 24033311.

[33] D. Ma, Y. Li, and Z. Li. Tuning the moisture stability of metal–organic frameworks by incorporating hydrophobic functional groups at different positions of ligands. *Chemical Communications*, 47:7377–7379, 2011.

[34] A.C. Kizzie, A. G. Wong-Foy, and A. J. Matzger. Effect of humidity on the performance of microporous coordination polymers as adsorbents for CO2 capture. *Langmuir*, 27(10):6368–6373, 2011.

[35] P. Z. Moghadam, D. Fairen-Jimenez, and R. Q. Snurr. Efficient identification of hydrophobic MOFs: application in the capture of toxic industrial chemicals. *Journal of Materials Chemistry A*, 4:529–536, 2016.

[36] P. Deria, J. E. Mondloch, E. Tylianakis, P. Ghosh, W. Bury, R. Q. Snurr, J. T. Hupp, and O. K. Farha. Perfluoroalkane functionalization of NU-1000 via solvent-assisted ligand incorporation: Synthesis and CO2 adsorption studies. *Journal of the American Chemical Society*, 135(45):16801–16804, 2013.

[37] C. Serre. Superhydrophobicity in highly fluorinated porous metal–organic frameworks. *Angewandte Chemie International Edition*, 51(25):6048–6050, 2012.

[38] J. Canivet, A. Fateeva, Y. Guo, B. Coasne, and D. Farrusseng. Water adsorption in MOFs: Fundamentals and applications. *Chemical Society Reviews*, 43(16):5594–5617, 2014.

[39] A. J. Howarth, Y. Liu, P. Li, Z. Li, T. C. Wang, J. T. Hupp, and O. K. Farha. Chemical, thermal and mechanical stabilities of metal-organic frameworks. *Nature Reviews Materials*, 1, 2 2016.

[40] J. G. Nguyen and S. M. Cohen. Moisture-resistant and superhydrophobic metal-organic frameworks obtained via postsynthetic modification. *Journal of the American Chemical Society*, 132(13):4560–4561, 2010.

[41] J. B. Decoste, G. W. Peterson, M. W. Smith, C. A. Stone, and C. R. Willis. Enhanced stability of Cu-BTC mof via perfluorohexane plasma-enhanced chemical vapor deposition. *Journal of the American Chemical Society*, 134(3):1486–1489, 2012.

[42] H. Jasuja, N. C. Burtch, Y.-G. Huang, Y. Cai, and K. S. Walton. Kinetic water stability of an isostructural family of zinc-based pillared metal–organic frameworks. *Langmuir*, 29(2):633–642, 2013.

[43] K.-Y. A. Lin and H.-A. Chang. Efficient adsorptive removal of humic acid from water using zeolitic imidazole framework-8 (ZIF-8). *Water, Air, & Soil Pollution*, 226(2):10, Feb 2015.

[44] H. Zhang, D. Liu, Y.Yao, B. Zhang, and Y.S. Lin. Stability of ZIF-8 membranes and crystalline powders in water at room temperature. *Journal of Membrane Science*, 485:103 – 111, 2015.

[45] N. C. Burtch, H. Jasuja, and K. S. Walton. Water stability and adsorption in metal–organic frameworks. *Chemical Reviews*, 114(20):10575–10612, 2014.

[46] J. J. Low, A. I. Benin, P. Jakubczak, J. F. Abrahamian, S. A. Faheem, and R. R. Willis. Virtual high throughput screening confirmed experimentally: Porous coordination polymer hydration. *Journal of the American Chemical Society*, 131(43):15834–15842, 2009.

[47] V. Colombo, S. Galli, H. J. Choi, G. D. Han, A. Maspero, G. Palmisano, N. Masciocchi, and J. R. Long. High thermal and chemical stability in pyrazolate-bridged metal–organic frameworks with exposed metal sites. *Chem. Sci.*, 2:1311–1319, 2011.

[48] M. Bosch, M. Zhang, and H.-C. Zhou. Increasing the stability of metal-organic frameworks. *Advances in Chemistry*, 8:182327, 2014.

[49] W.-G. Liu and D. G. Truhlar. Computational linker design for highly crystalline metal–organic framework NU-1000. *Chemistry of Materials*, 29(19):8073–8081, 2017.

[50] L. Pan, B. Parker, X. Huang, D. H. Olson, and J. Li. Zn(tbip) h2tbip 5-tert-butyl isophthalic acid a highly stable guest-free microporous metal organic framework with unique gas separation capability. *Journal of the American Chemical Society*, 128(13):4180–4181, 2006.

[51] T. Wu, L. Shen, Ma. Luebbers, C. Hu, Qi. Chen, Z. Ni, and R. I. Masel. Enhancing the stability of metal–organic frameworks in humid air by incorporating water repellent functional groups. *Chemical Communications*, 46:6120–6122, 2010.

[52] Q. Yang, A. D. Wiersum, P. L. Llewellyn, V. Guillerm, C. Serre, and G. Maurin. Functionalizing porous zirconium terephthalate UiO-66(Zr) for natural gas upgrading: a computational exploration. *Chemical Communications*, 47:9603–9605, 2011.

[53] J. Bae, J.-W. Jung, H. Y. Park, C.-H. Cho, and J. Park. Oxygen plasma treatment of HKUST-1 for porosity retention upon exposure to moisture. *Chemical Communications*, 53:12100–12103, 2017.

[54] J. B. DeCoste, J. A. Rossin, and G. W. Peterson. Hierarchical pore development by plasma etching of Zr-based metal–organic frameworks. *Chemistry – A European Journal*, 21(50):18029–18032, 2015.

[55] H. Jasuja and K. S. Walton. Effect of catenation and basicity of pillared ligands on the water stability of MOFs. *Dalton Transactions*, 42:15421–15426, 2013.

[56] D. Sun, L. Ye, F. Sun, H. García, and Z. Li. From mixed-metal MOFs to carbon-coated core–shell metal alloy@metal oxide solid solutions: Transformation of Co/Ni-MOF-74 to CoxNi1–x@CoyNi1–yO@C for the oxygen evolution reaction. *Inorganic Chemistry*, 56(9):5203–5209, 2017.

[57] M.I. Nandasiri, S. R. Jambovane, B. P. McGrail, H. T. Schaef, and S. K. Nune. Review. *Coordination Chemistry Reviews*, 311(C):38–52, 2016.

[58] D. Bazer-Bachi, L. Assié, V. Lecocq, B. Harbuzaru, and V. Falk. Towards industrial use of metal-organic framework: Impact of shaping on the mof properties. *Powder Technology*, 255:52 – 59, 2014. Innovative processes and materials.

[59] G. W. Peterson, J.B. DeCoste, F. Fatollahi-Fard, and D. K. Britt. Engineering UiO-66-NH2 for toxic gas removal. *Industrial & Engineering Chemistry Research*, 53(2):701–707, 2014.

[60] G.W. Peterson, J.B. DeCoste, T.G. Glover, Y. Huang, H. Jasuja, and K.S. Walton. Effects of pelletization pressure on the physical and chemical properties of the metal–organic frameworks Cu3(BTC)2 and UiO-66. *Microporous and Mesoporous Materials*, 179:48 – 53, 2013.

[61] D. Bradshaw, A. Garai, and J. Huo. Metal-organic framework growth at functional interfaces: thin films and composites for diverse applications. *Chemical Society Reviews*, 41:2344–2381, 2012.

[62] A. Betard and R.A. Fischer. Metal–organic framework thin films: From fundamentals to applications. *Chemical Reviews*, 112(2):1055–1083, 2012.

[63] O. Shekhah, J. Liu, R. A. Fischer, and C. Woll. MOF thin films: existing and future applications. *Chemical Society Reviews*, 40:1081–1106, 2011.

[64] A. S. Munch, J. Seidel, A. Obst, E. Weber, and F.O. Mertens. High-separation performance of chromatographic capillaries coated with MOF-5 by the controlled SBU approach. *Chem.– A Eur. J.*, 17(39):10958–10964, 2011.

[65] R. Ameloot, A. Liekens, L. Alaerts, M. Maes, A. Galarneau, B. Coq, G. Desmert, B.F. Sels, J.F.M. Denayer, and D.E. De Vos. Silica–MOF composites as a stationary phase in liquid chromatography. *Eur. J. Inorg. Chem.*, 2010(24):3735–3738, 2010.

[66] N. Chang, Z.Y. Gu, and X.P. Yan. Zeolitic imidazolate framework-8 nanocrystal coated capillary for molecular sieving of branched alkanes from linear alkanes along with high-resolution chromatographic separation of linear alkanes. *Journal of the American Chemical Society*, 132(39):13645–13647, 2010.

[67] S. Han, Y. Wei, C. Valente, I. Lagzi, J.J. Gassensmith, A. Coskun, J.F. Stoddard, and B.A. Grzybowski. Chromatography in a single metal-organic framework (MOF) crystal. *Journal of the American Chemical Society*, 132(46):16358–16361, 2010.

[68] Q. Zhu, Q.-L.and Xu. Metal-organic framework composites. *Chemical Society Reviews*, 43:5468–5512, 2014.

[69] D. Zacher, R. Schmid, C. Woll, and et al. Surface chemistry of metal–organic frameworks at the liquid–solid interface. *Angewandte Chemie International Edition*, 50(1):176–199, 2011.

[70] H.T. Kwon, H.K. Jeong, A.S. Lee, and et al. Heteroepitaxially grown zeolitic imidazolate framework membranes with unprecedented propylene/propane separation performances. *Journal of the American Chemical Society*, 137(38):12304–12311, 2015.

[71] T. Granato, F. Testa, and R. Olivo. Catalytic activity of HKUST-1 coated on ceramic foam. *Microporous and Mesoporous Materials*, 153:236 – 246, 2012.

[72] C. Le Calvez, M. Zouboulaki, C. Petit, L. Peeva, and N. Shirshova. One step synthesis of MOF-polymer composites. *RSC Advances*, 6:17314–17317, 2016.

[73] S. Li, W. Zhang, and F. Huo. The structural and catalytic properties of nanoparticles@MOF composites: A case study of Au@ZIF-8 hybrid crystals. *Phys. E: Low-dimensional Systems and Nanostructures*, 69:56 – 60, 2015.

[74] J.T. Yoo, S.H. Lee, C. K. Lee, C.R. Kim, T. Fujigaya, H.J. Park, N. Nakashima, and J.K. Shim. Homogeneous decoration of zeolitic imidazolate framework-8 (ZIF-8) with core-shell structures on carbon nanotubes. *RSC Advances*, 4:49614–49619, 2014.

[75] H. Al-Kutubi, A. Dikhtiarenko, H. R. Zafarani, E. J. R. Sudholter, J. Gascon, and L. Rassaei. Facile formation of ZIF-8 thin films on ZnO nanorods. *Crystal Engineering Communications*, 17:5360–5364, 2015.

[76] H. Bux, A. Feldhoff, J. Cravillon, M. Wiebcke, and J. Caro. Oriented zeolitic imidazolate framework-8 membrane with sharp H_2/C_3H_8 molecular sieve separation. *Chemistry of Materials*, 23(8):2262–2269, 2011.

[77] L. E. Kreno, K.Leong, O. K. Farha, M. Allendorf, R. P. Van Duyne, and J. T. Hupp. Metal–organic framework materials as chemical sensors. *Chemical Reviews*, 112(2):1105–1125, 2012.

[78] S. Aguado, J. Canivet, and D. Farrusseng. Facile shaping of an imidazolate-based MOF on ceramic beads for adsorption and catalytic applications. *Chemical Communications*, 46:7999–8001, 2010.

[79] M. Sindoro, A.-Y. Jee, and S. Granick. Shape-selected colloidal MOF crystals for aqueous use. *Chemical Communications*, 49:9576–9578, 2013.

[80] M. Pang, A. J. Cairns, Y. Liu, Y. Belmabkhout, H. C. Zeng, and M. Eddaoudi. Synthesis and integration of Fe-soc-MOF cubes into colloidosomes via a single-step emulsion-based approach. *Journal of the American Chemical Society*, 135(28):10234–10237, 2013.

[81] T. Tian, J. Velazquez-Garcia, T. D. Bennett, and D. Fairen-Jimenez. Mechanically and chemically robust zif-8 monoliths with high volumetric adsorption capacity. *Journal of Materials Chemistry A*, 3:2999–3005, 2015.

[82] B. M. Connolly, M. Aragones-Anglada, J. Gandara-Loe, N. A. Danaf, D. C. Lamb, J. P. Mehta, D. Vulpe, S. Wuttke, J. Silvestre-Albero, P. Z. Moghadam, A. E. H. Wheatley, and D. Fairen-Jimenez. Tuning porosity in macroscopic monolithic metal-organic frameworks for exceptional natural gas storage. *Nature Communications*, 10:2345, 2019.

[83] J. H. Cavka, S. Jakobsen, U. Olsbye, N. Guillou, C. Lamberti, S. Bordiga, and K. P. Lillerud. A new zirconium inorganic building brick forming metal organic frameworks

with exceptional stability. *Journal of the American Chemical Society*, 130(42):13850–13851, 2008.

[84] L. Valenzano, B. Civalleri, S. Chavan, S. Bordiga, M. H. Nilsen, S. Jakobsen, K. P. Lillerud, and C. Lamberti. Disclosing the complex structure of UiO-66 metal organic framework: A synergic combination of experiment and theory. *Chemistry of Materials*, 23(7):1700–1718, 2011.

[85] L. J. Murray, M. Dincă, and J. R. Long. Hydrogen storage in metal–organic frameworks. *Chemical Society Reviews*, 38:1294–1314, 2009.

[86] H. Wu, Y. S. Chua, V. Krungleviciute, M. Tyagi, P. Chen, T. Yildirim, and W. Zhou. Unusual and highly tunable missing-linker defects in zirconium metal–organic framework UiO-66 and their important effects on gas adsorption. *Journal of the American Chemical Society*, 135(28):10525–10532, 2013.

[87] C.G. Piscopo, A. Polyzoidis, M. Schwarzer, and S. Loebbecke. Stability of UiO-66 under acidic treatment: Opportunities and limitations for post-synthetic modifications. *Microporous and Mesoporous Materials*, 208:30 – 35, 2015.

[88] H. Wu, T. Yildirim, and W. Zhou. Exceptional mechanical stability of highly porous zirconium metal–organic framework UiO-66 and its important implications. *The Journal of Physical Chemistry Letters*, 4(6):925–930, 2013.

[89] C. Gomes-Silva, I. Luz, F. X. Llabrés-i-Xamena, A. Corma, and H. García. Water stable Zr–benzenedicarboxylate metal–organic frameworks as photocatalysts for hydrogen generation. *Chemistry – A European Journal*, 16(36):11133–11138, 2010.

[90] M. Kandiah, M. H. Nilsen, S. Usseglio, S. Jakobsen, U. Olsbye, M. Tilset, C. Larabi, E. A. Quadrelli, F. Bonino, and K. P. Lillerud. Synthesis and stability of tagged UiO-66 Zr-MOFs. *Chemistry of Materials*, 22(24):6632–6640, 2010.

[91] Y. Tan, W. Zhang, Y. Gao, J. Wu, and B. Tang. Facile synthesis and supercapacitive properties of zr-metal organic frameworks (UiO-66). *RSC Advances*, 5:17601–17605, 2015.

[92] Y.-P. Yuan, L.-S. Yin, S.-W. Cao, G.-S. Xu, C.-H. Li, and C. Xue. Improving photocatalytic hydrogen production of metal–organic framework UiO-66 octahedrons by dye-sensitization. *Applied Catalysis B: Environmental*, 168-169:572 – 576, 2015.

[93] M. Vandichel, J. Hajek, F. Vermoortele, M. Waroquier, D. E. De Vos, and V. Van Speybroeck. Active site engineering in UiO-66 type metal–organic frameworks by intentional creation of defects: a theoretical rationalization. *CrystEngComm*, 17:395–406, 2015.

[94] F. Zhang, S. Zheng, Q. Xiao, Y. Zhong, W. Zhu, A. Lin, and M. Samy El-Shall. Synergetic catalysis of palladium nanoparticles encaged within amine-functionalized

UiO-66 in the hydrodeoxygenation of vanillin in water. *Green Chem.*, 18:2900–2908, 2016.

[95] F. Vermoortele, M. Vandichel, B. Van-de-Voorde, R. Ameloot, M. Waroquier, V. Van-Speybroeck, and D.E. De-Vos. Electronic effects of linker substitution on lewis acid catalysis with metal–organic frameworks. *Angewandte Chemie International Edition*, 51(20):4887–4890, 2012.

[96] F. Vermoortele, B. Bueken, G. Le Bars, B. Van de Voorde, M. Vandichel, K. Houthoofd, A. Vimont, M. Daturi, M. Waroquier, V. Van Speybroeck, C. Kirschhock, and D. E. De Vos. Synthesis modulation as a tool to increase the catalytic activity of metal–organic frameworks: The unique case of UiO-66(Zr). *Journal of the American Chemical Society*, 135(31):11465–11468, 2013.

[97] D. Cunha, M. Ben Yahia, S. Hall, S. R. Miller, H. Chevreau, E. Elkaïm, G. Maurin, P. Horcajada, and C. Serre. Rationale of drug encapsulation and release from biocompatible porous metal–organic frameworks. *Chemistry of Materials*, 25(14):2767–2776, 2013.

[98] I. Abánades Lázaro, S. Haddad, S. Sacca, C. Orellana-Tavra, D. Fairen-Jimenez, and R. S. Forgan. Selective surface PEGylation of UiO-66 nanoparticles for enhanced stability, cell uptake, and pH-responsive drug delivery. *Chem*, 2(4):561 – 578, 2017.

[99] S. Tai, W. Zhang, J. Zhang, G. Luo, Y. Jia, M. Deng, and Y. Ling. Facile preparation of UiO-66 nanoparticles with tunable sizes in a continuous flow microreactor and its application in drug delivery. *Microporous and Mesoporous Materials*, 220:148 – 154, 2016.

[100] K. Blindheim Lausund and O. Nilsen. All-gas-phase synthesis of UiO-66 through modulated atomic layer deposition. *Nature Communications*, 7(13578), 2016.

[101] G. Nickerl, I. Senkovska, and S. Kaskel. Tetrazine functionalized zirconium MOF as an optical sensor for oxidizing gases. *Chemical Communications*, 51:2280–2282, 2015.

[102] I. Stassen, B. Bueken, H. Reinsch, J. F. M. Oudenhoven, D. Wouters, J. Hajek, V. Van Speybroeck, N. Stock, P. M. Vereecken, R. Van Schaijk, D. De Vos, and R. Ameloot. Towards metal–organic framework based field effect chemical sensors: UiO-66-NH_2 for nerve agent detection. *Chem. Sci.*, 7:5827–5832, 2016.

[103] I. Stassen, M. Styles, T. Van Assche, N. Campagnol, J. Fransaer, J. Denayer, J.-C. Tan, P. Falcaro, D. De Vos, and R. Ameloot. Electrochemical film deposition of the zirconium metal–organic framework UiO-66 and application in a miniaturized sorbent trap. *Chemistry of Materials*, 27(5):1801–1807, 2015.

[104] F.-Y. Yi, D. Chen, M.-K. Wu, L. Han, and H.-L. Jiang. Chemical sensors based on metal–organic frameworks. *ChemPlusChem*, 81(8):675–690, 2016.

[105] F.-S. Ke, Y.-S. Wu, and H. Deng. Metal-organic frameworks for lithium ion batteries and supercapacitors. *Journal of Solid State Chemistry*, 223:109 – 121, 2015.

[106] R. Ameloot, M. Aubrey, B. M. Wiers, A. P. Gómora-Figueroa, S. N. Patel, N. P. Balsara, and J. R. Long. Ionic conductivity in the metal–organic framework UiO-66 by dehydration and insertion of lithium tert-butoxide. *Chemistry – A European Journal*, 19(18):5533–5536, 2013.

[107] J. B. DeCoste, G. W. Peterson, B. J. Schindler, K. L. Killops, M. A. Browe, and J. J. Mahle. The effect of water adsorption on the structure of the carboxylate containing metal–organic frameworks Cu-BTC, Mg-MOF-74, and UiO-66. *Journal of Materials Chemistry A*, 1:11922–11932, 2013.

[108] P. Ghosh, Y.l J. Colón, and R. Q. Snurr. Water adsorption in uio-66: the importance of defects. *Chemical Communications*, 50:11329–11331, 2014.

[109] F. Jeremias, V. Lozan, S. K. Henninger, and C. Janiak. Programming mofs for water sorption: amino-functionalized MIL-125 and UiO-66 for heat transformation and heat storage applications. *Dalton Transactions*, 42:15967–15973, 2013.

[110] X. Liu, N. K. Demir, Z. Wu, and K. Li. Highly water-stable zirconium metal–organic framework UiO-66 membranes supported on alumina hollow fibers for desalination. *Journal of the American Chemical Society*, 137(22):6999–7002, 2015.

[111] K.-Y. A. Lin, Y.-T. Liu, and S.-Y. Chen. Adsorption of fluoride to UiO-66-NH_2 in water: Stability, kinetic, isotherm and thermodynamic studies. *Journal of Colloid and Interface Science*, 461:79 – 87, 2016.

[112] Y. Li, Y. Liu, W. Gao, L. Zhang, W. Liu, J. Lu, Z. Wang, and Y.-J. Deng. Microwave-assisted synthesis of UiO-66 and its adsorption performance towards dyes. *CrystEngComm*, 16:7037–7042, 2014.

[113] C. Wang, X. Liu, J. P. Chen, and K. Li. Superior removal of arsenic from water with zirconium metal-organic framework UiO-66. *Scientific Reports*, 5, 2015.

[114] A. Schaate, P. Roy, A. Godt, J. Lippke, F. Waltz, M. Wiebcke, and P. Behrens. Modulated synthesis of Zr-based metal–organic frameworks: From nano to single crystals. *Chemistry – A European Journal*, 17(24):6643–6651, 2011.

[115] S. Diring, S. Furukawa, Y. Takashima, T. Tsuruoka, and S. Kitagawa. Controlled multiscale synthesis of porous coordination polymer in nano/micro regimes. *Chemistry of Materials*, 22(16):4531–4538, 2010.

[116] T. Tsuruoka, S. Furukawa, Y. Takashima, K. Yoshida, S. Isoda, and S. Kitagawa. Nanoporous nanorods fabricated by coordination modulation and oriented attachment growth. *Angewandte Chemie*, 121(26):4833–4837, 2009.

[117] M. J. Cliffe, Wei Wan, X. Zou, P. A. Chater, A. K. Kleppe, M. G. Tucker, H. Wilhelm, N. P. Funnell, F.-X. Coudert, and A. L .Goodwin. Correlated defect nanoregions in a metal–organic framework. *Nature Communications*, 5, 2014.

[118] G. C. Shearer, S. Chavan, S. Bordiga, S. Svelle, U. Olsbye, and K. P. Lillerud. Defect engineering: Tuning the porosity and composition of the metal–organic framework UiO-66 via modulated synthesis. *Chemistry of Materials*, 28(11):3749–3761, 2016.

[119] T. D. Bennett, A. K. Cheetham, A. H. Fuchs, and F.-X. Coudert. Interplay between defects, disorder and flexibility in metal-organic frameworks. *Nature Chemistry*, 9:11–16, 2017.

[120] H. Furukawa, F. Gándara, Y.-B. Zhang, J. Jiang, W. L. Queen, M. R. Hudson, and O. M. Yaghi. Water adsorption in porous metal–organic frameworks and related materials. *Journal of the American Chemical Society*, 136(11):4369–4381, 2014.

[121] Z.-Q. Li, J.-C. Yang, K.-W. Sui, and N. Yin. Facile synthesis of metal-organic framework MOF-808 for arsenic removal. *Materials Letters*, 160:412 – 414, 2015.

[122] H. Reinsch, S. Waitschat, S. M. Chavan, K. P. Lillerud, and N. Stock. A facile "green" route for scalable batch production and continuous synthesis of zirconium MOFs. *European Journal of Inorganic Chemistry*, 2016(27):4490–4498, 9 2016.

[123] E. Plessers, G. Fu, C. Tan, X. Yong, D.E. De Vos, and M. B. J. Roeffaers. Zr-based MOF-808 as meerwein–ponndorf–verley reduction catalyst for challenging carbonyl compounds. *Catalysts*, 6(7), 2016.

[124] J. Jiang, F. Gándara, Y.-B. Zhang, K. Na, O. M. Yaghi, and W. G. Klemperer. Superacidity in sulfated metal–organic framework-808. *Journal of the American Chemical Society*, 136(37):12844–12847, 2014.

[125] H. G. T. Ly, G. Fu, A. Kondinski, B. Bueken, D. De Vos, and T. N. Parac-Vogt. Superactivity of MOF-808 toward peptide bond hydrolysis. *Journal of the American Chemical Society*, 140(20):6325–6335, 2018.

[126] Y. H. Vo, T. V. Le, H. D. Nguyen, T. A. To, H. Q. Ha, A. T. Nguyen, A. N.Q. Phan, and N. T.S. Phan. Synthesis of quinazolinones and benzazoles utilizing recyclable sulfated metal-organic framework-808 catalyst in glycerol as green solvent. *Journal of Industrial and Engineering Chemistry*, 64:107 – 115, 2018.

[127] H.-Q. Zheng, C.-Y. Liu, X.-Y. Zeng, J. Chen, J. Lü, R.-G. Lin, R. Cao, Z.-J. Lin, and J.-W. Su. MOF-808: A metal–organic framework with intrinsic peroxidase-like catalytic activity at neutral pH for colorimetric biosensing. *Inorganic Chemistry*, 57(15):9096–9104, 2018.

[128] H.-H. Mautschke, F. Drache, I. Senkovska, S. Kaskel, and F. X. Llabrés i Xamena. Catalytic properties of pristine and defect-engineered Zr-MOF-808 metal organic frameworks. *Catalysis Science & Technology*, 8:3610–3616, 2018.

[129] H. Liu, Z. Zhang, J. Tang, Z. Fei, Q. Liu, X. Chen, M. Cui, and X. Qiao. Quest for pore size effect on the catalytic property of defect-engineered MOF-808-SO_4 in the addition reaction of isobutylene with ethylene glycol. *Journal of Solid State Chemistry*, 269:9 – 15, 2019.

[130] C. Ardila-Suárez, S. Perez-Beltran, G. E. Ramírez-Caballero, and Perla B. Balbuena. Enhanced acidity of defective MOF-808: effects of the activation process and missing linker defects. *Catalysis Science & Technology*, 8:847–857, 2018.

[131] K. S. Park, Z. Ni, A. P. Côté, J. Y.g Choi, R. Huang, F. J. Uribe-Romo, H. K. Chae, M. O'Keeffe, and O. M. Yaghi. Exceptional chemical and thermal stability of zeolitic imidazolate frameworks. *Proceedings of National Academy of Sciences*, 103(27):10186–10191, 2006.

[132] S. J Rettig, A. Storr, D. A Summers, R. C Thompson, and J. Trotter. Iron(ii) 2-methylimidazolate and copper(ii) 1,2,4-triazolate complexes: systems exhibiting long-range ferromagnetic ordering at low temperatures. *Canadian Journal of Chemistry*, 77(4):425–433, 1999.

[133] Y.-Q. Tian, C.-X. Cai, Y. Ji, X. Z. You, S.-M. Peng, and G.-H. Lee. [Co5(im)10]: A metal-organic open-framework with zeolite-like topology. *Angewandte Chemie International Edition*, 41(8):1384–1386, 2002.

[134] X. Huang, J. Zhang, and X. Chen. $[Zn(bim)_2]x(h_2o)_{1.67}$: A metal-organic open-framework with sodalite topology. *Chinese Science Bulletin*, 48(15):1531–1534, Aug 2003.

[135] A. Phan, C. J. Doonan, F. J. Uribe-Romo, C.B. Knobler, M. O'Keeffe, and O. Omar Yaghi. Synthesis, structure, and carbon dioxide capture properties of zeolitic imidazolate frameworks. *Accts. Chem. Res.*, 43(1):58–67, 2010.

[136] P. Z. Moghadam, D. Fairen-Jimenez, and R. Q. Snurr. Efficient identification of hydrophobic MOFs: application in the capture of toxic industrial chemicals. *Journal of Materials Chemistry A*, 4:529–536, 2016.

[137] B. Chen, Z. Yang, Y. Zhu, and Y. Xia. Zeolitic imidazolate framework materials: recent progress in synthesis and applications. *Journal of Materials Chemistry A*, 2:16811–16831, 2014.

[138] L. Bouessel du Bourg, A. U. Ortiz, A. Boutin, and F.-X. Coudert. Thermal and mechanical stability of zeolitic imidazolate frameworks polymorphs. *APL Materials*, 2(12), 2014.

[139] T. Tian, M. T. Wharmby, J. B. Parra, C. O. Ania, and D. Fairen-Jimenez. Role of crystal size on swing-effect and adsorption induced structure transition of ZIF-8. *Dalton Transactions*, 45:6893–6900, 2016.

[140] D. Fairen-Jimenez, S. A. Moggach, M. T. Wharmby, P. A. Wright, S. Parsons, and T. Düren. Opening the gate: Framework flexibility in ZIF-8 explored by experiments and simulations. *Journal of the American Chemical Society*, 133(23):8900–8902, 2011. PMID: 21553843.

[141] W. Depmeier. The sodalite family: A simple but versatile framework structure. *Rev. Min. Geochem.*, 57(1):203–240, 2005.

[142] T. Friscic, I. Halasz, P. J. Beldon, A.M. Belenguer, F. Adams, S.A.J. Kimber, V. Honkimäki, and R.E. Dinnebier. Real-time and in situ monitoring of mechanochemical milling reactions. *Nature Chemistry*, 5(1):66–73, 2013.

[143] Y.-R. Lee, M.-S. Jang, H.-Y. Cho, H.-J. Kwon, S. Kim, and W.-S. Ahn. ZIF-8: A comparison of synthesis methods. *Chemical Engineering Journal*, 271:276 – 280, 2015.

[144] H.-Y. Cho, J. Kim, S.-N. Kim, and W.-S. Ahn. High yield 1-L scale synthesis of ZIF-8 via a sonochemical route. *Microporous and Mesoporous Materials*, 169:180 – 184, 2013.

[145] P. J. Beldon, L. Fábián, R. S. Stein, A. Thirumurugan, A. K. Cheetham, and T. Friščić. Rapid room-temperature synthesis of zeolitic imidazolate frameworks by using mechanochemistry. *Angewandte Chemie International Edition*, 49(50):9640–9643.

[146] Q. Shi, Z. Chen, Z. Song, J. Li, and J. Dong. Synthesis of ZIF-8 and ZIF-67 by steam-assisted conversion and an investigation of their tribological behaviors. *Angewandte Chemie International Edition*, 50(3):672–675, 2011.

[147] I. Stassen, M. Styles, G. Grenci, H. Van Gorp, W. Vanderlinden, S. De Feyter, P. Falcaro, D. De Vos, P. Vereecken, and R. Ameloot. Chemical vapour deposition of zeolitic imidazolate framework thin films. *Nature Materials*, 15:304–310, 2016.

[148] Y. Pan, Y. Liu, G. Zeng, L. Zhao, and Z. Lai. Rapid synthesis of zeolitic imidazolate framework-8 (ZIF-8) nanocrystals in an aqueous system. *Chemical Communications*, 47:2071–2073, 2011.

[149] K. Kida, K. Fujita, T. Shimada, S. Tanaka, and Y. Miyake. Layer-by-layer aqueous rapid synthesis of ZIF-8 films on a reactive surface. *Dalton Transactions*, 42:11128–11135, 2013.

[150] M. Jian, B. Liu, R. Liu, J. Qu, H. Wang, and X. Zhang. Water-based synthesis of zeolitic imidazolate framework-8 with high morphology level at room temperature. *RSC Advances*, 5:48433–48441, 2015.

[151] L. H. Wee, N. Janssens, S. P. Sree, C. Wiktor, E. Gobechiya, R. A. Fischer, C. E. A. Kirschhock, and J. A. Martens. Local transformation of ZIF-8 powders and coatings into ZnO nanorods for photocatalytic application. *Nanoscale*, 6:2056–2060, 2014.

[152] H.-P. Jing, C.-C. Wang, Y.-W. Zhang, P. Wang, and R. Li. Photocatalytic degradation of methylene blue in ZIF-8. *RSC Advances*, 4:54454–54462, 2014.

[153] D. Ragab, H.G. Gomaa, R. Sabouni, M. Salem, M. Ren, and J. Zhu. Micropollutants removal from water using microfiltration membrane modified with zif-8 metal organic frameworks (MOFs). *Chemical Engineering Journal*, 300:273 – 279, 2016.

[154] Z. Hu, Y.i Chen, and J. Jiang. Zeolitic imidazolate framework-8 as a reverse osmosis membrane for water desalination: Insight from molecular simulation. *The Journal of Chemical Physics*, 134(13):134705, 2011.

[155] Y. Pan, T.Li, G. Lestari, and Z. Lai. Effective separation of propylene/propane binary mixtures by ZIF-8 membranes. *Journal of Membrane Science*, 390-391:93 – 98, 2012.

[156] Q. Song, S. K. Nataraj, M. V. Roussenova, J. C. Tan, D. J. Hughes, W. Li, P. Bourgoin, M. A. Alam, A. K. Cheetham, S. A. Al-Muhtaseb, and E. Sivaniah. Zeolitic imidazolate framework (ZIF-8) based polymer nanocomposite membranes for gas separation. *Energy & Environmental Science*, 5:8359–8369, 2012.

[157] J. McEwen, J.-D. Hayman, and A. O. Yazaydin. A comparative study of CO2, CH4 and N2 adsorption in ZIF-8, Zeolite-13X and BPL activated carbon. *Chemical Physics*, 412:72 – 76, 2013.

[158] G. Lu and J. T. Hupp. Metal-organic frameworks as sensors: A ZIF-8 based Fabry-Pérot device as a selective sensor for chemical vapors and gases. *Journal of the American Chemical Society*, 132(23):7832–7833, 2010.

[159] S.-A. Moggach, T.-D. Bennett, and A.-K. Cheetham. The effect of pressure on ZIF-8: Increasing pore size with pressure and the formation of a high-pressure phase at 1.47-gpa. *Angewandte Chemie International Edition*, 48(38):7087–7089.

[160] M. E. Casco, Y. Q. Cheng, L. L. Daemen, and et al. Gate-opening effect in ZIF-8: the first experimental proof using inelastic neutron scattering. *Chemical Communications*, 52:3639–3642, 2016.

[161] O. Karagiaridi, M.B. Lalonde, W. Bury, and et al. Opening ZIF-8: A catalytically active zeolitic imidazolate framework of sodalite topology with unsubstituted linkers. *Journal of the American Chemical Society*, 134(45):18790–18796, 2012.

[162] B. Russell, J. Villaroel, K. Sapag, and et al. O_2 adsorption on ZIF-8: Temperature dependence of the gate-opening transition. *J. Phys. Chem. C*, 118(49):28603–28608, 2014.

[163] Kenneth S.W. Sing S. J. Gregg. *Adsorption, Surface Area and Porosity*. Academic Press, 2nd edition, 1982.

[164] S. Brunauer, P.H. Emmett, and E. Teller. Adsorption of gases in multimolecular layers. *Journal of the American Chemical Society*, 60(2):309–319, 1938.

[165] S. Lowell and J.E. Shields. *Powder Surface Area and Porosity*. Chapman and Hall, 2nd edition, 1984.

[166] G. Fagerlund. Determination of specific surface by the B.E.T. method. *Mat. Constr.*, 6(3):239–245, 1973.

[167] M. Thommes, K. Kaneko, A. V. Neimark, J.P. Olivier, F. Rodriguez-Reinoso, J. Rouquerol, and K. S.W. Sing. Physisorption of gases, with special reference to the evaluation of surface area and pore size distribution (IUPAC technical report). 87(9-10):1051–1069, 2015.

[168] F. Rouquerol; J. Rouquerol; K.S.W. Sing. *Adsorption by powders and porous solids : principles, methodology, and applications*. Academic Press, 1st edition, 1999.

[169] J. Rouquerol; F. Rouquerol; P. Llewellyn; G. Maurin; K.S.W. Sing. *Adsorption by powders and porous solids : principles, methodology, and applications*. Academic Press, 2nd edition, 2013.

[170] D.A. Gomez-Gualdron, P. Z. Moghadam, J. T. Hupp, O.K. Farha, and R. Q. Snurr. Application of consistency criteria to calculate BET areas of micro- and mesoporous metal–organic frameworks. *Journal of the American Chemical Society*, 138(1):215–224, 2016.

[171] M. De Graef and M.E. McHenry. *Structure of Materials: An Introduction to Crystallography, Diffraction and Symmetry*. Cambridge University Press, 1st edition, 2007.

[172] K.E. Van Holde. *Principles of Physical Biochemistry*. Prentice Hall, 1st edition, 1998.

[173] W.F. Hosford. *Materials for Engineers*. Cambridge University Press, 1st edition, 2012.

[174] Sven Henning and Rameshwar Adhikari. *Scanning Electron Microscopy, ESEM, and X-ray Microanalysis*. 2017.

[175] 2 - scanning electron microscopy (SEM) and transmission electron microscopy (TEM) for materials characterization. In Gerhard Hübschen, Iris Altpeter, Ralf Tschuncky, and Hans-Georg Herrmann, editors, *Materials Characterization Using Nondestructive Evaluation (NDE) Methods*, pages 17 – 43. Woodhead Publishing, 2016.

[176] P.W. Hawkes and L. Reimer. *Scanning Electron Microscopy: Physics of Image Formation and Microanalysis*. Springer Series in Optical Sciences. Springer Berlin Heidelberg, 2013.

[177] R. Banerjee, H. Furukawa, D. Britt, C. Knobler, M. O'Keeffe, and O. M. Yaghi. Control of pore size and functionality in isoreticular zeolitic imidazolate frameworks and their carbon dioxide selective capture properties. *Journal of the American Chemical Society*, 131(11):3875–3877, 2009.

[178] H. J. Choi, Mi. Dincă, A. Dailly, and J. R. Long. Hydrogen storage in water-stable metal–organic frameworks incorporating 1,3- and 1,4-benzenedipyrazolate. *Energy & Environmental Science*, 3:117–123, 2010.

[179] D. Feng, K. Wang, Z. Wei, Y.-P. Chen, C. M. Simon, R.K. Arvapally, R. L. Martin, M. Bosch, T.-F. Liu, S. Fordham, D. Yuan, M. A. Omary, M. Haranczyk, B. Smit, and H.-C. Zhou. Kinetically tuned dimensional augmentation as a versatile synthetic route towards robust metal–organic frameworks. *Nature Communications*, 5:5723, 2014.

[180] T.-F. Liu, L. Zou, D. Feng, Y.-P. Chen, S. Fordham, X. Wang, Y. Liu, and H.-C. Zhou. Stepwise synthesis of robust metal–organic frameworks via postsynthetic metathesis and oxidation of metal nodes in a single-crystal to single-crystal transformation. *Journal of the American Chemical Society*, 136(22):7813–7816, 2014.

[181] W. Morris, B. Volosskiy, S. Demir, F. Gándara, P. L. McGrier, H. Furukawa, D. Cascio, J. F. Stoddart, and O. M. Yaghi. Synthesis, structure, and metalation of two new highly porous zirconium metal–organic frameworks. *Inorganic Chemistry*, 51(12):6443–6445, 2012. PMID: 22676251.

[182] S.-S. Chen, M. Chen, S. Takamizawa, M.-S. Chen, Z. Su, and W.-Y. Sun. Temperature dependent selective gas sorption of the microporous metal-imidazolate framework [Cu(L)] [H2L = 1,4-di(1h-imidazol-4-yl)benzene]. *Chemical Communications*, 47:752–754, 2011.

[183] T.F. Liu, D. Feng, Y.-P. Chen, L. Zou, M. Bosch, S. Yuan, Z. Wei, S. Fordham, K. Wang, and H.-C. Zhou. Topology-guided design and syntheses of highly stable mesoporous porphyrinic zirconium metal–organic frameworks with high surface area. *Journal of the American Chemical Society*, 137(1):413–419, 2015.

[184] D. Feng, Z.-Y. Gu, J.-R. Li, H.-L. Jiang, Z. Wei, and H.-C. Zhou. Zirconium-metalloporphyrin PCN-222: Mesoporous metal–organic frameworks with ultrahigh stability as biomimetic catalysts. *Angewandte Chemie International Edition*, 51(41):10307–10310, 2012.

[185] V. Bon, I. Senkovska, I. A. Baburin, and S. Kaskel. Zr- and Hf-based metal–organic frameworks: Tracking down the polymorphism. *Crystal Growth & Design*, 13(3):1231–1237, 2013.

[186] S. Tanaka, K. Fujita, Y. Miyake, M. Miyamoto, Y. Hasegawa, T. Makino, S. Van der P., J. Cousin Saint Remi, T. Van Assche, G. V. Baron, and J. F. M. Denayer. Adsorption and diffusion phenomena in crystal size engineered ZIF-8 MOF. *The Journal of Physical Chemistry C*, 119(51):28430–28439, 2015.

[187] T. D. Bennett and A. K. Cheetham. Amorphous metal–organic frameworks. *Accounts of Chemical Research*, 47(5):1555–1562, 2014.

[188] M. R. DeStefano, T. Islamoglu, S. J. Garibay, J. T. Hupp, and O. K. Farha. Room-temperature synthesis of UiO-66 and thermal modulation of densities of defect sites. *Chemistry of Materials*, 29(3):1357–1361, 2017.

[189] C. Atzori, G. C. Shearer, L. Maschio, B. Civalleri, F. Bonino, C. Lamberti, S. Svelle, K. P. Lillerud, and S. Bordiga. Effect of benzoic acid as a modulator in the structure of UiO-66: An experimental and computational study. *The Journal of Physical Chemistry C*, 121(17):9312–9324, 2017.

[190] O. V. Gutov, S. Molina, E. C. Escudero-Adán, and A. Shafir. Modulation by amino acids: Toward superior control in the synthesis of zirconium metal–organic frameworks. *Chemistry – A European Journal*, 22(38):13582–13587.

[191] Y. Han, M. Liu, K. Li, Y. Zuo, Y. Wei, S. Xu, C. Zhang, G.and Song, Z. Zhang, and X. Guo. Facile synthesis of morphology and size-controlled zirconium metal–organic framework UiO-66: the role of hydrofluoric acid in crystallization. *CrystEngComm*, 17:6434–6440, 2015.

[192] J. E. Mondloch, M. J. Katz, N. Planas, D. Semrouni, L. Gagliardi, J. T. Hupp, and O. K. Farha. Are Zr_6-based MOFs water stable? Linker hydrolysis vs. capillary-force-driven channel collapse. *Chemical Communications*, 50:8944–8946, 2014.

[193] P. Avila, M. Montes, and E. E. Miró. Monolithic reactors for environmental applications: A review on preparation technologies. *Chemical Engineering Journal*, 109(1):11 – 36, 2005.

[194] P. Küsgens, A. Zgaverdea, H.-G. Fritz, S. Siegle, and S. Kaskel. Metal-organic frameworks in monolithic structures. *Journal of the American Ceramic Society*, 93(9):2476–2479, 2010.

[195] M. Soltani, S. Hosseini, and M. R. Malekbala. A review on monolithic honeycomb structures and fabrication techniques. *Journal of Applied Sciences Research*, 9, 01 2013.

[196] E.D. Banús, V.G. Milt, E.E. Miró, and M.A. Ulla. Catalytic coating synthesized onto cordierite monolith walls. its application to diesel soot combustion. *Applied Catalysis B: Environmental*, 132-133:479 – 486, 2013.

[197] T. A. Nijhuis, A. E. W. Beers, T. Vergunst, I. Hoek, F. Kapteijn, and J. A. Moulijn. Preparation of monolithic catalysts. *Catalysis Reviews*, 43(4):345–380, 2001.

[198] J. Li, J. Zhang, Z. Lei, and B. Chen. Pd–Co coating onto cordierite monoliths as structured catalysts for methane catalytic combustion. *Energy & Fuels*, 26(1):443–450, 2012.

[199] S. Lawson, A. Hajari, A. A. Rownaghi, and F. Rezaei. MOF immobilization on the surface of polymer-cordierite composite monoliths through in-situ crystal growth. *Separation and Purification Technology*, 183:173 – 180, 2017.

[200] E.V. Ramos-Fernandez, M. Garcia-Domingos, J. Juan-Alcañiz, J. Gascon, and F. Kapteijn. Mofs meet monoliths: Hierarchical structuring metal organic framework catalysts. *Applied Catalysis A: General*, 391(1):261 – 267, 2011. Recent Developments in Model Catalysis - Closing the Gap to Technical Applications.

[201] F.E. Ghodsi and H. Absalan. Comparative study of ZnO thin films prepared by different sol-gel route. *Acta Physica Polonica A*, 118:659–664, 2010.

[202] W. Xiao, Y. Guo, Z. Ren, G. Wrobel, Z. Ren, T. Lu, and P.X. Gao. Mechanical-agitation-assisted growth of large-scale and uniform ZnO nanorod arrays within 3D multichannel monolithic substrates. *Cryst. Growth & Design*, 13(8):3657–3664, 2013.

[203] I. Safaee, M. Kazemzad, M. Alizadeh, and M.R. Rahimipour. On finding of the optimized condition for preparation of aligned ZnO nanorod arrays on monolithic cordierite honeycomb. *Ceram. Intl.*, 41(10, Part A):12589 – 12594, 2015.

[204] U. P. N. Tran, K. K. A. Le, and N. T. S. Phan. Expanding applications of metal-organic frameworks: Zeolite imidazolate framework ZIF-8 as an efficient heterogeneous catalyst for the knoevenagel reaction. *ACS Catalysis*, 1(2):120–127, 2011.

[205] B. Hachuła and J. Nowak, M.and Kusz. Crystal and molecular structure analysis of 2-methylimidazole. *Journal of Chemical Crystallography*, 40:201–206, 03 2010.

[206] C. Rösler, A. Aijaz, S. Turner, M. Filippousi, A. Shahabi, W. Xia, G. Van-Tendeloo, M. Muhler, and R. A. Fischer. Hollow zn/co zeolitic imidazolate framework (ZIF) and yolk–shell metal@zn/co zif nanostructures. *Chemistry – A European Journal*, 22(10):3304–3311.

[207] Xiaolei Qu, Pedro J.J. Alvarez, and Qilin Li. Applications of nanotechnology in water and wastewater treatment. *Water Research*, 47(12):3931 – 3946, 2013. Nanotechnology for Water and Wastewater Treatment.

[208] E. Diamanti-Kandarakis, J.-P. Bourguignon, L. C. Giudice, R. Hauser, G. S. Prins, A. M. Soto, R. T. Zoeller, and A. C. Gore. Endocrine-disrupting chemicals: An endocrine society scientific statement. *Endocrine Reviews*, 30(4):293–342, 2009.

[209] K. Okuda, T. Fukuuchi, M. Takiguchi, and S. Yoshihara. Novel pathway of metabolic activation of bisphenol a-related compounds for estrogenic activity. *Drug Metabolism and Disposition*, 39(9):1696–1703, 2011.

[210] M. Zhou, Y. Wu, J. Qiao, J. Zhang, A. McDonald, G. Li, and F. Li. The removal of bisphenol A from aqueous solutions by MIL-53(Al) and mesostructured MIL-53(Al). *Journal of Colloid and Interface Science*, 405:157 – 163, 2013.

[211] M. Zielińska, K. Bułkowska, A. Cydzik-Kwiatkowska, K. Bernat, and I. Wojnowska-Baryła. Removal of bisphenol A (BPA) from biologically treated wastewater by microfiltration and nanofiltration. *International Journal of Environmental Science and Technology*, 13(9):2239–2248, Sep 2016.

[212] M. Umar, F. Roddick, L. Fan, and H. Abdul Aziz. Application of ozone for the removal of bisphenol A from water and wastewater – a review. *Chemosphere*, 90(8):2197 – 2207, 2013.

[213] W.-T. Tsai, H.-C. Hsu, T.-Y. Su, K.-Y. Lin, and C.-M. Lin. Adsorption characteristics of bisphenol-A in aqueous solutions onto hydrophobic zeolite. *Journal of Colloid and Interface Science*, 299(2):513 – 519, 2006.

[214] J. Xu, L. Wang, and Y. Zhu. Decontamination of Bisphenol A from aqueous solution by graphene adsorption. *Langmuir*, 28(22):8418–8425, 2012. PMID: 22571829.

[215] M. del-Rio, C. Palomino-Cabello, V. Gonzalez, F. Maya, J. B. Parra, V. Cerdà, and G. Turnes-Palomino. Metal oxide assisted preparation of core–shell beads with dense metal–organic framework coatings for the enhanced extraction of organic pollutants. *Chemistry – A European Journal*, 22(33):11770–11777, 2016.

[216] B. Van de Voorde, B. Bueken, J. Denayer, and D. De Vos. Adsorptive separation on metal–organic frameworks in the liquid phase. *Chemical Society Reviews*, 43:5766–5788, 2014.

[217] B. K. Jung, J. W. Jun, Z. Hasan, and S. H.Jhung. Adsorptive removal of p-arsanilic acid from water using mesoporous zeolitic imidazolate framework-8. *Chemical Engineering Journal*, 267:9 – 15, 2015.

[218] K. W. Chapman, G. J. Halder, and P. J. Chupas. Pressure-induced amorphization and porosity modification in a metal-organic framework. *Journal of the American Chemical Society*, 131(48):17546–17547, 2009. PMID: 19916507.

[219] Françoise Rouquerol, Jean Rouquerol, and Kenneth Sing. Chapter 7 - assessment of mesoporosity. In Françoise Rouquerol, Jean Rouquerol, and Kenneth Sing, editors, *Adsorption by Powders and Porous Solids*, pages 191 – 217. Academic Press, London, 1999.

[220] H. Wu, Q. Gong, D. H. Olson, and J. Li. Commensurate adsorption of hydrocarbons and alcohols in microporous metal organic frameworks. *Chemical Reviews*, 112(2):836–868, 2012. PMID: 22257090.

[221] A. Bhatnagar and I. Anastopoulos. Adsorptive removal of Bisphenol A (BPA) from aqueous solution: A review. *Chemosphere*, 168:885 – 902, 2017.

[222] Y. Dong, D. Wu, X. Chen, and Y. Lin. Adsorption of Bisphenol A from water by surfactant-modified zeolite. *Journal of Colloid and Interface Science*, 348(2):585 – 590, 2010.

[223] Y.F. Onundi, B. A. Drake, R. T. Malecky, M. A. DeNardo, M. R. Mills, S. Kundu, A. D. Ryabov, E. S. Beach, C. P. Horwitz, M. T. Simonich, L. Truong, R.L. Tanguay, L. J. Wright, N. Singhal, and T. J. Collins. A multidisciplinary investigation of the

technical and environmental performances of TAML/peroxide elimination of bisphenol A compounds from water. *Green Chem.*, 19:4234–4262, 2017.

[224] A.I. Schäfer, L.D. Nghiem, and N. Oschmann. Bisphenol A retention in the direct ultrafiltration of greywater. *Journal of Membrane Science*, 283(1):233 – 243, 2006.

[225] Y. Jiao, Y. Liu, G. Zhu, J. T. Hungerford, S. Bhattacharyya, R. P. Lively, D. S. Sholl, and K. S. Walton. Heat-treatment of defective UiO-66 from modulated synthesis: Adsorption and stability studies. *The Journal of Physical Chemistry C*, 121(42):23471–23479, 2017.

[226] M. J. Katz, Z. J. Brown, Y.J. Colón, P. W. Siu, K. A. Scheidt, R. Q. Snurr, J. T. Hupp, and O.K. Farha. A facile synthesis of UiO-66, UiO-67 and their derivatives. *Chemical Communications*, 49:9449–9451, 2013.

[227] M. R. Azhar, H. R. Abid, V. Periasamy, H. Sun, M. O. Tade, and S. Wang. Adsorptive removal of antibiotic sulfonamide by UiO-66 and ZIF-67 for wastewater treatment. *Journal of colloid and interface science*, 500:88—95, August 2017.

[228] M. Sarker, J. Y. Song, and S. H. Jhung. Carboxylic-acid-functionalized UiO-66-NH_2: A promising adsorbent for both aqueous- and non-aqueous-phase adsorptions. *Chemical Engineering Journal*, 331:124 – 131, 2018.

Appendix A

Calculations and Fittings

Application of Rouquerol Criteria for BET Area Evaluation

BET area of all samples was evaluated by following Rouquerol's consistency criteria [169, 170]. This section will outline the BET area calculation procedure. The following example calculation uses the data obtained for sample $_{ZnO}$ZIF-8@Cordierite(Aq) after 5 growth cycles (later Figure A.3 **a**). The central equation of this calculation is the BET correlation, represented by equation A.1, as follows:

$$\frac{P}{V\,(P_0 - P)} = \frac{1}{V_m C} + \frac{C-1}{V_m C} \times \frac{P}{P_0} \tag{A.1}$$

Where V represents the quantity of gas adsorbed (cm^3/g), V_m stands for the adsorbate monolayer volume (cm^3/g), C represents a dimensionless constant related to the heat of adsorption. P and P_0 represent absolute and saturation pressure (mmHg), respectively. BET area of the samples was evaluated by following a number of steps:

- **Step 1**: *Obtaining plot of V(1-P/P$_0$) vs. P/P$_0$. Selection of maximum P/P$_0$.*
  Figure A.1 illustrates V(1-P/P$_0$) and (P/P$_0$)/[V(1-P/P$_0$)] (BET representation in Step 2) as functions of P/P$_0$. According to the 1^{st} of Rouquerol's criteria, the V(1-P/P$_0$) trend determines the maximum limit of P/P$_0$, a specific P/P$_0$ range is selected over which a monotonic increase in V(1-P/P$_0$) is registered. According to Figure A3, a sharp increase in V(1-P/P$_0$) is observed up to $\sim$ 0.05 P/P$_0$ from which point the curve slopes

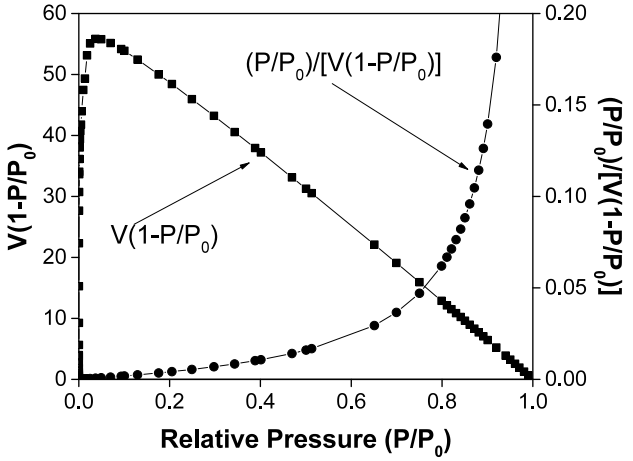

Fig. A.1 Data selection for S_{BET} area calculation for sample A1 @ 5 cycles

downwards towards 1.0 P/P_0. Consequently, the curve representing $(P/P_0)/[V(1-P/P_0)]$ follows a straight line up to the same P/P_0, 0.05, after which it starts to gradually increase in a non-linear fashion. This concludes that only data from 0 to $\sim$0.05 P/P_0 will be used for the BET area evaluation.

- **Step 2**:*Obtaining plot of $(P/P_0)/[V(1-P/P_0)]$ vs P/P_0 (up to maximum P/P_0 selected in Step 1). Evaluation of C and readjustment of P/P_0 range.*

  For every P/P_0 range of interest, the correlation coefficient and C value is evaluated. As illustrated by equation A.1, both V_m and C can be obtained from the values of the intercept and slope of the simulated curve. Figure A.2 demonstrates the selection process of the P/P_0 range by use of BET representation. It can be observed that reducing the maximum P/P_0 to $\sim$ 0.03 and omitting data points in the very low P/P_0 region (below $\sim$ 0.004), a significantly improved correlation coefficient and P/P_0 error are yielded. See Step 4 for the evaluation of P/P_0 error.

- **Step 3**: *Calculation of monolayer loading (V_m) across the selected P/P_0 range.*

  Average monolayer loading is evaluated across the selected P/P_0 linear range via rearrangement of equation A.1, using the value of C obtained in Step 2.

  For every single isotherm data point within the selected range the monolayer loading is evaluated by re-arranging equation A.1 and using the value of C obtained in Step 2. The value of V_m obtained from then matched and its P/P_0 is located.

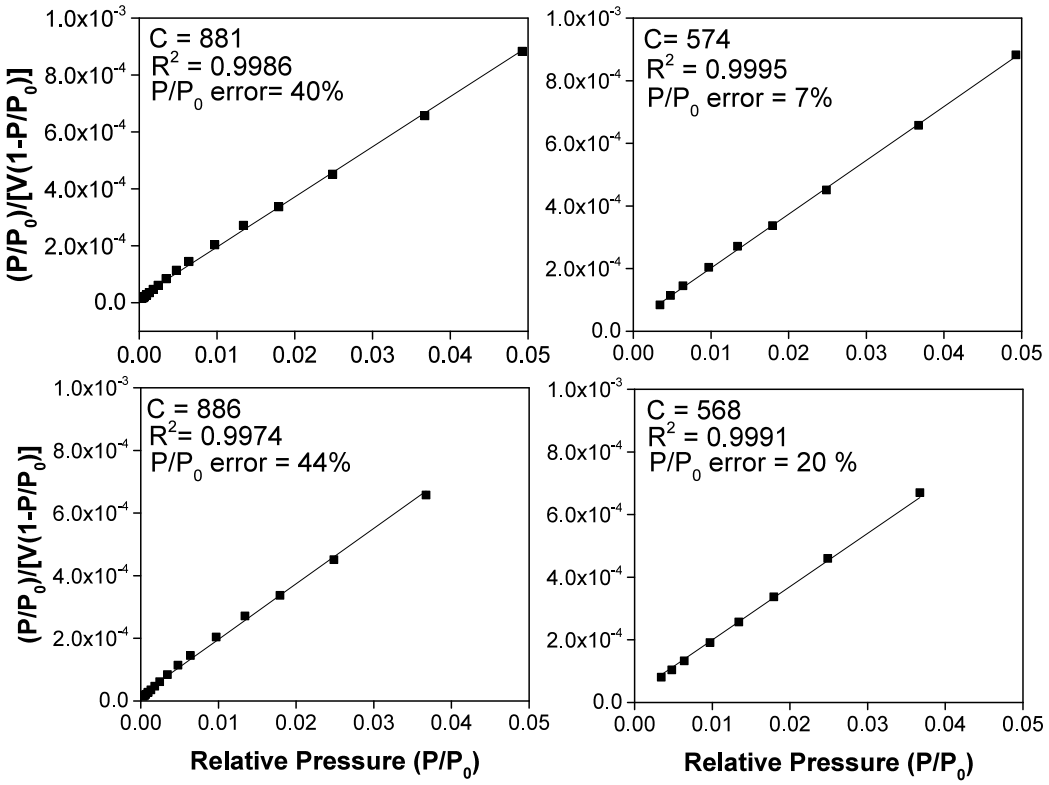

Fig. A.2 P/P_0 selection to minimise P/P_0 error and to maximise goodness of fit

- **Step 4**: *Error evaluation between P/P_0 corresponding to monolayer loading determined in Step 3 and P/P_0 determined from BET theory ($1/(1+\sqrt{C})$)* In this case, the BET estimate of P/P_0 is 0.040, this value is compared to the graphically determined P/P_0 (in Step 3), corresponding to the initially calculated monolayer loading. Thus, the closest P/P_0 value generates a 7% error.
- **Step 5**: *If Steps 1-4 are satisfied, the surface area is evaluated for the selected P/P_0 range.*

Specific BET area is evaluated using the following equation:

$$S_{BET} = \frac{V_m N_a A}{M_v} \tag{A.2}$$

Where N_a represents Avogadro's constant, A is the cross-sectional area of the adsorbate gas (for N_2, 0.162 nm^2) and M_v is the volume occupied by 1 mole of adsorbate gas at standard conditions (for N_2, 22.4 L).

Figure A.3 illustrates the selection process of relevant P/P_0 range for the evaluation of BET area. The graphs on the left demonstrate the application of the 1^{st} consistency criterion (monotonic increase of $V(1-P/P_0)$ [170]) whereby the maximum P/P_0 is selected. The graphs on the right illustrate the linear BET representation of the respective data, consistent with the 2^{nd} consistency criterion, within the selected range of P/P_0, that yields a positive C constant (dimensionless) and a correlation coefficient higher than the required $R^2 \geq 0.995$.

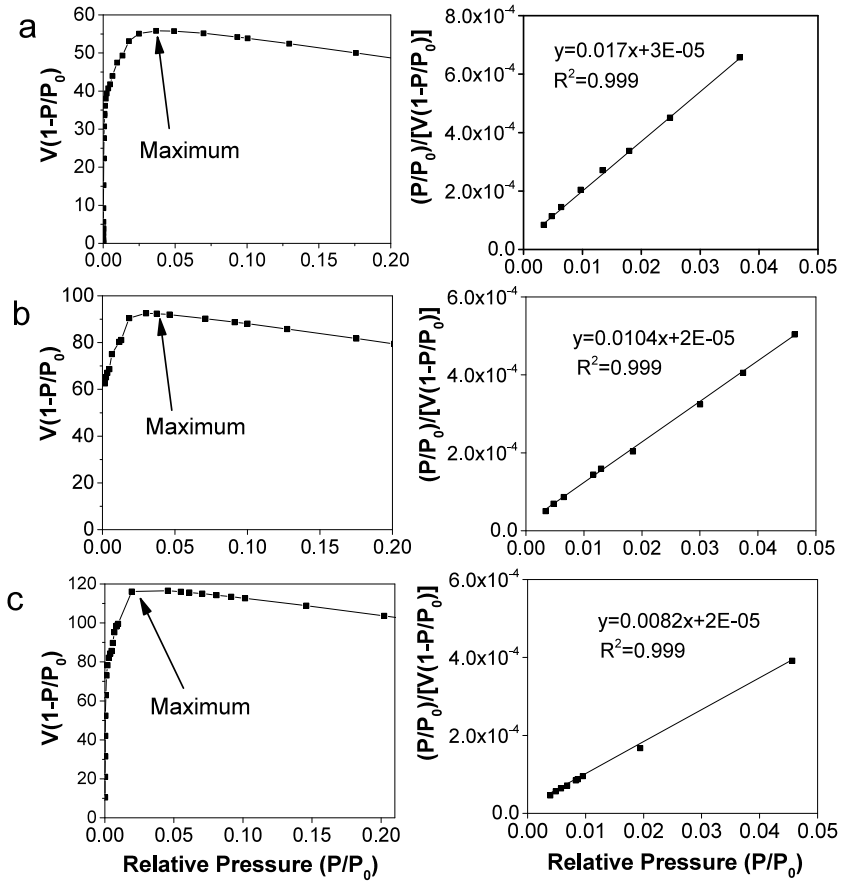

Fig. A.3 Criteria used for the evaluation of BET surface area of $_{ZnO}$ZIF-8@Cordierite(Aq). The determination of the point of maximum relative pressure illustrated on the left and the fitted BET representation of the selected relative pressure region used for BET calculation on the right. **a** 5 cycle growth, **b** 30 cycle growth, **c** 47 cycle growth

Pseudo-second order kinetic fittings

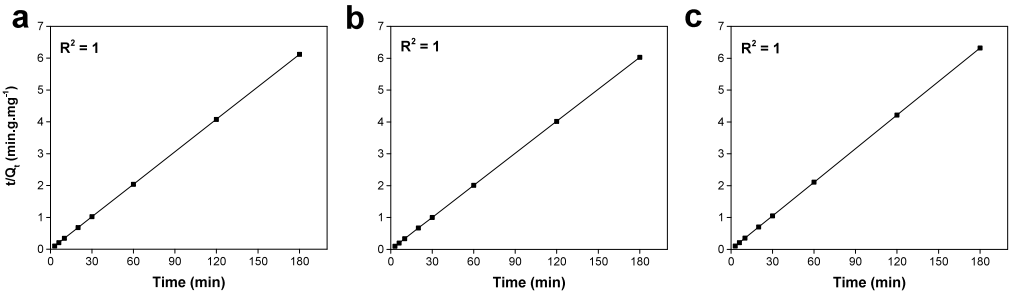

Fig. A.4 Pseudo-second-order kinetic fits for **a)** $_{powd}$ZIF-8, **b)** $_{mono}$ZIF-8(FP) and **c)** $_{mono}$ZIF-8(SP) for C_0 = 300 ppm, m = 100 mg and V = 10 mL

Figure A.5 shows the dynamic adsorption data for ZIF-8 samples exposed to initial concentrations of BPB of 100 and 200 ppm.

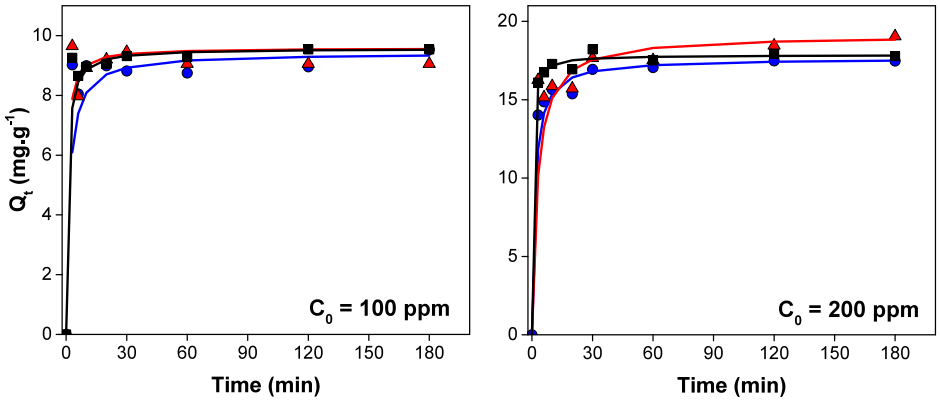

Fig. A.5 Dynamic adsorption of BPB on ZIF-8 adsorbent in 10 mL solutions and fitted pseudo-second-order rate curves with C_0 = 200 and 100 ppm, m = 100 mg and V = 10 mL where $_{powd}$ZIF-8, black line and black squares; $_{mono}$ZIF-8(SP), blue line and blue circles; $_{mono}$ZIF-8(FP), red line and red triangles. Error bars represent the standard deviation of each data point.

Figure A.6 Table A.1 illustrate the pseudo-second-order kinetic rate fittings and parameters for ZIF-8 samples exposed to starting concentration of 100 ppm.

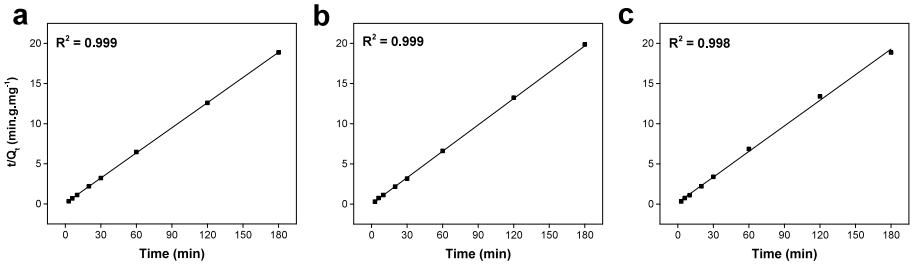

Fig. A.6 Pseudo-second-order kinetic fits for **a)** $_{powd}$ZIF-8, **b)** $_{mono}$ZIF-8(FP) and **c)** $_{mono}$ZIF-8(SP) for C_0 = 100 ppm, m = 100 mg and V = 10 mL

Sample	k_2 x 10^3 (mg.g^{-1}.min^{-1})	Q_e (mg.g^{-1})	R^2
$_{mono}$ZIF-8(FP)	1662 .1	9.1	0.999
$_{mono}$ZIF-8(SP)	64.9	9.4	0.998
$_{powd}$ZIF-8	132.2	9.6	0.999

Table A.1 Pseudo-second order kinetic constant, k_2, and capacity, Q_e, derived from the kinetic adsorption experiments conducted with 10 mL of 100 ppm BPB and 0.1 gram of adsorbent.

Figure A.7 and Table A.2 illustrate the pseudo-second-order kinetic rate fittings and parameters for ZIF-8 samples exposed to starting concentration of 200 ppm.

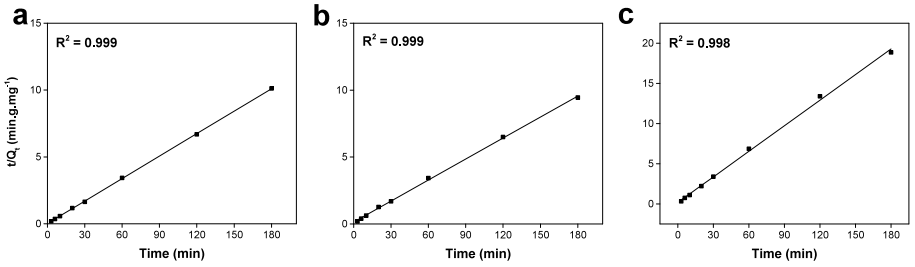

Fig. A.7 Pseudo-second-order kinetic fits for **a)** $_{powd}$ZIF-8, **b)** $_{mono}$ZIF-8(FP) and **c)** $_{mono}$ZIF-8(SP) for C_0 = 200 ppm, m = 100 mg and V = 10 mL

Figure A.8 illustrates the pseudo-second order kinetic fittings for UiO-66 samples exposed to 300 ppm starting concentration of BPB.

Sample	k_2 x 10^3 (mg.g^{-1}.min^{-1})	Q_e (mg.g^{-1})	R^2
$_{mono}$ZIF-8(FP)	187.0	29.9	1
$_{mono}$ZIF-8(SP)	102.7	28.5	1
$_{powd}$ZIF-8	128.4	29.4	1

Table A.2 Pseudo-second order kinetic constant, k_2, and capacity, Q_e, derived from the kinetic adsorption experiments conducted with 10 mL of 200 ppm BPB and 0.1 gram of adsorbent.

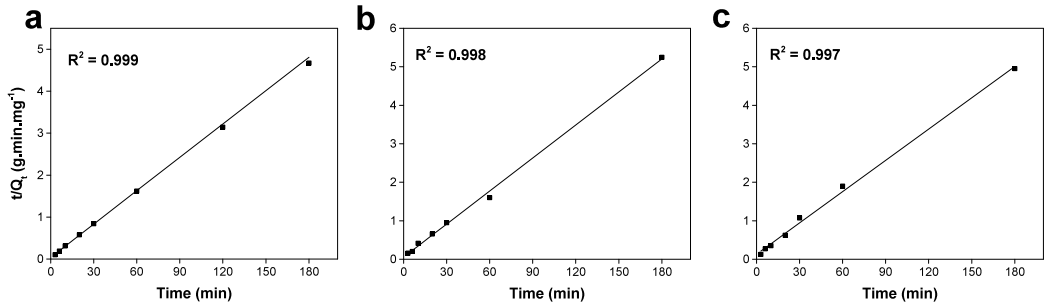

Fig. A.8 Pseudo-second-order kinetic fits for **a)** $_{powd}$UiO-66, **b)** $_{mono}$UiO-66(EtOH) and **c)** $_{mono}$UiO-66(DMF) for C_0 = 300 ppm, m = 100 mg and V = 15 mL

Langmuir Fittings

Sample	Q_{max} (mg.g^{-1})	K_L (mg^{-1}.ml^{-1})	χ^2
$_{mono}$UiO-66(EtOH)	44.8	0.66	28.2
$_{mono}$UiO-66(DMF)	58.5	0.02	81.2
$_{powd}$UiO-66	75.8	18.85	29.6

Table A.3 Pseudo-second order kinetic constant, k_2, and capacity, Q_e, derived from the kinetic adsorption experiments conducted with 10 mL of 200 ppm BPB and 0.1 gram of adsorbent.

Appendix B

Additional Data

HKUST-1 Stability data

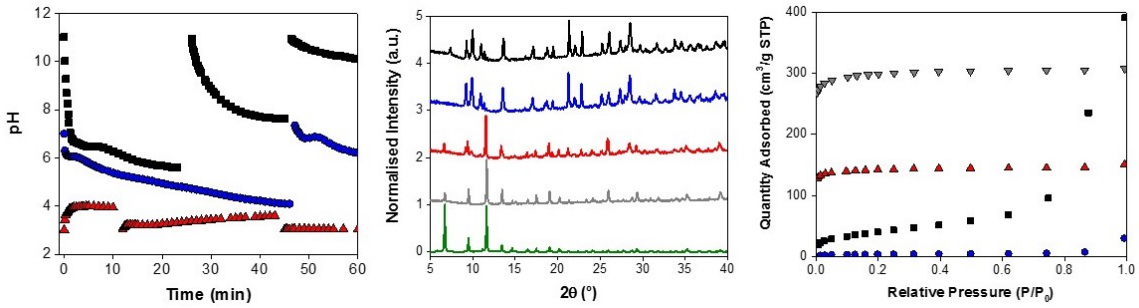

Fig. B.1 Stability data for powdered HKUST-1. **Left**: pH evolution curves at starting pH of 3, 7 and 11 showing that HKUST tends to equilibrate in the acidic region. Showing very big pH changes in basic and neutral environments. **Centre**: X-ray diffraction patterns of untreated (grey), simulated (olive) and recovered materials from pH 3 (red), 7 (blue) and 11 (black) samples showing the formation of a different phase other than HKUST-1 when this material is exposed to pH 11 and 7, some HKUST-1 phase is preserved at pH 3. **Right**: Nitrogen adsorption isotherms at 77 K illustrating the uptake for untreated (grey inverted triangles) HKUST-1 as well as recovered samples from pH 3 (red triangles), pH 7 (blue circles) and 11 (black squares). This shows that, in agreement with the respective X-ray diffractogram, some porosity is maintained at pH 3, on the other hand, at pH 7 and 11 the porosity is completely collapsed.

MOF-808 SEM

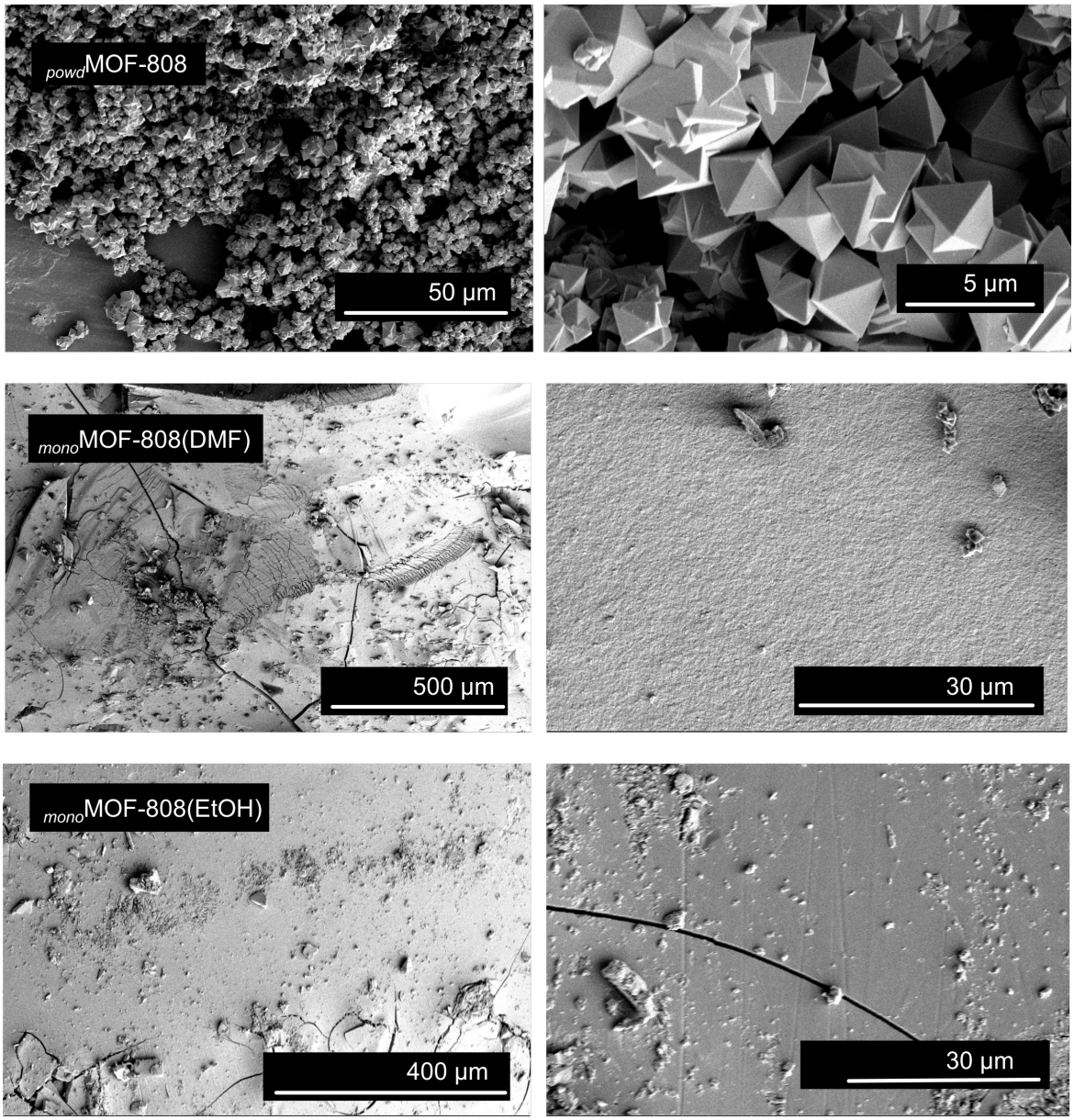

Fig. B.2 SEM micrographs of MOF-808 samples

Recovered ZIF-8 samples post BPB adsorption

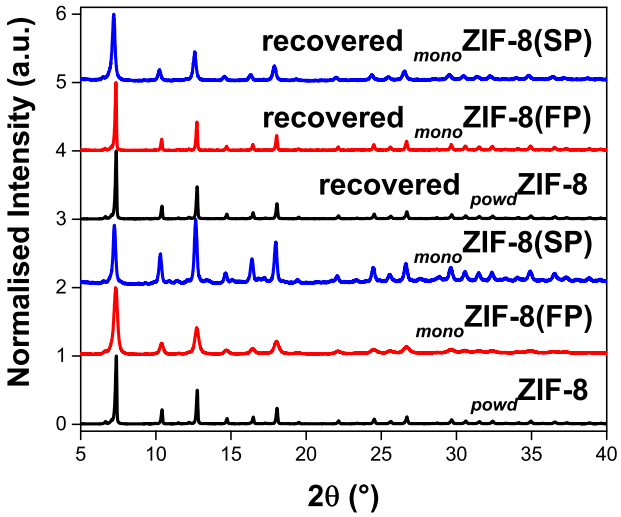

Fig. B.3 X-ray diffraction patterns of EtOH washed recovered ZIF-8 samples

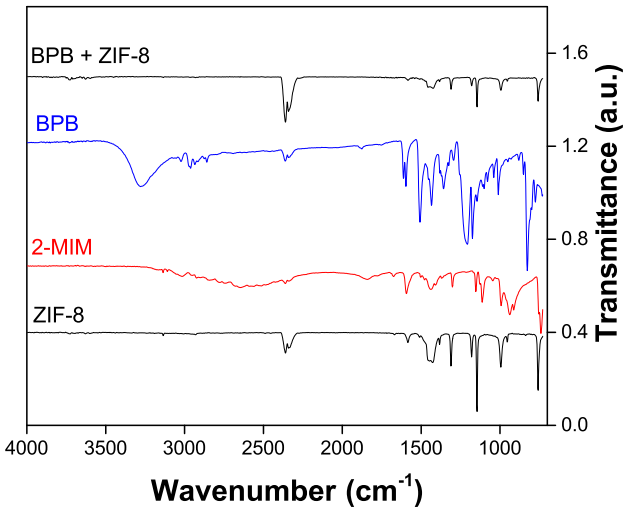

Fig. B.4 FT-IR spectra of pristine BPB, 2-MIM and ZIF-8 as well as that of a used ZIF-8 sample

Removal efficiency of BPB with ZIF-8 adsorbent

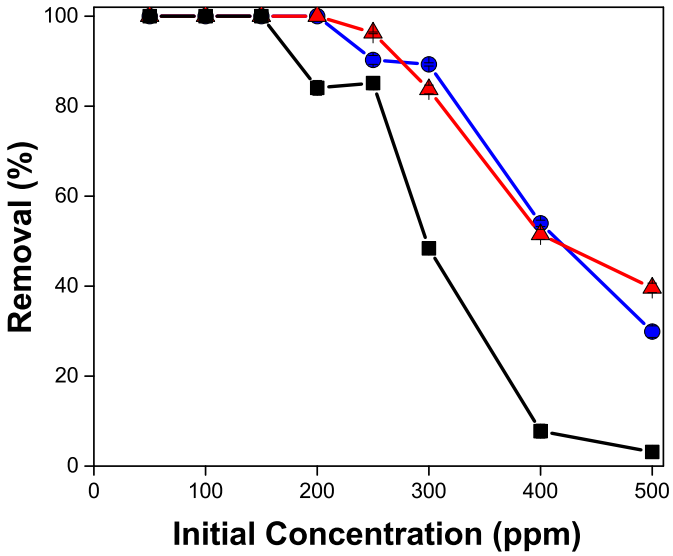

Fig. B.5 Removal efficiency of BPB with $m = 100$ mg, $V = 5$ mL on $_{powd}$ZIF-8, black squares; $_{mono}$ZIF-8(SP), blue circles; $_{mono}$ZIF-8(FP), red triangles.

Removal efficiency with varying ZIF-8 adsorbent dosage

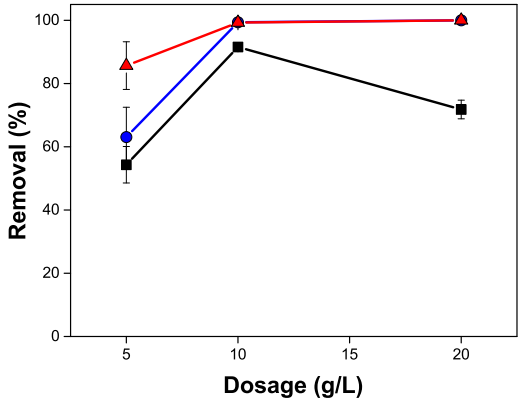

Fig. B.6 Removal efficiency of BPB with varying adsorbent dosage on $_{powd}$ZIF-8, black squares; $_{mono}$ZIF-8(SP), blue circles; $_{mono}$ZIF-8(FP), red triangles.

Elemental analysis of monolithic UiO-66 samples

Sample	Theoretical	$_{mono}$UiO-66(DMF)	$_{mono}$UiO-66(EtOH)
Zirconium	32.9	31.6	29.7
Carbon	34.6	32.0	31.7
Hydrogen	1.7	2.0	2.2
Nitrogen	0.0	0.3	0.0

Table B.1 Elemental analysis of $_{mono}$UiO-66. The experimentally determined elemental composition (%) of $_{mono}$UiO-66 was obtained by inductively coupled plasma-optical emission spectroscopy (ICP-OES). The theoretical composition was calculated from the chemical formula (Zr_6(-OH)$_4$O$_4$(BDC)$_6$). Any experimental deviation from the theoretically calculated elemental composition is considered a defectuous crystal structure. In this case, missing linker defects are inferred from the lower experimentally observed carbon composition relative to the theoretical composition, as well as the deviation from the adsorption capacity shown in Chapter 5. Additionally, the increased hydrogen content of the experimental samples may indicate the presence of water in the crystal structure. Although all samples were thoroughly degassed prior to analysis, foreign species from the air can be adsorbed by the MOFs during the ICP-OES sample preparation procedure.

Removal efficiency with varying UiO-66 adsorbent dosage

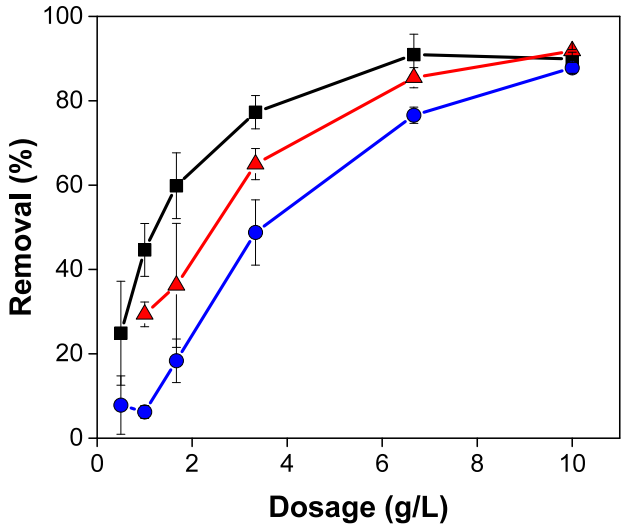

Fig. B.7 Removal of BPB as a function of dosage on $_{\text{powd}}$UiO-66, black squares; $_{mono}$UiO-66(EtOH), blue circles; $_{mono}$UiO-66(DMF), red triangles. As shown, the three different samples demonstrate differing BPB removal behaviour with increasing adsorbent dosage, with increasing removal from $_{mono}$UiO-66(EtOH), $_{mono}$UiO-66(DMF) and, finally, $_{\text{powd}}$UiO-66. The three curves eventually converge at the highest adsorbent dosage (10 g.L^{-1}). This difference in removal behaviour, especially at low adsorbent dosage, is attributed to the high external surface area (for $_{powd}$UiO-66) whereas the difference in the behaviour of the monolithic samples is correlated to the density of the respective monoliths. Sample $_{mono}$UiO-66(DMF) expresses a higher density (0.848 g.cm^{-3})hence a higher overall removal capacity and vice versa for $_{mono}$UiO-66(EtOH) (0.434 g.cm^{-3}).

ZIF-8@Cordierite SEM

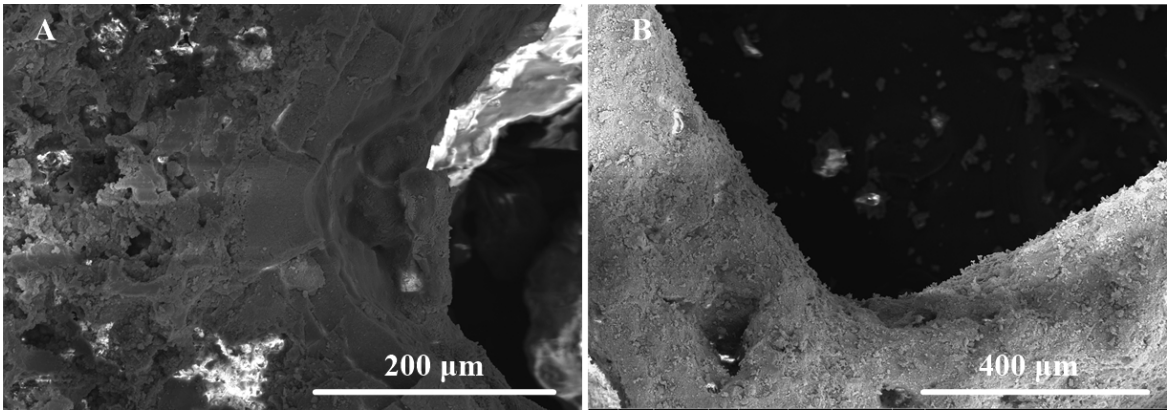

Fig. B.8 Cross-sectional SEM micrographs of sample $_{ZnO}$ZIF-8@Cordierite(Aq) after **A** 30 growth cycles and **B** 47 growth cycles. This suggests that extending the number of growth cycles appears to completely saturate the cordierite surface with ZIF-8, showing a uniformly covered channel.

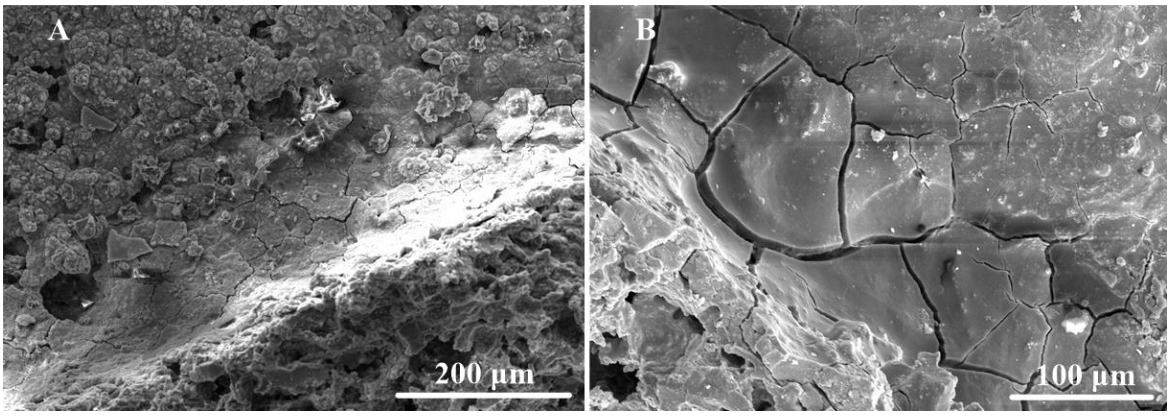

Fig. B.9 Lateral SEM micrographs of sample $_{ZnO}$ZIF-8@Cordierite(EtOH) **A** after 30 growth cycles, **B** after 72 growth cycles. Similarly to Figure B.8, a layer of ZIF-8 concentrated around the corner and more evenly deposited along the length of the channel is observed for sample $_{ZnO}$ZIF-8@Cordierite(EtOH) after 30 growth cycles. The same sample after 72 growth cycles does not show the surface imperfections of the cordierite monolith substrate, due to complete coverage with a thick and uniform ZIF-8 film.